POLITECNICO DI MILANO
DEPARTMENT OF MECHANICAL ENGINEERING
DOCTORAL PROGRAMME IN MECHANICAL ENGINEERING

Development of Processing and Monitoring Strategies for Laser Surface Texturing of TiN coatings

Doctoral Dissertation of
Ali Gökhan DEMİR
25th Cycle
ID No 753704

Supervisor:
Prof. Barbara Previtali

Co-Supervisor:
Prof. William O'Neill

Tutor:
Prof. Bortolino Saggin

The Chair of the Doctoral Program:
Prof. Bianca Maria Colosimo

2013

For that which became a passion.

Contents

List of Figures

List of Tables

Abstract

Laser micromachining and structuring of thin ceramic surface coatings is an appealing process, especially for tribological applications. Studies show increased wear resistance and friction properties of dimpled surface coatings. The nature of the material and the delicacy of the integrity of the applied layer raise the problem of tight processing conditions, especially in terms of the ablated depth. However, for the industrial scale of the application, processing strategies with industrial grade laser systems are required. Fibre lasers with ns pulses are characterized by high productivity with good machining quality, and allow flexible and robust operation due to their simple solid state architecture. Therefore these sources stand out as tool that can meet the requirements of industrial scale large area texturing operations.
On the other hand, machining depth in laser micromachining remains as a parameter that is determined by the complex interaction mechanism between material and beam. Depth variations commonly occur due factors such as material anisotropy and laser energy fluctuations. A monitoring technique for ablation depth therefore becomes of great interest for machining coating materials with limited thickness.
This work reports the processing and monitoring strategies for laser surface texturing of ceramic TiN coatings. Three pulsed fibre laser sources with pulse durations ranging between 1-250 ns and wavelengths of 0.5 µm and 1 µm were employed. Processing strategies were developed for each laser system and effective control of the dimple diameter and depth without excessive machining to cause substrate contamination was demonstrated. A depth monitoring system based on self-mixing interferometry was designed and implemented. The system had resolution of 29 ns in time and 0.4 µm in depth. The measurement performance was compared to a commercial focused variation microscopy profiler and no statistical evidence of difference in measurements was found.
Keywords: TiN; Dimpling; Fibre laser; Self-mixing interferometry

Sommario

Le microlavorazioni per la texturizzazione superficiale dei rivestimenti ceramici sottili sono processi interessanti che generano grande attrattiva, soprattutto per le applicazioni tribologiche. Gli studi mostrano l’aumento della resistenza ad usura e di attrito dei rivestimenti texturizzati con micro-fossette (dimples). La natura del materiale e la necessità di avere integrità per lo strato applicato sollevano il problema di avere a che fare con condizioni di lavorazione strette, soprattutto in termini di profondità di ablazione. Tuttavia, per la collocazione industriale dell'applicazione, sono necessarie strategie di microlavorazione con sistemi laser di tipo industriale. I

laser in fibra con impulsi ai ns sono caratterizzati da elevata produttività e da una buona qualità di lavorazione e permettono un funzionamento flessibile e robusto grazie alla loro architettura semplice data dallo stato solido. Pertanto queste sorgenti si distinguono come strumenti in grado di soddisfare le esigenze di natura industriale nel caso delle operazioni di texturizzazione delle grandi aree. D'altra parte, la profondità di ablazione nelle microlavorazioni laser rimane un parametro che viene determinato dal meccanismo di interazione complessa tra materiale e fascio laser. Variazioni di profondità si verificano, comunemente, a causa di fattori quali l'anisotropia del materiale e le fluttuazioni di energia laser. Una tecnica di monitoraggio per la profondità di ablazione diventa quindi di grande interesse per la lavorazione dei rivestimenti con spessori limitati.
Questo lavoro riporta le strategie di lavorazione e di monitoraggio per la texturizzasione laser delle superfici nei rivestimenti TiN. Sono stati impiegate tre sorgenti di laser in fibra impulsato con durate di impulso che variano tra 1-250 ns e lunghezze d'onda di 0,5 µm e 1 µm. Le strategie di lavorazione sono state sviluppate per ciascun sistema laser; il controllo effettivo del diametro e della profondità delle fossette ha permesso di dimostrare che non si ha contaminazione del substrato nel caso di lavorazioni non eccessive. Un sistema di monitoraggio di profondità basato sull'interferometria laser da automiscelazione è stato progettato ed implementato. Il sistema ha risoluzione di 29 ns di tempo e 0,4 micron di profondità. Le prestazioni di misura sono state confrontate con un profilometro ottico basato sul principio della variziaone di fuoco e non è stata trovata nessuna evidenza statistica che dimostrasse differenza nelle misure.
Parole chiave: TiN; Dimpling; Laser in fibra; Interferometria laser da automiscelazione di fase

Özet

İnce seramik yüzey kaplamalarının lazerle mikro işleme ve yüzey yapılandırma yöntemleri özellikle trıibolojik uygulamar açısından oldukça cezbedici imkanlar sağlamaktadır. Bilimsel araştırmaların sonuçları mikro çukurlarla işlenmiş yüzek kaplamalarının sürtünme özellikleri ve aşınma dayanımını iyileştidiğini göstermektedir. Kaplama malzemesinin doğası ve kaplanan katmanın hassasiyeti lazer işleme koşullarını, özellikle ablasyon derinliğinin kontrolünü zorlaştırmaktadır. Ancak endüstriyel ölçekte uygulamar için endüstriyel koşullara uygun lazer sistemleri ile işleme stratejilerinin geliştirilmesi gerekmektedir. Nanosaniye impuls genişliğiyle çalışan fiber lazer sistemeleri yüksek üretkenlik ve uygun işleme kalitesi karakterüstiklerine sahiptir ve de katı hal lazer yapıları sayesidnde esnek ve endüstriyel ortamlara dirençli imalat olanağı sağlamaktadır. Bu bakımdan, bu lazer

sistemleri endüstriyel boyutta geniş alan yüzey dokulandırma işlemleri için uygun araçlar olarak öne çıkmaktadırlar.
Öte yandan laze mikroişlemede işleme derinliği lazer ışını ile malzeme arasındaki karmaşık etkileşim mekanizmalarına bağlıdır. İşleme sırasındaki derinlik değişimleri malzeme anizotropisi ve lazer enerjisindeki dalgalanmalara bağlı olarak gelişmektedir. Bu yüzden işleme derinliğini işleme sırasında ölçebilecek bir yöntem sınırlı kalınlığa sahip yüzey kaplamaları söz konusu olduğunda yüksek önem arz etmektedir.
Bu tezde seramik TiN kaplamalarının lazerle yüzey dokulandırılması işlemi için işleme ve izleme stratejileri geliştirilmiştir. İmpuls genişlikleri 1 ila 250 ns arasında ve dalga boyları 0,5 ile 1 µm olan üç farklı fiber lazer sistemi kullanılmıştır. Her lazer sistemi için ayrı işleme stratejileri geliştirilmiş ve mikro çukurların çap ve derinlikleri etkin bir şekilde değiştirilebilmiş, alt tabaka malzemenin kaplamaya karışması engellencek hassasiyet sağlanmıştır. Kendine karışımlı interferometri yöntemiyle çalışan bir derinlik izleme sistemi tasarlanmış ve uygulanmıştır. İzleme sistemi 29 ns zaman 0,4 µm derinlik çözünürlüğüne sahiptir. Sistemin ölçüm performansı odak değilimi mikroskopisi prensibiyle çalışan ticari bir yüzey profilometre sistemiyle karşılaştırılmış ve ölçümler arasında istatiksel bir fark gözlemlenmemiştir.

Anahtar kelimeler: TiN; Çukurlama; Fiber lazer; Kendine karışımlı interferometri

Introduction

Control of surface topography and texture has been a subject matter of different applications, from macro scale mechanical components in terms of surface roughness to conform the quality restrictions and associated tolerances; to micro scale MEMS applications, where stiction phenomenon plays a crucial role in the functionality of the component. In the vast majority of engineering applications, the major attention has been so far concentrated on the first subject. Today, the attention on treating surfaces as functional aspect of a component grows, and the ideal of achieving designed or tailored surfaces becomes more relevant. Direct writing with the laser beam is the most flexible among different processes, since the same optical chain can be manipulated to work on different materials and patterns. A single tool for flexible machining conditions which can be adapted to different applications is an attractive solution for industrial use. The other advantages of laser processing such as fast machining and being environmentally friendly, renders this process more appealing. Today laser surface texturing (LST) is an ever growing application field that unites the micro geometries to large areas to render the surface functional for the specific application. However, the role of laser as an enabling tool is limited in the larger extent of surface texturing.

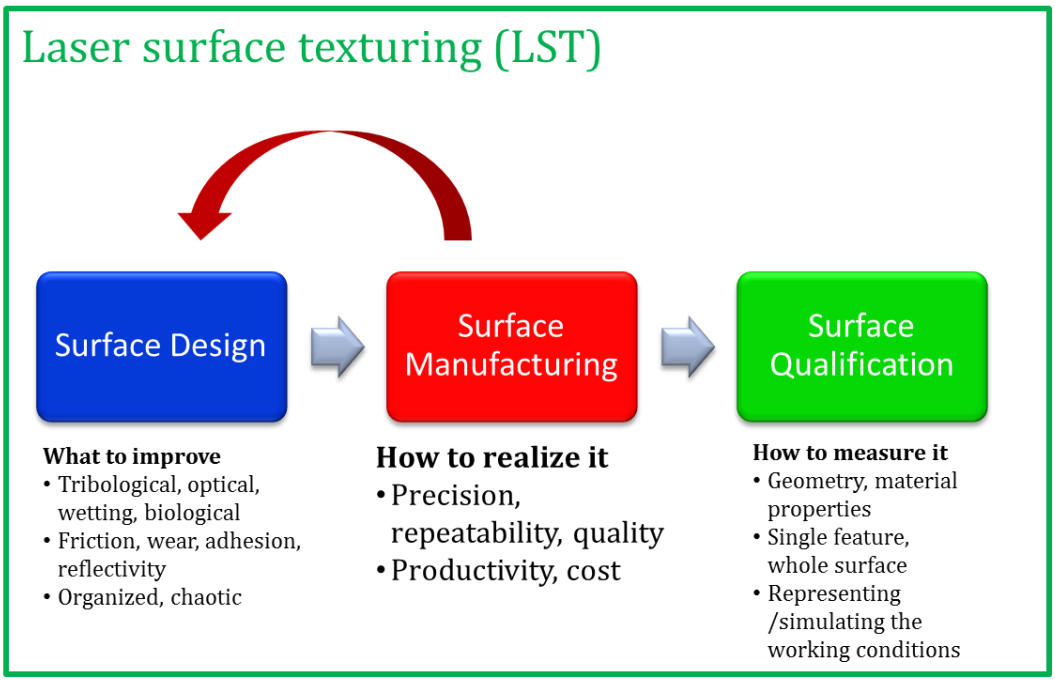

Figure 1. The linear approach to functional surface generation by LST.

A general scheme as seen in Figure 1 can be proposed to explain the different phases considering LST, which can be extended to other surface texturing processes as well. The scheme involves a linear approach to functional surface generation based on 3 main steps. The first step considers a surface design that should improve a certain property of the textured component by giving functionality to the surface. The surface design should determine the exact requirements and use modelling methods to converge to a geometric solution. The role of surface manufacturing is realizing the surface texture by respecting the design criteria. Moreover, it is crucial that the surface manufacturing method is capable of providing required precision, repeatability and quality with high productivity and low cost. Surface qualification is the step where the manufactured surface is verified both geometrically and in terms of functionality by simulated tests or under actual working conditions. The presented linear approach represents the ideal conditions, since today LST operations are based on continuous iterations between the three phases. This is due to the different levels of maturity in different parts of the scheme. Manufacturing methods, especially laser micromachining processes have made a tremendous leap in the last few decades in scientific domain, and today have reached industrial acceptance in many industries. Pulsed laser sources are becoming more robust and less costly, which increase their availability. Surface metrology is one of the most important factors that enabled the leap in micromachining, since they provided the means to measure sub-mm features in 3D. Today the number of commercially available instruments based on confocal microscopy, white light interferometry, and focus variation microscopy are higher than ever. However, micro metrology has still a long way to go compared to its well established counterpart, macro metrology. Problems related to detaching surface geometry and texture components, resolution, and repeatability are recent discussion topics in research. The other side of surface qualification regarding the testing of surface functionality is another complex issue. The most direct approach to test the functionality on the final product is not convenient, whereas conditions simulating the product are difficult to determine. The most widely studied tribological tests for instance can be applied in many different combinations such as pad-on-disc, pin-on-disc, ball-on-disc and have numerous load, speed, and lubrication combinations. This is due to the complexity of the simulated phenomenon, since the example case wear has a number of different mechanisms. Perhaps the weakest link in the surface texturing chain is the surface design. As a matter of fact, the scientific world is still exploring the possibilities that the surface offers and trying to model the physics behind the observed phenomenon. Due to this fact, in practice several different surface geometries are considered and the optimal result is sought empirically and physical interpretations are used to explain the best performance. This approach is not time and cost effective and results are valid for a limited application region. Future applications of textured surfaces need direct design parameters for flexible industrial application, and the use of digital manufacturing technologies such as laser micromachining can allow the realization of the designed surfaces by means of

CAD/CAM systems. Today such approach is used for aesthetic laser surface engraving in mm dimensions. The use of designed surface geometry on mould making has opened up many possibilities in automotive and consumer product sectors by reducing operational costs, increasing precision and repeatability, as well as adding value to the product. It is expected that such approach will be implemented in near future to functional surface design.

Another important factor for the feasibility of the linear approach is that the obtainable surface geometries should be known to the surface designer. This involves dimensional ranges, precision, and available geometries. Such information regarding the laser micromachining would be minimum feature size obtainable by direct writing, different beam geometries obtainable with diffractive optics, or the possibility to obtain sub-micron sized features with interference patterns. The present PhD thesis therefore finds itself in the middle of the proposed linear approach and aims to provide means to high precision micromachining solutions with the use highly productive and robust fibre laser sources. Furthermore addresses the most critical point in the machining process, depth, with a monitoring solution to investigate possibilities to render the process more controllable. The results are analysed both from industrial manufacturing and process physics perspectives for better comprehension of the micromachining method. The main parts of the project are depicted in Figure 2.

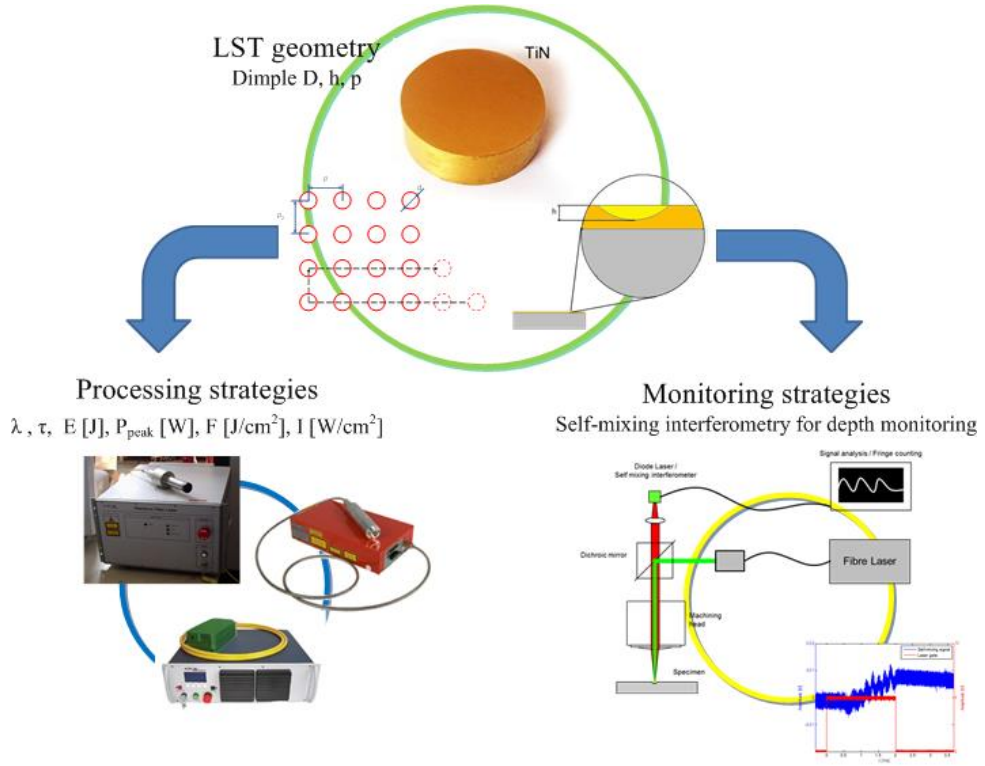

Figure 2. The PhD project scheme depicting the two main parts of the work.

The thesis proposes pulsed fibre lasers as an industrial option in laser micromachining. The last decade has seen the so called revolution of fibre lasers; the use of high brilliance beams in industrial manufacturing processes such as welding, cutting, and cladding. While the impact of fibre lasers on the macro applications field was remarkable, such impact was not present in micro applications field. This is mainly due to the fact that the principal requirement of micro field is the feasibility of generating high quality micro features, which is predominantly determined by the pulse duration, and wavelength of the laser. Despite their delicate structure and the high complexity, ultra-fast lasers were accepted to be the best solution for improved machining quality. On the other hand, the use of fibre lasers provide flexibility both in terms of tunability of the process parameters, but also the process nature itself as demonstrated in this work. This fact renders them more appealing for main-stream industrial micro applications. Today, pulsed fibre lasers are approaching even more increased flexibility in terms of pulse shape and duration regulation in ns regime with increased peak powers. Pulse durations are reducing to ps regime, and wavelengths in visible and UV range are introduced, without compromising the robustness and simplicity of the source. It can be foreseen that the real added value of pulsed fibre lasers in near future will be the simplification of operation in micro field, and bridging micro features to the macro surfaces as depicted herein with the surface texturing applications.

The investigated material in the thesis is ceramic TiN coatings on steel substrates. The case study constitutes an industrially relevant issue; friction reduction of cold drawing dies in limited lubrication conditions. The multi-layer material is a challenging condition for high precision laser micromachining due to distinct material properties of the coating and the substrate. The micromachining of ceramic materials alone is highly relevant research topic in other sectors such as electronics and biomedical device making. The laser micromachining results are of further value for these sectors and their use can be extended to other applications. In particular 3 different laser systems with pulse durations varying between 1-250 ns and 0.5 µm and 1 µm have been employed. Different laser processing strategies are developed for each laser source, and quality and productivity aspects are assessed.

The thesis proposes an in-line process monitoring method for laser microdrilling that realizes individual micro geometry during LST. Such monitoring conditions constitute many difficulties due to complex and fast process dynamics. Attempting to measure the ablation depth in the region of a few µm, inside a microhole, within the time scale of a few µs is a difficult task both optically and mechanically. Laser ablation is a local explosion phenomenon, where material is removed in the form of melt, vapour, and small particles with the generation of plasma emission. The use of an interferometric technique is opportune since it allows high resolution both in space and time. However, the method should be adapted to measure the ablation depth passing through the turbid ablation region. Moreover, the problems related to the accuracy of such a measurement system have not been addressed in the literature.

This thesis work details the design criteria, limitations, and the measurement performance of the self-mixing interferometry system.
The development of processing and monitoring of LST of TiN coatings with ns pulsed fibre lasers are reported in the following 7 chapters after this Introduction. Chapter 1 reports the Aims of the Work detailing the project objectives. Chapter 2 summarizes the general Methodology listing the used approaches and models. Chapter 3 reports the literature survey and State of the Art in related research fields. In Chapter 4 the materials and instrumentation used in laser micromachining are presented. In Chapter 5 the processing strategies are developed for each fibre laser source and evaluated by designed experiments. Chapter 6 explains the design and development of the self-mixing interferometry system for online ablation depth monitoring. Chapter 7 summarizes the work, listing the Conclusions and the possible future works.

Chapter 1

Aims of the Work

This PhD thesis aims to development both processing and monitoring strategies for laser surface texturing (LST) of TiN coatings. Although it is a much wider term, LST is mostly referred to processes regarding the generation of numerous blind micro holes (dimples) on relatively large surfaces to improve tribological performance, which is also the application of this study. The necessity to develop processing strategies derives from the peculiarity of machining a coating material with finite thickness, and that is essentially different from the substrate material in terms of physical and optical properties. The necessity to develop a monitoring strategy derives from the need to have a robust process in large processing areas. Indications regarding the industrial feasibility and productivity are provided, though it is not the aim of this work to provide industry-ready surface texturing solutions.

In particular, the investigated application is the texturing of cold drawing dies with hard solid ceramic coatings. These components undergo high friction forces, which can generate defects on the die itself or the component realized with it. Laser surface texturing is a promising method to reduce friction and wear of the component, which requires further attention to adapt to the current combination. The tribological performance of the component depends on the dispersion of dimples in space and their geometrical attributes defined by the laser processing conditions. Additionally, the machining quality directly affects the surface functionality. On the other hand, LST has to become an economical process for industrial viability. The characteristics of the used laser system that consists of the laser source, beam manipulation, and regarding automation are essential for improved productivity with desired quality. In the present context, LST is destined to be applied to single or small batch components of high value. These components, due to dimensions are also difficult to measure or control after process. Bearing in mind the texture dimensions, the control method would be based on high resolution microscopy applied on large surfaces. Such instruments adaptable to free form of different dies are still not commercially available. This means the process stability is crucial, which emphasizes the need of on machine, in-line measurement capabilities.

The thesis work is developed in a much smaller and well-defined region of interest within the very large LST concept. The following describes first the aspects related to other disciplines that determine the macro application region of the LST, and then limits imposed by the project partners. Within this generated focus scheme, technologies proposed to develop the LST solution are described. Finally the project outline is depicted.

1.1 The cross-disciplinary character of the work

The performance of the textured surface depends on the tribological system that involves the bulk material of the component, coating, the texture, lubrication conditions, and the second body relatively moving across the component. Such interaction is a complex study, which can involve the use of analytical or numerical models, simulations, or empirical studies simulating the wear conditions. The objectives of this study concern only the texture side of this complex system. The other components of the system are empirically studied by groups of Prof. Nora Lecis in the Department of Mechanical Engineering at the Politecnico di Milano and Prof. Daniele Ugues of Department of Applied Science and Technologies at the Politecnico di Torino. Inside the tribological systems, the bulk and coating materials have a direct influence on the laser microdrilling process, thus the texture. In order to confine the numerous possibilities of bulk and coating material couples, a preliminary decision was made, and TiN was chosen as the coating material due to its wide industrial application. On the other hand, 3 choices for bulk material that constitutes the coating substrate were identified, namely 42CrMo4, AISI M2, and 39NiCrMo3. These substrates were chosen opportunely to simulate different material combinations in cold drawing dies. In this context, a laser micromachining technique capable of machining on the TiN coating deposited steel surfaces with high productivity was required to be developed. The requirements regarding the machining quality, productivity, and flexibility were determined by the surface function. The in-line process monitoring technique can be regarded as a subgroup of the laser micromachining context, however the function and the purpose of the monitoring process is determined by the surface geometry, thus surface function (see Figure 3). It was apparent that the most critical aspect in laser microdrilling is the processing depth. While the position of dimples can be precisely adjusted with the positioning system, the dimple geometrical characteristics, diameter and depth are dependent on the laser-material interaction. This interaction can also vary within a fixed laser and material combination, due to variations in material characteristics or laser emission. In case of microdrilling of coating material, the depth control plays an important role due to two main factors:

1- The complete removal of coating exposes the substrate material, which is prone to oxidation and wear. This may be acceptable in some tribological systems, such as the ones that use solid lubricants inserted to the dimples.
2- Changes in processing conditions from one material to the other can generate deleterious effects, such as dross generation and closure of the dimple. The substrate dross can strip off within use and generate more debris that can contribute to wear.

Therefore the process monitoring technique had to be developed to measure the ablation depth, in-line, on machine, and close to real time.

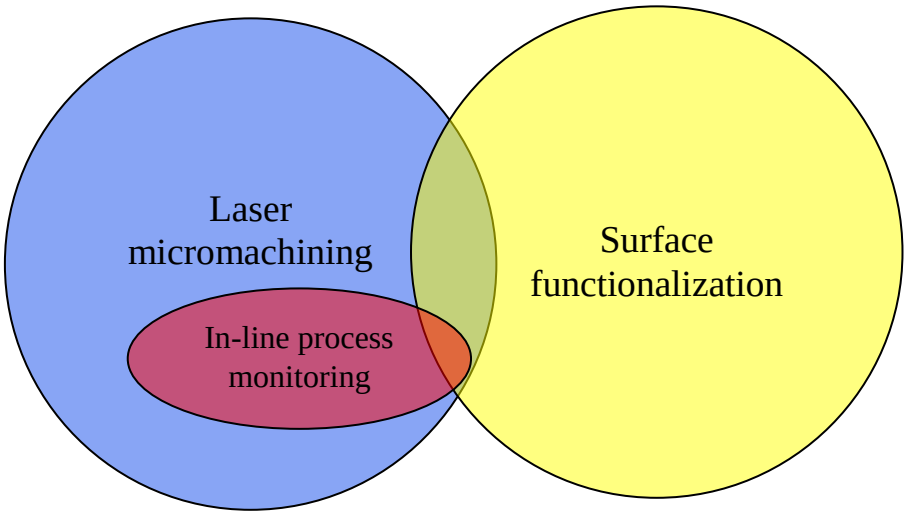

Figure 3. The cross-disciplinary context of the work.

1.2 Definition of the employed technologies

For the given context, the LST process required highly flexible, productive, and accurate laser micro processing tools. In order to maintain a good compromise between the contrasting demands, laser micromachining with ns pulsed fibre laser coupled to scanner heads was preferred. The ns pulse regime was chosen for the high productivity provided by the longer pulse duration compared to fs-ps pulse range, and improved quality compared to µs- ms pulse range. Fibre laser architecture was chosen due to its robustness and reliability in industrial operations. Moreover, today these lasers provide a greater control in micromachining with the control on pulse duration, shape and laser wavelength. The scanner heads were preferred due to high flexibility based on direct writing of the patterns. Although not studied in this work, they can be adapted to multi-axis stages to work on 3D surfaces, used in parallel to cover larger areas, and changes in surface pattern in terms of dimple spacing is immediate with the changes applied in the CAM module.

The ablation depth monitoring objective required a method capable of measuring in µs time range with preferable ns resolution to capture the dynamic evolution of the ablation process. Because the interest in only in depth evolution, the method can be based on a single dimensional acquisition in space, which is in favour of increasing the time resolution. Since the depth of the realized dimples is in the range of a few µm, the required resolution is in the order of nm. Self-mixing interferometry was chosen as the measurement method. The method provides direct information of displacement, observed from the occurrence of fringes due to constructive or destructive interference as a function of phase difference of the reflected and reference beams. Interferometry based on coherent light possesses sub micrometric resolution, and virtually free of restrictions on temporal resolutions. However, the

temporal resolution restrictions apply to the electronics that measure the optical interference and generate a digital signal. Compared to conventional interferometry, self-mixing technique uses a simpler scheme, since the interference occurs within the laser diode cavity and measured with the photodiode attached to the laser diode. This means the method is intrinsically less prone to environmental conditions.

1.3 Outline of the work

As illustrated in Figure 4, the thesis work is divided in two main parts: i- process feasibility and regulation, and ii- process monitoring by self-mixing interferometry. The first part deals with the laser micromachining of TiN coatings with pulse fibre lasers. Three different laser systems with pulse durations between 1-250 ns and wavelengths of 1064 nm and 532 nm are employed. These laser systems are first characterized to define the process parameter region that is available for percussion drilling operation. The system characterization furthermore includes the definition of other system components and employed automation to realize the dimples. Then the processing strategies are developed for each laser system, making use of their own particularities. These peculiarities rise from the fact differences in pulse generation schemes (Q-switched or master oscillator-power amplifier/MOPA), as well as the control modality available to the specific laser. The results are interpreted from a physical point of view to understand the mechanisms in different process regimes within the large ns pulse duration range. Moreover, a comparison for industrial applicability between the different processing conditions is provided.
The first stage of the process monitoring strategy deals with the limits regarding the chosen method. These limitations regard the use of the monitoring method during the ablation process. The theoretical feasibility of the monitoring method is evaluated with the knowledge generated in the empirical study such as the ablation rate and plasma emission band. Finally the method is applied to a chosen material-laser couple for concept validation.

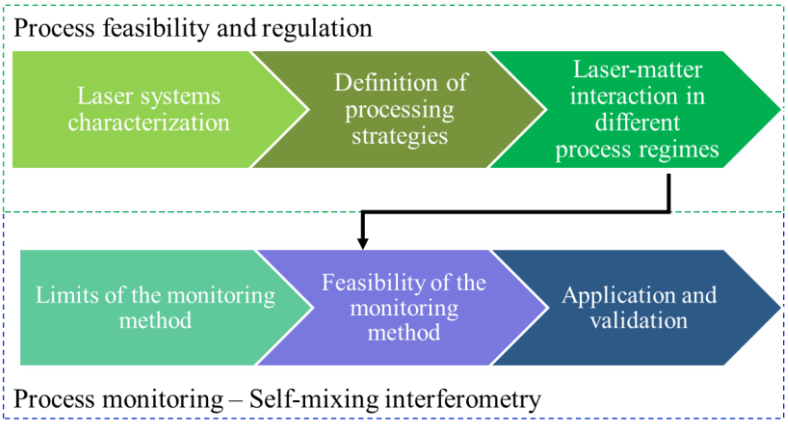

Figure 4. The outline of the PhD project.

Chapter 2

Methodology

The present thesis work is mainly based on empirical work, analysed with basic physical models, statistical methods, and supported with conceptual models. As expressed in Aims of the Work, the project deals with a number of different laser source and TiN coated substrate combinations. As a matter of fact, a complete parametric study dealing with different laser sources is difficult to be made due to the presence of source characteristics that cannot be controlled (*i.e.* laser wavelength), and due to the difficulty of making comparison of characteristics that cannot be represented by a single parameter (*i.e.* the spatial profile of the laser energy, pulse shape). Moreover, for the controllable parameter the ranges can differ greatly (*i.e.* pulse energy, pulse repetition rate). This is the natural result of the inexistence of a universal laser source that can be regulated to change every single characteristic. For this reason a common methodology has to be described prior to experimental work.
The project has been developed in two different institutions with different instrumentation depending on the availability. A great deal of the work presents experimental work carried out with custom-made equipment. The differences in the laser processing and characterization instruments require in-depth description to furnish a clear idea of the experimental conditions to the reader. This is essential to compliment to the lack of the limits of the parametric analysis. For this reason, throughout the thesis the experimental setups and conditions are described in detail. For the laser source characteristics that cannot be possibly explained by single parameters images or graphical data are provided.
The present thesis uses in general analytical models, statistical methods, and conceptual models based on physical observations. The analytical models were employed where the process regulation allowed control over laser parameters such as pulse energy, pulse duration, number of emitted pulses. When such control over the parameters was not possible statistical methods were employed to fit models using the machine parameters as predictors and measured geometrical attributes of the dimples as response variables. Physical interpretations were made over the observed trend in the fitted data. When the process complexity increased to a level where neither direct measurement, nor regulation of the governing parameters were possible conceptual models were developed. The hypotheses were depicted schematically using graphical aids. The following describes these methods in detail.

2.1 Analytical models

Laser micromachining based on ablation phenomenon is a complex process, which many have attempted to model. Due to the dynamic nature of the process the physical models are either too simplistic or too complicated to be solved analytically. In this thesis work two analytical models that have been developed to explain fundamental phenomenon in ablation are used. Moreover the analytical model for self-mixing interferometry was employed to explain the measurement capabilities and the signal characteristics of the monitoring system employed in the studies. The used models are listed below.

1. The ablation threshold model based on the Gaussian energy distribution, proposed by Liu [1].
2. The damage accumulation model in multiple pulsed laser ablation proposed by Jee et al [2].
3. Analytical steady state solution in laser diode power in self-mixing interferometry [3].

2.1.1 Liu's model for ablation threshold

These models are used for their simplicity and effectiveness on describing differences between the different processing domains. Their applicability was only limited to conditions where the processing strategies allowed accurate control of the pulse energy and number of pulses.
In the literature several analytical models are available for laser ablation processes used to predict material behaviour in terms of heat exchange and temperature change around the irradiated zone, however the one proposed by Liu [1], which initially aimed to predict the beam spot diameter by the relationship between the spatial energy distribution of the laser beam and the ablate area size has found more acceptance from the scientific community. The model is based on the assumption that the laser beam has a Gaussian energy distribution with TEM_{00}, and the pulse duration is shorter than the lattice heating time, so that the so called cold ablation condition is fulfilled. The model uses the material characteristic "ablation threshold" to predict the ablated area diameter through the Gaussian energy distribution, which means that it can be used also for predicting dimple diameter.
For a Gaussian beam, the spatial fluence distribution is as described in Eq (2.1).

$$F(r) = F \cdot e^{\left(-\frac{r^2}{r_0^2}\right)} \qquad \text{Eq.(2.1)}$$

where r is the distance from the beam centre, F is the peak fluence at the beam centre, and r_0 is the radius of the beam if it were uniform at F level. The UNI EN ISO 11146 standard defines the laser beam the second order of the intensity distribution, as:

$$w_0 = \sqrt{2} r_0 \qquad \text{Eq.(2.2)}$$

Within w_0 86% of the laser energy is contained. Rewriting the expression in Eq.1 one can obtain:

$$F(r) = F \cdot e^{\left(-\frac{2r^2}{w_0^2}\right)} \qquad \text{Eq.(2.3)}$$

Integration the equation in space the pulse energy is obtained:

$$E_p = \int_0^{\infty} \int_0^{2\pi} F_{(r,\theta)} d\theta dr = \pi r^2 F = \frac{\pi w_0^2 F}{2} \qquad \text{Eq.(2.4)}$$

For a Gaussian beam, the peak fluence and the pulse energy E are connect as:

$$F = \frac{2E}{\pi w_0^2} \qquad \text{Eq.(2.5)}$$

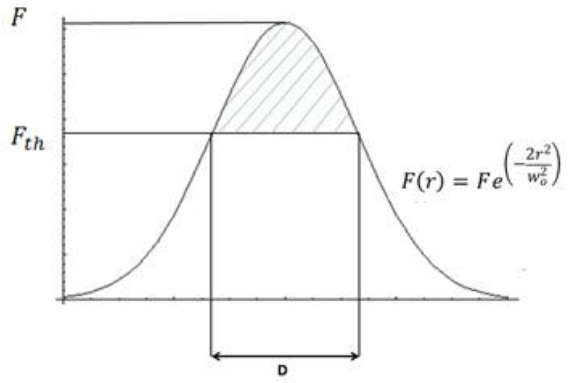

Figure 5. The fluence distribution in a Gaussian beam, depicting the peak fluence (*F*) and ablation threshold (F_{th})

Figure 5 represents the spatial distribution of fluence, where the straight line represents the threshold fluence for ablation, which is an intrinsic characteristic of the material. Above the threshold fluence, material is ablated creating a hole with diameter *D*. The ablated area diameter *D* can be calculated by equating $F(r)=F_{th}$ in Eq.(2.3) to obtain:

$$\frac{F_{th}}{F} = e^{\left(-\frac{2r^2}{w_0^2}\right)} \qquad \text{Eq.(2.6)}$$

Taking natural logarithms of both sides and making the necessary substitutions the relationship between the ablated area diameter and fluence can be obtained.

$$ln\left(\frac{F_{th}}{F}\right) = -\frac{2r^2}{w_o^2} = -\frac{D^2}{2w_o^2} \quad \text{Eq.(2.7)}$$

$$D^2 = 2w_o^2 ln\left(\frac{F}{F_{th}}\right) \quad \text{Eq.(2.8)}$$

For also clean ablation conditions without melt, the model is capable of estimating the beam diameter. Thus, once the beam diameter is measured or calculated and the threshold fluence is determined experimentally, the model can be also used for estimating diameter of the laser ablated area for single pulses.
A similar treatment can be done using irradiance (*I*) instead of fluence, substituting pulse energy (*E*) with pulse peak power (P_{peak}) to obtain the following set of equations:

$$I = \frac{2P_{peak}}{\pi w_0^2} \quad \text{Eq.(2.9)}$$

$$D^2 = 2w_o^2 ln\left(\frac{I}{I_{th}}\right) \quad \text{Eq.(2.10)}$$

The ablation threshold is evaluated in terms of both fluence and irradiance, therefore both were used and compared in the experimental work.

2.1.2 Damage accumulation in ablation with multiple pulses

For multiple pulse ablation conditions the ablated area diameter depends also on the damage accumulation phenomenon, first demonstrated by Jee et al [2]. The damage accumulation behaviour was attributed to two possible mechanisms. The first one depicts the storage cycle of thermal stress-strain energy induced by a laser pulse. The second one is based on the absorbance change due to increased roughness around the ablated area. In the end damage accumulation reduces the ablation threshold fluence after each consecutive pulse, as schematized in Figure 6. The threshold reduction in accumulation is formulated as:

$$F_{th}(N) = F_{th}(1)N^{S-1} \quad \text{Eq.(2.11)}$$

where *N* is the number of pulses, $F_{th}(1)$ is the ablation threshold with a single pulse, $F_{th}(N)$ with *N* number of pulses, and *S* is the incubation coefficient that is a material intrinsic property. For a given material no damage incubation is observed as *S*=1, whereas incubation effect increases as *S* becomes smaller. The incubation coefficient *S* can also be determined experimentally. Once it is known the expression in Eq.(2.8) can be rewritten as:

$$D^2 = 2w_o^2 ln\left(\frac{F}{F_{th}(1)N^{S-1}}\right) \quad \text{Eq.(2.12)}$$

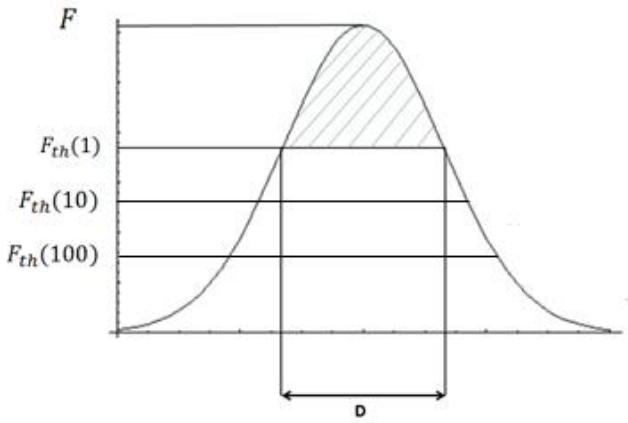

Figure 6. The change in ablation threshold fluence as a function of number of pulses.

Similar to the ablation threshold model, the damage accumulation model requires melt-free machining conditions.

2.1.3 Analytical model of self-mixing effect in laser diodes

Self-mixing interferometry has been chosen as the ablation depth monitoring in laser surface texturing, therefore a theoretical treatment of the functioning principals is presented here.
Self-mixing interferometry uses principal of interference occurring in the laser cavity (see Figure 7). Therefore compared to the conventional Michelson interferometer, which uses a reference arm and a measurement arm, the system is less complicated. Although the light interference phenomenon remains the same, the physical phenomenon occurring in the specific case of self-mixing effect occurring in laser diodes requires a treatment.

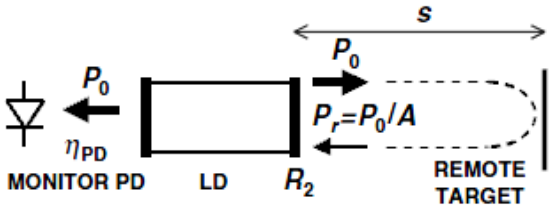

Figure 7. Conventional laser diode self-mixing configuration [3].

The analytical steady-state solution leading to the power emitted by the laser diode was used to express the change in self-mixing signal characteristics [3]. The power

back reflected from a remote target enters the cavity after being attenuated in the external cavity. The solution can be treated by starting from treatment of light as an electromagnetic field as expressed in Figure 8. Light-matter interaction consisting of absorption, reflection, and reflection is the result of the electric field interacting with the electrons of the matter. The electric field of the laser can be expressed as the following:

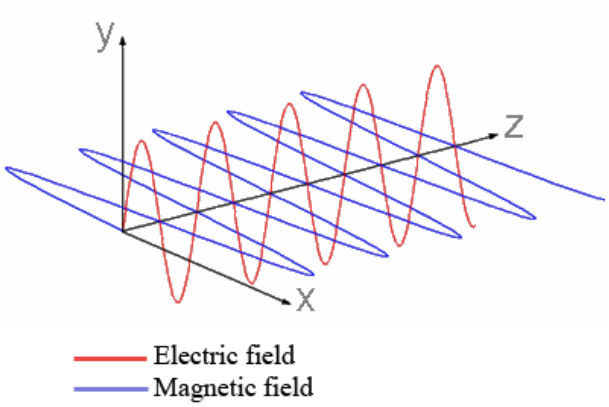

Figure 8. Light as an electromagnetic field.

$$E_l = E_{l,0} \cdot \sin\left(\frac{2\pi}{\lambda}(ct - z) + \varphi_l\right) \quad \text{Eq.(2.13)}$$

where λ is the laser wavelength, c is the speed of light, and z is the propagation distance. On the other hand the reflected laser field can be expressed as:

$$E_r = E_{r,0} \cdot \sin\left(\frac{2\pi}{\lambda}(ct - z) + \varphi_r(t)\right) \quad \text{Eq.(2.14)}$$

The reflected laser field possesses phase component that depends the distance of the reflecting body at a given time instance, expressed as:

$$\varphi_r(t) = 2ks(t) \quad \text{Eq.(2.15)}$$

with

$$k = 2\pi/\lambda \quad \text{Eq.(2.16)}$$

and *s(t)* is the distance of the remote target. The back reflected field E_r, adds to the lasing field E_0. Therefore the lasing field amplitude and frequency are modulated by the phase φ_r. This interferometric phase (φ_i) can be retrieved from the change of the optical power measured by the photodiode attached to the back of the laser diode, and a measurement of the target displacement can be made. On the other hand, an

analytical steady-state solution for the power emitted by the laser diode can be expressed as:

$$P(\varphi_i) = P_0[1 + mF(\varphi_i)] \quad \text{Eq.(2.17)}$$

where P_0 is the output power of the unperturbed laser diode, m is the modulation index and $F(\varphi_i)$ is the periodic function of the interferometry phase φ_i, of period 2π. Both the modulation index and the shape of the shape of the function $F(\varphi_i)$ depend on the feedback parameter C expressed as:

$$C = \frac{Ks\sqrt{1+a^2}}{L_{las}n_{las}} \quad \text{Eq.(2.18)}$$

where a is the linewidth enhancement factor, L_{las} is the laser cavity length, n_{las} is the cavity refractive index. On the other hand K is given by:

$$K = \frac{\sigma}{\sqrt{A_p}}\frac{1-R_2}{\sqrt{R_2}} \quad \text{Eq.(2.19)}$$

Where σ accounts for a mismatch between the reflected and lasing modes with the condition $\sigma \leq 1$, A_p is the total optical power attenuation in the external cavity and R_2 is the laser output facet power reflectivity. Thus, feedback parameter C depends on both the amount of feedback and target distance, and is of great importance for self-mixing interferometry measurements. As a matter of fact feedback parameter C is used to define different feedback regimes as the following.

- Very weak feedback regime ($C<<1$): The $F(\varphi_i)$ function is a cosine and the modulation index m is inversely proportional to $\sqrt{A_p}$.
- Weak feedback regime ($0.1<C<1$): The $F(\varphi_i)$ function gets distorted, showing a non-symmetrical shape (see Figure 9.a), the modulation index m is inversely proportional to $\sqrt{A_p}$.
- Moderate feedback regime ($1<C<4.6$): The $F(\varphi_i)$ function becomes three-valued for certain values of the phase φ_i, thus the system is bistable, with two stable states and one unstable (see Figure 9.b). The modulation index m increases for decreasing $\sqrt{A_p}$ but it is no longer inversely proportional to it. The interferometric signal becomes sawtooth-like and exhibits hysteresis. This regime is suitable for non-ambiguous interferometric displacement measurement.
- Strong feedback regime ($C>4.6$): The $F(\varphi_i)$ function may become five-valued (see Figure 9.c). In some cases the laser diode enters the mode-hopping regime, which stands for the sudden change of emission wavelength, and interferometric measurements are no longer possible.

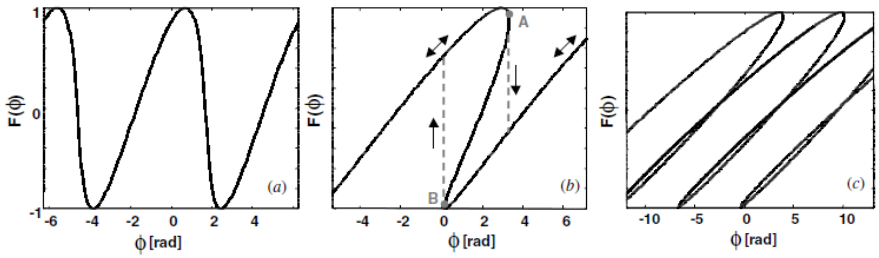

Figure 9. Caculated waveforms of the $F(\varphi_i)$ function for different feedback parameters: a) C=0.7, b) C=3, d) C=10 [3].

The feedback parameter can be regulated empirically by the use of an attenuator downstream the laser diode to control the amount of backreflected light entering the cavity.

2.2 Statistical methods

Experimental studies contain uncontrolled effects such as the material homogeneity, laser stability, or the environmental effects. Such effects can be considered within the variability of the process, which has to be accurately evaluated. The importance of statistical data comes into evidence, especially when the significance of the effect of a certain parameter within a process with certain variability is tested. Therefore, this thesis makes use of statistical methods to test significance of experimented treatments/parameters, develop models to predict or depict trend that can be useful for physical interpretations. Moreover, throughout the thesis designed experiments are used to first define the processing windows and then explore the processing conditions within them. The three fundamental aspects of the designed experiments are replication, randomization, and blocking. Due to logistical problems with handling large number experimental conditions with micrometric dimensions of the analysed geometries, randomization aspect could not be respected at all times.
In particular, three types of statistical analysis, analysis of variance (ANOVA), linear regression, and non-linear regression were used.

2.2.1 Analysis of Variance (ANOVA)

The method is used to determine the statistical significance of factors by simply comparing whether the means of several groups, or in this case the effect of different parameter combinations, are equal [4]. ANOVA can be used to test the significance of parameters on a chosen response parameter, but also can be used to test the difference of different measurement conditions. The technique uses the effects model and tests the significance of the effects with Fisher's test. An example for the effects model for a case a factorial plan with two factors can be written as:

$$y_{ijk} = \mu + \delta_i + \beta_j + (\delta\beta)_{ij} + \epsilon_{ijk} \quad \begin{cases} i = 1, 2, \dots, a \\ j = 1, 2, \dots, b \\ k = 1, 2, \dots, n \end{cases} \qquad \text{Eq.(2.20)}$$

where, μ is the overall mean effect, δ_i is the effect of the i^{th} level of the row factor A, β_j, is the effect of the j^{th} level of column factor B, ($\delta\beta_{ij}$) is the effect of the interaction between δ_i and β_j, ϵ_{ijk} is a random error component, and y_{ijk} is the k^{th} observation when these effects are present. For factorial plans, the effects of factors as well as their interactions are of interest. Therefore the statistical tests are made on the hypothesis of having all the factors (or interactions) being insignificant against at least one of them being significant. Thus, for the case of 2 parameter factorial plan the hypothesis on factor A is,

$$H_0: \delta_1 = \delta_2 = \cdots = \delta_a = 0$$
$$H_0: \ at\ least\ one\ \delta_i \neq 0 \qquad \text{Eq.(2.21)}$$

Similarly for factor B,

$$H_0: \beta_1 = \beta_2 = \cdots = \beta_b = 0$$
$$H_1: \ at\ least\ one\ \beta_j \neq 0 \qquad \text{Eq.(2.22)}$$

And finally for the interaction between A and B,

$$H_0: \delta\beta_{ij} = 0\ for\ all\ i, j$$
$$H_1: \ at\ least\ one\ \delta\beta_{ij} \neq 0 \qquad \text{Eq.(2.23)}$$

The tests require the calculation of the expected mean square of the factors, interactions, and error, which are not explained here for brevity. The Fisher's test is done on the F-value (F_0) calculated as in the case of single parameter A,

$$F_0 = \frac{MS_A}{MS_E} \qquad \text{Eq.(2.24)}$$

where MS_A and MS_E are the expected mean squares of parameter A and error. To reject null hypothesis (H_0), and therefore to conclude that the parameter is significant, the following condition must be satisfied.

$$F_0 > F_{\alpha, a-1, (a-1)(b-a)-1} \qquad \text{Eq.(2.25)}$$

where α is the significance level, which is the maximum acceptable level of risk for rejecting a true null hypothesis (type I error). In this thesis, ANOVA was applied by means of Minitab statistics software.

2.2.2 Linear regression

Linear regression models are useful, when one or more numerical parameters with multiple levels are used. This is a common situation when a relationship between the process parameters and the measured variables is sought to develop an empirical model. Instead of treating all the parameter-level combinations separately with separate coefficients, a model based on global coefficients associated to parameters can be used. In general the response variable *y* may be related to *k* variables, which can be expressed as:

$$y = \beta_0 + \beta_1 x_1 + \beta_2 x_2 + \cdots + \beta_k x_k + \epsilon \qquad \text{Eq.(2.26)}$$

The variables $x_1, x_2, \ldots, x_k$ are called predictor variables or regressors, whereas the parameters $\beta_1, \beta_2, \ldots, \beta_k$ are regression coefficients. This model is called multiple linear regression model with k regressors. The model is constructed as a linear function, however can contain higher order or non-linear regressors such as:

$$y = \beta_0 + \beta_1 x_1 + \beta_2 x_2 + \beta_{11} x_1^2 + \beta_{12} x_1 x_2 + \epsilon \qquad \text{Eq.(2.27)}$$

If we let $x_3 = x_1^2$, $x_4 = x_1 x_2$, $\beta_3 = \beta_{11}$, and $\beta_4 = \beta_{12}$ then the equation becomes

$$y = \beta_0 + \beta_1 x_1 + \beta_2 x_2 + \beta_3 x_3 + \beta_4 x_4 + \epsilon \qquad \text{Eq.(2.28)}$$

and the linearity in the formulation remains. In this case, the hypothesis verification is done on the regression coefficients, which are estimated by least squares method. To test the significance of the regression model the appropriate hypothesis are

$$H_0: \beta_1 = \beta_2 = \cdots = \beta_k = 0$$
$$H_1: \beta_j \neq 0 \ \ for\ at\ least\ one\ j \qquad \text{Eq.(2.29)}$$

Rejection of H_0 means at least one of the regressor variables contributes significantly to the model. The tests require the calculation of the expected mean square of the regression and error, which are not explained here for brevity. The Fisher's test is done on the F-value (F_0) calculated as

$$F_0 = \frac{MS_R}{MS_E} \qquad \text{Eq.(2.30)}$$

where MS_R and MS_E are the expected mean squares of regression model and error. To reject null hypothesis (H_0), and therefore to conclude that the model is significant, the following condition must be satisfied.

$$F_0 > F_{\alpha,k,n-k-1} \quad \text{Eq.(2.31)}$$

where *n* is the number of data points to fit the model to. The same verification has to be done on the individual regression coefficients as

$$H_0: \beta_j = 0$$
$$H_1: \beta_j \neq 0 \quad \text{Eq.(2.32)}$$

If the null hypothesis cannot be rejected, the x_j can be excluded from the model. The test statistic for this hypothesis is

$$t_0 = \frac{\widehat{\beta_j}}{se(\widehat{\beta_j})} \quad \text{Eq.(2.33)}$$

where $\widehat{\beta_j}$ is the coefficient estimated by least squares method, and $se(\widehat{\beta_j})$ is the standard error of regression coefficient $\widehat{\beta_j}$. The test is based on t-distribution and to reject null hypothesis the condition to fulfil is

$$|t_0| > t_{\alpha/2,n-k-1} \quad \text{Eq.(2.34)}$$

The adequacy of the model is expressed by two fundamental indicators. R^2_{adj} is a measure of the amount of reduction in the variability of *y* obtained by using the regressor variables. The test on lack-of-fit, on the other hand, describes the adequacy of the model without the need of any other additional predictors.
In this thesis, the linear regression models were fitted by means of Minitab statistics software. The regression models require iterative approach to find a useful model that satisfies firstly all the statistical hypotheses and also represent the expected physical phenomenon adequately. Therefore, the iterations leading to the final regression model are not reported hereafter, but only the final model itself is presented.

2.2.3 Non-linear regression

In some cases, linear parameters do not adequately fit the experimental data. Or it can be required to develop a regression equation based on an existing analytical relationship that is non-linear. The linear regression can be used to fit a linear model that can be transformed to its non-linear form. However, there are two main limitations to this approach. First, some non-linear models cannot be transformed to a linear relationship. Second, the standard errors of the coefficients estimated by the linear regression are difficult to be converted to the standard error of the non-linear coefficient. Especially in the case of fitting regression models based on analytical expressions, the standard error is an important indicator to estimate the confidence

interval of a coefficient, since it estimates the error margin on a physical coefficient. Non-linear regression generates an equation to describe the nonlinear relationship between a continuous response variable and one or more predictor variables [5]. The general form of the non-linear regression is:

$$y = h(x_i, \beta) + \epsilon_i \quad \text{Eq.(2.35)}$$

In this thesis, the non-linear regression models were fitted by means of Minitab statistics software. The user defined expectation functions were inserted to the software, and an iterative algorithm (Gauss-Newton) matched the unknowns of the non-linear regression equation (regression coefficients) starting from set values [6]. Calculation of the regression coefficients was only possible if a divergence to the best fit was obtained. In particular, the analytical models regarding laser ablation were fitted to the measured data using this method to calculate physical coefficients with their estimated confidence intervals.

2.3 Conceptual models

The thesis includes also findings that could not be formalized by mathematical models directly. This is due to the complexity of multi-physics phenomenon occurring in ablation processes. For such cases, in order to describe the physical phenomenon, conceptual models have been described for the cognition of the process. These conceptual models describe the observed phenomenon through a group of well-known physical phenomenon and their plausible interactions, in a simplified manner without the use of equations. Conceptual models have been used to describe the observed phenomenon during the development of ablation depth monitoring system based on self-mixing measurements, where optical interference in turbid media had to be studied.

Chapter 3

State of the Art

Laser micromachining is a flexible process in terms of machinable materials, forms, and dimensions. This fact generates a high margin of innovation and a variety of possible applications. This is also confirmed by the rapid changes observed in the state of the art in laser micromachining field. A generic look to the state of the art concerning this PhD thesis involves key research fields of: laser micromachining, laser surface texturing, TiN coatings, and ablation depth monitoring techniques.

Laser micromachining is an ablation based process and the term "laser ablation" generates 39,277 results under Thomson Reuters Web of Knowledge database. This shows the great interest in the scientific field, which has maintained over the years to study the ablation process physics and applications. The industrialization of laser ablation based machining equipment resulted in increased attention to the application side. Figure 10 demonstrates the increasing trend over the number of published works years in laser micromachining. Over the last 10 years, over 150 papers are published yearly in this field by international scientific community (see Figure 4). This period coincides with the wider diffusion of the solid state lasers that provided easier and more robust operation. Fibre laser being one of such, have been nominated to face micromachining tasks as early as 1999 by Schoenfelder in an industrial magazine [7]. Their introduction to the market as turn-key products have been around 2002, from this point on several works investigating manufacturing processes regarding cutting, welding, and marking have been produced. Today ns-pulsed fibre lasers are used in the industry for a wide variety of operations; however their potentiality to close the gap in large area micromachining is not fully exploited.

Pulsed lasers have been long used for texturing operations, before the arrival of fibre lasers. The term of "laser surface texturing" however, has been used in a publication by Wong et al in 1997 for the first time [8]. This paper showed one of the early examples of laser treated surfaces for improving adhesion behaviour. The treatment used a Nd:YAG system to generate mm-size dimples, which was yet far from today's micromachining based texturing techniques. The first laser surface texturing paper dealing with improved tribological properties was published by Etsion in 2000, as he discussed the improvement in load capacity, wear resistance, and friction coefficient of mechanical seals by regular micro surface structure in the form of micro pores [9]. Hereon, the laser surface texturing terms has been mainly used to refer to the use of micro dimpled surfaces to improve the tribological behaviour of a component, and Etsion continued to pioneer the studies in this field. Over the last three years there has been a drastic increase in the published works in this field, which is expected to expand the process to wider industrial application (see Figure 11).

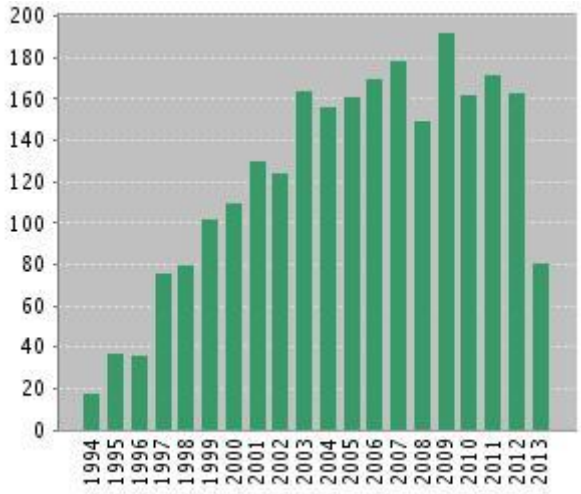

Figure 10. The number of articles indexed within Web of Knowledge per year in "laser micromachining".

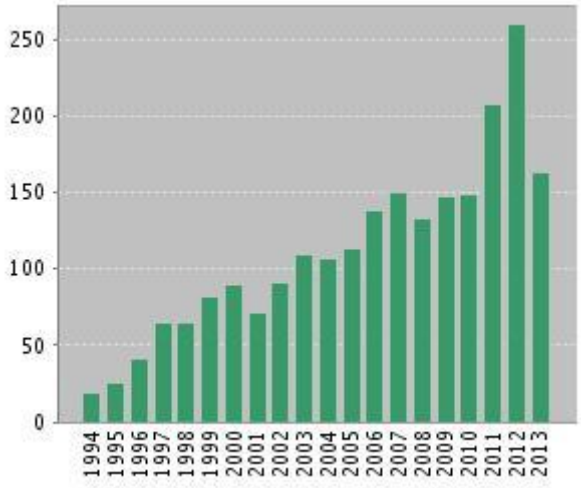

Figure 11. The number of articles indexed within Web of Knowledge per year in "laser surface texturing".

The deposition techniques of hard TiN coatings are established processes today. Many applications regarding automotive, food, biomedical, and electrical sectors are industrially use TiN coatings. In accordance to this fact, a search in Web of Knowledge database with "TiN coatings" term generates 13,836 records, with 8558 of them being published between 2004 and 2013. Their interaction with lasers for hardening, deposition, and growth purposes has been also widely investigated as 816 articles are recorded in the same database. However, the surface patterning, structuring, or texturing is still a point that requires more attention, since only a handful of articles are reported that study the ablation process. The tribological performance of laser surface textured TiN coatings has received even less attention.

Looking into the state of the art in process monitoring of laser micromachining processes, it is observed that many have attempted to measure, quantify, and interpret the ablation phenomenon. The used methods are usually based on measurements of the optical emission during the process, and analytical approaches are used to quantify key parameters to reveal the underlying physical phenomena. On the other, few have attempted to develop engineering solutions to monitor the ablation phenomenon to maintain dimensional restriction of a processed component. As the laser machining process becomes accepted by the industry recently, the interest in monitoring laser micromachining processes becomes more relevant. The literature survey has been concentrated considering ablation depth as the key point to measure and quantify, which is detailed later in the dedicated section.
In the following, the state of the art in the before listed research fields are discussed in technical detail with the aim of furnishing a theoretical basis to the used techniques.

3.1 Laser micromachining of surfaces

Laser micromachining is most commonly applied with pulsed wave laser sources. In order to maintain micrometric dimensions with laser manufacturing, the laser beam should interact with the material in limited space and time. Therefore, the main components that influence the outcome of the laser surface micromachining operation are the laser wavelength and pulse duration. However, a direct relationship between the laser-material interaction and these two parameters is difficult to be defined. In general, laser micromachining is applied with pulsed laser sources with pulse durations ranging from ms to fs range, and with laser wavelengths from far IR (λ=10 µm) to deep UV (0.1 µm). The machining quality and productivity is the result of how the laser energy is absorbed, and material is transformed to a mobile phase that is then extracted from the bulk. Although, this mechanism is highly complex, it is preferred to provide a descriptive analysis on the main parameters.

3.1.1 Effect of pulse duration

The effect of pulse duration has received high level of attention from both the physics perspective and engineering applications. A general distinction based on the classes of pulse durations is used both in academic research and industry that can be listed as:

- Long pulses – ms, µs regime: These pulses are used for high speed drilling of high thickness materials, in cutting operations, as well as welding applications. The repetition rates are limited to kHz level, whereas the pulsation techniques are usually based on fast switching of laser pumping media such as diodes in fibre lasers or flash lamps in Nd:YAG systems.
- Short pulses – ns regime: Short pulses are used in various applications ranging from marking, engraving, drilling, and cutting of low thickness materials. The repetition levels are usually in the range of tens of kHz, although with reduced pulse durations they can go up to hundreds of kHz levels. Nanosecond pulses

are typically generated with Q-switching, whereas more recent sources operate with MOPA (master oscillator power amplifier) architectures, allowing greater range of pulse shapes.

- Ulta-short (ultra-fast) pulses – fs, ps regime: Ultra-short pulses are used in high precision marking and engraving operations mostly, whereas recently their use in cutting operations has been also demonstrated. In addition to processes based on material removal, in this range welding of transparent materials is also achievable due to induced non-linear effects. The pulse repetition rates of such systems vary from generation to generation. Previous generations employed repetition rates up to a few Hz, whereas the most recent industrial solutions provide systems capable of reaching MHz repetition rates. The ultra-short pulses are generated with mode locking, and MOPA structure can be used to amplify ps range pulses, whereas chirped pulse amplification technique can be used for shorter ps pulses.

The technical distinction between different pulse regimes depend on the changes regarding how the laser beam interacts with the material in different time scales. In particular it is useful to consider the two temperatures belonging to the electron and the lattice subsystems (T_e and T_i) to give a generic description to the occurring phenomenon [10-12]. Essentially during the light-matter interaction the laser energy is absorbed first by free surface electrons. Then energy is transported to the lattice, and energy losses due to the electron heat transport into the target occur. The difference between the two temperatures in the system is a function of the corresponding heat capacities (C_e and C_l). The electronic heat capacity is much smaller than the lattice heat capacity ($C_e << C_l$); therefore electrons can be heated to very high transient temperatures. In this scheme two characteristic time scales can be defined as τ_e and τ_l, where τ_e is the electron cooling time and τ_l is the lattice heating time, with $\tau_e << \tau_l$.
For pulse durations lower than 100 fs, the ablation phenomenon occurs in the so cold state, as the thermalization of first the electrons and later on the lattice is terminated while the matter is in condensed state. This condition represents $\tau << \tau_e$, where an equilibrium between the lattice and the electrons is not present, thus the material bulk is not heated (see Figure 12). With high pulse energy different states of gaseous phase can be present in the form of vaporization, fragmentation, and nucleation of ablated particles. For pulse energy close to the ablation threshold, spallation phenomenon occurs, where material is deformed due to the thermo-mechanical load exceeding the yield stress of the material.

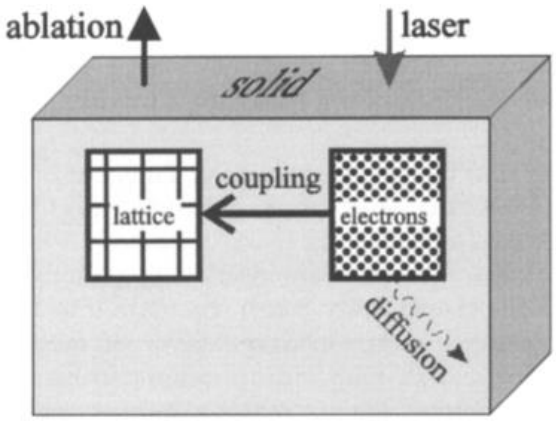

Figure 12. Scheme of ablation with fs pulses (τ_e<<τ) [10]

Increasing the pulse duration to around 10 ps, the so called hot ablation conditions are fulfilled, with τ_e<<τ<<τ_l. The electron and lattice temperatures tend to go closer to a thermal equilibrium, although thermal diffusivity of the lattice is negligible compared to that of electrons. Thus the lattice temperature remains much smaller. Surface evaporation is still the dominant mechanism for material removal; however melt generation inside the material is also present, which can degrade the machining quality.

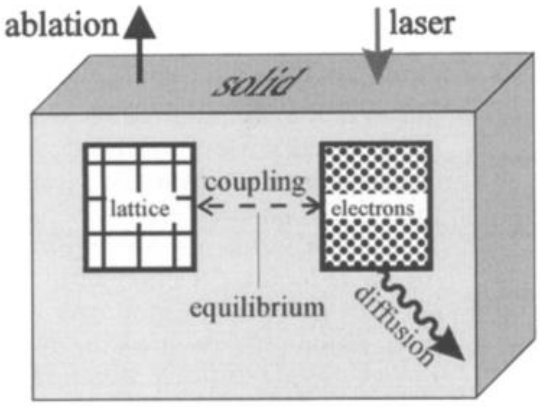

Figure 13. Scheme of ablation with ns pulses (τ_l<<τ) [10].

For pulse durations higher than ~10 ps, thermal equilibrium between the lattice and the electrons forms, as the laser energy dissipates to the material bulk (see Figure 13). The material removal is a mixture of vaporization from condensed matter, vaporization from molten phase, and melts expulsion. The fraction of these components depends on the pulse duration and irradiance level. Due to the dissipation of the energy in the material bulk higher levels of energy is required for material removal. The generated molten layer, if not removed during the process, causes redeposited material layer around the ablation area that is regarded as dross or spatter.

Although they vary as a function of temperature distinct values of τ_e and τ_l are present with different materials. The τ_e is reported to vary in the range of a few hundreds of fs, whereas τ_l varies in the ps region. Table 1 reports the characteristic times for some of the pure metals.

Table 1. Electron cooling and lattice heating times for pure metals at T_e=T_l=300 K [11].

	Au	Al	Cu	Pb
τ_e (ps)	0.579	0.067	0.467	0.377
τ_l (ps)	70.6	4.27	57.5	11.2

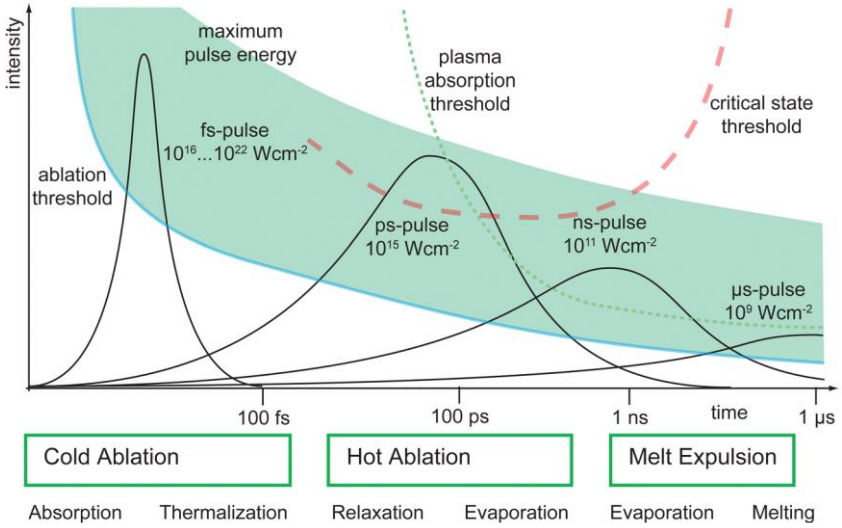

Figure 14. Different ablation domains as a function of pulse duration [11].

Figure 14 summarizes the different ablation domains as a function of pulse durations and the related physical phenomenon. It can be observed that the ablation threshold intensity decreases with increased pulse duration, whereas going towards longer pulses the radiation also interacts with the ablated material in the gaseous phase, as expressed with the plasma absorption threshold. The addition of the plasma to the process generates further complexity, since the plasma can act as an absorbent media, causing diffraction and loss of irradiance. On the other hand the plasma pressure can be advantageous in melt expulsion, which can facilitate the removal of melt layer inside the processing zone when ns pulses are used.

The critical state threshold denotes the situation where no boundaries between phases exist. The existence of critical state further complicates ablation conditions and is present in the case of a few ps to a few hundreds of ns pulse durations. With increased irradiance the photons plumb deeper in the matter to further increase the temperature and pressure inside the material. If liquid phase is present, its temperature can increase towards the thermodinamical critical point, and eventually homogenous nucleation takes place. The collapse of the nucleated gaseous phase results in the failure of crystal structure, and the material is expelled as a mixture of vapour and molten droplets. With higher irradiance, heating above the critical temperature

directly from the solid phase becomes possible. Consequently the material expands, which leads to a pressure drop to the thermodynamically unstable region causing material decomposition. This material decomposition phenomenon, from solid to super critical fluid to the unstable region is referred to as critical point phase separation.

3.1.2 Effect of wavelength

A wide range of optical properties are observed in solid state materials, whereas a simple grouping can be named as reflection propagation, and transmission with,

$$R + T + A = 1 \qquad \text{Eq.(3.1)}$$

where *T* is the transmissivity, and *A* is the absorption percentages of the material [13]. When light travels through a transparent media refraction and absorption might occur. Refraction is the phenomenon regarding the reduction of the propagation velocity in the media, and does not necessarily cause intensity decrease. On the other hand, absorption occurs during propagation when the frequency of the light is resonant with the transition frequencies of the atoms in the medium. Since light frequency is inversely proportional to the light wavelength, absorption is also strictly connected to the laser wavelength. Both refraction and absorption can be described by the complex refractive index, which can be defined as:

$$\tilde{n} = n + i\varepsilon \qquad \text{Eq.(3.2)}$$

where n is the real, and ε is the imaginary parts. The real part n is the same as the normal refractive index, whereas the complex part ε is called the extinction coefficient. The absorption coefficient α [cm^{-1}] can be calculated as:

$$\alpha = \frac{4\pi\varepsilon}{\lambda} \qquad \text{Eq.(3.3)}$$

where λ is the wavelength of the transmitted light. The inverse of the absorption coefficient is also used as the absorption depth ($l_\alpha = \alpha^{-1}$), which represents the depth of light penetration into the material. On the other hand the reflectivity of the material can be expressed as:

$$R = \left|\frac{\tilde{n}-1}{\tilde{n}+1}\right|^2 = \frac{(n-1)^2+\varepsilon^2}{(n+1)^2+\varepsilon^2} \qquad \text{Eq.(3.4)}$$

On the other hand the transmissivity can be expressed as:

$$T = (1-R)^2 e^{-\alpha l} \qquad \text{Eq.(3.5)}$$

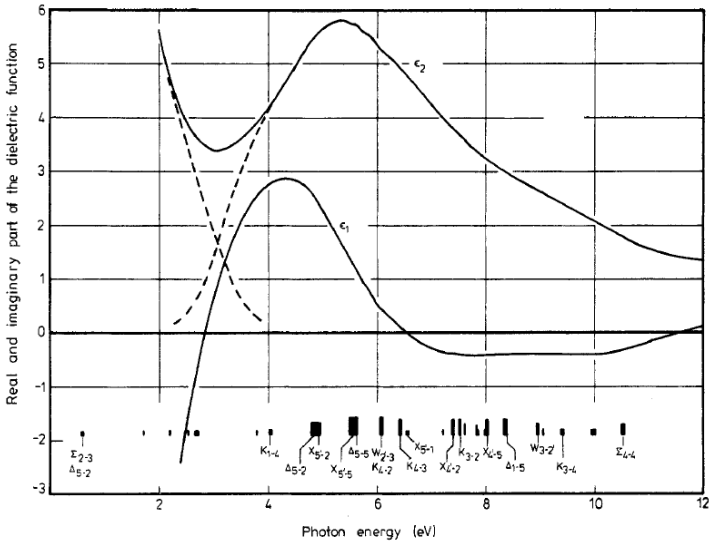

Figure 15. Real and complex parts of the complex refractive index of TiN. Real part is denoted by ϵ_1 and imaginary part by ϵ_2 [14].

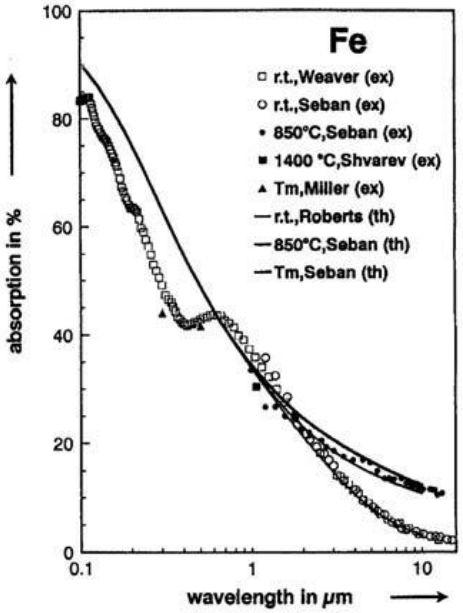

Figure 16. The experimental and calculated values of absorption of Fe as a function of wavelength [15].

where *l* is the material thickness. The expression denotes an exponential decay in the transmitted light due to absorption, as expressed by Beer's Law. For most of the metallic materials tranmissivity is negligibly small, where only the absorption occurs only on the skin of the material. In the case of dielectrics and semiconductors the optical penetration depth may increase to higher levels that the light can penetrate much deeper into the material and eventually be transmitted.

The complex refractive index of materials can be determined experimentally and can be used to calculate the absorption and reflection coefficients (see Figure 15). Material transmissivity or reflectivity can be directly measured, and the remaining portion can be regarded as the absorbed quantity (see Figure 16). The surface reflectivity is also strongly associated to the surface topography. Rough surfaces can induce multiple reflections, which may increase the absorbed amount. Along with the wavelength, absorption is strongly influenced by temperature and material phase.
Another specific influence of the wavelength is present in the so called cold processing conditions. The use of UV radiation permits working with photon energy that is similar to the bond energy of many organic materials (4.9 eV). With sufficient flux of photons, material bonds are broken without heating similar to the use ultashort pulses, which in return allows achieving high quality machining conditions.
In addition to the change in absorption characteristics, the wavelength changes also the geometrical characteristics of the laser beam. The diameter of a diffraction limited beam at focal point d_0 can be calculated from [16]:

$$d_0 = \frac{4M^2\lambda f}{\pi d_c} \qquad \text{Eq.(3.6)}$$

where M^2 is the beam quality factor, f is the focal distance of the focusing lens, d_c is the collimated beam diameter. Thus, laser shorter wavelengths intrinsically produce smaller focused beams, which can be referred as improved focusability. With smaller beams the intensity and fluence levels increase, as well as the resolution increases due to the use of a smaller tool.

3.1.3 Effect of pulse shape

Among other parameters, pulse shape is the least investigated one in laser ablation. This is a consequence of the fact that until recently a control over the arbitrary waveform of a laser pulse over time was not present. The common approach to laser ablation parameters has been based on the use of laser irradiance or fluence among with the pulse duration. However, with the same irradiance, fluence, and pulse duration parameters infinite possibilities of pulse shapes exist. The pulse shape, especially in ns pulses can alter the outcome of the process drastically, as the energy deposition rate changes in time, in a time scale much longer than the lattice heating time. The new generation MOPA systems opened up further flexibility in pulse shape selection and programmability [17]. Today these systems are commercially available with pre-programmed pulse shapes in ns range, or arbitrarily programmable pulse shapes in µs-ms range, however further analysis is required to determine the correct pulse shape for different applications.

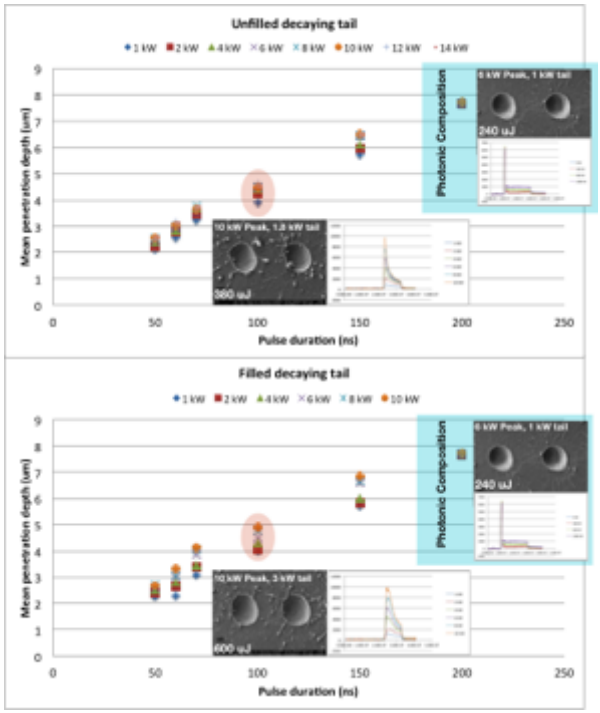

Figure 17. A comparison between decaying tails and designer pulse shapes (photonic composition). The machining conditions with designer pulse shapes in the insets show improved machining quality with higher efficiency [19].

As a matter of fact, the pulse shape generates the problem of parameterisation in laser machining, since the arbitrary waveform cannot be represented by a single parameter. Therefore, the general approach has been to identify the position of the pulse peak within the pulse duration. O'Neill and Li have demonstrated that nanosecond pulses with fast ascending peaks were effective to drill Si with 1064 nm wavelength, to which material is transparent in ambient conditions. They have proposed a mechanism that by the fast reach of the peak power the material is molten and the remaining energy after the pulse peak is absorbed much efficiently by the molten material, which has a much shorter optical penetration depth, thus higher absorption [18,19]. Pangovski et al later on showed that the pulse shape decomposition can be a crucial element to design specific shapes for specific materials [20]. They have demonstrated pulse decomposition for nanosecond pulses, where a fast ascending peak and a flat tail was present. They have determined that further addition in the tail energy did not result in any further increase of the ablation depth, and that a certain pulse shape enabled highest energetic efficiency in machining of Si (see Figure 17). Eiselen et al proposed another attempt on shape parameterisation of 20-30 ns pulses [21]. They have shown that both ablation threshold and efficiency varied significantly when the position of the pulse peak was varied between leading, cantered, and trailing positions (see Figure 18).

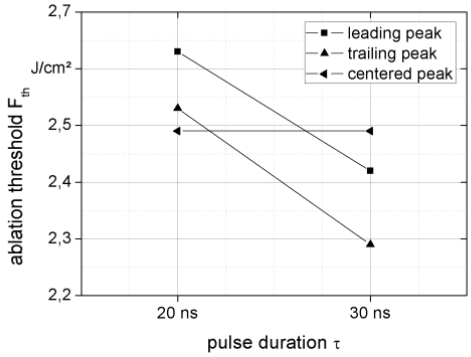

Figure 18. The effect of peak position on the ablation threshold in ablation of on 1.4404stainless steel [20].

3.2 Laser surface texturing for functional surfaces

Laser surface texturing is used as a generic term for laser micromachined surfaces for changing certain surface properties to fulfil a destined function. The majority of the LST applications are developed to improve tribological performance [22-74]. LST is also used to improve adhesion [75-81], optical [82-89], biological response [90-97], and wetting [98-100] properties. Therefore the main components for the specific LST application can be regarded as:

- Material
- Micro-geometry
- Distribution of the micro geometry on the surface

LST is most widely applied with solid state pulsed laser sources at 1 μm as fundamental wavelength. Gas lasers are also employed, where excimer lasers are used with masked projection. CO_2 lasers are used on the bases of direct writing and preffered especially in the case of organic materials. Different combinations of pulse durations, in short (ns), ultrashort (ps, fs) ranges, as well as harmonics of the fundamental wavelength have being investigated. The used material is dictated by the application, where a range variety of material types are reported in literature. Metals, especially steel is the most common type of material in LST applications. Ceramics and coatings are the other common types on which LST is applied to.
The micro-geometries options depend on the capabilities of the micromachining system, and especially on the optical arrangement used in the laser system. LST is commonly applied via direct writing by manipulating either the laser beam or the workpiece with the use of linear stages or scanner heads. Use of masks is also a common approach with excimer lasers. More recently the use of beam shaping and

Table 2. A selection of different LST micro-geometries reported in the literature.

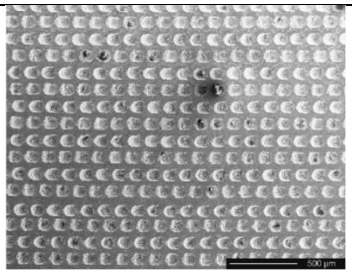 Micro-geometry: Dimple Material: 30NiCrMo12 Application: tribological/automotive Ref [46]	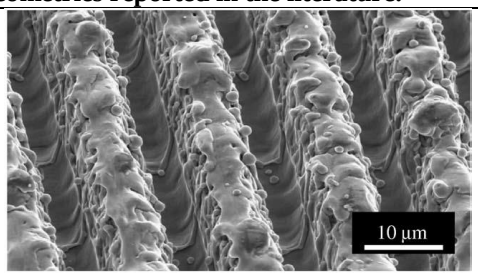 Micro-geometry: Groove Material: Ti6Al4V Application: Biomedical Ref [89]
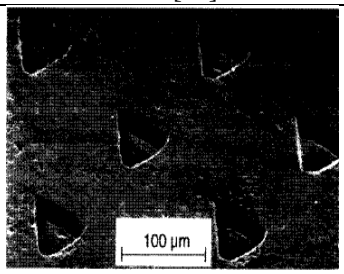 Micro-geometry: Triangle Material: SiC Application: Tribology Ref [24]	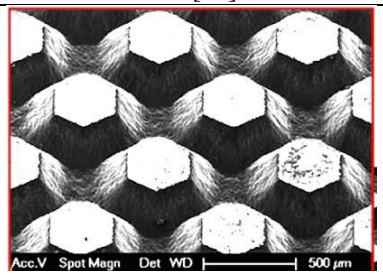 Micro-geometry: Hexagon Material: CVD diaomond Application: Tribology/Manufacturing Ref [57]
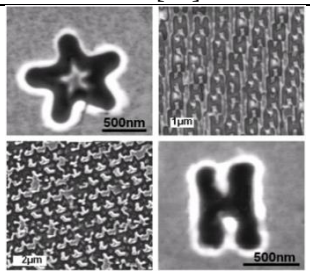 Micro-geometry: User defined nano patterns Material: $Sb_{70}Te_{30}$ film Application: Not specified Ref [101]	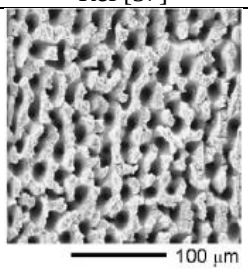 Micro-geometry: Porous Material: Nickel-based superalloy C263 Application: Aerospace Ref [50]
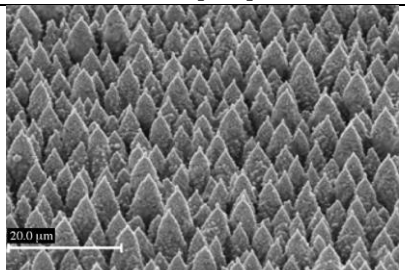 Micro-geometry: Conical pillars Material: Ge Application: Optical Ref [87]	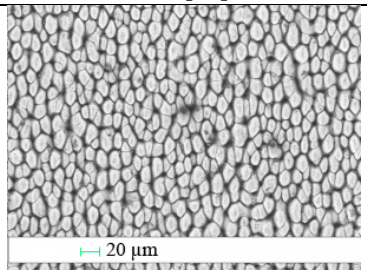 Micro-geometry: Conical pillars Material: Stainless steel Application: Wettability control Ref [99]

diffractive optics has been proposed for larger area and/or parallel machining of multiple patterns. The use of micro-spheres as micro lens array has been reported, where sub-micron resolution machining on multiple points with a single beam was possible [101-103]. In another work, the use optical fibre to focus the laser beam in the form of a line has been demonstrated [104]. The use of interference patterns for machining larger areas has also been reported, with which an interference pattern using multiple beams can be calculated prior to machining to generate the desired texture [105-107]. A more flexible approach to beam shaping is the use of spatial light modulators [108-110]. These devices allow generating holographic patterns using optically or electronically addressed voxels that can either alter the intensity or the phase of the light. Flexible generation of holograms with the use of dedicated software is a promising point for flexible manufacturing. However, these systems require higher pulse energies to effectively machine larger areas, but in contrast with current commercial technology they cannot withstand high power beams (up to ~15 W average power with cooling).
Table 2 reports a selection of some of the most interesting geometries reported in the literature. It can be seen that most of the negative geometries are realized via material removal based on direct writing [24,46,57,90]. This way the generated shape is dimensionally in the range of the laser beam size. Exceptions are present where the non-linear effects are exploited to generate sub-micron structures on the material. This mechanism is caused by the interference patterns generated by surface reflections. When the pulse duration is sufficiently short to avoid thermal process and the beam is polarized in a direction the interference patterns align in certain directions that can realize rippled, porous [50], or pillar-like structures [87,99], and they are dimensionally in the range of the laser wavelength.

3.2.1 Effect on tribological properties

Extremely smooth surfaces do not exhibit optimal properties working under hydrostatic or hydrodynamic lubrication conditions, especially with limited amount of lubricant being used. For the transport of the lubricant and the debris generated during the contact, surface valleys can induce preferential effect (see Figure 19). Material surface topography can induce positive effects for tribological performance only to certain extent; on the other hand a controlled surface texture can be optimized to meet the requirements. Accordingly, laser surface texturing as a means for enhancing the tribological properties has been widely studied. In general the contributing effects that improve the tribological properties are associated to the lowering of surface area, enhancing lubricant retention, contributing to hydrostatic pressure, and allowing debris entrapment in the micro-geometries that can effectively decrease third body wear [22,23]. In return friction and wear is reduced, which lowers the energetic consumption as well as improving the useful life of the component. Several studies have been reported in the literature that attempted to define the relationship between the parameters of the surface texture with the tribological performance [24-35].

Circular dimples are by far the most commonly applied micro-geometry, where the greater attention has been focused on their size and dispersion (see Figure 20 for an example). Yu et al [29] have also studied the effect of the micro-geometry by simulation and reported that elliptical dimples with the shorter axis parallel to the movement direction are more favourable for enhancing the load retaining capacity, thus reducing friction and wear.

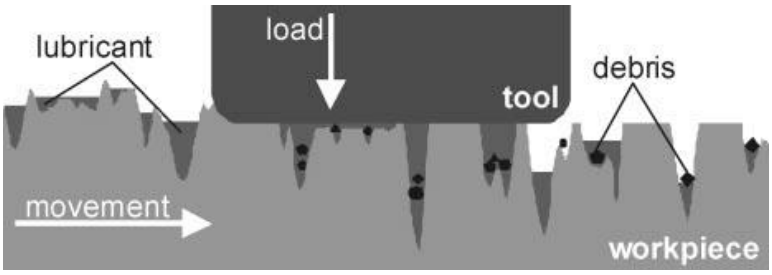

Figure 19. Principle of tribological effects on rough surfaces in metal forming [53].

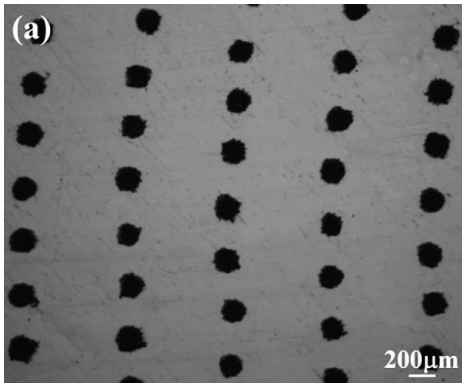

Figure 20. An LST pattern on T8 steel to improve to reduce friction and wear of a face seal [45].

LST applications have been reported to be developed for a variety of sectors. The greater part of these works has been devoted to mechanical and automotive applications [36-50]. Laser textured piston rings [36,38,40,41,43,47], gas seals [37,40,43,45,46] bearings [39,40,48,49] have been studied extensively both analytically and experimentally. In particular Etsion and Sher have demonstrated the direct impact of laser textured piston rings on the improvement of fuel efficiency of a Diesel engine [47].

Another important sector, for which LST is widely studied, is manufacturing [51-57]. Laser textured cold forging dies [51,53,55], deep drawing and punching dies [53], rollers [52], and cutting tools [56,57]. In particular 46% increase in tool life was observed with textured cold forging dies [53]. Laser textured cemented carbide cutting tools was employed in the form of shallow grooves with controlled pitch perpendicular and/or parallel directions to chip flow [56]. The authors reported up to 50% reduction in cutting forces in the turning of A5052 aluminium alloy.

In electronics, LST has been under study mainly related to resolve the stiction phenomenon in magnetic recording media [58-61]. For such applications the storage density highly relies on the flying height, which needs to be reduced to <10 nm. Direct use of lasers [58,59] or laser assisted [60,61] processes have been showed to reduce friction and avoid stiction.
In medical sector improved tribological performance has been reported for laser textured surgical blades [62]. The use of an array of dimples on reduced the friction up to 48%, which resulted in reduced cutting forces on tissue mimicking material.
The combination of LST to surface coatings has also received an increasing attention in the research community [63-74]. Different approaches are present where LST can be applied before [65,66,69] or after surface coating [63,64,71]. LST can be further incorporated with solid lubricants in the dimples as well [64,65,72-74]. The combination of all 3 is also possible. The employed micro-geometry was dimple in most of the cases, whereas elliptical and linear channels have also been employed [73]. Figure 21 depicts these combinations.

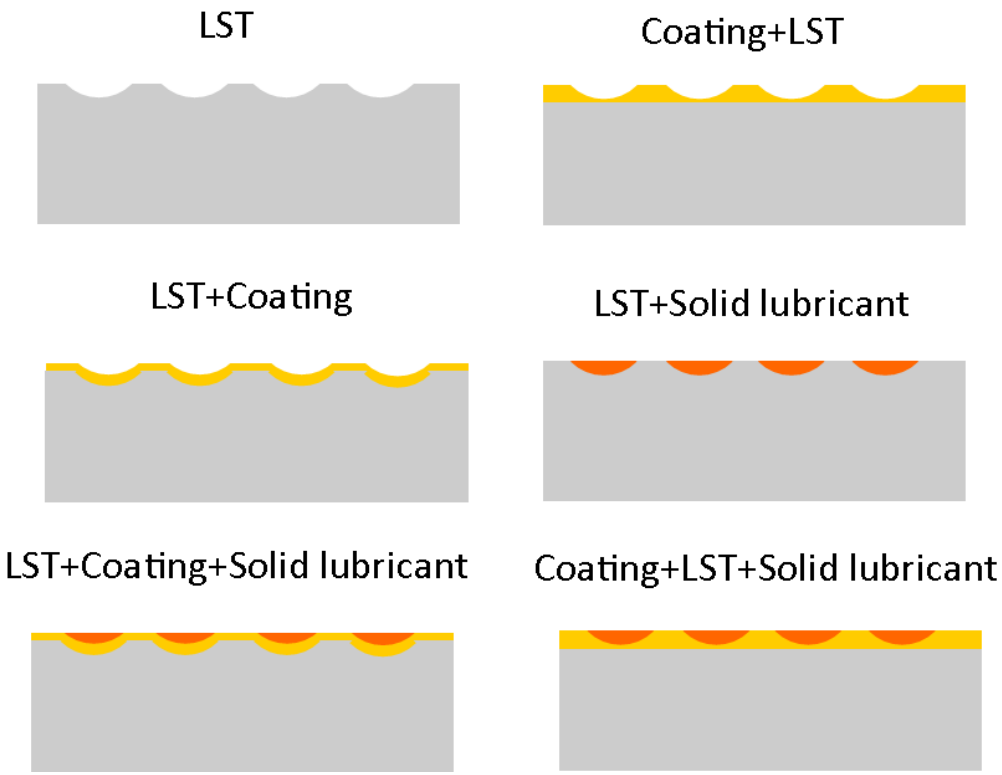

Figure 21. The incorporated use of LST, surface coating, and solid lubricant with regarding combinations.

3.2.2 Effect on adhesion

The use of adhesives allow light weight joints both in the case of assembling components of same material, and dissimilar materials. Surface preparation plays a crucial part in the adhesive joint design. LST provides a flexible control over the surface geometry that can induce advantageous effects such as the increase of contact surface, mechanical grip, change of surface chemistry that improve bonding to the polymer molecules of the adhesive. As a matter of fact, the laser treatment contributes to change all of these aspects simultaneously.

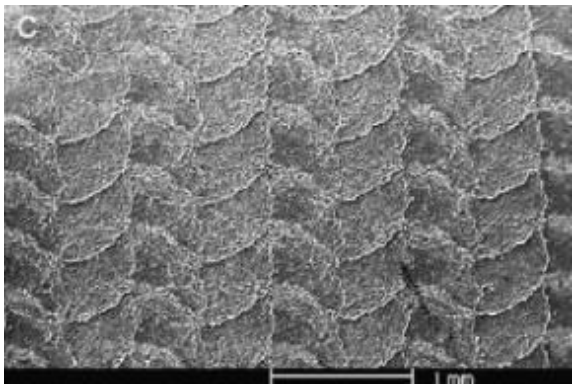

Figure 22. Laser texturing of 2024 aluminium surfaces for improving adhesion joint strength for transport and consrtuction applications [78].

The use of LST studies to improve adhesion in the literature are found especially in aerospace field. Galantucci et al used excimer laser treatment of metals and carbon fibre composites to improve the adhesion joint strength [75]. The authors used large laminar spot to change the surface roughness, which they have observed to reduce glycerine contact angle. On pure aluminium samples they have improved the adhesion strength by 70% compared to plain samples. Molitor and Young proposed the use of excimer laser to structure the titanium surfaces by large area melting and ablation [76]. They showed that the treatment significantly improved the surface wettability and adhesion properties of Ti-15-3 titanium alloy/glass fibre reinforced epoxy composite bond. Baburaj et al later on proposed micro-column arrays on commercially pure titanium obtained with excimer laser [77]. Their results showed threefold increase in the shear rupture strength of bonded specimens compared to non-treated ones. Spadaro et al on the other hand, used a Nd:YAG system to obtain surface textures based on remelting to increase surface area, on 2024 aluminium specimens (see Figure 22) [78]. The results indicated an improvement of up to double the adhesive fracture energy compared to specimens that have been only degreased. Man et al demonstrated the use of a fibre laser to texture titanium alloy surfaces with varying microhole densities to induce mechanical grip [79]. These authors demonstrated that a density of 100 micorholes per cm^2, 125 µm in diameter and 550 µm in depth improved the fracture load 30% and 80% compared to grit grinding and

sand-blasting respectively. Laser surface texturing was also used to improve adhesion of coatings and medical implants. In particular, Lamraoui et al showed the use of laser surface texturing on Al 2017 substrates prior to thermal spray coating of a Ni-Al powder [80]. Array of microholes generated by a fibre laser source enabled better contact between the coating and the substrate leading to improve the interface toughness. LST has also been employed on dental hard tissue, which has improved the bonding shear strength of the filler material [81]

3.2.3 Effect on optical properties

Changes in surface topography generated by LST can be beneficial for optical applications as well. The surface texture can change reflection and absorption of the material, which are essentially important for various applications in opto-electronics. Efficiency of solar cells, light emitting diodes can be enhanced as a direct consequence of the change in light absorption. Reduction in glare of consumer products such as cell phone or TV displays is another potential application.
LST for enhancing optical properties has been applied with different strategies involving direct writing in form of dimples (see Figure 23) [82], annealing to generate controlled surface roughness [83], and generation of self-organized micro/nano structures under ultra-short pulse irradiation in the form of ripples and columnar arrays [84-89]. Due to larger application in photovoltaic and semi-conductor based optical applications Si has received more attention [81-84], whereas works on titanium [86,88,89], germanium [85,87], stainless steel [88,89] aluminium [88,89], and copper [88,89] have also been reported.

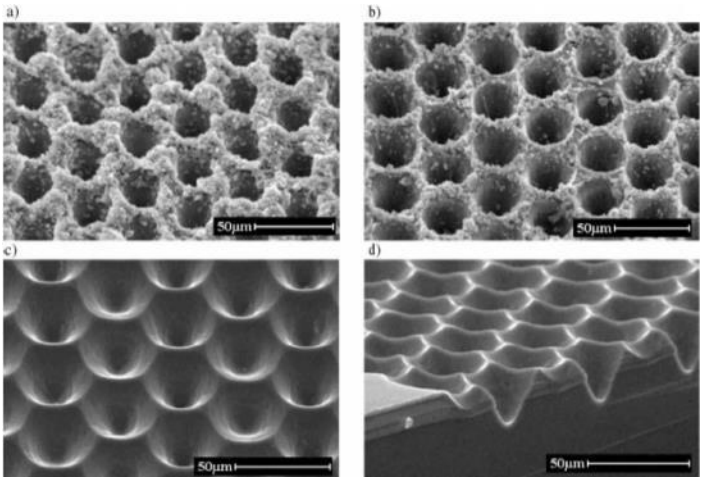

Figure 23. Laser textured Si surfaces for photovoltaic applications. (a) Immediately after ablation; (b) after NaOH etch; (c) finished texture after isotropic etch; (d) cross-section of finished texture viewed at an angle [82].

3.2.4 Effect on biological response

Surface topography and chemistry play an important role on the integration of the biomedical implant to the body. For controlled surface topography on medical implants, LST has been employed on metallic [90-95] and polymeric [96,97] materials for improving biological response of the tissue to the implant material. Laser texturing induces changes in surface chemistry, topography, and mechanical characteristics as well as increasing effective area and changing wetting behaviour which can be useful for cell integration. For example dimpled Ti6Al4V surfaces improved number of viable osteoblast cells up to 130% [91]. Similarly, grooved nylon 6,6 have been demonstrated to increase osteoblast cell cover density by 100% compared to as received surfaces (see Figure 24) [97]

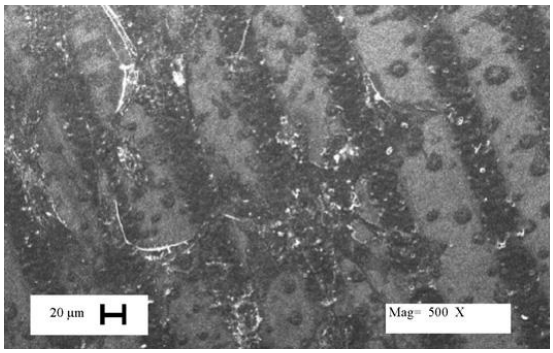

Figure 24. Osteoblast cell seeding on laser textured nylon 6,6 surface [97].

3.2.5 Effect on wettability

Surface wettability is a fundamental parameter in terms of how the surface interacts with the surrounding environment. The two states of surface wetting can be identified as: hydrophobic and hydrophilic. Wettability is often measured with the contact angle (CA) of the liquid on the surface, which is often water. Contact angles between 0° and 90° represents the hydrophilic region and between 90°-180° represent the hydrophobic region. The control of surface wetting is essential for surface adhesion, biocompatibility, and water absorption. Hydrophilic surfaces are often preferred for better adhesion properties and liquid harvesting, whereas hydrophobic surfaces are interesting for self-cleaning surfaces and stiction prevention. Wettability depends directly on surface topography, as increase of surface area and hierarchical organization of surface nano and micro features can either increase or decrease the contact angle. The of laser surface texturing for wettability control has been reported on polymeric [96,97] and metallic materials [98-100]. The works reporting micro surface textures result in limited changes in contact angle, whereas the use of nano surface textures obtained with ripple patterns using ultra short pulses result highly hydrophobic surfaces [98-100]. This is due to the entrapment of gaseous phase, which acts as a cushion layer. Moreover, the dependence of contact angle of the textured

surfaces on time has been also reported. It has been shown that the hierarchical surface textured composed of micro and nano features (as seen in Figure 25) on metallic surfaces were initially hydrophilic (CA=20°) and in time become hydrophobic (CA=150°) [98]. Such change was attributed to the change of surface chemistry.

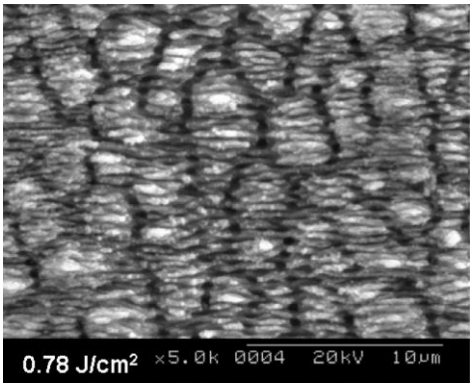

Figure 25. An example to laser textured surface showing hierarchical micro and nano scale features showing highly hydrophobic behaviour. Material: AISI 316L [98].

3.3 TiN coatings and their laser micromachining

Ceramic surface coatings are extensively applied for various purposes encompassing mechanical, biomedical, and electronic applications. Their superior properties in terms of mechanical, thermal and chemical stability render them interesting for improving the performance of the component by being applied only on a superficial layer. In particular, TiN coatings are industrially used in a large extent on cutting tools, dies and moulds, biomedical implants, components used in food industries, and decorative purposes [111-113]. TiN coatings have been also used in micro-electronic devices as a diffusion barrier [114]. Laser micromachining of TiN has been reported to be applied with excimer and CO_2 lasers with *µs* to *ns* pulses for relatively large surface areas, for the purpose of the removal of the coating itself [115-119]. On the other hand, ultrashort pulsed laser ablation of TiN has been demonstrated to be highly promising for dimpling purposes, due to non-thermal machining process [120-122]. Molten, recast areas and cracks in and around the dimpled areas can be potentially avoided with such sources.

Table 3 reports images selected from the literature representing different machining conditions. It can be seen that a clear distinction is visible between the machined surfaces moving from longer wavelengths and longer pulses to shorter wavelengths and shorter pulses. The uses of CO_2 [116] and HF excimer systems [117] show unacceptable results for micromachining, whereas the use of KrCl system shows visible improvement due to shorter length and pulse duration compared to the previous [116]. However, all these machining conditions show poor geometrical quality mainly due to poor beam quality of these sources. Moving towards ps [119]

and fs [120,122] pulsed system, debris free holes with high geometrical aspects are observed. These systems benefit from high beam quality as well as ablation conditions free of thermal effects. The use of fibre sources is an unexplored option, which at this point stands out as a promising option as they incorporate high beam quality with ns pulses and high energy content.

Table 3. Ablation of TiN ablation with different wavelengths and pulse durations as reported in the literature.

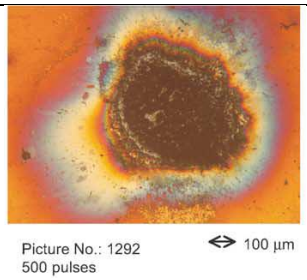 Source: CO_2 Wavelength: 10600 nm Pulse duration: 2 µs Ref [116]	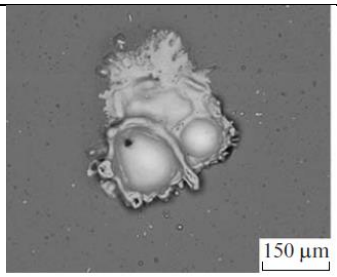 Source: HF – Excimer Wavelength: 2800 nm Pulse duration: 100 ns Ref [117]	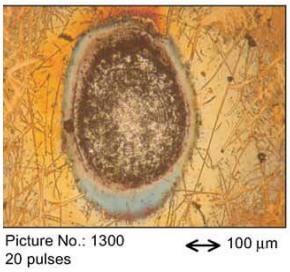 Source: KrCl - Excimer Wavelength: 222 nm Pulse duration: 12 ns Ref [116]
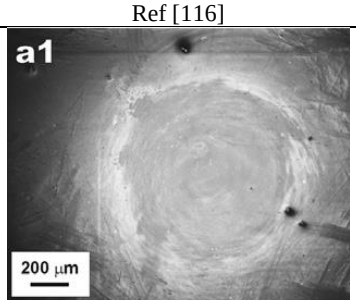 Source: Nd:YAG Wavelength: 532 nm Pulse duration: 40 ps Ref [119]	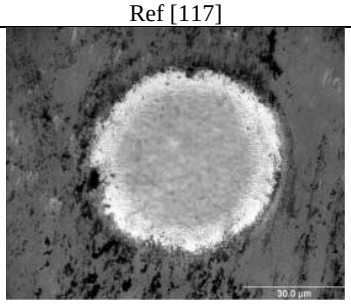 Source: Ti:Sapphire Wavelength: 800 nm Pulse duration: 150 fs Ref [122]	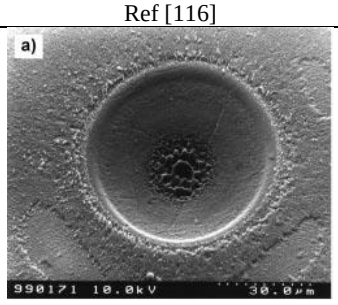 Source: Ti:Sapphire Wavelength: 800 nm Pulse duration: 150 fs Ref [120]

3.4 Strategies and methods for laser ablation monitoring

The literature survey on the strategies for laser ablation monitoring shows a very sparse behaviour of published material over the years. However, in terms of applied methods over the acoustic [123-135] and mechanical [126,127] methods, optical [128-156] measurement methods are dominant (see Figure 26).

The use of process sound as an indicator to ablation and drilling depth has been reported. Kurita et al found a close relationship between the maxima of the process sound and the groove cross sectional area per depth (see Figure 27) [123]. A similar approach was used by Stournaras and Chryssolouris for the depth measurement in laser drilling of deep holes [125]. The authors determined an empirical relationship between the signal mean and the hole depth. Bordachev and Nikumb investigated the mean and variance values of sound signals, as well as different spectral components

as identifiers of in ablation process, however they did not supply any information regarding the link between the signals and ablation geometry [124]. Although being a relatively simpler solution, the drawbacks of using acoustic signals are the fact that it does not provide a direct measurement and noise contribution in the signal.

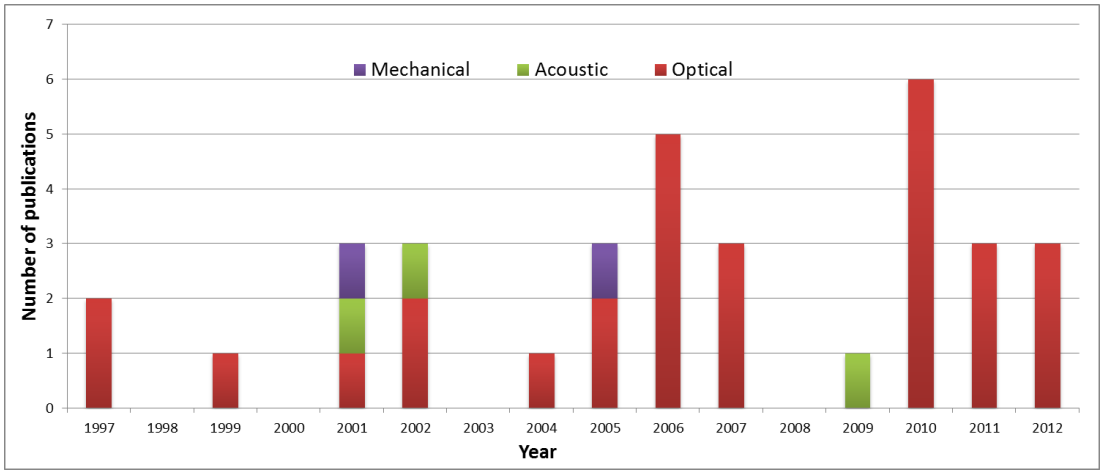

Figure 26. The number of articles published per year in laser ablation depth monitoring.

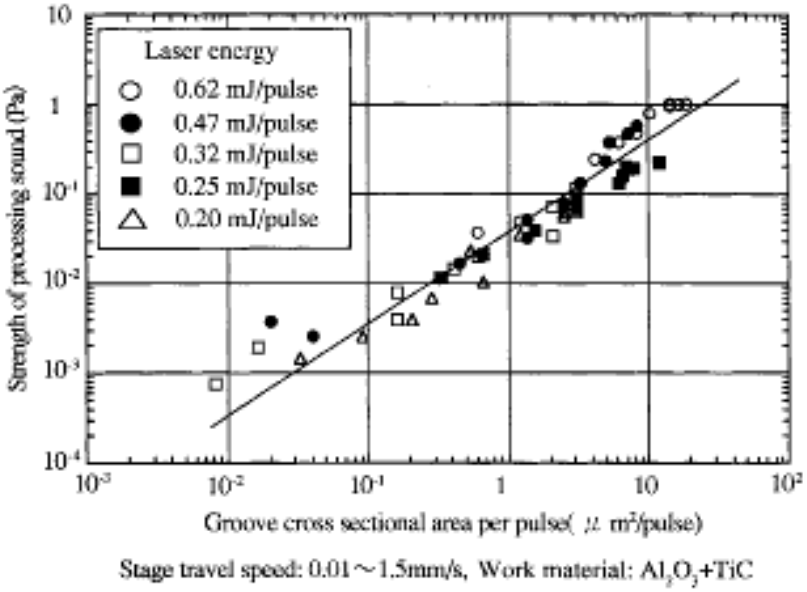

Figure 27. The relationship between the acoustic singal strength and groove sectional area per unit pulse [123].

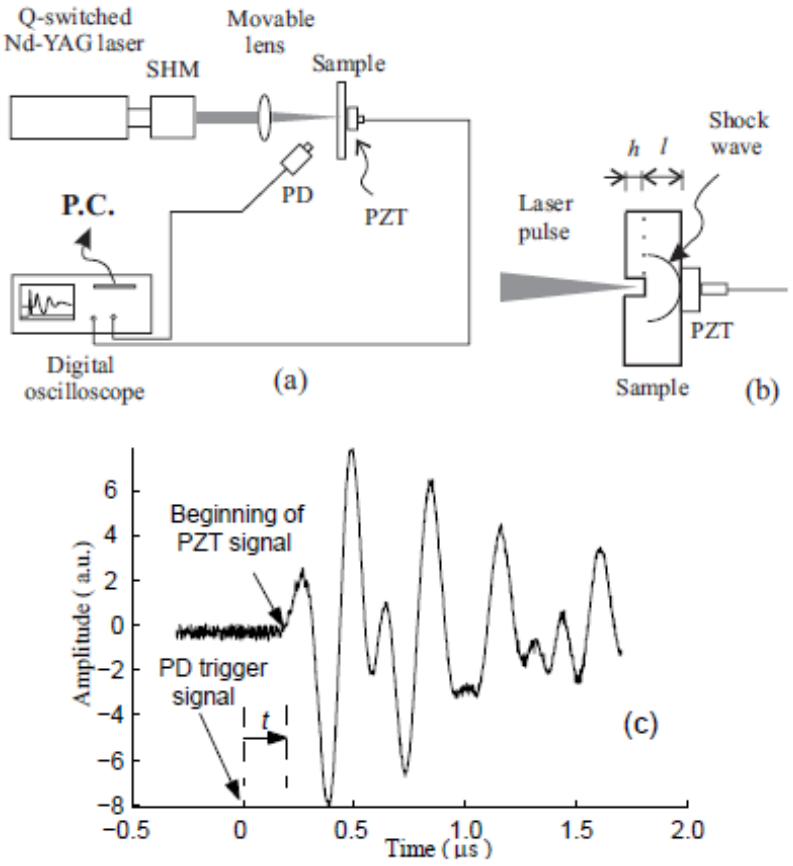

Figure 28. Laser drilling depth monitoring based on shockwave propagation measurement [127].

Strgar and Mozina, and Stafe et al studied the vibrations generated on the workpiece by ablation shockwave (see Figure 28). These groups measured the shockwave propagation to the bottom of the drilled hole. They pointed out that knowing the material thickness and assuming a constant shockwave velocity one can estimate the hole depth as the distance covered by the shockwave in the material. Although the authors declare good agreement between the estimated and measured hole depths, no actual value was reported. The method relies on a constant and known shockwave velocity, which are strong assumptions. Moreover, the possibility of multiple shockwave generation was not addressed. The method requires installing a piezoelectric transducer on the piece, which is invasive in an industrial micromachining scheme, and is prone to disturbances and vibrations in the environment.

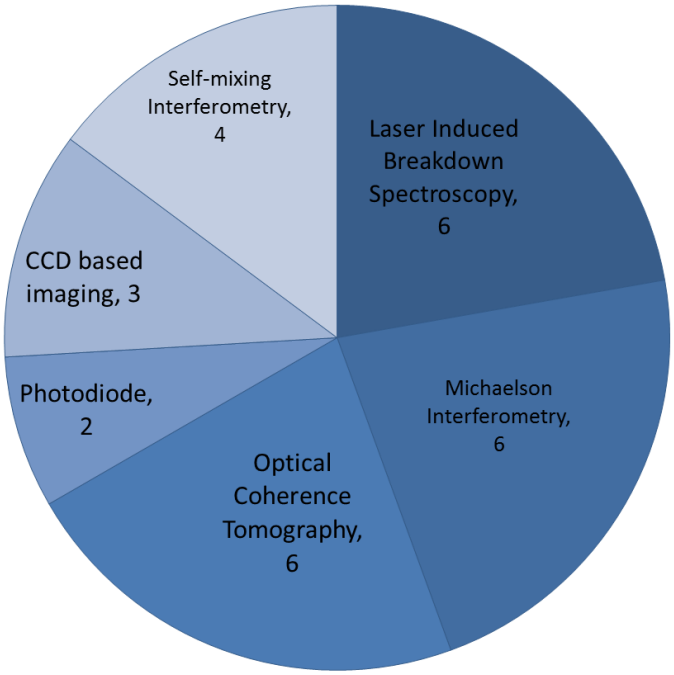

Figure 29. The number of published articles using different optical ablation depth monitoring methods.

Looking closer into the different optical methods used for depth measurement, it can be observed that direct and indirect measurement methods have been applied to measure the ablation depth (see Figure 29). Uses of photodiodes [129,145] and optical emission spectrum [128,134,135,137,142,147] are the indirect methods that enable to correlate the signal to the measured depth or change of material layer by observing the presence of a new signal component. Figure 30 shows an example case from Le Guen et al showing the use of laser induced breakdown spectroscopy (LIBS) for ablation depth measurement. The authors used LIBS to determine the thickness of tritium co-deposited layer on graphite substrate. The authors first determined a specific emission line in the LIBS spectrum and linked its intensity to the ablation depth.

Several optical methods have been proposed for direct measurement of the ablation depth. Figure 31 shows the trans-illumination imaging principal proposed by Döring et al for drilling depth measurement [146].The authors recorded the hole profile on a transparent material (Si), during ps pulsed ablation by using a standard CCD camera and opportune illumination. Although the applicability of such method is limited to transparent materials, it can be useful for industrial implementations for monitoring machining depth in transparent polymeric materials and glasses.

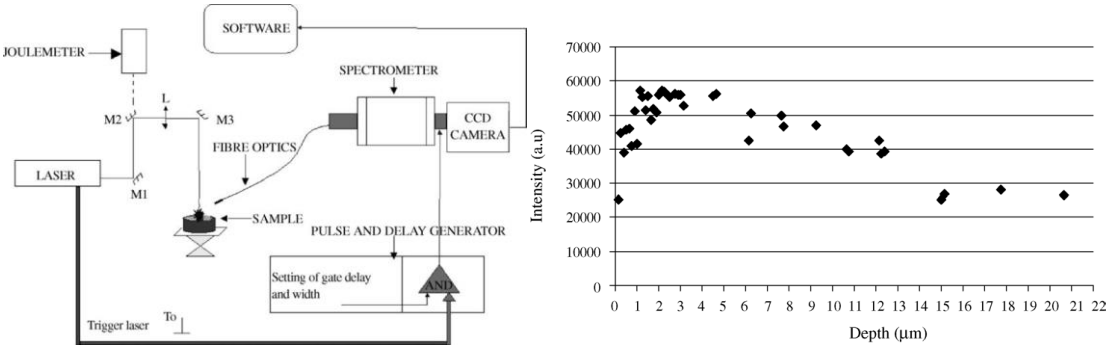

Figure 30. The use LIBS to determine ablation depth of co-deposited tritium layer on graphite substrates [137].

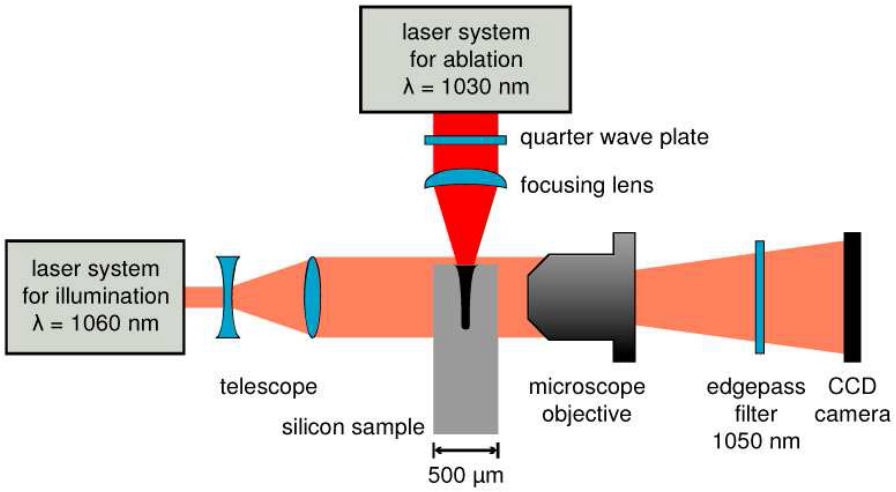

Figure 31. Trans-illumination imaging of the laser drilling process in the silicon sample [146].

Measurement of distance or displacement based on interferometric methods has been reported in a number of works due to high resolution of such methods in time and space [133,133,138-140,143,148,149,151-156]. Aperathitis et al used laser interferometry to measure the processing depth in reactive ion etching [132]. The authors used a high coherence light source that could detect the depth change by the counting interference fringes occurring at every half wavelength distance. Moreover the authors showed that the method could detect layer and roughness change by the differences in the signal amplitude due to change in material reflectivity (see Figure 32). Papazoglu et al used white light interferometry to obtain 3D images after laser microdrilling on AlGaAs/InGaAs semiconductor wafers (see Figure 33) [145]. They declared a depth resolution of 30 nm with the used system. Although high resolution images were obtained, the system capabilities do not match the requirements of online measurement.

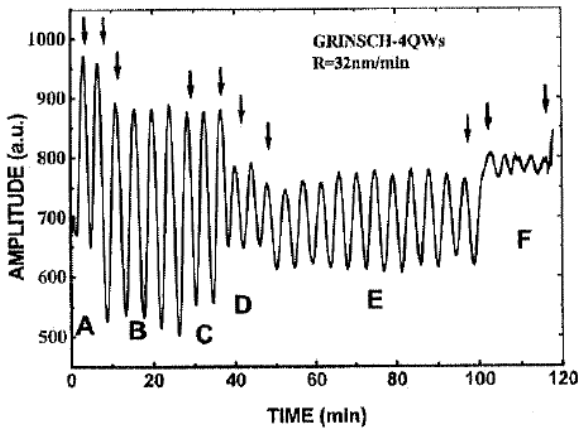

Figure 32. Monitoring of layer change and roughness increase in semiconductor chemical etching with interferometry [132].

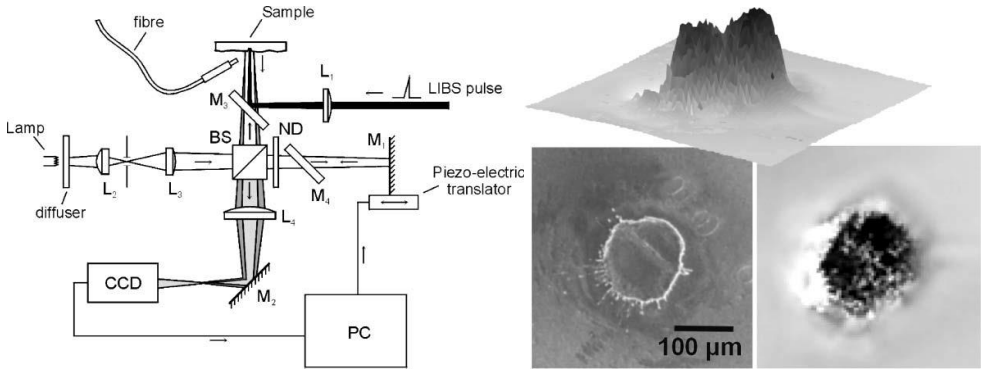

Figure 33. The topograhic measurement system used to measure drilling depth on AlGaAs/InGaAs semiconductor wafers (left) and an example acquisition (right) [145].

On the other hand, an increasing number of publications in optical coherence tomography (OCT) [131,135,139,140,144,145] and self-mixing interferometry [142,143,146,147] is observed recently. OCT is applied with low-coherence light sources and the resolution of these systems depends on the bandwidth of the light source. The method generates tomographic images when applied to transparent or semi-transparent materials, whereas on opaque materials surface topography can be measured. The measurement scheme is very similar to Michaelson interferometry, where the laser beam is divided into reference and measurement arms, and the interference pattern is generated on a digital sensor. OCT can be used in time or Fourier domains to improve spatial or temporal resolution. In time domain, images with high lateral resolution with on different planes are acquired by moving the reference arm with piezoelectric translators. Due to the use of the low coherence laser beam the depth field is limited in the acquired image. The 3D image is then constructed with high depth resolution using the 2D images of different planes. The acquisition and construction stages are much longer than the processing time in laser microdrilling. Therefore this approach is useful for quality control or on board

metrology in laser micromachining. On the other hand, OCT can be used with high temporal resolution in Fourier domain. In this scheme the interference pattern is measured with a spectrometer to divide the pattern in its spectral components. The Fourier transform of the spectrum yields the position information of all the illuminated area, without a distinction in lateral position. No depth scan is required, as the measurable depth is determined by the Rayleigh length of the light source. The so called M-mode images (M: motion) are constructed, where reflectivity at different depth positions are represented. These images can be useful to detect the deepest position that reflects at a given time instance, such as the hole depth. Therefore Fourier domain OCT can be used as a mono-dimensional measurement tool with high temporal resolution. Figure 34 depicts such system with a real-time M-mode image showing advancement of a hole obtained during microdrilling of steel with a ns fibre laser [153]. The authors this work declared 6.2 µm depth and 100 ns time resolution. Fourier domain OCT appears to be a highly promising technique for industrial implementation regarding applications that do not require sub-µm depth resolution.

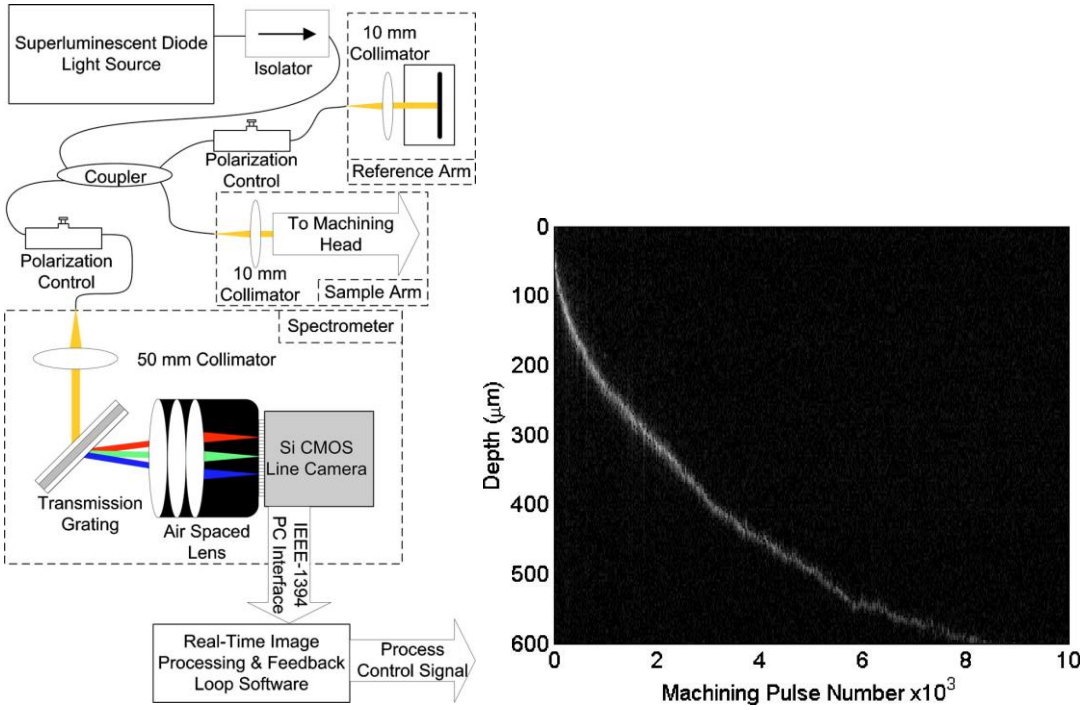

Figure 34. The Fourier domain OCT measurement setup (left) and an M-mode image showing the hole depth advancement in the microdrilling of steel with a ns fibre laser (right) [153].

The use of self-mixing interferometry for laser drilling depth has been demonstrated by Mezzapesa et al [151]. The authors launched a laser diode beam with 823 nm wavelength into the micro hole during processing with a ps laser (see Figure 35). The authors also calculated the drilling depth change as a function of time on 50 µm steel specimens. The same authors used the measurement technique on other works using

the same processing laser on different materials [152,155,156]. For the use of self-mixing interferometry for ablation depth monitoring, the same group also applied for a patent under patent number WO 2012101570 A1 [157].
The method is promising for high resolution measurements using simpler measurement scheme. However, coherence imaging of this kind is prone coherence and optical power, which is expected to occur passing through turbid media [158]. In laser micro machining, the ablation plume constitutes the turbid media and is characterized by high pressure, temperature, and refraction index variations. These problems have not been yet addressed in the literature.

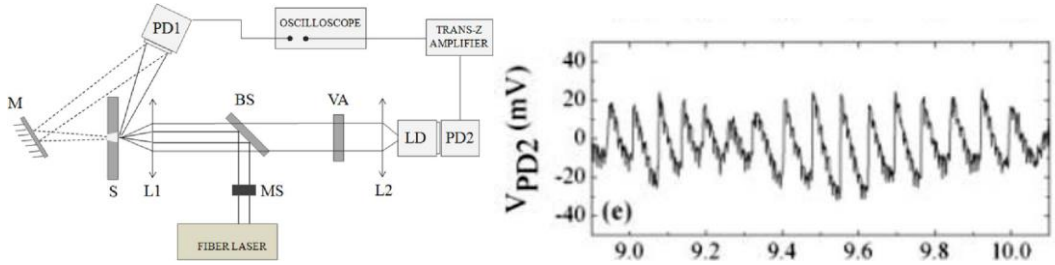

Figure 35. Self-mixing interferometry setup for ablation depth measurement (left), and a self-mixing signal showing displacement fringes.[152].

3.5 Applications of laser self-mixing interferometry

The laser self-mixing phenomenon based on the interference of backreflected laser beam inside the cavity, which generates oscillations of the optical power. Early research was concerned to control and eliminate such oscillations, whereas later on attention developed to make use of the phenomenon for interferometric measurements. The first exploitation of laser self-mixing effect to measure Doppler-shifted backscattered signal with a He-Ne laser was reported as early as 1968 by Rudd [159]. The author measured the interference signal from the back of the laser cavity, rather than using a Michelson interferometry setup. In 1977 Donati showed the first example of fringe counting with self-mixing interferometry for displacement and speed measurements using a He-Ne laser [160]. The use of semiconductor lasers introduced further simplification of the self-mixing interferometry scheme due to compactness, more stable performance, and direct measurement from the photodetector attached to the laser diode, and full-electronic system [3]. Today, self-mixing interferometry is commonly employed with semiconductor laser diodes with different emission wavelength and high coherence lengths. The interference signal is extracted from the optical power oscillation, and the counting of fringes can be used for displacement measurement with $\lambda/2$ resolution, thus in the range of a few hundreds of nm. Further data treatment can increase the resolution. Self-mixing interferometry allows mono-dimensional displacement measurement with high temporal resolution is possible using cheap instruments that are less sensitive to environmental changes.

Moreover self-mixing interferometry is sensitive to spurious reflections and speckle effects. Spurious reflections of even very small amounts should be avoided, because the high sensitivity of the self-mixing detection scheme may result in disturbances superimposed onto the desired signal. Self-mixing interferometry has used in various applications ranging from velocity [161], vibration [161,162], and range finding [163] applications. In these applications cooperating targets are used, meaning the external effects that change the feedback parameter are avoided by compensating the target's movement in other directions. However, a target locking approach would be extremely difficult in the case of a micro dimple. Zabit et al have recently reported a signal recovery process in the presence of speckle when non cooperating targets are used [164]. The changes in the feedback parameter due to external disturbances that moved the target surface in other directions were compensated by signal normalization.
In summary the potential advantages and disadvantages of self-mixing interferometry for ablation depth measurement can be listed as the following.

Advantages:

- Direct measurement of displacement magnitude and direction
- High temporal and spatial resolution
- Simple architecture and equipment
- Cost effective

Disadvantages:

- Prone to disturbances and changes in the optical path
- Sensitive alignment of the beam that needs to enter into a dimple
- Read-out photodiode can integrate the process laser and emission
- Mode hopping can be expected due to excessive feedback and temperature gradients during process

Chapter 4

Experimental setup for Laser Surface Texturing (LST) of TiN coatings with ns-pulsed fibre lasers

Laser surface texturing (LST) of TiN coatings was studied with 3 different pulsed fibre laser sources in *ns* pulse regime ranging from long ns pulses (250 ns) to short ns pulses (1 ns). The experimentation was carried out in two different institutions as in the following:

- SITEC – Laboratory for Laser Applications of Department of Mechanical Engineering at the Politecnico di Milano in Italy between the periods of January 2010 – May 2012 and November 2012 – July 2013
- Centre for Industrial Photonics of the Institute for Manufacturing of the Department of Engineering at the University of Cambridge in UK between the period of May 2012 – November 2012.

Along with the used laser sources 3 different types of TiN coated samples were used within the experimentation. The combinations and the differences of the used instrumentation require an extensive characterization of the used materials and instruments, which is explained in the beginning of this chapter. Following, the micromachining strategies for the different laser sources are reported, along with the characterization techniques for evaluating the process characteristics. Finally, a comparative analysis is presented to explain the different characteristics in different laser micromachining domains in terms of quality and industrial applicability.

4.1 Characteristics of the used PVD TiN coatings

Within the experimental study for LST of TiN coatings, 3 different substrate materials were used. The preference of different substrate materials were due to the collaborative research efforts conducted with partner research teams and institutions. The tribological performance and metallurgical behaviour of LST of TiN coatings were evaluated in collaboration with:

- Centre of Study and Development for Metallurgy and Materials for Engineering (Poli@l CS2M2), Department of Applied Science and Technologies, Politecnico di Torino, Dr. Daniele Ugues
- Metallurgy Section of the Department of Mechanical Engineering, Politecnico di Milano, Prof. Nora Lecis

The used TiN coatings were deposited by physical vapour deposition (PVD) technique on 42CrMo4, AISI M2, 39NiCrMo3 tool steels to represent the conditions of commonly found on cold forming dies. The different substrate materials allowed the study of the effect of the substrate material on the tribological system related to adhesion of the coating to the substrate, substrate toughness and hardness. The chemical compositions of the 3 substrate materials are listed in Table 4.

Table 4. Chemical composition of the used substrate materials [165,166]

Designation		Chemical composition (wt%)									
UNI	SAE	C	Si	Mn	P	S	Ni	Cr	Mo	V	W
42CrMo4	4140	0.37–0.42	0.20–0.35	0.75–1.00	0.035	0.035	-	0.80–1.20	0.15–0.25	-	-
HS 6-5-2	AISI M2	0.86-0.94	-	-	-	-	-	3.80-4.50	4.70-5.20	1.70-2.00	6.00-6.70
39NiCrMo3	8637	0.35–0.43	0.15–0.40	0.50–0.80	0.035	0.035	0.70–1.00	0.60–1.00	0.15–0.25	-	-

Although the difference in substrate material is not negligible, it is relatively much smaller compared to the effect of the laser process parameters due to the fact that:

- All substrates are coated with the same coating TiN, with the same PVD method
- The chemical compositions of the subtrate materials are very similar, which maintain similar physical properties.

Due to material availability the 42CrMo4 and 39NiCrMo3 substrates were prepared from 50 mm bars with 12 mm thickness, whereas AISI M2 substrates were prepared from a flat slab of 10 mm thickness in rectangular form with dimensions on 25 mm x 15 mm. The 42CrMo4 substrates constituted the first generation of the used specimens as they were polished after cutting and PVD coated separately. On the other hand AISI M2 and 39NiCrMo3 specimens were turned and grinded to reach a more productive solution for industrial applications, and PVD coated separately to reach a higher coating thickness. All substrates were quenched and tempered.

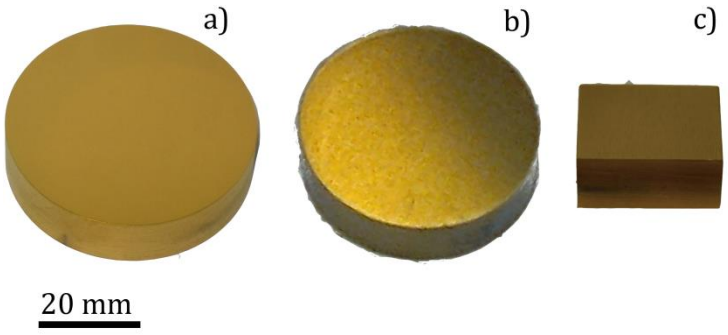

Figure 36. TiN coated samples with a) 42CrMo4, b)39NiCrMo3, and c) AISI M2 as the substrate.

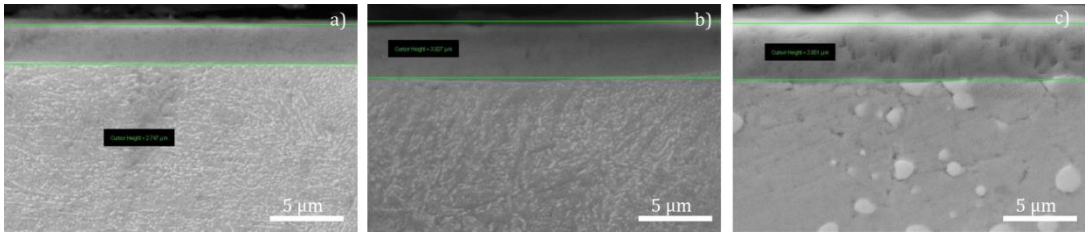

Figure 37. SEM images of the cross-sections belonging to TiN coated a) 42CrMo4, b)39NiCrMo3, and c) AISI M2 as the substrate.

Table 5. Main characteristics of the TiN coated specimens.

Substrate type	Coating Thickness h [µm]	Longitudinal average roughness R_a [µm]	Transversal average roughness R_a [µm]	Substrate Hardness [HV]
42CrMo4	2.73 ± 0.01	0.04 ± 0.01	0.04 ± 0.01	308.7 ± 9.5
AISI M2	3.91 ± 0.09	0.57 ± 0.09	0.80 ± 0.06	906.5 ± 17.5
39NiCrMo3	3.87 ± 0.14	0.37 ± 0.09	0.69 ± 0.03	317.3 ± 3.7

Table 6. Physical properties of the coating and substrate materials [13,14,165-168]

Property		TiN	42CrMo4	AISI M2	39NiCrMo3
Density	ρ (kg/m^3)	5220	7850	8160	7830
Melting temperature	T_m (K)	3223	1738	1723	1758
Heat capacity	c_p (J/kgK)	702.6	470	500	471
Thermal conductivity	K (W/mK)	19.2	45	21.3	44.5
Thermal diffusivity	κ (m^2/s)	5.24e-6	12.20e-6	5.22e-6	12.07e-6
Reflectivity at 1064 nm	R	80%	65% (Fe)	65% (Fe)	65% (Fe)
Reflectivity at 532 nm	R	80%	58 % (Fe)	58 % (Fe)	58 % (Fe)

Figure 36 shows the TiN coated substrates, whereas Figure 37 reports SEM images of the cross sections of the different specimens indicating the coating thickness. The main properties of the different specimen types are listed in Table 6. It can be observed that due to the different preparation techniques the average surface roughness values of the coatings on 42CrMo4 substrates are much less compared to the ones belonging to the coatings on 39NiCrMo3 and AISI M2 samples. On the other hand, the second generation samples were notably thicker than the first generation samples on 42CrMo4 substrates by about 1.3 µm. In terms of substrate hardness the AISI M2 specimens showed values 3 folds of the other two. Among these properties the surface roughness and coating thickness are considerably more important for the outcome of the laser micromachining process, since surface roughness can change the surface reflection, and the coating thickness determines the distance between the coating surface and the substrate. In highly energetic conditions it is expected to reach the substrate and machine beyond the coating. For this purpose

it was decided to match the different coating types, noted by their substrate type from here on, with a single laser system. The effect of the different ns pulsed laser systems is then confronted by means of investigating the ablation characteristics.

4.2 Specifications of the used ns-pulsed fibre laser systems

Three different pulsed laser systems were employed in the study of micromachining of TiN coatings. All 3 systems were pulsed active fibre lasers operating in ns pulse regime. In contrasts, they differed mainly in architecture, which in return changes the pulse duration of these systems and emission wavelength. Table 7 reports the main characteristics of the laser systems. As a first step, the laser systems were characterized in terms of power/energy curves and pulse shape. Next, the processing systems in terms of instrumentation for automation, control, and processing was described. Once the laser and the beam positioning system characteristics were defined, possible processing strategies were evaluated.

Table 7. Comparison of the used ns pulsed fibre laser systems.

Brand and model	IPG YLP-1/100/50/50	SPI G3 20P-HS	IPG YLPG-5
Architecture	Fibre, Q-switched	Fibre, MOPA	Fibre, MOPA
Wavelength	1064 nm	1064 nm	532 nm
Max. average power	50 W	20 W	6 W
Pulse repetition rate	20-80 kHz	1-500 kHz	20-300 kHz
Max. pulse energy	1020 µJ	800 µJ	20 µJ
Pulse duration	250 ns	9-200 ns	1 ns
M^2	1.7	2	1.1
Collimated diameter	5.9 mm	3.1 mm	3.49 mm
Processing head	Scanner head	Scanner head	Optical assembly
Positioning system	Galvanometric mirrors	Galvanometric mirrors	Fixed optics/Manual
Location	Politecnico di Milano	University of Cambridge	Politecnico di Milano

4.2.1 Q-Switched, long ns, 1 µm fibre laser – λ=1064 nm; τ=250 ns

a) General specifications

The used laser source was an IPG YLP-1/100/50/50 Q-switched pulsed active fibre laser (see Figure 38). The laser is characterized by longer ns pulses and high energy content, which enables high material removal rate. This fact makes it suitable for industrial marking applications that do not require high machining quality. However, the laser source exhibits potentiality in terms of acceptable machining quality with improved productivity. The laser source uses and opto-acoustic Q-switch mechanism that generates pulses with fixed duration around 250 ns. The seed laser passes through the Q-switch and enters the Yb-doped active fibre cavity, where it is amplified. The exiting pulse shape depends on how the laser cavity, i.e. the active fibre, releases the energy. Therefore, pulse duration or shape variations are not possible. The laser

source is capable of with pulse repetition rates between 20-80 kHz, 50 W maximum average power and 1 mJ maximum pulse energy. For the functional block diagram of the laser source see Figure 39. The general characteristics of the laser sources are summarized in Table 8.

Figure 38. IPG YLP-1/100/50/50 Q-switched, long ns pulsed, 1 µm fibre laser source.

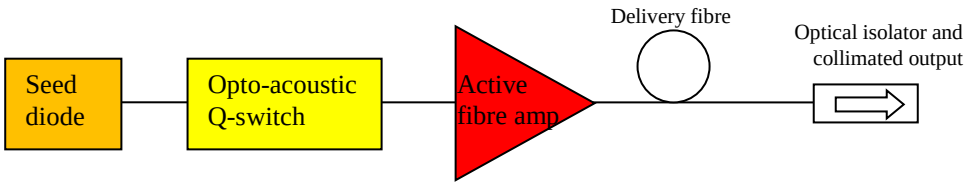

Figure 39. Functional block diagram of the IPG YLP-1/100/50/50 laser source.

Table 8. General characteristics of the IPG YLP 1/100/50/50 laser source.

Wavelength	1064 nm
Max. average power	50 W
Pulse repetition rate	20-80 kHz
Pulse energy range	42- 1120 µJ
Pulse duration	250 ns
M^2	1.7
Collimated diameter	5.9 mm
Beam expansion	None
Focusing lens	100 mm
Focused beam diameter	39 µm

The laser source is controlled by 2 essential parameters:

1. Pump current percentage (*PI%*): the parameter that allows controlling the power level for pulse repetition rate through the regulation of the current inserted in the diodes that pump the active fibre amplifier. The *PI%* can be varied from 10 to 100.

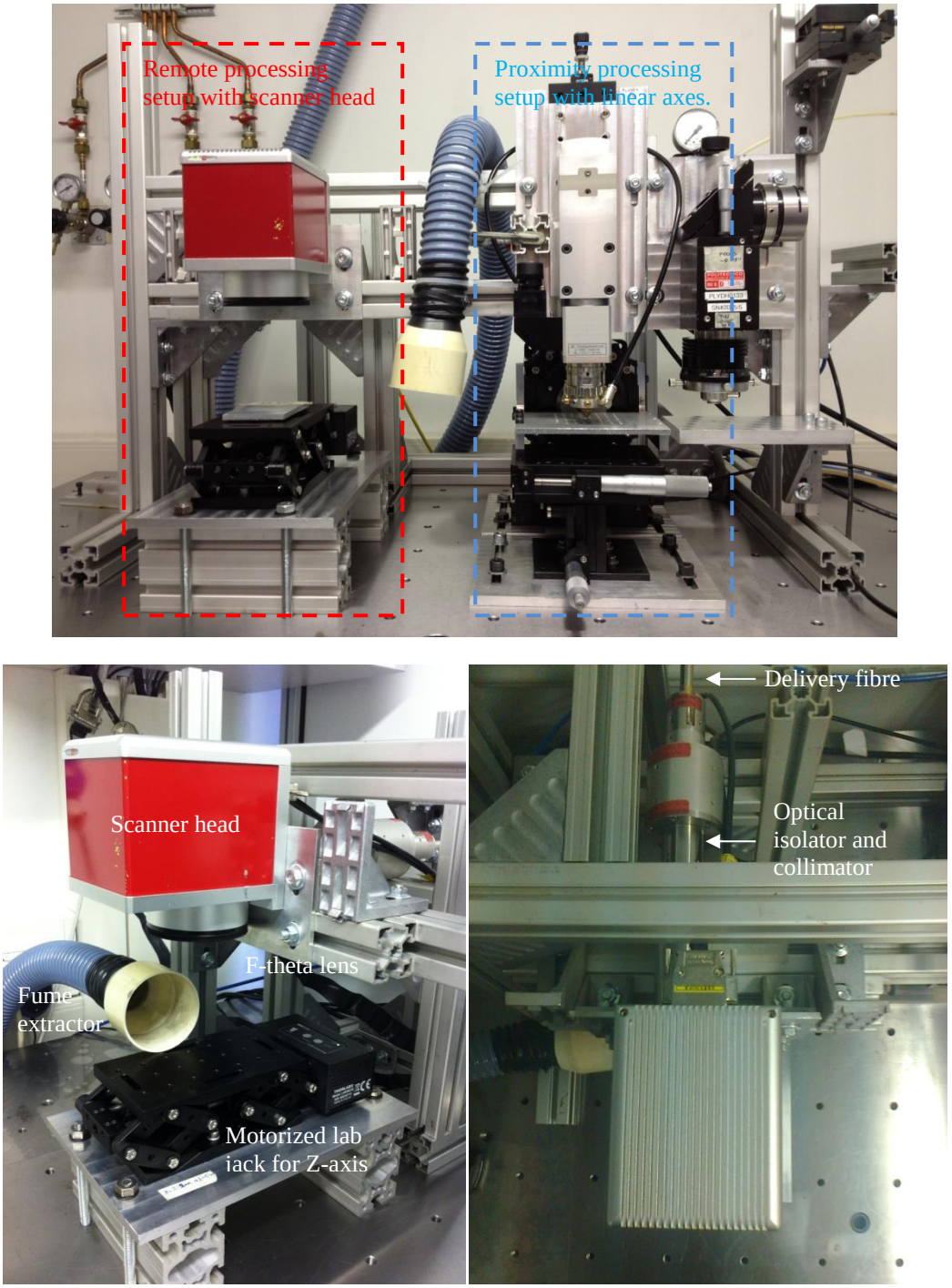

Figure 40. The IPG YLG-1/100/50/50 experimental setup.

2. Pulse repetition rate (*PRR*): the parameter that determines the pulse frequency. The average power emitted by the laser is also a function of *PRR*. The average

power output is required to be mapped as a function of both of the parameters. The *PRR* can be varied between 20 and 80 kHz.

b) Experimental setup

The laser source provided a collimated beam with 5.9 mm diameter, which was not further expanded. Beam manipulation was achieved via a THS 8310 scan head from Century Sunny that used two high speed galvanometric mirrors for positioning the beam in X and Y axes. The scan head housed a 100 mm f-theta focal lens. In this configuration the calculated beam diameter was 39 µm. The workpiece was positioned in Z-axis with L490MZ/M motorized lab jack from Thorlabs with 5 µm repeatability. The system components are shown in Figure 40. For control of laser source parameters the IPG control utility was used as seen in Figure 41. For machining pattern generation CS Mark software from Century Sunny was used. The software controlled the beam manipulation parameters. Since the laser surface texturing studies were conducted with a point-to-point strategy, where dimples were generated with percussion drilling method, the parameters related to beam manipulation that were controlled via the CS Mark software were:

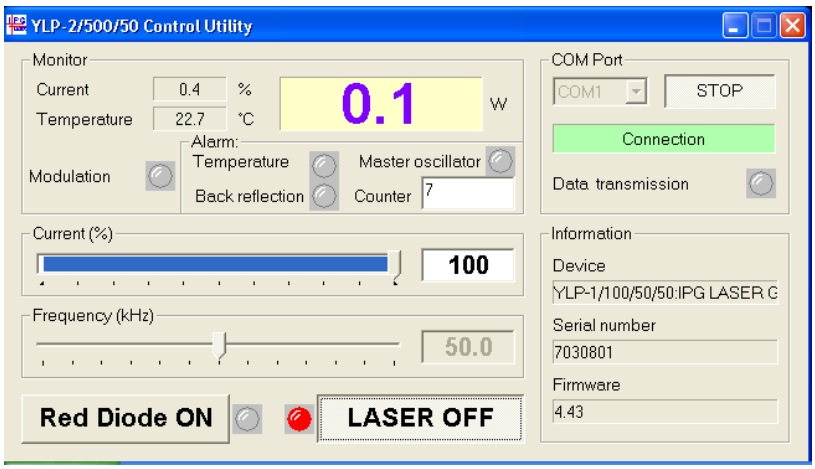

Figure 41.The IPG control utility for laser parameter setup.

1. Modulation duration (t_{mod} [ms]): the gate time that determines the duration of the pumping diodes being injected with current. In the CS Mark software the control parameter is named “Pulse width” to attribute to the modulation of a continuous wave laser via switching. When used with the present Q-switched fibre laser, the parameter determines the gate for emission.
2. Jump speed (v_{jump} [mm/s]): the speed used for jumping from the position of one dimple to the other.
3. Jump delay (t_{delay} [ms]): the amount of time before jumping to the next dimple. This parameter ensures the position stability of the dimples. Low

jump delays result in incorrect positioning due to drifts and overshoots in the movement of the galvanometric mirrors.

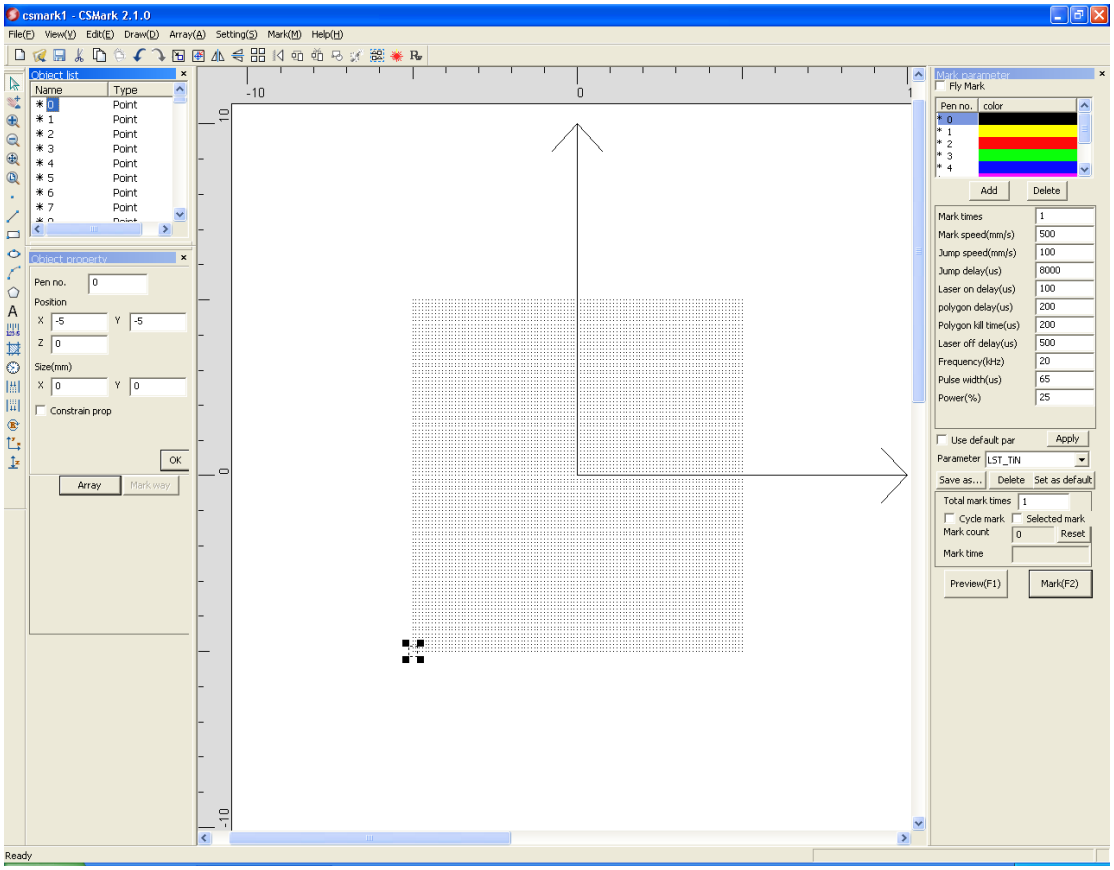

Figure 42. Control interface of the CS Mark software.

c) Laser source characterization

An extensive characterisation of the present laser source has been a matter of another PhD thesis [169]. However, some measurements were repeated because of the change in the optical path and other important details are reported here for a better comparison with the other two laser sources. The 2 control parameters of this laser sources were mapped for the average power output with the new scanner head. For this purpose a Plus+ power meter from Laser Point was used. To allow stabilization of the device the laser source was modulated to emit for 10 seconds for each parameter combination. Pump current was varied between 20% and 100%, while pulse repetition rate was varied between 20 and 80 kHz. Table 7 reports the complete list of parameter levels used for this characterization.

Figure 43 shows the measured average power levels. The highest average power output was recorded as 53.30 W, whereas the lowest was 0.85 W. On the other hand, two distinct regions can be identified in terms available *PRR* range:

1. Between 20 and 50 kHz, where the average power increases with PRR
2. Between 50 and 80 kHz, where the average power remains stable.

Table 9. Fixed and varied parameters for the characterization of single pulsed emission of IPG YLP-1/100/50/50 laser

Fixed parameters	
Modulation duration (t_{mod})	10 s
Varied parameters	
Pump current (PI%)	20, 30, 40, 50, 60,70, 80, 90, 100
Pulse repetition rate (PRR [kHz])	20, 35, 50, 65, 80
Measured variable	
Average power (P_{avg} [W])	

Although not directly declared by the manufacturer, the observation confirms that 50 kHz corresponds to the so called switching frequency, which is used to prevent the laser source getting damaged by high peak power pulses. The average pulse power measurements were then used to calculate the pulse energy (E) in different parameter combinations from the equation:

$$E[J] = P_{avg}\,[W] \cdot PRR\,[Hz] \qquad \text{Eq.(4.1)}$$

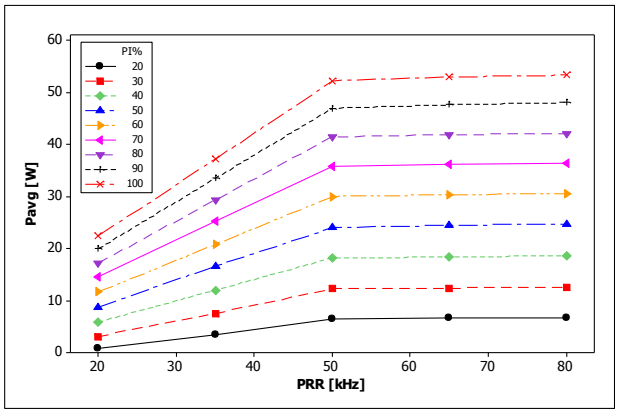

Figure 43. Measured average power values for PI% and PRR combinations (connection lines are to depict the trend).

Figure 44 shows the calculated pulse energies. It can be observed that for *PRR* values lower and higher than the switching frequency different trends occur. For *PRR* values higher than the switching frequency the pulse energy drops as *PRR* increases due to constant P_{avg} in this regime. For *PRR* values lower than the switching frequency a constant pulse energy regime can be identified with *PI* values higher than 50%; with *PI* values between 20% and 50% the pulse energy increases.

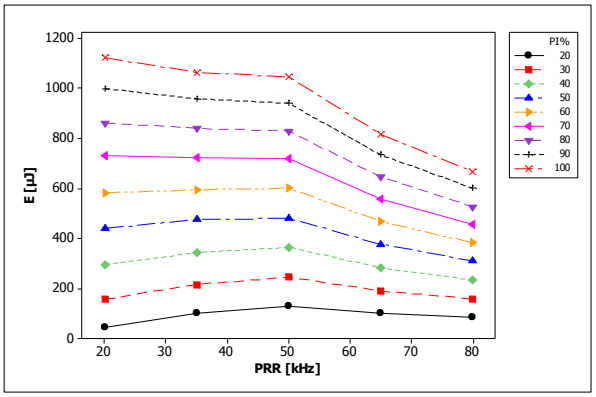

Figure 44. Calculated energy values for *PI%* and *PRR* combinations (connection lines are to depict the trend).

Figure 10 and 11 show the pulse shape characteristics as adapted from Ref. [169]. Pulses generated with the IPG YLP-1/100/50/50 source are characterised by slow ascending peaks, as the pulse peak power (P_{peak}) is reached between 50-80 ns. The peak power is reached much later as the pulse energy increases (see Figure 45). With low energy pulses the pulse peak disappears, and a blunt shape is present (see Figure 46).

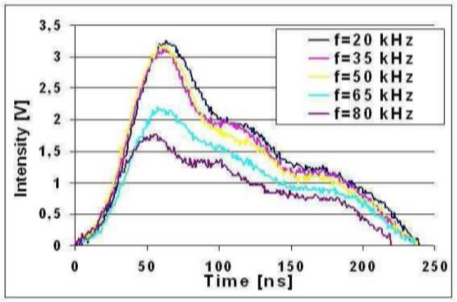

Figure 45. Oscilloscope traces of the pulse shapes as a function of pulse repetition rate (*f*) at 100% pump current level [169].

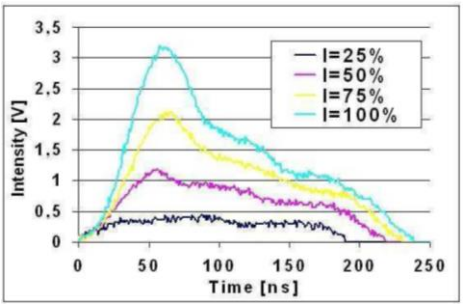

Figure 46. Oscilloscope traces of the pulse shapes as a function of pump current (*I*) at *PRR*=50 kHz [169]

An example of the pulse profile was acquired with a FGA10 InGaAs based photodiode (see Figure 47). The photodiode had an acquisition range 800-1800 nm wavelengths, and 7 ns rise time. A Tektronix TDS5034B digital oscilloscope with 350 MHz maximum bandwidth, 5 GS/s sampling rate and $16 \cdot 10^6$ record length was used for recording the signal. Calculated pulse energy was used for discrete derivation calculating the power profile, since:

$$E = \int_0^{\tau} P(t)dt \qquad \text{Eq.(4.2)}$$

thus,

$$P(t) = \frac{dE}{dt} \qquad \text{Eq.(4.3)}$$

The parameter combination shown in Figure 12 corresponds to the highest peak power available, which was calculated to be 9 kW.

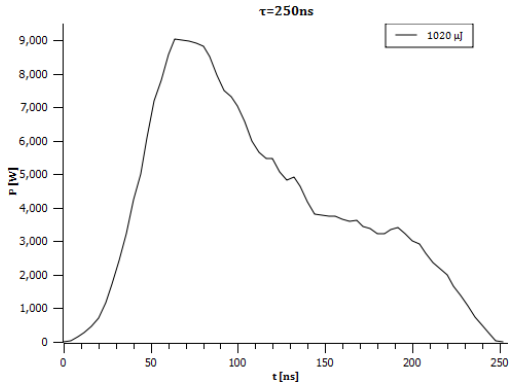

Figure 47. Power profile and energy content of the pulse shape for PI=100% and PRR=50 kHz.

4.2.2 MOPA, pulse duration tunable, 1 µm fibre laser – λ=1064 nm; τ=12-200 ns

a) General specifications

The used laser source was SPI G3 20P-HS pulsed active fibre laser based on master oscillator power amplifier (MOPA) architecture with pulse PulseTune^{TM} capability, allowing choosing from different waveform presets. The different waveforms generate pulses with different shapes and durations, which renders this laser source very appealing for studying the effect of pulse duration in a wide range. The laser source can be seen in Figure 48 and the general specifications of the source are summarized in Table 10. The functional block diagram of the laser source is shown in Figure 49. The seed optical pulses are generated by a single mode semi-conductor laser diode. A pre-amplifier and a power amplifier stages based on Yb-doped fibre are

present after the seed stage, which are pumped by multimode laser diodes. The seed pulse is amplified in these stages and then delivered to free-space via an optical fibre terminated by an optical isolator and an optional beam expander. The laser source is capable of running both in continuous wave and pulse wave between 1-500 kHz, with pulse durations ranging between 9-200 ns, 20 W maximum average power and 0.8 mJ pulse energy.
In order to prevent the laser source getting damaged by high peak power pulses, the laser source utilizes a switching frequency for each waveform number denoted by PRF_0. Below PRF_0, the laser source emits with fixed maximum energy, whereas when operating above PRF_0 the maximum average power is kept constant and the maximum pulse energy drops (see Figure 50). Table 11 reports the switch pulse repetition rate and pulse energies of the waveforms along with their pulse durations.

Table 10. General characteristics of the SPI G3 20P-HS laser source.

Wavelength	1064 nm
Max. average power	20 W
Pulse repetition rate	1-500 kHz
Pulse energy range	25-800 µJ
Pulse duration	9-200 ns
M^2	2
Collimated diameter	3.1 mm
Beam expansion	x3
Focusing lens	125 mm
Focused beam diameter	36.4 µm

The laser source is controlled by 4 essential parameters when running in pulsed emission mode:

1. Waveform number (*WF*): the parameter that allows choosing from the pre-determined pulse duration and shapes as seen in Table 4. The waveform number can be varied from 0 to 63.
2. Power-amplifier active state current set point (*PI%*): the parameter that allows controlling the power level for fixed waveform and pulse repetition rate parameters. This parameter controls the average power level emitted. The PI% can be varied from 0 to 100. The *PI%* level was controlled through the power (P) parameter of the used software. The software allowed the control of power between 0 and 20 W, however, the emitted average power differed depending on the used waveform and pulse repetition rate.
3. Simmer current set point (power amplifier stand-by current – *SI%*): the parameter that determines the amount of current stored in the power amplifier that allows controlling the energy of the first pulses. This way the rise of the emission profile to a stable energy level is determined in a much faster way (see Figure 51). The *SI%* can be varied between 0.0 and 100.0.
4. Pulse repetition rate (*PRR*): the parameter that determines the pulse frequency. The *PRR* can be varied between 1 and 500 kHz.

Apart from the control parameters, the laser has to be gated through a modulation signal, which is 5V TTL.

Figure 48. SPI G3 20P-HS MOPA, pulse duration tunable, 1 µm fibre laser source.

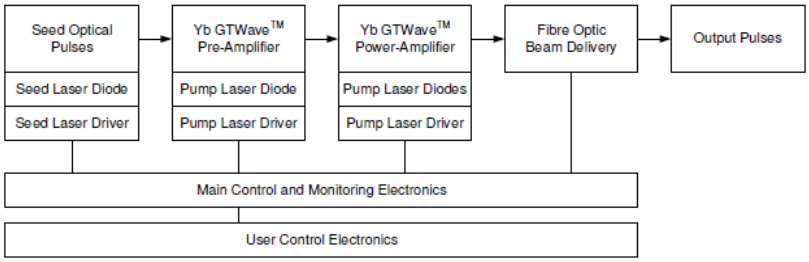

Figure 49. Functional block diagram of the SPI G3 20P-HS laser source [170].

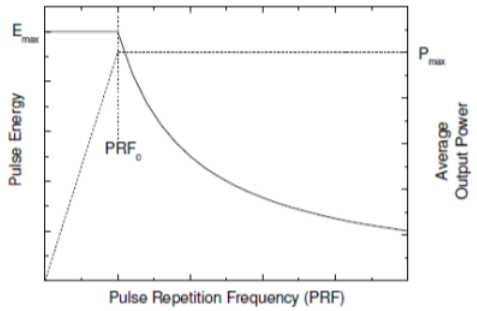

Figure 50. Pulse energy and average output power as a function of the pulse repetition rate (frequency) for a given waveform number [170].

Table 11. Pulse durations, switch pulse repetition rates and maximum energy levels of different waveforms [170].

Waveform number	Approximate pulse duration τ [ns]	PRF_0 [kHz]	E_{max} [mJ]
0	200	25	0.800
1	65	65	0.310
2	15	250	0.080
3	12	375	0.053
4	9	500	0.040
5	Duplicate of 5	Duplicate of 5	Duplicate of 5

6	Duplicate of 5	Duplicate of 5	Duplicate of 5
7	Duplicate of 5	Duplicate of 5	Duplicate of 5
9	Duplicate of 5	Duplicate of 5	Duplicate of 5
10	Duplicate of 5	Duplicate of 5	Duplicate of 5
11	200	25	0.800
12	190	26	0.77
13	180	27	0.740
14	170	28	0.710
15	160	29	0.690
16	150	30.5	0.660
17	140	32	0.630
18	130	33.5	0.600
19	120	35.5	0.560
20	110	38	0.530
21	100	41	0.490
22	90	45	0.440
23	80	50	0.400
24	70	57	0.350
25	60	66	0.300
26	50	78	0.260
27	40	97	0.210
28	30	135	0.150
29	20	250	0.080
30-63	Duplicate of 29	Duplicate of 29	Duplicate of 29

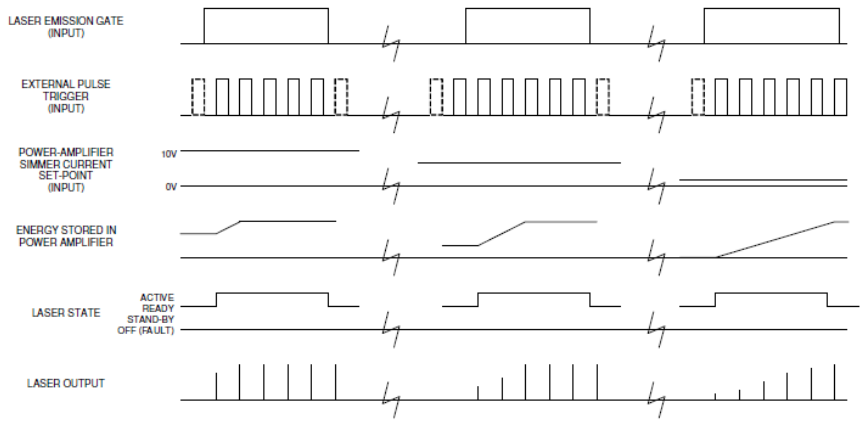

Figure 51. The effect of changing the simmer current level on the laser output profile [170].

b) Experimental setup

The laser source was coupled to a beam expander to enlarge the collimated beam to 3 times its initial value, thus 9.3 mm. Beam manipulation was achieved via a XLR8 scan head from Nutfield Technology Inc that used two high speed galvanometric mirrors for positioning the beam in X and Y axes. The scan head housed a 125 mm f-theta focal lens. In this configuration the calculated beam diameter was 36.4 μm. The

scan head and assembly was positioned in z-axis with a motorized axis with 1 µm resolution. The system components are shown in Figure 52. For laser source control and machining pattern generation WaveRunner software by Nutfield was used. The software was fully integrated to the laser source to adjust the control parameters, as well as controlling the beam manipulation parameters such as scan speed. Since the laser surface texturing studies were conducted with a point-to-point strategy, where dimples were generated with percussion drilling method, the parameters related to beam manipulation that were controlled via the WaveRunner software were:

1. Drill time (t_{drill} [ms]): the gate time that determines the number of pulses to be emitted for drilling a single dimple.
2. Jump speed (v_{jump} [mm/s]): the speed used for jumping from the position of one dimple to the other.
3. Jump delay (t_{delay} [ms]): the amount of time before jumping to the next dimple. This parameter ensures the position stability of the dimples. Low jump delays result in incorrect positioning due to drifts and overshoots in the movement of the galvanometric mirrors. Throughout the experimentation jump delay was set to 1.5 ms that allowed correct positioning each time.

c) Laser source characterization

The 4 control parameters of this laser sources are supposed be mapped for the requirements of the study. For this study, SPI G3 20P-HS system has been analysed for single and multiple pulse emission. In the beginning the pulse durations were limited to 5 choices that spun a wide range between 12-200 ns. Accordingly, pulse profiles and energy levels were characterized with varied *SI%* levels, for selected waveforms 0, 1, 2, 4, 16 and 21, which had pulse durations of 200, 65, 30, 12, 150 and 100 respectively. The characterization of this laser source required the acquisition of the waveforms, the measurement of the pulse energies as a function of the laser source parameters and generating the pulse profiles in power. Pulse profiles were acquired with a Thorlabs DET10A fast Si based photodiode from. The photodiode had an acquisition range 200-1100 nm wavelengths, and 1 ns rise time. A Tektronix MSO3014 Mixed Signal Oscilloscope with 100 MHz maximum bandwidth, 2.5 GS/s sampling rate and $5 \cdot 10^6$ record length was used for recording the signals. Energy of single pulses was measured with Thorlabs ES111C energy sensor with 11 mm aperture and capable of measuring 0.01 – 150 mJ energy range coupled to a PM100D energy meter capable of measuring pulse repetition rates up to 20 Hz.

The pulse shapes were obtained for the first emitted pulse in a pulse train *SI*=100% and *PRR*=10 kHz. The acquisitions were made off-axis and in far-field no prevent the photodiode from saturating. Figure 53 depicts the pulse shapes of the chosen waveforms.

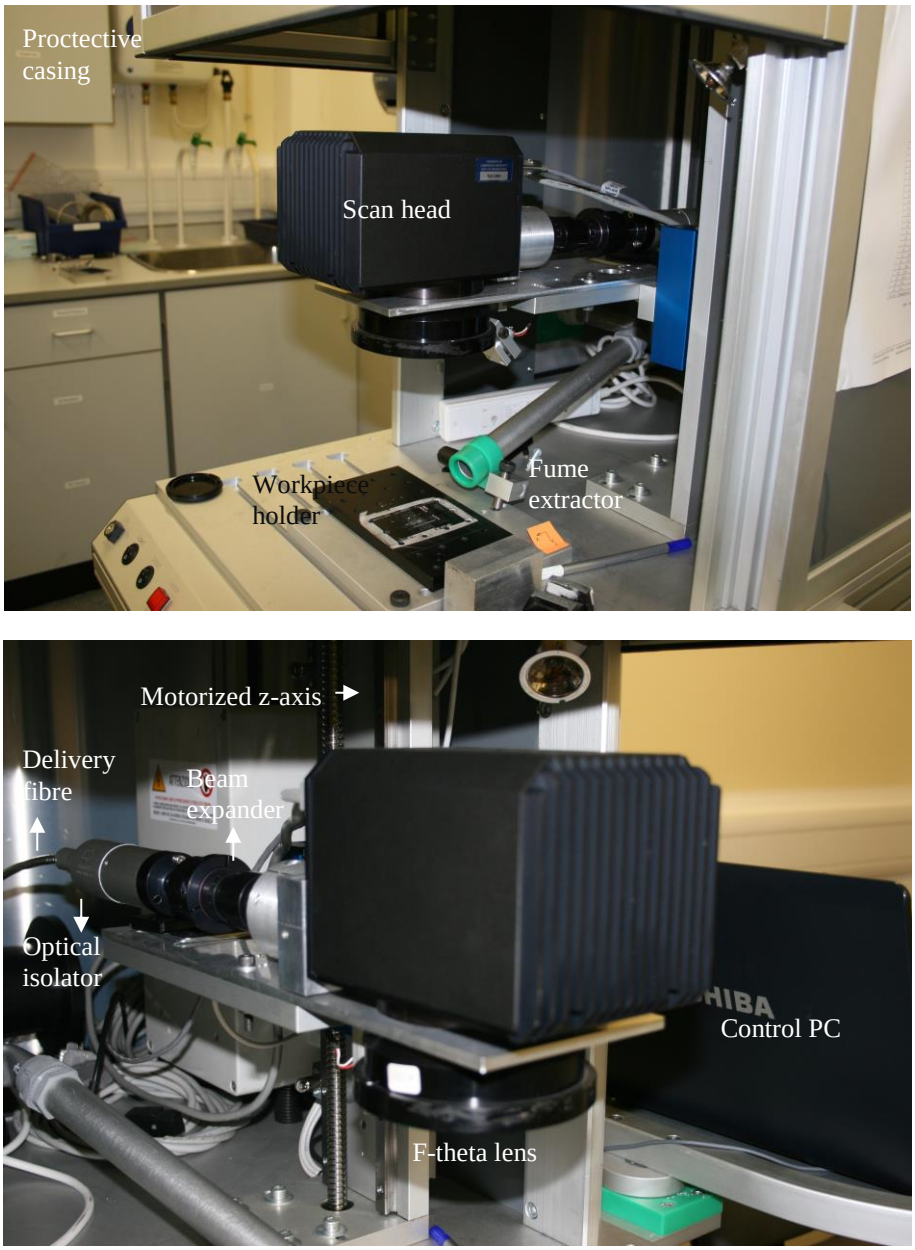

Figure 52. The SPI G3 20P-HS experimental setup.

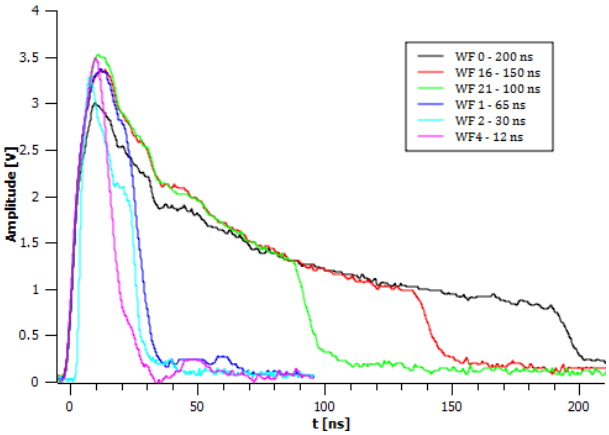

Figure 53. Oscilloscope traces of the selected waveforms at 100% simmer current level.

Next, the single pulse emission control via the simmer current was studied. Since the intended use of the simmer current level is to set the energy level of the first pulse or pulses, it was found out that the *PI%* level does not affect any change on the pulse energy for fixed *WF*, *PRR*, and *SI%* levels. Thus, pulse profiles were obtained for the chosen waveforms with *PRR*=10 kHz and drill time of 120 µs, while the *SI%* level was varied between 70% and 100% with incremental steps of 3%. The drill time allowed the emission of one single pulse being longer than the period of the corresponding *PRR* (*i.e.* 1/10 kHz = 100 µs). Pulse energy was also measured for the same combinations. Measured pulse energy was also used for discrete derivation calculating the power profile, as explained previously. In some cases, energy levels were too low to be measured with the energy meter, though an oscilloscope trace was possible to be obtained. In these cases, energy of the pulse was estimated from the proportion of the integral of the pulse with the highest pulse energy to the low energy pulse. Table 12 depicts the fixed and varied parameters with the measured variables for the characterization of single pulsed emission with SPI G3 20P-HS laser.

Table 12. Fixed and varied parameters for the average power characterization of SPI G3 20P-HS laser.

Fixed parameters	
Pulse repetition rate (PRR)	10 kHz
Drill time (t_{drill})	120 ms
No of pulses	1
Varied parameters	
Waveform	WF 0 (200 ns), WF 16 (150 ns), WF 21 (100 ns), WF 1 (65 ns), WF 2 (30 ns), WF 4 (12 ns)
Simmer current (SI%)	73, 76, 79, 82, 85, 88, 91, 94, 97, 100
Measured variables	
Pulse energy (E [µJ])	
Pulse peak power (P_{peak} [W])	

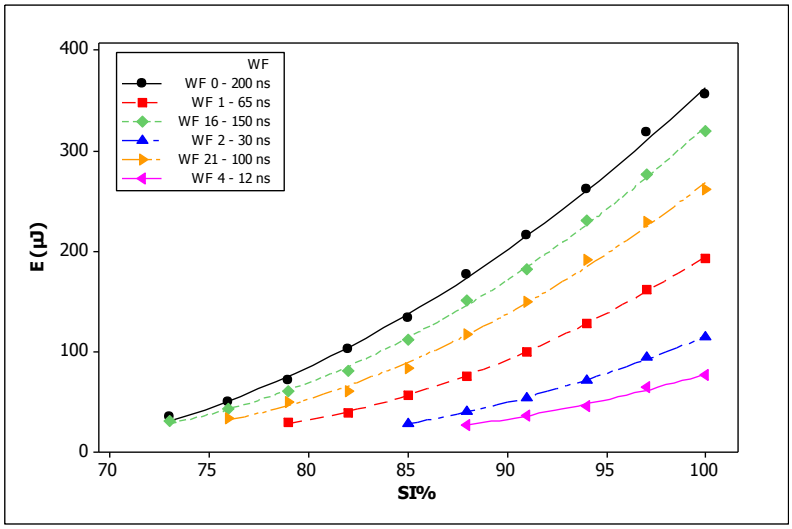

Figure 54. Measured energy values for different waveform *SI%* combinations (second order regression lines are fit to depict the trend).

The measured energy levels are plotted in Figure 54. It can be seen that for each waveform after a certain threshold of *SI%* the energy level drops below the measurable interval with the used energy meter. For all waveforms the measured minimum energy level is around 27 µJ. on the other hand a quadratic relationship is present between *SI%* and *E*. It is also observed that the *SI%* level does not necessarily match the maximum available pulse energy for the chosen waveforms. For instance *WF* 0 allows a maximum peak power of 800 µJ, whereas only 356 µJ is available with a single pulse emitted using *SI*=100%. On the other hand, *WF* 4 allows maximum 40 µJ pulse energy, however when a single pulse is concerned 74 µJ of energy is obtainable with *SI*=100%. This points out that for multiple-pulsed emission *SI%* values should be matched carefully to prevent increasing or decreasing ramps.
Figure 55 exhibits the power profiles of the chosen waveforms as a function of *SI%*. It should be noted that these pulses are characterized by fact ascending peaks and slow decaying tails. Compared to pulse shape of the IPG YLP - 1/100/50/50 laser, pulses of G3 20P-HS laser reach their peak 60 ns faster. It can be observed that although shorter pulses have smaller energy content they are able reach higher peak power levels. For instance WF 0 with 200 ns pulse duration can reach up to 3.5 kW peak power with a single pulse, whereas WF 4 with 12 ns pulse duration can reach up to 5 kW. Accordingly, Figure 56 shows the peak power of the different waveforms as a function of *SI%*. It can be seen that until about 82% all waveforms tend to have similar peak power, and after this level the trends differ.

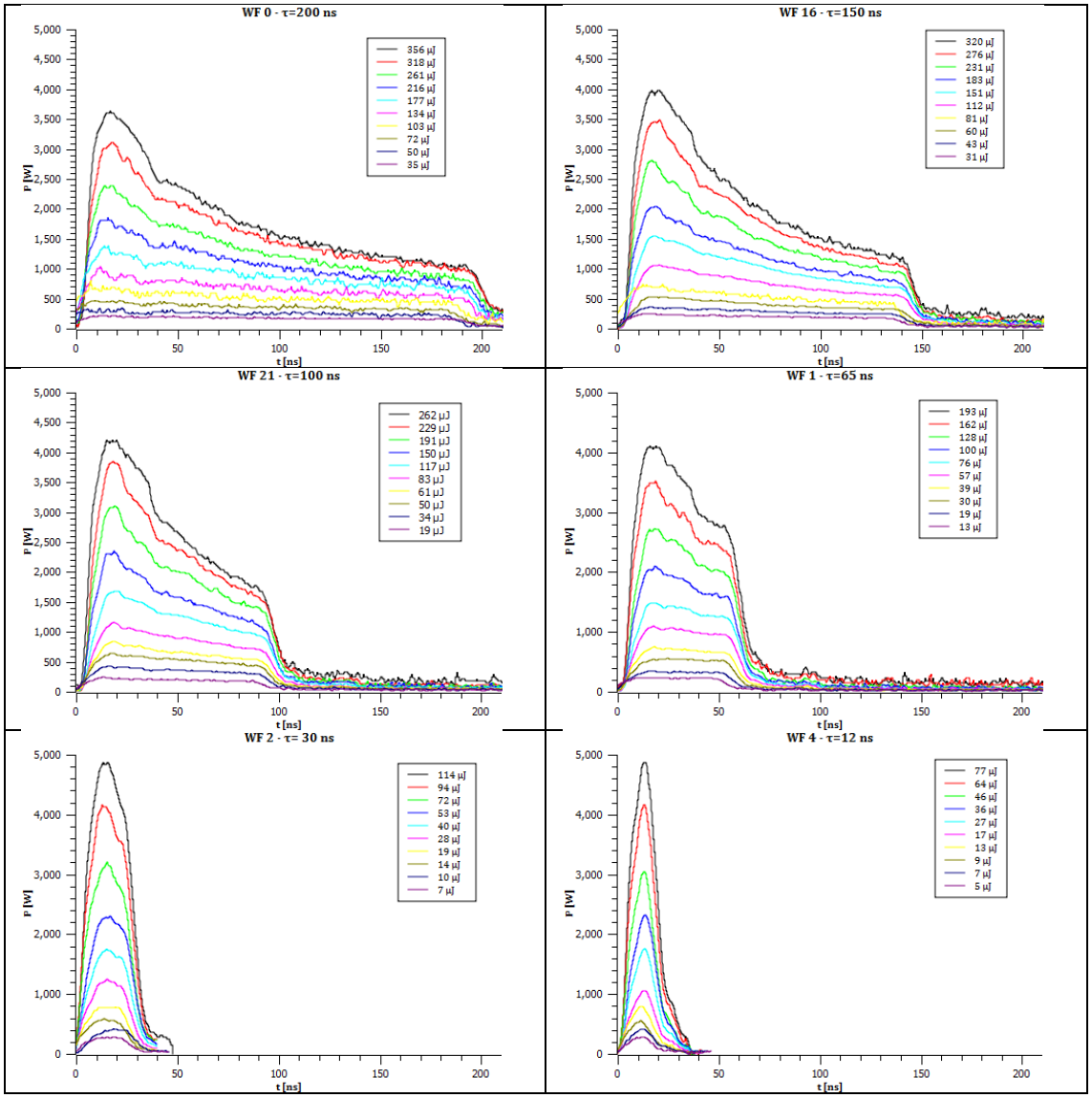

Figure 55. Power profiles and energy contents of the chosen waveforms as a function of *SI%*.

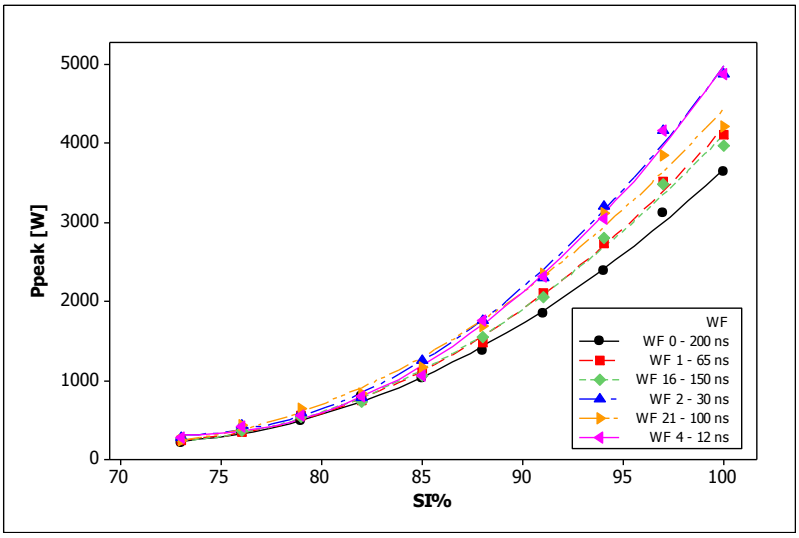

Figure 56. Measured peak power values for different waveform *SI%* combinations (second order regression lines are fit to depict the trend).

4.2.3 MOPA, short ns, 0.5 µm fibre laser – λ=532 nm; τ=1 ns

a) General specifications

The used laser source was IPG YLPG-5 pulsed active fibre laser based on master oscillator power amplifier (MOPA) architecture fitted with a harmonic generator for emission in green wavelength. The laser source can be seen in Figure 57 and the general specifications of the source are summarized in Table 13. The functional block diagram of the laser source is shown in Figure 59. Similar to the SPI G3 20HP laser, the IPG YLPG-5 uses seed pulses generated with a laser diode, which are amplified in two distinct stages inside Yb-doped fibre amplifiers. The amplification stages are pumped with multi-mode diodes, however this time the second amplification (booster) occurs in a remote amplifier. The pumping signal is carried coaxially to the pre-amplified seed pulse to the remote amplifier with the delivery fibre. The active media inside the remote amplifier (booster) is pumped with this pump signal, and the pre-amplified seed passes through. This scheme is used for generating high peak power pulses, which can cause damage to the transport media, the delivery fibre. Before reaching open space, the laser beam passes through a 2nd harmonic generator to convert from the fundamental wavelength 1064 nm to 532 nm. The optical chain is terminated with an optical isolator. The output beam is collimated also in this case. The laser source is capable of running both with pulse repetition rates between 20-300 kHz, with fixed pulse duration at 1.2 ns, 6 W maximum average power and 0.02 mJ pulse energy.

Figure 57. IPG YLPG-5 MOPA, short ns pulsed, 0.5 µm fibre laser source.

Table 13. General characteristics of the IPG YLPG-5 laser source.

Wavelength	532 nm
Max. average power	6 W
Pulse repetition rate	20-300 kHz
Pulse energy range	1-20 µJ
Pulse duration	1.2 ns
M^2	1.12
Collimated diameter	3.492 mm
Beam expansion	None
Focusing lens	100 mm
Focused beam diameter	21.7 µm

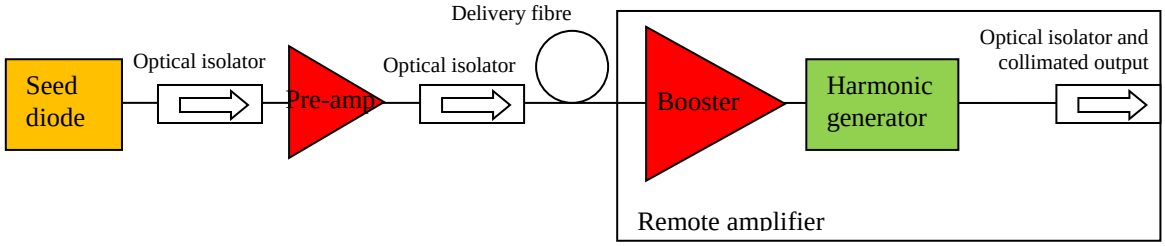

Figure 58. Functional block diagram of the IPG YLPG-5 laser source.

The laser source is controlled by 2 essential parameters, much similar to IPG YLP-1/100/50/50:

1. Pump current percentage (*PI%*): the parameter that allows controlling the power level for pulse repetition rate through the regulation of the current inserted in the diodes that pump the active fibre amplifiers. This parameter for this laser is named set setpoint. The *PI%* can be varied from 10 to 100.
2. Pulse repetition rate (*PRR*): the parameter that determines the pulse frequency. The average power emitted by the laser is also a function of *PRR*. The average power output is required to be mapped as a function of both of the parameters. The *PRR* can be varied between 20 and 300 kHz.

b) Experimental setup

The laser source provided a collimated beam with 3.492 mm diameter, which was not further expanded. For the study of TiN coatings beam manipulation was achieved manually in Y axis with a micrometric manual stage; it was also possible to integrate the system to high precision linear axes (as seen the proximity processing system in Figure 59). A custom build optical assembly housed a 90° beam bender, and a 100 mm achromatic doublet lens (see Chapter 6 for further details). In this configuration the calculated beam diameter was 21.7 μm. The focusing lens was positioned in Z-axis with a manual micrometric stage, or the workpiece could be positioned in Z axis with the same stage used for positioning in Y. The system components are shown in Figure 24. For control of laser source parameters the interface on the laser source was used as seen in Figure 25. To generate the gate signal for laser emission an AFG310 arbitrary function generator from Sony-Tektronix was used. In manual operation the only control parameter was:

> Modulation duration (t_{mod} [ms]): the gate time that determines the duration of the pumping diodes being injected with current. To generate the required modulation duration, one has to set the function generator to realize 5V TTL pulses of required length.

c) Laser source characterization

The 2 control parameters of this laser sources were required to be mapped for the requirements of the study. For this study IPG YLPG-5 system has been analyzed for average power. The same procedure for the average power characterization used for IPG YLP-1/100/50/50 was employed. Pump current was varied between 20% and 100%, while pulse repetition rate was varied between 20 and 300 kHz. Table 14 reports the complete list of parameter levels used for this characterization.

Figure 61 shows the measured average power values. The lowest and the highest average power values were 0.02 W and 6.08 respectively. A second order relationship is observed between the average power and pulse repetition rates. The laser does not exhibit a switching frequency, as the highest output power is achieved at the highest *PRR* level available. Figure 62, on the other hand, depicts the pulse energies calculated from Eq.(4.1). A stable behaviour at 20 μJ is present along the available *PRR* range with *PI*=100%. However, for lower *PI%* levels asymptotic behaviours are observed along the available PRR range.

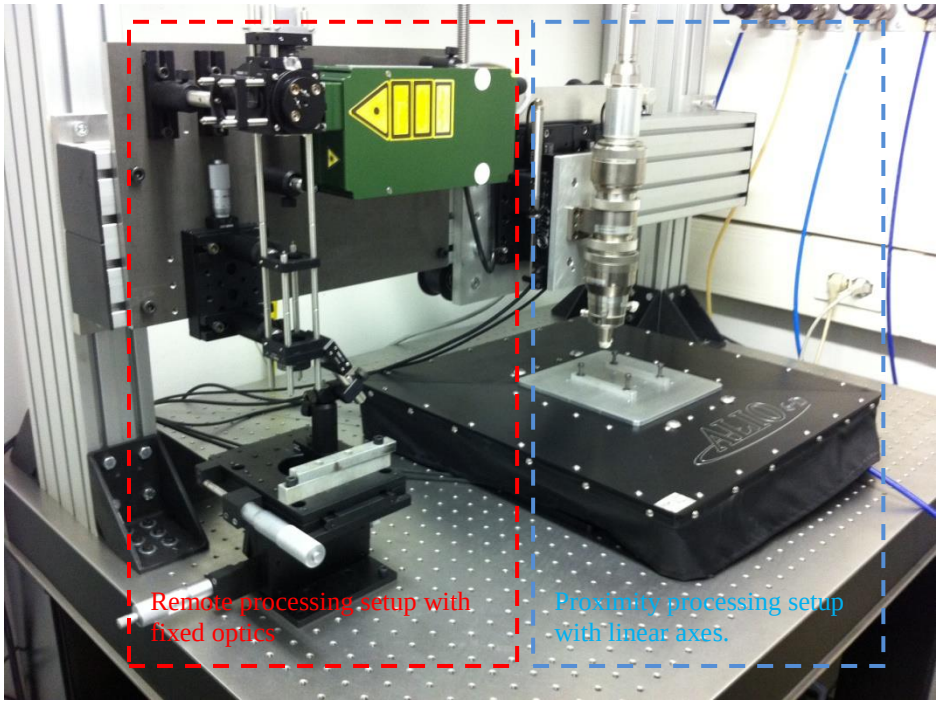

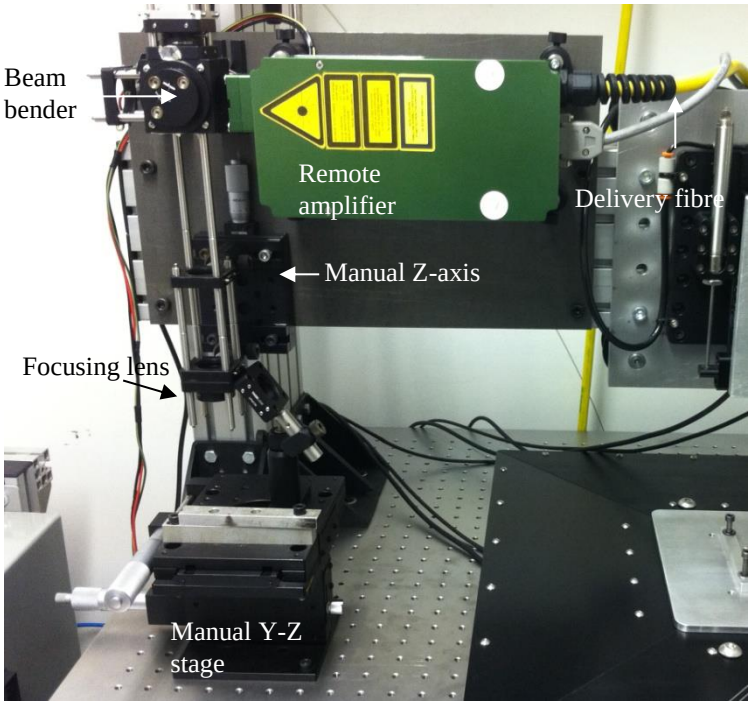

Figure 59. The IPG YLPG-5 experimental setup.

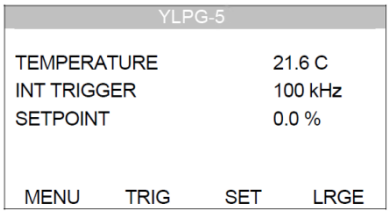

Figure 60. The IPG control interface for laser parameter setup.

Table 14. Fixed and varied parameters for the average power characterization of IPG YLPG-5 laser.

Fixed parameters	
Modulation duration (t_{mod})	10 s
Varied parameters	
Pump current (PI%)	20, 40, 60, 80, 100
Pulse repetition rate (PRR [kHz])	20, 40, 60, 80, 100, 120, 140, 160, 180, 200, 220, 240, 260, 280, 300
Measured variable	
Average power (P_{avg} [W])	

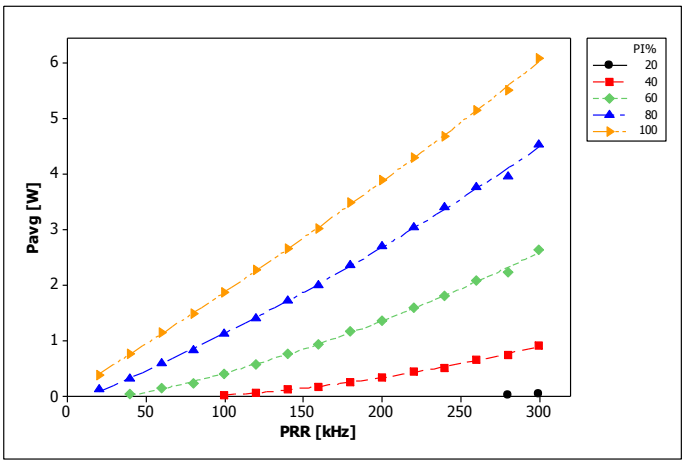

Figure 61. Measured average power values for *PI%* and *PRR* combinations (second order regression lines are to depict the trend).

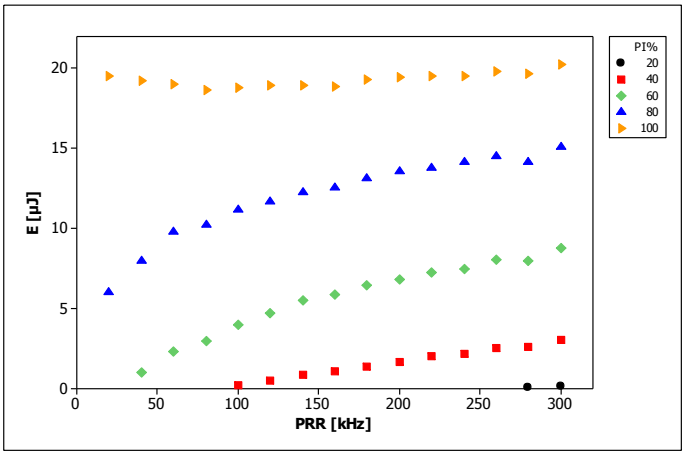

Figure 62. Calculated average power values for *PI%* and *PRR* combinations.

Due to the very short duration, the pulse shape was not measurable with the available equipment. However, the peak power of the pulses can be estimated with the assumption of having a square wave shape as,

$$E = \int_0^{\tau} P(t)dt = P_{peak} \cdot \tau \qquad \text{Eq.(4.4)}$$

thus,

$$P_{peak} = \frac{E}{\tau} \qquad \text{Eq.(4.5)}$$

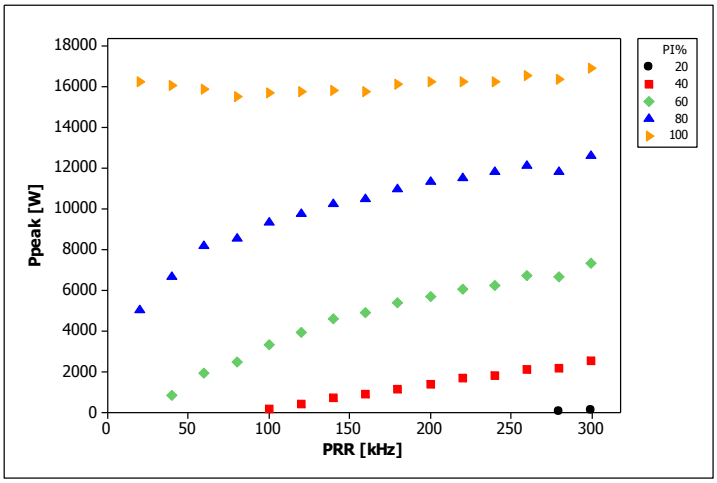

Figure 63. Estimated peak power values for *PI%* and *PRR* combinations.

The estimated peak power values are shown in Figure 63. The maximum peak power corresponds to 16 kW, which is much higher than the previous two laser sources, despite the comparably low pulse energy. It should be noted that the pulse shape is

expected to include rising and decaying ends, which would require a higher peak with the same pulse duration and energy, therefore the estimated values are expected to underestimate the exact peak power levels.

Chapter 5

Fibre laser micromachining of TiN with different laser architectures, pulse domains, and wavelengths

Laser surface texturing for tribological applications involve realization of micro cavities, the so called dimples, on a relatively large area of the mechanical component. The characteristic dimensions of a dimple are the diameter (*D*) and depth (*h*) are controlled by the laser process parameters, whereas the spatial desertion defined by the pitch (*p*) of the dimples depend on the beam manipulation strategy (see Figure 64). Since the characteristic dimension of a dimple is in the order of tens of μm, and the textured area in the order of hundreds of cm, the proportion of the area covered by a single dimple and the overall area to be covered would be in the order of $1/10^6$. This fact renders the texturing strategy crucial for productivity of the operation. The texturing operation can be realized with different strategies involving the beam manipulation, but they derive from the commonly used laser drilling strategies: single pulse, percussion, and helical drilling. While all of these are suitable candidates for the LST operation, they provide different solutions for increased productivity or increased precision.

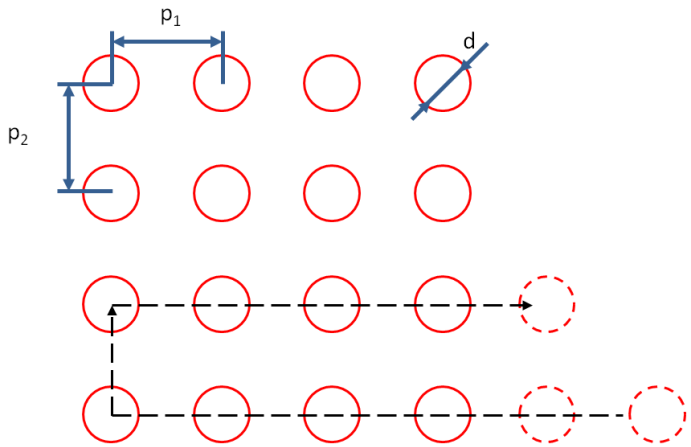

Figure 64. The scheme of LST based on point-by-point percussion drilling operation.

Single pulse drilling appears to be the fastest texturing method as it can be used on-the-fly, but would require high pulse energy to drill the material in sufficient depth and lack precision in positioning of the dimples. Helical drilling requires more time

for drilling a single dimple as the dimple is realized by the circular movement of the laser beam in multiple passes. Moreover, very small beam diameters are required to limit the dimple diameter. On the other hand, the quality of the helical drilled holes is better due to the use of multiple passes. Percussion drilling provides a compromise between productivity and quality issues. Dimples can be realized by point-by-point percussion drilling operations, while beam manipulation would be used only to determine dimple spacing (*i.e.* pitch).
Additionally, the drilling of coatings with limited thickness in the order of a few µm requires further attention to control the drilling depth to avoid damage.
Therefore, this chapter deals with the micromachining of TiN coatings with different fibre lasers to develop percussion drilling strategies, evaluate the processing conditions to control the dimple geometry, and moreover observe the physical phenomenon especially in terms of the effect of the pulse duration, over the process that determines the process quality. For each laser source a processing strategy is presented, an experimental plan using the chosen strategy is proposed, and the efficacy of the processing strategy is evaluated. After the separate studies, a comparative analysis between the processing quality and productivity of the different laser sources is provided.
A single type of substrate type of the three is associated to each laser, as listed in Table 15.

Table 15. The combination of TiN coated substrates and laser sources used in the experimental study.

Substrate type	Laser source
42CrMo4	Q-Switched, long ns, 1 µm fibre laser – λ=1064 nm; τ=250 ns
AISI M2	MOPA, pulse duration tunable, 1 µm fibre laser – λ=1064 nm; τ=12-200 ns
39NiCrMo3	MOPA, short ns, 0.5 µm fibre laser – λ=532 nm; τ=1 ns

5.1 Q-Switched, long ns, 1 µm fibre laser – λ=1064 nm; τ=250 ns

5.1.1 Development of the processing strategy

Within the modulation duration the laser emission is characterized by a transitory behaviour with an increasing ramp in the initial stage, and after the end of the modulation duration a falling ramp. The durations of the rising and falling ramps depend on the combination of the same laser operational parameters that determine the energy level. An example of such emission behaviour is reported in Figure 65, with the characteristic regions. The region where the increasing ramp occurs until a stable emission level is obtained is defined as the stabilization duration (t_{stable}). Whereas, the descending ramp after the end of the modulation duration is defined as the fall time (t_{fall}). While such conditions would not be problematic for cutting or incision operations that involve high number of pulses dispersed both in time and

space, for percussion drilling of shallow dimples that consist of single or a limited number of pulses sent on a fixed point, these conditions generate certain limitations. These limitations can be listed as:

- Single pulses with controlled energy level cannot be emitted;
- For on-the-fly operations, where a dimple is made with a single laser pulse, a certain number of initial and final dimples are going to be out of tolerance, and the number is going to increase for longer transitory conditions, this also renders the synchronization of laser pulse repetition rate with scanning velocity more problematic;
- For point to point operations, where a train of laser pulses are used to percussion drill the dimples a set number of pulses with constant energy content, cannot be achievable, thus, long transitory durations have to be avoided to have a better control of the energy content of the pulse train, and also faster operation.

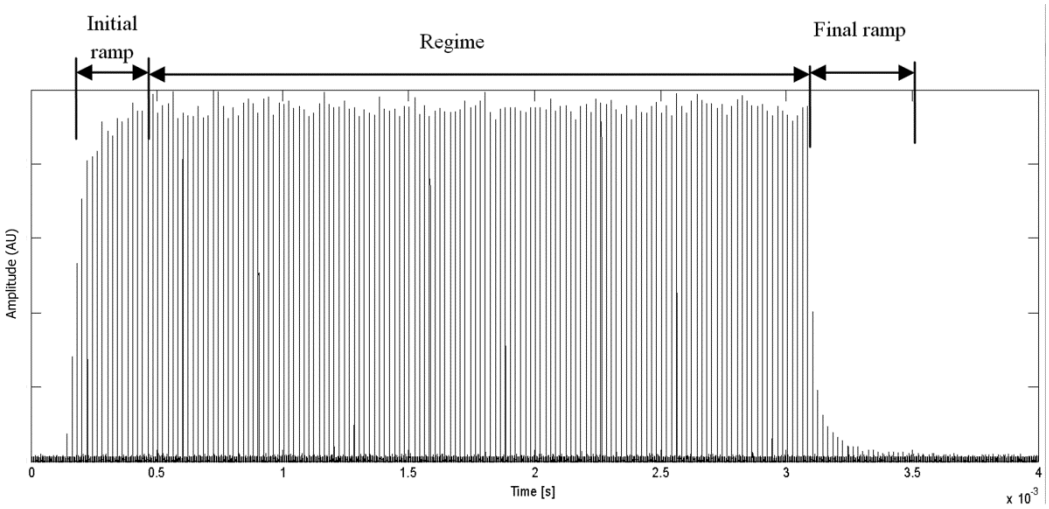

Figure 65. The characteristic emission profile of the used IPG YLP-1/100/50/50 source, showing the initial and final transitory ramps along with the regime region (*PI%*=100; *PRR*=50 kHz; t_{mod}=3 ms)

The laser surface texturing process can be flexibly employed with a point to point percussion drilling method that involves a few pulses. Therefore, high precision in spatial positioning and dimple geometry in terms of diameter and depth can be achieved, despite the fact that the productivity decreases. In order to realize similar processing conditions with the available laser source it was necessary to work within the initial transitory ramp. However, the chosen laser parameters (PI% and PRR) should be suitable to allow rapid rise in the initial ramp, without generating too many redundant pulses before and after reaching the required energetic levels to generate the dimples. Therefore, the transitory behaviour of the laser system was characterized with the use of an InGaAs fast photodiode (Thorlabs FGA10), and recorded with a

digital oscilloscope (Tektronix TDS5034B). The emission of the laser was captured in far field to avoid saturation. The modulation duration was set to 2.5 ms. The stable laser emission level was set as the mean of the peak levels of the final 20 pulses of the emission. The laser fall was accepted to be completed when the mean of the peak levels of the laser 20 pulses of the emission was 10% of the average peak level in stable emission. The experiments were carried out for 5 levels of PI% (20%-100%) and 5 levels of PRR (20-80 kHz) with 5 replications for each combination. Measured parameter combinations and measured outputs are summarized in Table 16.

Table 16. Fixed and varied parameters for the emission transitory characterization of IPG YLP-1/100/50/50 laser.

Fixed parameters	
Modulation duration (t_{mod})	2.5 ms
Varied parameters	
Pump current (PI%)	20, 40, 60, 80, 100
Pulse repetition rate (PRR [kHz])	20, 35, 50, 65, 80
Measured variable	
Emission stabilization duration (t_{stable}.[µs])	
Emission fall duration (t_{fall}.[µs])	

Figures Figure 66 and Figure 67 report the measurements of t_{stable} and t_{fall} respectively. The t_{stable} values varied between 280-2000 µs, whereas t_{fall} varied 60-330 µs. It can be observed that the laser source reaches stable emission conditions and falls down to the emission end faster with higher pumping current and pulse repetition rate levels. The change in t_{stable} can be attributed to quicker response and better efficiency of the pumping diodes with higher current levels. On the other hand, between 50-80 kHz of pulse repetition rates, the duration of stabilization remains constant for fixed pumping current levels. As a matter of fact the point where the constant stabilization duration start corresponds to the switching pulse repetition rate of the laser (50 kHz), above which the average output power remains the same but the pulse energy drops as the pulse repetition rate increases. Thus the transitory behaviour can be linked to the time required to store the energy in the active media to the set level. As the maximum level of energy stored in the active media is reached at the switching pulse repetition rate, for values higher than this the stabilization duration remains the same. Although the duration may remain the same in the 50-80 kHz range for a fixed pump current level, the number of redundant pulses increases for higher pulse repetition rates. Thus it was decided that the PI=100% and PRR=50 kHz combination was a viable option to study emission by modulation the laser with durations shorter than the initial ramp ($t_{mod} < t_{stable}$). For the chosen laser parameters t_{stable} and t_{fall} were measured to be 282.2±35.5 µs (14±2 pulses), and 70.89±8.02 µs (3±1 pulses) respectively.
Figure 68.a. reports the resulting ramped emission profile achieved by modulating the laser within the initial transitory for different values of t_{mod} (65 µs, 72.5 µs, and 80

µs). It can be observed that the pulse train rises to a peak value but never reaches the regime, and then falls down again. The increase in t_{mod} results in the increase of the energy levels of the pulses in the ramped pulse train. Figure 68.b exhibits the comparison between the peak pulses of the trains. The energy contents of the pulses were estimated by comparing their intensity integral with pulses from the emission regime, which are measured to contain 1.02 mJ in average. Temporal power curves were plotted by applying time discrete derivative to the intensity curves using the estimated energy levels. The energy and peak power values of the pulses in the generated pulse trains are as in Table 17.

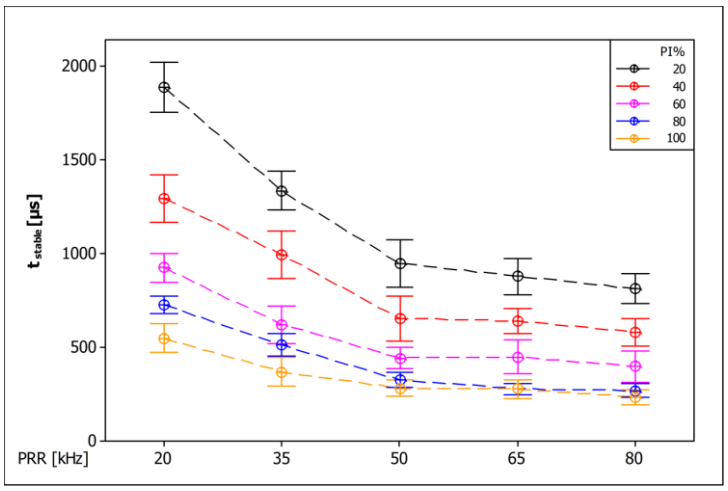

Figure 66. The emission stabilization duration (t_{stable}) as a function of laser source control parameters (error bars represent 95% confidence interval for the mean, the connection lines depict trend).

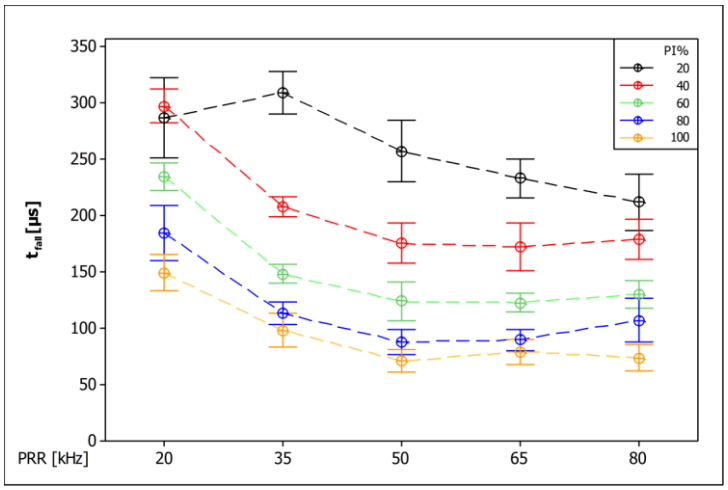

Figure 67. The emission fall time (t_{fall}) as a function of laser source control parameters (error bars represent 95% confidence interval for the mean, the connection lines depict trend).

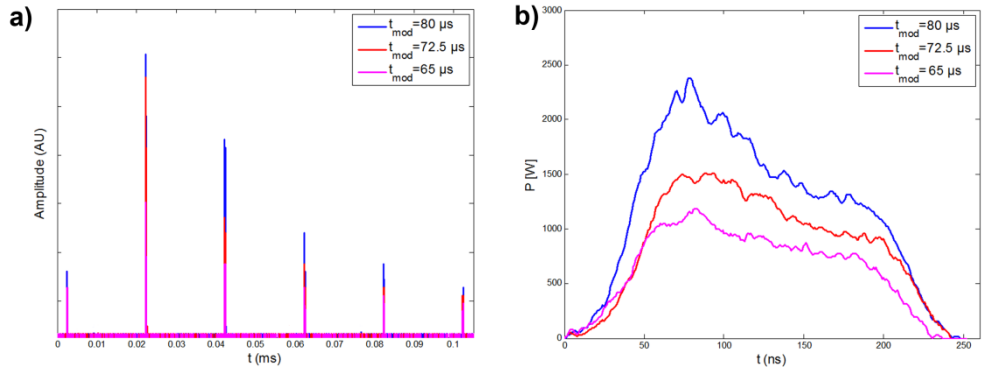

Figure 68. Characteristics of the ramped pulse trains. a) Comparison between pulse trains generated with 65 µs, 72.5 µs, and 80 µs of modulation durations, b) comparison between the most energetic pulses of the pulse trains.

Table 17. The estimated energy and peak power contents of the pulses in the ramped pulse trains.

Pulse no.	1	2	3	4	5	6
t_{mod}=65 µs	67 µJ / 0.60 kW	175 µJ / 1.46 kW	107 µJ / 0.89 kW	76 µJ / 0.67 kW	58 µJ / 0.50 kW	47 µJ / 0.44 kW
t_{mod}=72.5 µs	68 µJ / 0.62 kW	252 µJ / 1.94 kW	165 µJ / 1.29 kW	105 µJ / 0.85 kW	75 µJ / 0.61 kW	59 µJ / 0.50 kW
t_{mod}=80 µs	95 µJ / 0.79 kW	313 µJ / 2.59 kW	233 µJ / 1.85 kW	132 µJ / 1.10 kW	93 µJ / 0.83 kW	69 µJ / 0.59 kW

In addition to the energetic component of the laser beam, the spatial form of the laser beam should also be taken into account. The caustic shape of the laser beam, provided that the focal plane is controlled accurately, can be used in advantage of the laser dimpling in order to control dimple geometry. Defocusing the beam to a controlled position allows the user to obtain different beam diameters (d_s), and moreover different laser power densities (fluence, F) described as:

$$F = \frac{2E_p}{w_s^2 \pi} \qquad \text{Eq.(5.1)}$$

where E_p is the laser pulse energy, w_s is the laser spot radius ($d_s/2=w_s$). It is therefore intriguing to investigate the effect of focal position, as well as the laser energy, especially due to the contradictory effect of the focal position on the dimple diameter and depth. As the defocusing increases the laser spot on the surface increases, which should potentially increase the dimple diameter; whereas the irradiance decreases resulting in less etching depth. As the beam diameter keeps increasing, the useful portion of the projected beam area will start decreasing due to falling below the ablation threshold. The beam shape variation can be estimated by the caustic equation that defines the shape of a diverging laser beam from, by the following set of equations [15]:

$$d_0 = \frac{4M^2 \lambda f}{\pi d_c} \qquad \text{Eq.(5.2)}$$

$$d(z) = \sqrt{d_0^2 + h_f^2 \theta^2} \qquad \text{Eq.(5.3)}$$

where d_0 is the beam diameter at focal plane, M^2 is the beam quality factor, f is the focal distance of the focusing lens, d_c is the collimated beam diameter, $d(z)$ is the beam diameter at a given z distance from the focal lens, h_f is the focal height that is the relative distance to the focal plane and θ is the divergence angle of the beam, with $\theta \cong d_c/f$. Figure 69 represents the propagation of the laser beam after the focusing lens. Combining these two phenomena, conditions allowing processing by a single pulse (or a few pulses) can be sought. By suitable choice of modulation period one pulse could be made much larger than the others in the train. By controlling the focal height, the surface fluence for this pulse can be brought close to the ablation threshold of the TiN coating, so that this is the only pulse that contributes to the ablation process.

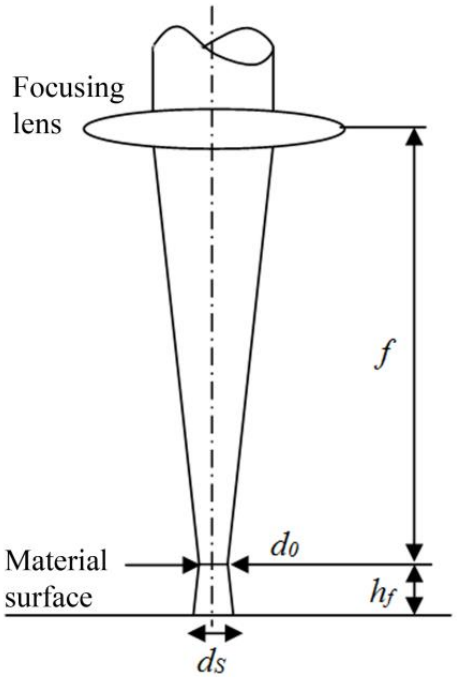

Figure 69. Propagation of a laser beam after the focusing lens.

5.1.2 Experimental design for machining TiN coated 42CrMo4 steel with Q-switched, long ns, 1 µm fibre laser with the developed processing strategy

For the study of LST by point by point percussion drilling of TiN, the effect of defocusing was studied in a wide range of focal heights to assess the effect of process

parameters on the generated dimples. In particular processing conditions allowing a superficial ablation only on the coating material without excessive drilling are required. The other geometrical attribute that is of interest was radius, which is supposed to be regulatable within the identified zone.
Preliminary experiments showed, with the employed laser emission control method, for values of t_{mod} below 35 µs no damage was visible on the material, whereas below 50 µs the ramp-to-ramp stability was found to be poor from the resulting dimples obtained. Accordingly, three different values of t_{mod} at 65 µs, 72.5 µs and 80 µs were determined to be used for ramped emission profiles. A jump delay (t_{delay}) of 8 ms was used between consecutive dimples for better positioning accuracy of the scanner, and to maintain the same energy content within the ramped pulse trains. Shorter delays have been found to cause an accumulation behaviour, which increases the energy content of ramped pulse trains, due to a faster response of the pumping diodes. Jump speed was set to be 100 mm/s. Varied and fixed parameters along with their levels are reported in Table 18.
The experimental plan was executed by making dimple grids of 4x4 dimples with 100 µm pitch on both axes. Two random replications were selected and SEM images were taken for measurements (Zeiss EVO-50). Back scattered emission SEM (BS-SEM) images were also used to reveal the contaminated area where substrate-coating mix occurs. Therefore the output variables were determined as dimple radii (r [µm]) and the area of substrate coating mix (A_{mix} [µm^2]). Figure 70 shows an example of the taken measures.
For all statistical tests α_{family}=5% was used with Bonferroni criteria.

Table 18. Experimental design for machining TiN coated 42CrMo4 steel with Q-switched, long ns, 1 µm fibre laser.

Fixed parameters		**Levels**
Pulse repetition rate	PRR	50 kHz
Pump current %	PI%	100%
Jump delay	t_{delay} [ms]	8000
Jump speed	v_{jump} [mm/s]	100
Varied parameters		**Levels**
Modulation duration	t_{mod} [µs]	65, 72.5, 80
Focal height	h_f [mm]	From -0.9 to 1.8 with steps of 0.1
Measured variables		
Dimple radius	r [µm]	
Area of substrate coating mix	A_{mix} [µm^2]	

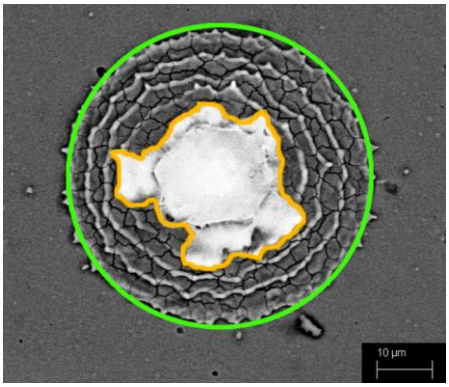

Figure 70. Measurements taken on a single dimple: radius of the fit circle (in green) and area of substrate coating mix (in orange).

5.1.3 Results and evaluation of the efficacy of the processing strategy

The SEM images reveal that the dimple geometry can be effectively varied with the used process parameters. Figure 71 depicts the SEM images of the dimples produced in intermediate conditions. As a matter of fact, the change in dimple radius and area of substrate-coating mix can be easily appreciated through the images. The measurements on the other hand, reveal the expected change in the measured variables. An almost symmetric behaviour is visible in terms of the both variables around the focal point (see Figure 72). For a fixed modulation duration, starting from a defocused position dimple radius first increases due to the increase in the irradiance and then decreases due to the increase in the beam diameter. Whereas, in the case of the substrate-coating mix area; the amount increases and saturates around the focal position on the surface and then reduces again as the beam is defocused progressively. This reveals a range, where dimple radius can be controlled with no contamination on substrate.

A regression model was sought for the dimple radii to better interpret the effect of the parameters and their interaction. The summary of the fit model is reported in Table 19. The model is in the 4^{th} order and represents fits the experimental data adequately as R^2_{adj}=94.45%. It can be observed that the influence of the focal height (h_f) goes up to the 4^{th} power, and a strong interaction between the modulation duration, which determines the energetic content of the pulse train is present. The plot of the fitted model shown in Figure 72 exhibits a symmetric trend along the h_f=0 mm that firstly increases and then decreases moving the focal position away from the surface. This phenomenon can be explained by the change in the spatial energy distribution in different focal positions. Considering the high beam quality of the used laser beam (M^2=1.7), and a spatial energy distribution very similar to TEM_{00} (measured profile indicates a single sharp lump), a quasi-Gaussian energy distribution can be used for modelling the effect of focal height on irradiance. The initial lower value when the

focal position is on surface is due to the fact that in this condition the laser beam is at its smallest diameter and the irradiance is at its highest. Therefore the energy is transferred to a smaller area, with limited spread in radial axis but with higher penetration in depth. The resulting dimples are therefore deeper with smaller radius. At h_f=0 mm increasing the energetic content by increasing t_{mod} still results in larger radii, as more energy is stored in the tails of the quasi-Gaussian energy distribution of the beam, therefore covering a larger area above the ablation threshold. The long *ns* pulse duration could also be attributed to contribute to this phenomenon, since the laser/material interaction is long enough to have heat dissipation in radial direction to increase the dimple radius. On the other hand, the increase in the radii as the focal position is moved away from the material surface is due to the increase of the laser beam diameter, which causes the energy content to be spread to a larger area. A comparison between laser intensity distribution curves for different focal heights are reported in Figure 73.

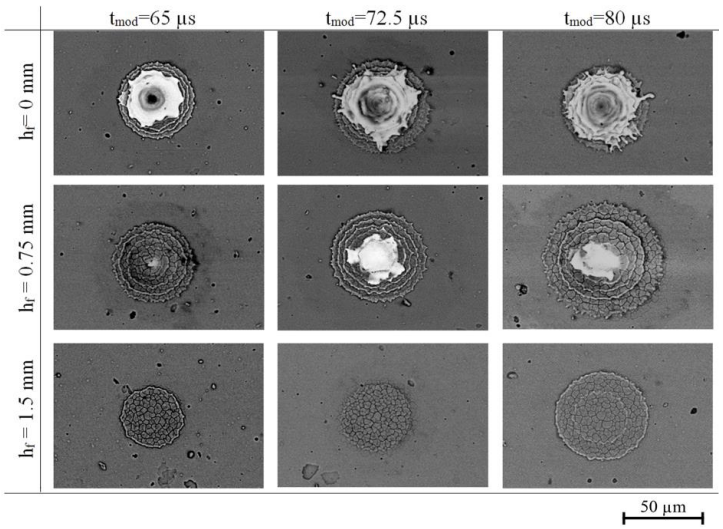

Figure 71. SEM images of the dimples obtained intermediate parameter combinations.

It can be viewed that for a given threshold intensity for ablating the material, the narrowest distribution given with the h_f =0 mm has also a narrow section above the threshold level. As the defocusing proceeds, the intensity distribution gets wider and the peak becomes shorter, thus a wider section above the threshold level can be achieved. More defocusing results in an even wider distribution, but this time only a little portion is above the threshold level due to the consequent lowering of the peak value. As a matter of fact, more defocusing after this stage will eventually cause no ablation conditions to occur. Moreover as the pulse trains used in this work are ramped, it is more likely that the pulses with lower energy content within the train would fall below the ablation threshold. The concentric layers of ablation are easily visible that for the conditions where focal position was on the material surface(h_f=0

mm) and 0.75 mm above, which points out that defocusing essentially reduces the number of pulses that are over the ablation threshold of the material. In the case of the highest defocusing condition with h_f=1.5 mm only a single ablation layer is visible. This ablated layer is expected to be created by the pulse with highest peak power, which points out that defocusing allows not only the control of irradiance, but also provides a passive selection of pulses in ramped pulse trains. On the other hand, it should be noted that this pulse arrives within a train of pulses. Therefore, thermal accumulation effects can occur, which renders this machining condition considerably different from the use of a single pulse with the same peak power. Due to smaller laser beam diameter, the drilling conditions for h_f=0 mm show up to 5 concentric ablation layers, which point out to 5 pulses reaching conditions above ablation threshold.

Table 19. Summary of the fitted regression model for the dimple radius (r [µm]).

Regression Equation

$r\,[\mu m] = -41.3983 + 1.59841\,t - 13.4425\,h_f^{\,2} - 1.78611\,h_f^{\,4} - 0.000149695\,h_f\,t^2 + 0.249307\,h_f^{\,2}t - 0.0094216\,t^2$

Summary of Model

$S = 0.787558 \quad R^2 = 94.65\% \quad R^2_{adj} = 94.45\%$
$PRESS = 109.410 \quad R^2_{pred} = 94.03\%$

Analysis of Variance

Source	DF	Seq SS	Adj SS	Adj MS	F	P
Regression	6	1735.09	1735.09	289.181	466.235	0
Lack-of-Fit	78	58.92	58.92	0.755	1.546	0.0270974

On the other hand, the A_{mix} exhibited a bell-shape spread around the zero value of the focal height (see Figure 74). The increase in the modulation duration resulted in an offset of the bell curve to higher values of A_{mix}, and also moving the focal position away from the material surface produced no contaminated zone at higher values. This is again due to the combined effect of the decreasing of irradiance moving as the focal position moves away from the surface and pulses with lower energy content fall below the ablation threshold. Parallel to the trend in the radius change, as the laser beam becomes larger with the increase in defocusing, the energy content is distributed to a larger area in surface plane, reducing the penetration in depth. When the defocusing is over a certain value, which in this case appears to be at h_f= 1 mm, the predominant factor in the loss of depth penetration becomes due to the reduced portion of the energy distribution above the ablation threshold. Thus, less energy is coupled to the material. This value also coincides with the disappearing of the contaminated area in the dimples for the lowest energy pulse train with t_{mod}=65 µs, it is shifted to 1.2 mm of defocusing for the highest energy pulse train with t_{mod}=80 µs.

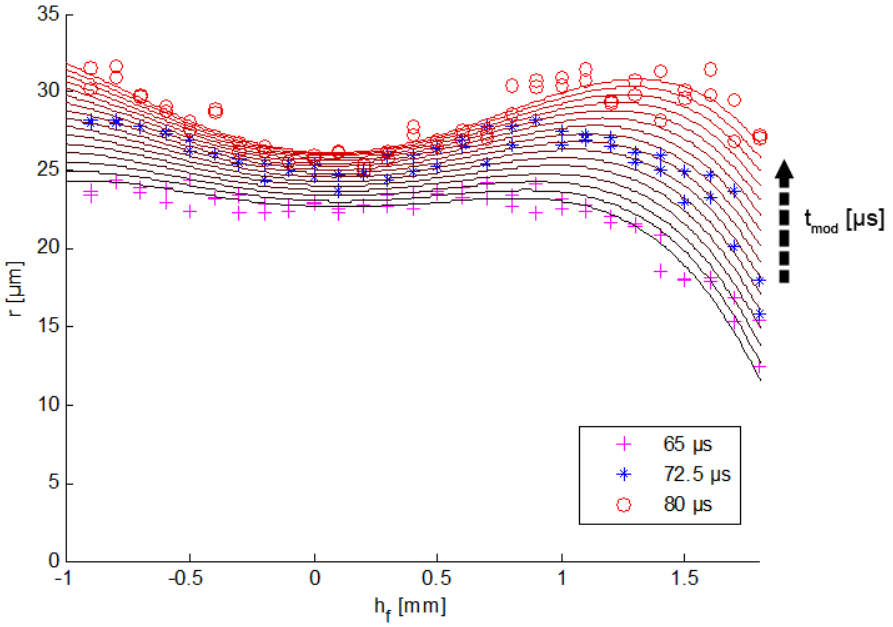

Figure 72. Dimple radius as a function of focal height (h_f) and laser modulation duration (t_{mod}). The lines represent the regression model fit with different modulation durations; the scattered symbols represent the measured values.

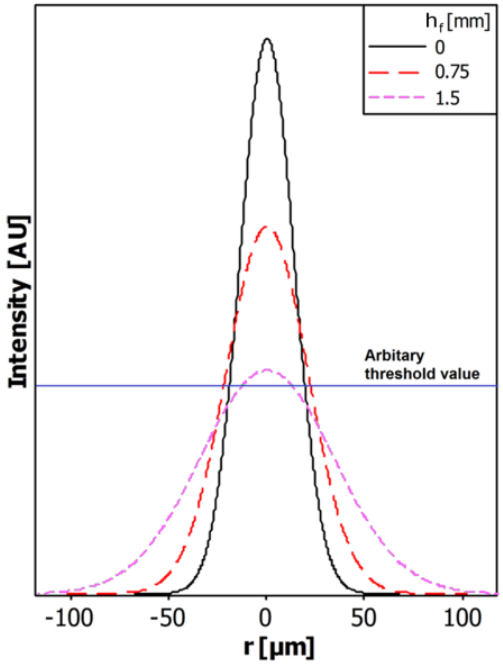

Figure 73. Comparison of laser energy distribution for different focal heights estimated from Gaussian distributions with µ=0 and $\sigma = d_0/2^{3/2}$.

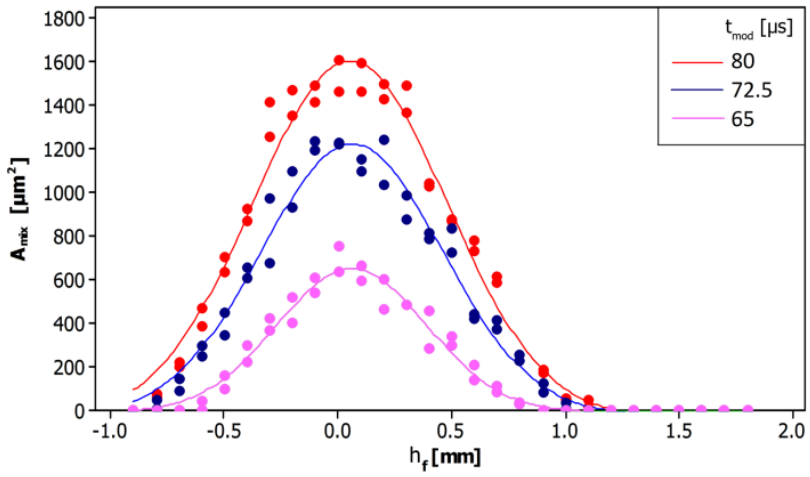

Figure 74. Area of the substrate-coating mix as a function of focal height and modulation duration (the fit lines are only for trend visualization).

5.2 MOPA, pulse duration tunable, 1 µm fibre laser – λ=1064 nm; τ=12-200 ns

5.2.1 Development of the processing strategy

The SPI G3-20HS laser provided the control over single pulsed emission, as well as the use of multiple pulses without initial and final ramps in the pulse train. However, it was necessary to study the correct set of parameters for obtaining stable pulse trains in multiple pulsed emission especially in terms of the used simmer current (*SI%*) and set power (*set P*) levels. Figure 75 depicts a case of mismatch in parameters, when multiple pulses are used. It can be observed that the first pulse is stronger than the next ones, resulting in decaying ramp. On the other hand, when the parameters are matched correctly, the emission profile becomes stable as seen in Figure 76. It should be noted that the machine parameter P=12.8, in this case does not necessarily reflect the actual output power level, since 3.56 W is emitted with this combination of parameters.

Accordingly the required *P* level to match the pulse energy levels obtained in the single pulse characterization was studied. The laser emission was observed on the oscilloscope with the photodiode and for a given *SI%* value corresponding *P* value was sought to stabilize the emission for *PRR* values of 10 kHz and 20 kHz. Figure 77 shows the final calibration curves. It can be observed that for waveform with shortest pulse duration *WF* 4 – 12 ns, it is not possible to match a *P* value for the high *SI%* values (*i.e.* 90%-100%). This is due to the fact that the laser is not able to maintain the high energy content available to the first pulse throughout the multiple pulsed emission. A cubic relationship is observed between *P* and *SI%*, though such relationship tends become linear for shorter pulse durations and pulse repetition rates.

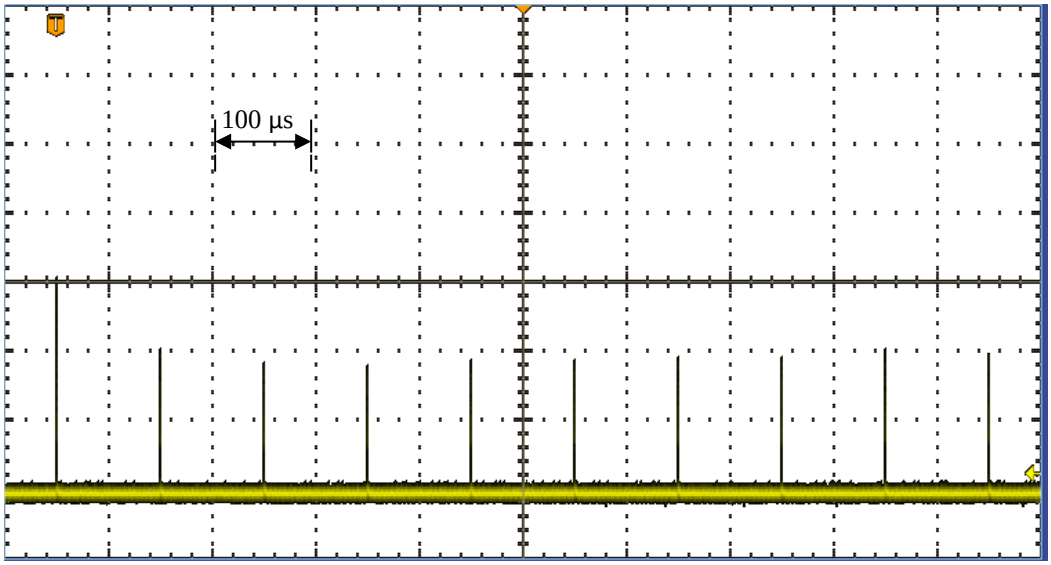

Figure 75. An example of mismatch between the laser control parameters for obtaining a stable pulse train (*Set P*=10, *SI%*=100, *PRR*=10 kHz).

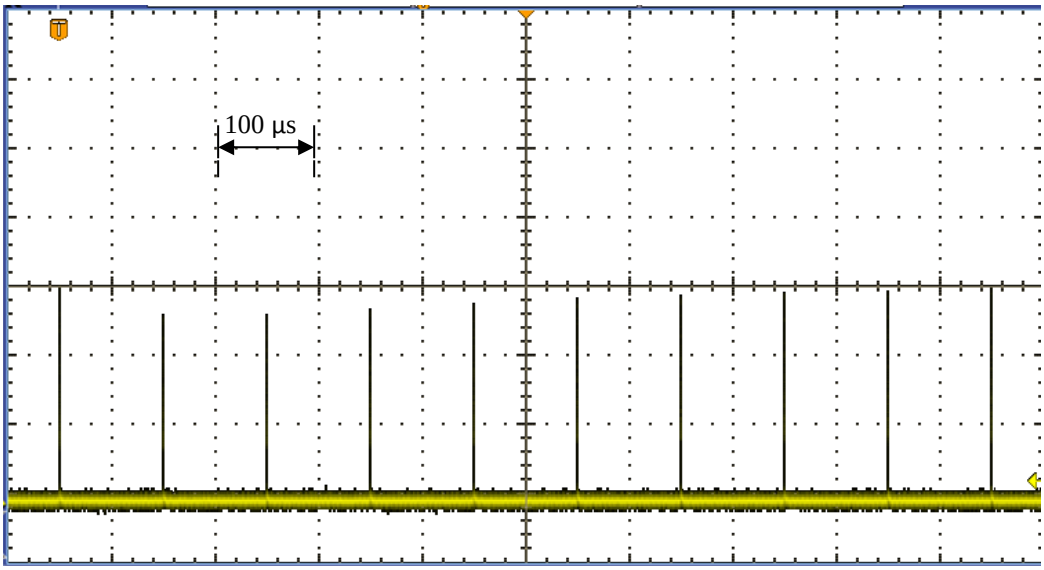

Figure 76. An example of correct matching between the laser control parameters for obtaining a stable pulse train (*Set P*=12.8, *SI%*=100, *PRR*=10 kHz).

Actual emitted average power values were calculated from the previously measured pulse energies from the following relationship:

$$P_{avg}\ [W] = \frac{E\ [J]}{PRR\ [Hz]} \qquad \text{Eq.(5.4)}$$

A clear linear trend is visible when *set P* values are plotted against actual emitted P_{avg} values (see Figure 78). This is attributed to the fact that the *set P* value linearly controls the actual *PI%* value.

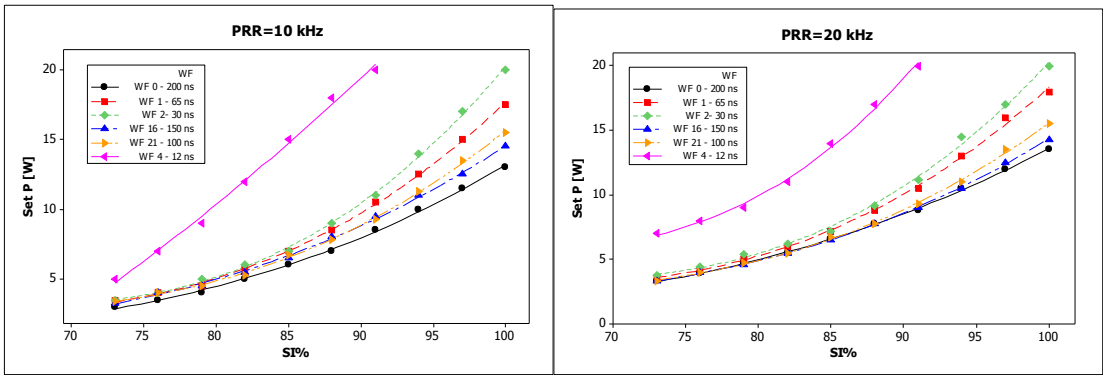

Figure 77. Calibration curves for matching machine parameters *set P* and *SI%* for stable pulsed emission (third order regression lines are fit to depict the trend).

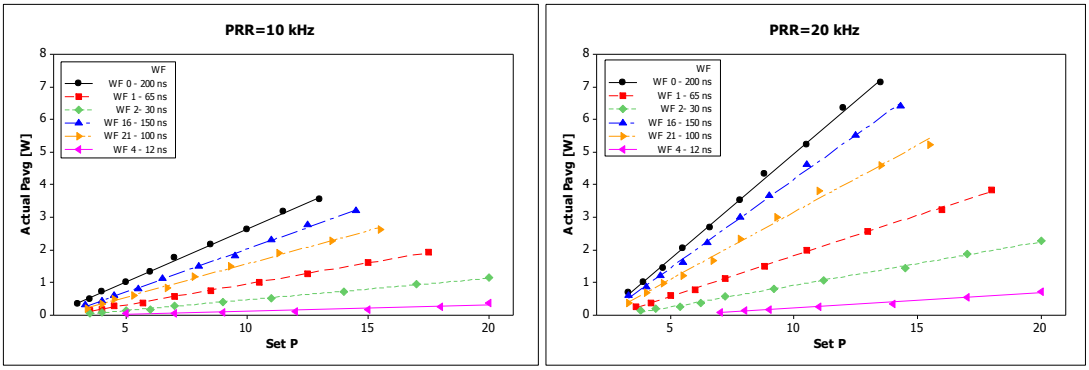

Figure 78. Calibration curves for actual power as a function of *set P* level (linear regression lines are fit to depict the trend).

With the use of stable pulse trains percussion drilling operation should become more stable. The co-centric ablated regions with different diameters observed in the case of the ramped emission with the IPG YLP-1/100/50/50 source should be no longer present. Using the tabulated parameter combinations one can study the effect of single and multiple pulses with different durations on the material in hand.

5.2.2 Experimental design for machining TiN coated AISI M2 steel with MOPA, pulse duration tunable, 1 μm fibre laser with the developed processing strategy

The experimentations consisted of two different phases: single and multiple pulsed machining of the TiN coated AISI M2 steel with different pulse durations. The control parameter was the simmer current (*SI%*) that regulated the first pulse energy

for the single pulse machining study. In the multiple pulsed machining study, the Set P parameter was matched to the *SI%* to obtain stable pulse trains, and the number of pulses to be emitted was varied with the t_{drill} parameter.
In the initial phase, single pulse ablation of TiN coatings was investigated as a function of fluence (F [J/cm^2]), irradiance (I [MW/cm^2]), and pulse duration (τ [ns]). Irradiance can be defined similar to fluence as:

$$I = \frac{2P_{peak}}{w_s^2 \pi} \qquad \text{Eq.(5.5)}$$

where P_{peak} is the pulse peak power, w_s is the laser spot radius at the material surface. All experiments were carried out with the focal plane on the surface, thus the laser spot radius w_s was equal to the radius at focal plane (w_s=w_0) recalling Eq.5.2:

$$w_0 = \frac{d_0}{2} = \frac{2M^2 \lambda f}{\pi d_c} \qquad \text{Eq.(5.6)}$$

Images were of the dimples were obtained with an optical microscope (Olympus BX51) and used to measure the ablated area diameter (D) as shown in Figure 79. Images were first compared to reveal the effect of peak power, energy, and pulse duration on the ablation mechanisms and quality.

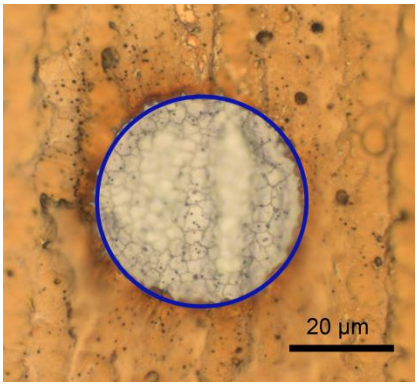

Figure 79. Measurement taken on a single dimple: diameter of the fit circle.

In order to be able to quantify the effects of the pulse energy and peak power separately, threshold fluence and irradiance values were calculated for different pulse durations. Threshold fluence and irradiance were calculated by the model proposed by Liu [1]. For threshold fluence:

$$D^2 = 2w_0^2 \ln\left(\frac{F}{F_{th}}\right) \qquad \text{Eq.(5.7)}$$

and for threshold irradiance:

$$D^2 = 2w_0^2 \ln\left(\frac{I}{I_{th}}\right) \quad \text{Eq.(5.8)}$$

where D is the ablated zone diameter, and F_{th} and I_{th} are the ablation threshold fluence and irradiance respectively. The model is so far found to be adaptable to shorter ps, and fs pulses, which provide ablation conditions free of thermal effects, thus free of melt generation. Therefore the measured area reflects the effective beam size that generates ablation on the material surface. Provided that the ablated region is free of melt and can be easily defined, the model can be applied also for longer pulse duration. The model is assumed to be used on Gaussian beams. Although the laser sources used in this work had a beam quality factor $M^2 \leq 2$, thus did not generate a perfect Gaussian beam, the beam shape was characterized by a single sharp peak at the centre suitable for being estimated as a near Gaussian beam [17]. Ablation threshold fluence and irradiation were calculated with nonlinear regression method. The know parameters of the non-linear regression would be the measured ablated area diameters D, and the pulse energy E in the case of threshold fluence (P_{peak} in the case of threshold irradiance). The unknowns that are estimated through the algorithm are beam radius at focal position w_0, and ablation threshold fluence F_{th} (or threshold irradiance I_{th}). It is preferable to set w_0 and F_{th} (or I_{th} in the case of threshold irradiance) as the unknowns of the equation together, as slight variations of the beam diameter is expected during experimentation. The advantage in this case is that the statistical confidence intervals for the mean are calculated to the equation unknowns, which provides a direct value of the error committed on the calculation of the threshold fluence (F_{th}) and (I_{th}) irradiation values. The forms of the used equations with the two unknowns are as below:

$$D^2 = 2w_0^2 \ln\left(\frac{\frac{2E}{w_0^2\pi}}{F_{th}}\right) \quad \text{Eq.(5.9)}$$

$$D^2 = 2w_0^2 \ln\left(\frac{\frac{2P_{peak}}{w_0^2\pi}}{I_{th}}\right) \quad \text{Eq.(5.10)}$$

Table 20 summarizes the details of the executed experimental plan for single pulsed machining study.

In the second phase of the experiments, a multiple pulse study was performed. Number of used pulse durations was reduced to three selected values 12 ns, 100 ns, and 200 ns. Pulse number was varied to drill on the coating and beyond to reveal the effect of change in material response while the switching from the coating material to the substrate. Optical microscopy images were made to investigate the machining behaviour and measuring the drilled hole diameter (D). Hole depths (h) were

measured with a white light interferometer system (Veeco NT3300) as shown in Figure 80 and Figure 81. Table 21 summarizes the details of the executed experimental plan for multiple pulsed machining study.

Table 20. Experimental design for single pulsed machining TiN coated AISI M2 steel with MOPA, pulse duration tunable, 1 µm fibre laser.

Fixed parameters							
Focal height	h_f	0 mm					
Jump speed	v_{jump}	5000 mm/s					
Jump delay	t_{jump}	1500 µs					
Varied parameters							
Simmer current	SI%	73, 76, 79, 82, 85, 88, 91, 94, 97, 100					
Pulse duration	τ	12 ns	30 ns	65 ns	100 ns	150 ns	200 ns
Resulting pulse energy range	E	5-77 µJ @ 12 ns	7-114 µJ @ 30 ns	13-193 µJ @ 65 ns	19-262 µJ @ 100 ns	31-320 µJ @ 150 ns	72-356 µJ @ 200 ns
Measured variables							
Dimple diameter	D [µm]						

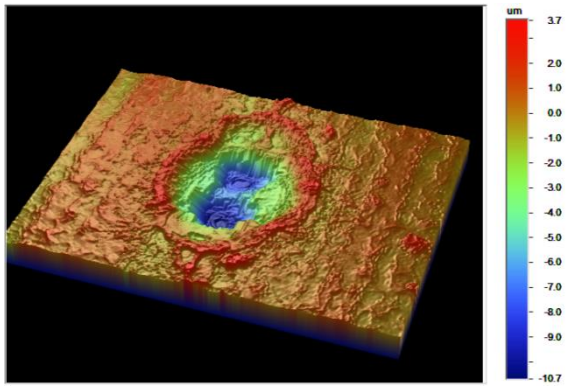

Figure 80. Example of a 3D profile of dimple obtained by Veeco NT3300 white light interferometer.

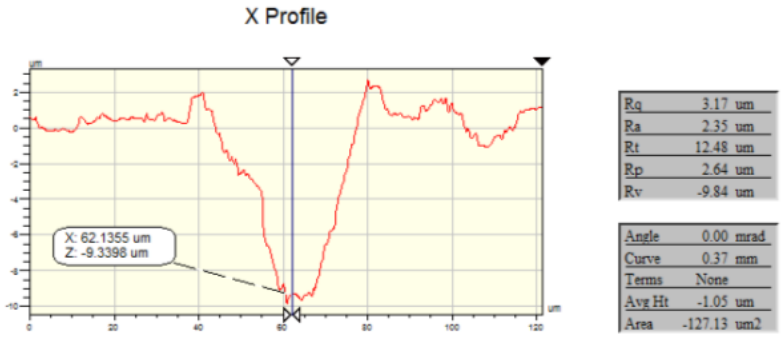

Figure 81. Example of a depth profile of dimple obtained by Veeco NT3300 white light interferometer.

Table 21. Experimental design for multiple pulsed machining TiN coated AISI M2 steel with MOPA, pulse duration tunable, 1 µm fibre laser.

Fixed parameters				
Pulse repetition rate	PRR	20 kHz		
Focal height	h_f	0 mm		
Jump speed	v_{jump}	5000 mm/s		
Jump delay	t_{jump}	1500 µs		
Varied parameters				
Simmer current	SI%	73, 76, 79, 82, 85, 88, 91, 94, 97, 100		
Pulse duration	τ	12 ns	100 ns	200 ns
Resulting pulse energy range	E_p	5-77 µJ @ 12 ns	19-262 µJ @ 100 ns	72-356 µJ @ 200 ns
No of pulses		3-81 @ 12 ns	3-14 @ 100 ns	3-9 @ 200 ns
Measured variables				
Dimple diameter	D [µm]			
Dimple depth	h [µm]			

5.2.3 Results and evaluation of the efficacy of the processing strategy

The ablated areas were first compared in terms of similar pulse energies with varying peak powers and durations. Figure 82 reports ablation conditions of different pulse durations with average pulse energy of 76.8 µJ. The main observation is that the injection of the same amount of energy in longer pulse durations causes smaller ablated zones. Although the process is vaporization dominant, slight formation of melt around the edges is visible in the case of longer 100 ns, 150 ns, and 200 ns pulses. However there is no evidence to formation of spatter or melt droplets around the holes. Cracks inside the ablated zones are visible with a tendency to become less evident with shorter pulses, pointing out that the thermal affection is decreasing along with the reduction of the pulse duration. Figure 83 reports ablation conditions different pulse durations with an average pulse peak power of 3 kW. It can be observed that the ablated area enlarges with longer pulse durations. However, the observations previously made in terms of melt generation and crack size inside the ablated zones are valid also in this case.

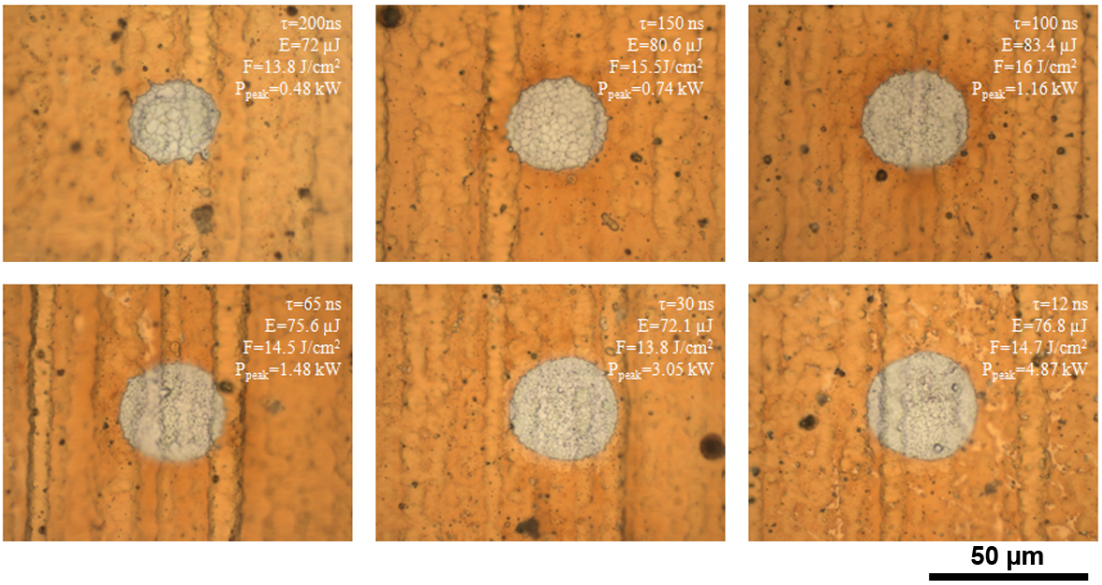

Figure 82. Evolution of ablated zones with similar energy (*E*) levels and different pulse durations.

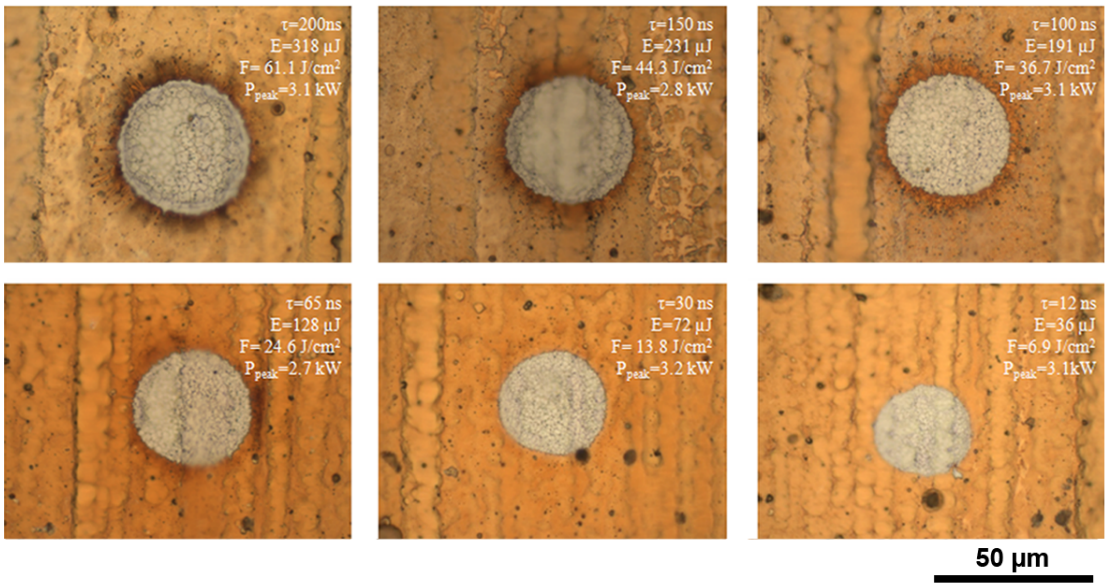

Figure 83. Evolution of ablated zones with similar peak power (P_{peak}) levels and different pulse durations.

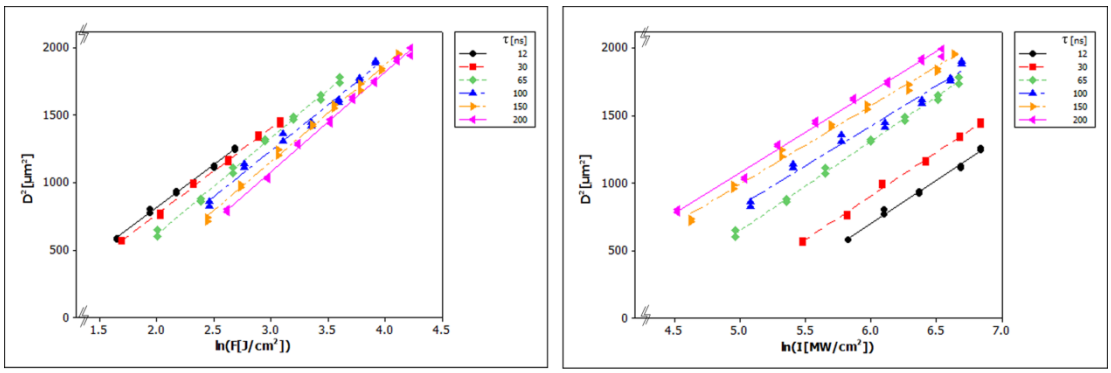

Figure 84. Squared diameters against natural logarithms of fluence and irradiance for different pulse durations.

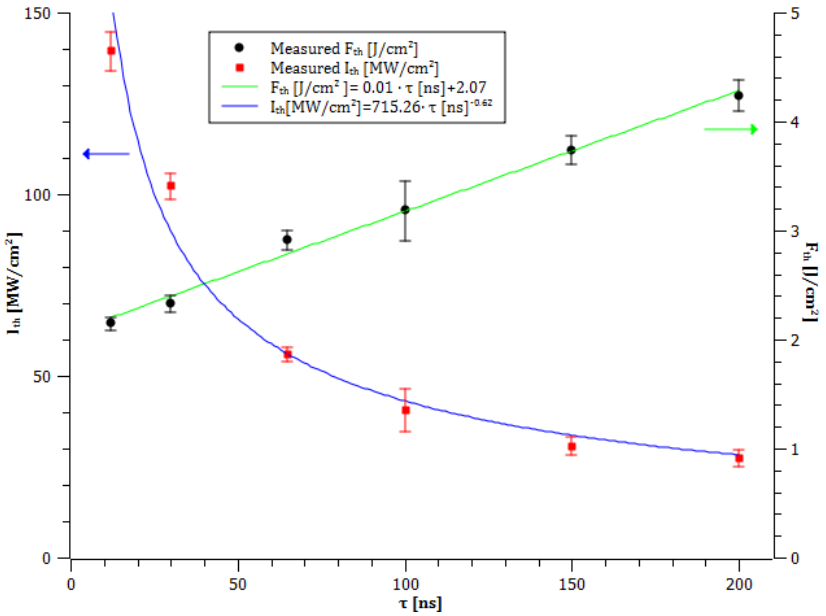

Figure 85. Change in fluence and irradiance thresholds as a function of pulse duration (error bars represent 95% confidence interval for the mean).

Since the ablation conditions were found to be free of excessive melt generation, and the ablated zone diameters were easily definable, the model by Liu was found to be applicable with the used ns pulses to estimate the threshold fluence and irradiance. Figure 84 reports the squared diameters against the natural logarithms of fluence and irradiance. The difference observed in the micrographies reflected to the calculated ablation threshold fluence and irradiance values, as plotted in Figure 85. It can be observed that a reverse behaviour is present, *i.e.* shorter pulses reduce fluence threshold, whereas increase the irradiance threshold. The ablation threshold fluence varied between 2-4 J/cm^2, whereas threshold irradiance was between 27-140 MW/cm^2 as a function of the pulse duration. A linear tendency in the increase of the ablation threshold is observed as a function of pulse duration, on the other hand a

power function suits the decrease in the irradiance threshold against the pulse duration. In other words the delivery of high peak power in the initial part of the pulse is sufficiently capable of ablation initiation, whereas added energy will not result in a significant increase after a certain amount. However, it should be noted that although the pulse durations remain the same, the pulses except for the ones with 12 ns, change shape in a non-symmetric way as their energy decreases. It is also worthwhile to note that the estimated laser spot radius (w_0) with the non-linear regression technique was also in close agreement to the theoretically calculates value. Figure 86 exhibits the values of w_0 estimated within the calculation of the ablation threshold fluence and irradiance for different pulse durations. Slight variations of ±1.5 µm compared to the calculated value are observed. Such variations are included in the calculation of the ablation threshold values with the used method rather than imposing them manually in the calculation.

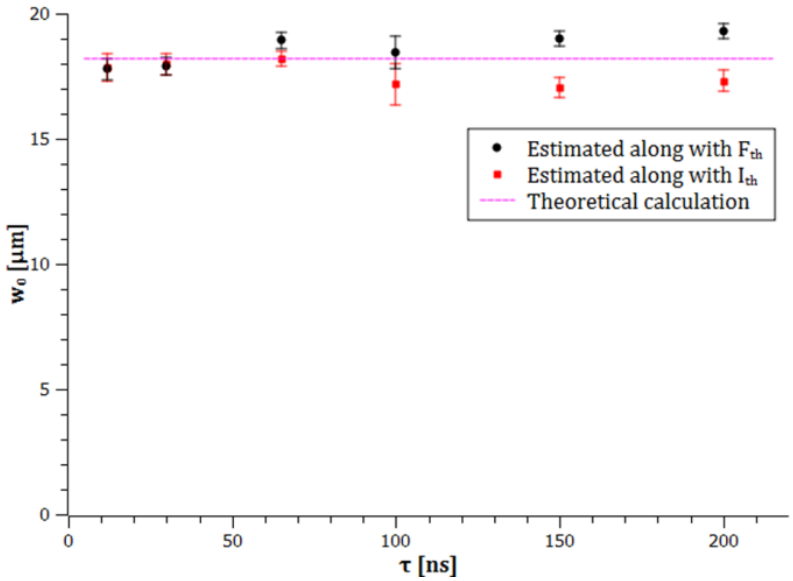

Figure 86. Comparison of the theoretical calculation of the laser radius (w_0) and estimated values with the non-linear regression method along with threshold fluence (F_{th}) and irradiance (I_{th}) for different pulse durations (error bars represent 95% confidence interval for the mean).

Although fluence and irradiation are conventionally used in laser ablation process as a single parameter, they result in the aggregation of a time dependant process into a single parameter and are not enough to differentiate the ablation behaviour. As a matter of fact the fluence is a parameter that integrates the time dependant process into a single value of energy, and irradiance is a punctual parameter that negates the effect of the power profile in time. None of the two parameters are capable of representing neither the change in the pulse shape when the pulse energy or peak power is decreased, nor the effect of pulse duration. A simple approach based on

pulse decomposition that takes the form effects into account to include the effects of peak power, energy and pulse duration can be developed. The comparisons suggest that the peak power delivered in the initial part of the pulses is initiating the ablation in larger region, whereas the energy delivered in the remainder of the pulse is capable of enlarging the ablation zone. Therefore, a decomposition of the pulse shape into different components, namely, primary peak, tail, and the added energy in the tail (ΔE). The analysis is based on comparing the conditions with the same peak power and different pulse shapes, thus the pulse energy and duration. Such conditions were identified in the previously measured conditions for peak powers at 2.3 kW, 3.1 kW and 4.1 kW. The data points were extracted in these groups and their energetic content was compared to the energy content of the shortest pulse of the group. As the shortest pulses were always of 12 ns duration, the comparison could be consistent. Moreover the pulse of 12 ns duration have a symmetric shape around the peak, which is similar to the fast ascending peak of the other pulse shapes with longer duration. Therefore, it was feasible to decompose the pulses as the primary peak and the slow descending remainder, where the primary peak was expressed by the shape of the 12 ns pulse (see Figure 87). For a fixed peak power condition *j*, the energy of the primary peak is expressed by the energy content of the 12 ns pulse with the same peak power ($E_{\tau=12\text{ns},P_{peak_j}}$). The amount of added energy in the tail for the fixed peak power condition *j* with a pulse duration higher than 12 ns *i* is defined with the following expression:

$$\Delta E_{\tau_i,P_{peak_j}} = E_{\tau_i,P_{peak_j}} - E_{\tau=12\text{ns},P_{peak_j}} \quad \text{Eq.(5.11)}$$

with

$$\tau_i = [12\ ns, 30\ ns, 65\ ns, 100\ ns, 200\ ns] \quad \text{Eq.(5.12)}$$

and

$$P_{peak_j} = [2.3\ kW, 3.1\ kW, 4.1\ kW] \quad \text{Eq.(5.13)}$$

The extracted data points showed saturation as the added energy in the tail (ΔE) increased (see Figure 88). A regression model was fitted to express the trend in the data. The details of the fitted model are summarized in Table 22. Although the results show evidence to lack of fit, the model was found to be satisfactory due to the high R^2_{adj} value and the general adequate fitting seen in the plotted graph. Addition of other predictors could lead to an improvement in the lack of fit test; however the fitted model is intended to realize the trend in the data to better express the physical phenomenon, which is well defined with the present model

Figure 88 shows the extracted data points and the fitted regression model for the chosen peak power levels. The fitted regression model was in agreement with this observation, depicting the saturation in the ablated zone diameter clearly.

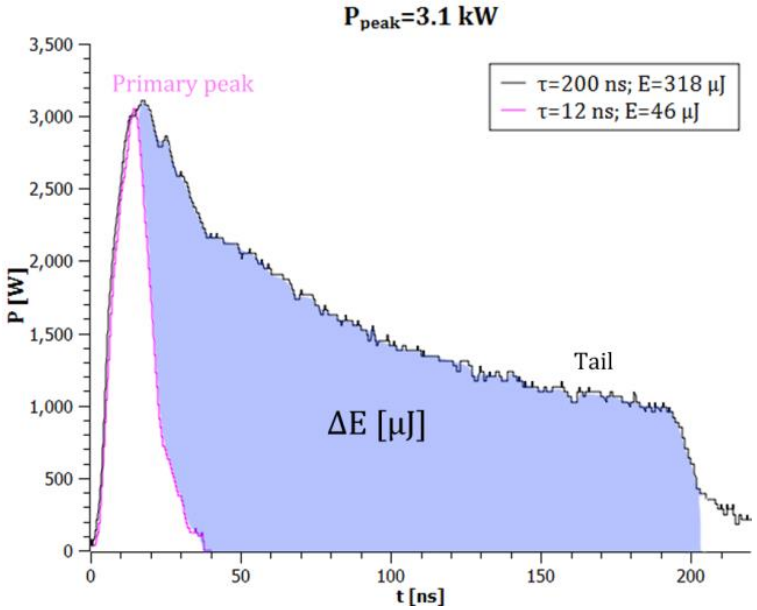

Figure 87. Decomposition of the pulse components showing the primary peak, tail and added energy in the tail (*ΔE*).

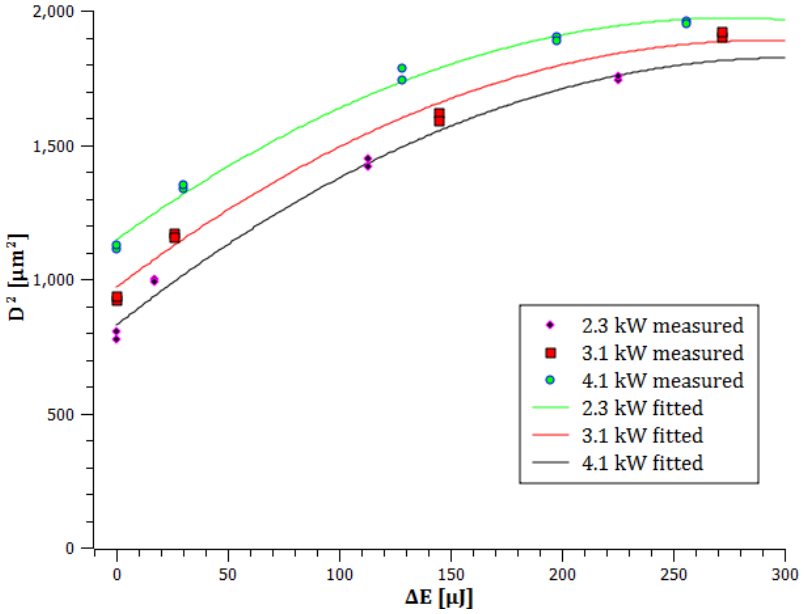

Figure 88. Effect of the decomposed pulse components on the ablated area radius.

The results show that the ablation process is dependent on the peak power as well as the pulse energy, and cannot be properly defined by a single term. As the analysis shows, the peak power is more effective in ablating a larger area, whereas the addition of more energy to after the initial peak will only contribute to a certain level. The remainder of the pulse may be useful for the increase in the crater depth, but the ablation threshold measures the area of material effectively interacting with the laser beam. The results show that for precision machining that require accurate dimensional control and sustaining material integrity pulse shape should be controlled both in terms of the initial peak power and the remainder part of the pulse. Moreover this gives insights about how the pulses should be shaped to favour or facilitate ablation, which would is crucial for materials with thermal and optical properties that render ablation more difficult.

Table 22. Summary of the fitted regression model for the dimple radius (*D* [µm]).

Regression Equation

D^2[µm]=419.651 + 7.32855 ΔE [µJ] + 177.115 P_{peak} [kW] - 0.0108269 $(\Delta E)^2$ - 0.328619 ΔE [µJ]*P_{peak} [kW]

Summary of Model

S = 38.8615 R^2 = 99.21% R^2_{adj} = 99.05%
PRESS = 45966.3 R^2_{pred} = 98.85%

Analysis of Variance

Source	DF	Seq SS	Adj SS	Adj MS	F	P
Regression	4	3958538	3958538	989634	655.293	0
Lack-of-Fit	8	28339	28339	3542	13.644	0.0000358

A similar comparison in terms of similar peak powers and energy levels with fixed pulse numbers is presented in Figure 89. The observations previously made on the ablated region extension as a function of the pulse energy and peak power reflect to the hole depth as well in multiple pulse study. For fixed energy conditions, shorter pulses that yield consequently higher peak powers result in larger holes in diameter, which is parallel to the observations made in the single pulse study. On the other hand, the same amount of energy delivered in longer pulse duration leads to deeper holes. This can be attributed to the fact that longer pulses have a larger heat penetration depth (*d*), as expressed in the well-known equation:

$$d=(4\kappa\tau)^{1/2} \qquad \text{Eq.(5.14)}$$

where κ is the thermal diffusivity [15]. The heat penetration depth on TiN is 0.5 µm, 1.5 µm, and 2 µm for 12 ns, 100 ns, and 200 ns of pulse durations respectively. As the heat penetrates deeper in the material, it is possible to remove a larger amount of material by increasing the amount of material to temperatures over the vaporization

temperature. Consequently, the molten fraction increases, and the direct vaporization from solid is accompanied by a removal mechanism occurring in the form of vaporization from the molten state. In the case of equal peak powers, longer peak pulses result in deeper and larger holes, as more energy is delivered in the decaying tail of the pulse which helps increasing the ablated area size, thus the diameter and consequently increases the machined depth. With the shortest duration of 12 ns no significant machining depth was achievable before 3 pulses. Since these pulses do not have the decaying tail after the initial peak, there is not the coupling of more energy in the material, which enlarges the hole both laterally and in depth. This phenomenon is more visible, when conditions yielding similar removed volumes are compared (see Figure 90). It can be seen that in order to remove the same amount of material, pulses of 200 ns duration are more efficient, as the total amount of energy used is about half of the one compared to the conditions with 12 ns pulse duration. This suggests that there is not a fixed threshold for neither energy nor peak power within the pulse itself, but once energy coupling is achieved and ablation is initiated in the initial part of the pulse, the energy within the remainder of the decaying pulse is also useful to remove material. Whereas, when such decaying tail is not present, the advantage of the energy coupling is not exploited. However, when the decaying tail is not present the material removal mechanism remains dominantly from solid to vapour, which sustains better machining quality.

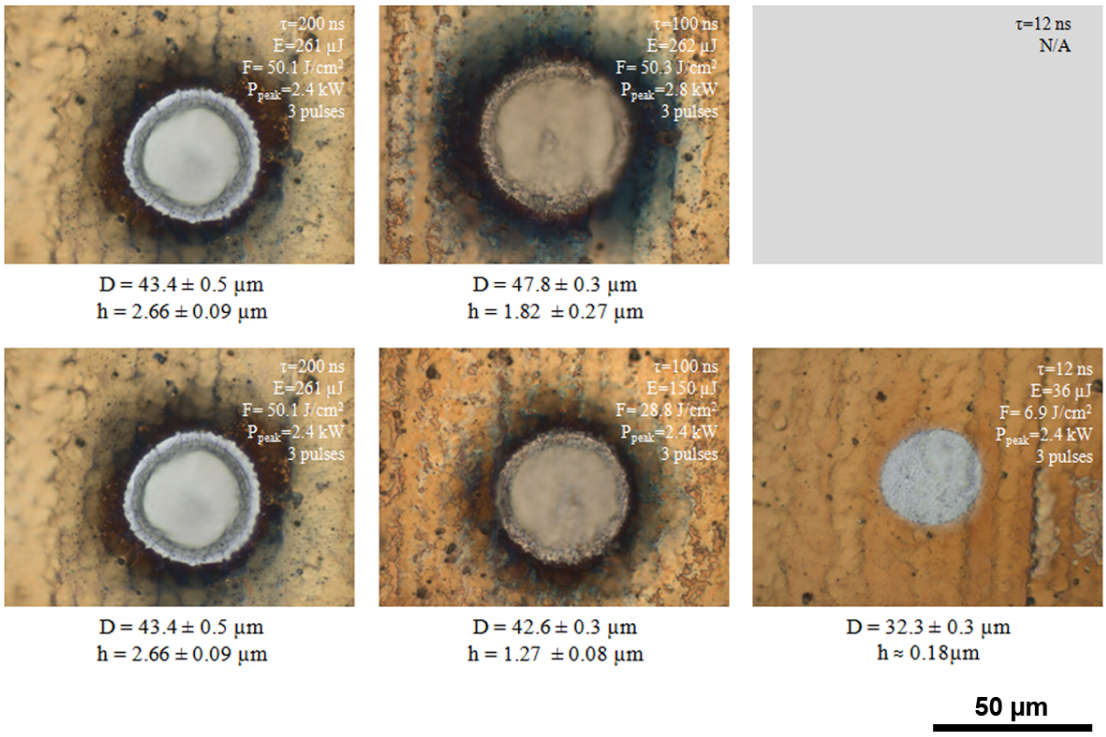

Figure 89. Evolution of hole diameter and depths in similar energy levels (top row); and similar power levels (bottom row) with different pulse durations.

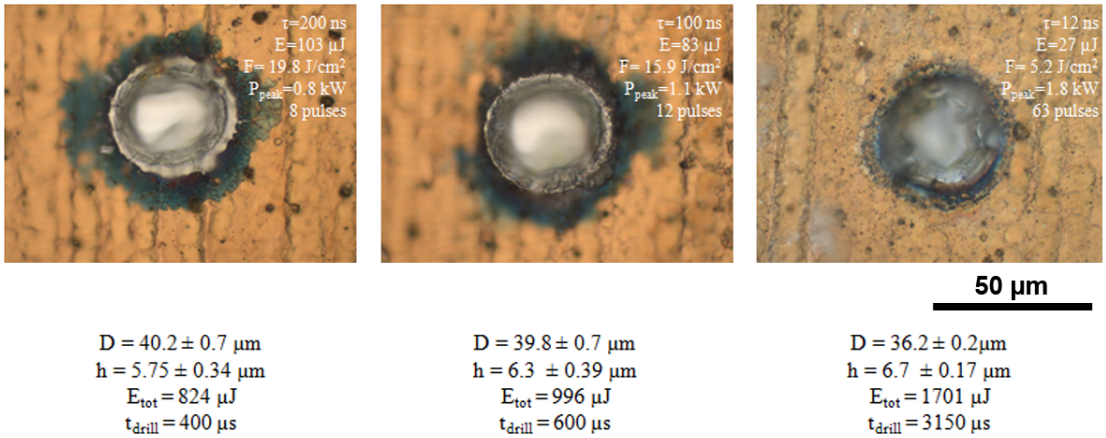

Figure 90. Comparison of holes with similar geometric properties obtained with different pulse durations, energy levels and number of pulses.

Figure 91 depicts the measured diameter and depth values of the drilled holes, as a function of pulse duration, fluence, and number of pulses. It can be observed that for 100 ns and 200 ns pulse durations, the number of pulses has little influence on the hole diameter, but highly effective on the increase of the depth, as a consequence of larger thermal penetration in the material. A drop in the measured diameters is visible for the two pulse durations with higher number of pulses (after the 10^{th} pulse for τ=100 ns, and the 7^{th} pulse for τ=200 ns), as a consequence of the deposited spatter of the substrate material around the hole entrance. This phenomenon reflects as the drop in the drilling depth increase rate, in both cases. The substrate material AISI M2, compared to TiN coating, possesses similar thermal diffusivity (κ), but half the reflectivity at the laser wavelength (R), and half the melting temperature (T_m) (see Table 6). Therefore, more of the laser energy can be absorbed and the penetrated heat can generate more molten phase within the substrate. When the molten phase reaches explosive boiling conditions the material at the bottom of the hole is ejected from the whole opening and deposited around as spatter.

In the case of 12 ns pulse duration, such drop in the diameter or the hole depth increase rate is not visible with the increase of the number of pulses emitted. The pulse duration is short enough to prevent excessive molten phase from generating on the substrate material. Even when the hole depth is beyond the coating thickness, the ablation is still vaporization dominant and melt ejection is avoided. In fact, an increase in the hole diameter is visible when the number of pulses increase, suggesting the presence of the damage accumulation phenomenon. The phenomenon was first reported by Jee et al [2], then extensively applied to ablation of various materials with ultrashort ps – fs pulses, which also include TiN [171-173]. The incubation effect is expressed as a reduction in the threshold fluence as:

$$F_{th}(N) = F_{th}(1)N^{S-1} \qquad \text{Eq. (5.15)}$$

where $F_{th}(N)$ and $F_{th}(1)$ are the ablation threshold fluence of N pulses and a single pulse respective, and S is the incubation coefficient. Lower numbers of S correspond to higher damage incubation, thus the lowering of the ablation threshold. To calculate the ablation thresholds for different number of pulses with 12 ns pulse duration, conditions between 3 and 36 pulses were extracted, since these conditions do not correspond to holes deeper than the coating material thickness.

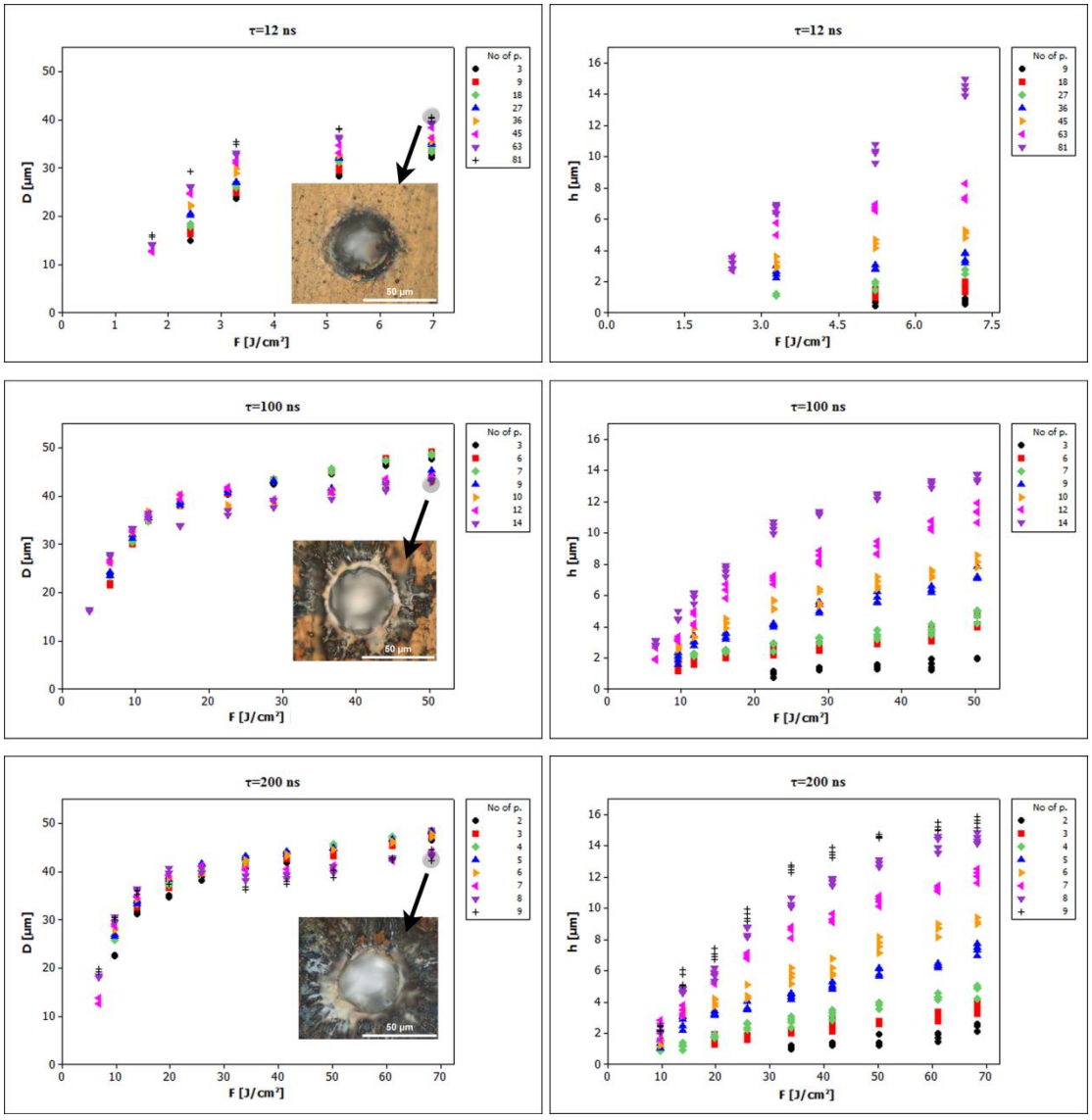

Figure 91. Hole diameters (*D*) and depths (*h*) as a function of fluence and number of pulses for different pulse durations.

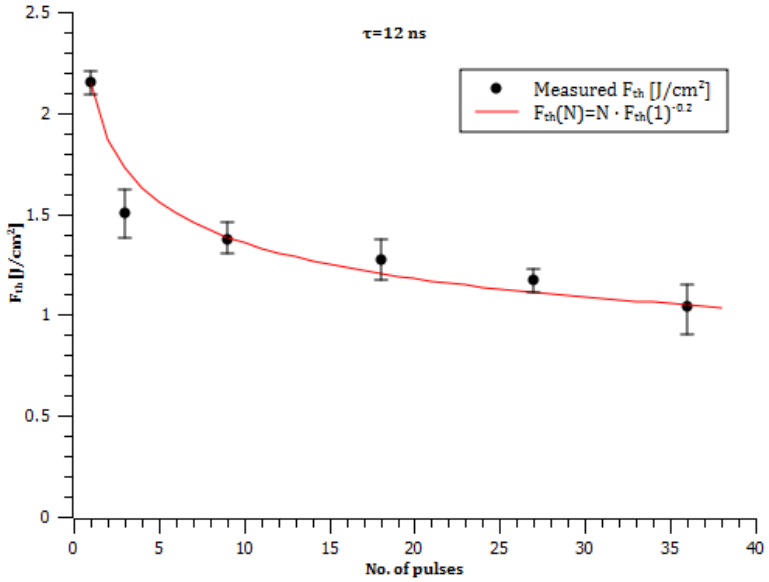

Figure 92. Fluence threshold as a function of number of pulses for 12 ns pulse duration (error bars represent 95% confidence interval for the mean).

Figure 92 shows the calculated threshold fluences with the fitted model as expressed in Eq.(5.15). The calculated incubation coefficient was S=0.80 ± 0.02. Compared to the reported value of S=0.87 for a pulse duration of 130 fs, at 2 Hz repetition rate and 800 nm laser wavelength [171], this value depicts much higher incubation. This can be attributed to the longer pulse duration and higher repetition rate (20 kHz). On metals, the incubation effect was attributed to stress-strain energy storage induced on the material during laser ablation and change in surface topography that leads to change in absorption characteristics by Jee et al (τ=10 ns, λ=1064 nm, *PRR*=10 Hz). The incubation observed on the processing of polymeric materials (PMMA) with UV wavelength was attributed to photoinduced formation of defect centres, which enhanced the absorption of UV light (τ=20 ns, λ=248 nm *PRR*=2 Hz) [172]. More recently the damage incubation on the laser micromachining of ITO semiconductor was found to be due to the accumulation of plastic deformation (τ=10 ps, λ=1064 nm, *PRR*=200-1000 kHz) [173]. The incubation observed on TiN in this study fits better with the increase in absorption due to change in surface topography, as can be observed from the optical microscopy images. The experimentally observed decrease in the threshold was from $F_{th}(1)$=2.15 J/cm^2 for a single pulse to $F_{th}(36)$=1.04 J/cm^2 for 36 pulses.

5.3 MOPA, short ns, 0.5 µm fibre laser – λ=532 nm; τ=1 ns

5.3.1 Development of the processing strategy

Similar to the IPG YLP-1/100/50/50 laser, the IPG YLPG-5 laser showed transitory behaviour within the initial part of the emission. In particular this source exhibits a delay at the beginning of the emission where no pulses are emitted, then an initial ramp is present. However, the laser source falls to no emission stage right after the end of the modulation signal. The durations of the rising and falling ramps depend on the combination of the same laser operational parameters that determine the energy level. An example of such emission behaviour is reported in Figure 93, with the characteristic regions. The region where the emission delay occurs is defined as emission delay duration, whereas the duration that is required to reach the stable emission level starting from the beginning of the modulation signal is defined as the stabilization duration (t_{stable}). This emission profile generates the same limitations regarding the percussion drilling, as reported in the case of IPG YLP-1/100/50/50 laser. However, due to the low pulse energy level, the use of single pulses would not be sufficient to drill deep enough on the material; therefore the system would require a different approach for the employed strategy. The use of multiple pulses is required, and as seen in the case of SPI G3 HS20 laser, the number of pulses needed to reach sufficient depth on the coating increase up to 30 as the pulse duration decreases to 12 ns.
For point to point operations, where a train of laser pulses are used to percussion drill the dimples a set number of pulses with constant energy content, cannot be achievable, thus, long transitory durations have to be avoided to have a better control of the energy content of the pulse train, and also faster operation.
In order to carry out the laser surface texturing with point to point percussion drilling method with multiple pulses, it is required to characterize the transitory profile of the laser, especially in terms of the emission delay. The transitory behaviour of the laser system was characterized with the use of an InGaAs fast photodiode (Thorlabs FGA10) in far field, and recorded with a digital oscilloscope (Tektronix TDS5034B). The modulation duration was set to 3 ms. The used photodiode showed a rise time of 1 ns. Since the pulse duration is almost identical to the rise time of the photodiode, the acquired pulses could only indicate the position and the relative amplitude in the pulse train, but they could not be used to regenerate the pulse shape. The stable laser emission level was set as the mean of the peak levels of the final 20 pulses of the emission. The emission delay was accepted to be completed at the arrival of the first significant pulse that is defined to possess 10% of stable emission level. The experiments were carried out for *PI*=100%, which provided constant pulse energy over the whole *PRR* range. Meanwhile, *PRR* was set between 20-300 kHz. Five replications for each combination were taken. Measured parameter combinations and measured outputs are summarized in Table 23.

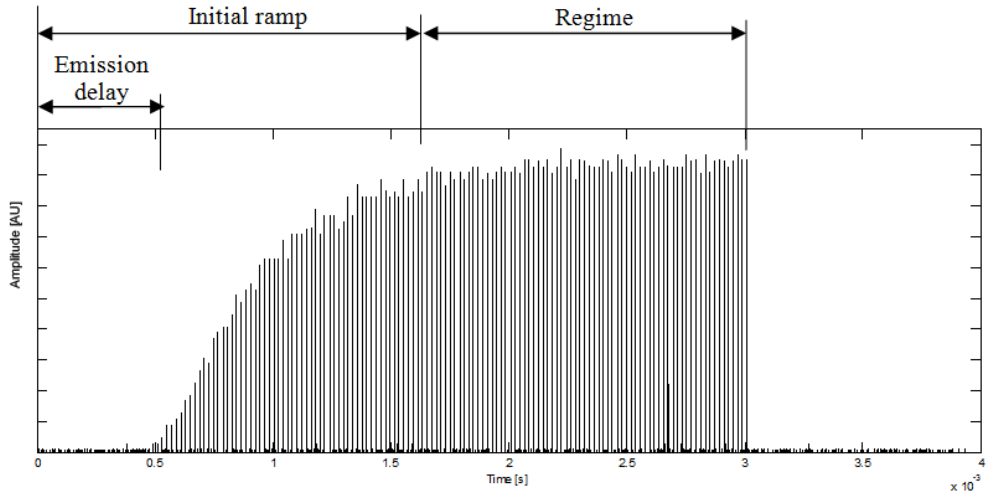

Figure 93. The characteristic emission profile of the used IPG YLPG-5 source, showing the emission delay and initial ramp along with the regime region (PI%=100; PRR=50 kHz; t_{mod}=3 ms)

Table 23. Experimental design for the emission transitory characterization of IPG YLPG-5 laser

Fixed parameters	
Pump current (PI%)	100
Modulation duration (t_{mod})	3 ms
Varied parameters	
Pulse repetition rate (PRR [kHz])	20, 50, 175, 300
Measured variable	
Emission delay ($t_{em.\ delay}$ [µs])	
Emission stabilization duration (t_{stable} [µs])	

Figure 94 represent the measured values of $t_{em.\ delay}$ and t_{stable}. It can be seen both of the durations exhibit a logarithmic decay in trend as the PRR increases. The decaying behaviour in the t_{stable}.is similar to the observed phenomenon for with the IPG YLP-1/100/50/50 for the PRR values below the switching pulse repetition rate. Similarly, the stabilization of the pulse energy occurs faster as the PRR increases. However, at maximum PI% level YLPG-5 exhibits much longer transitory behaviour (t_{stable}=0.7-2.5 ms) compared to the IPG YLP-1/100/50/50 (t_{stable}=0.3-0.5 ms). On the other hand the presence of $t_{em.\ delay}$ is attributed to the combination of the late response of the pumping diodes and the active media. Although, the emission delay decreases in terms of time, the number of delayed pulses (N_{dp}) increases as a consequence of increasing PRR (see Figure 95). The number of delayed pulses, which is tabulated in Table 24, is important for percussion drilling operation to assess the actual number of effective pulses that contribute to the machining process.

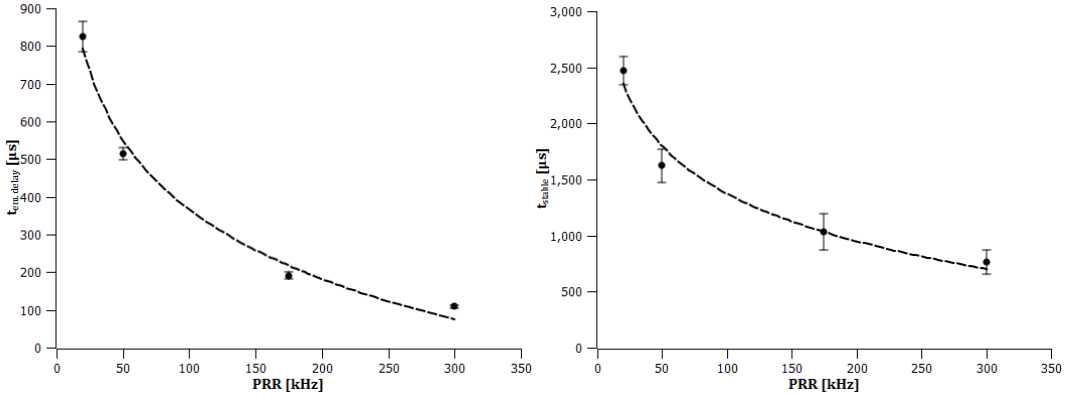

Figure 94 The emission delay ($t_{em.\ delay}$), and emission stabilization duration (t_{stable}) as a function of laser source control parameters (error bars represent 95% CI for the mean, the connection lines depict trend).

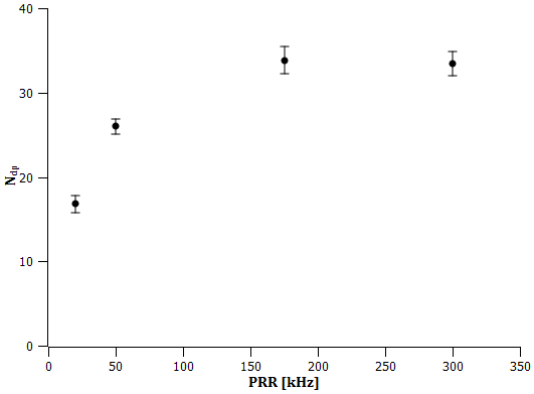

Figure 95. The number of delayed pulses (N_{dp}) as a function of PRR.

Table 24. The average and standard deviation of N_{dp} as a function of PRR.

PRR [kHz]	No of delayed pulses (N_{dp})
20	17±1
50	25±1
175	32±2
300	32±2

On the other hand, the use of change in focal height was found to be unnecessary. Although the control over the pulse trains is still reduced due to the transitory behaviour, the preliminary investigations revealed the need to use multiple pulses due to the low energy content, with emission durations much longer than the $t_{em.\ delay}$, to effectively drill on the material. The employed strategy with this laser source was to set a number of pulses (N), above the number of delayed pulses by modulating the laser with the appropriate duration calculated as:

$$t_{mod} = \frac{N}{PRR} \qquad \text{Eq.(5.16)}$$

Considerations regarding the number of emitted pulses were done afterwards.

5.3.2 Experimental design for machining TiN coated 39NiCrMo3 steel with MOPA, short ns, 0.5 µm fibre laser with the developed processing strategy

In the experimental phase, the laser source was used preferred to be used in the stable energy region over the different *PRR* conditions, thus *PI* was fixed to 100%. In this condition, the average pulse energy and fluence were 19.3±0.4 µJ, and 10.44±0.22 J/cm^2 respectively. The varied parameters were determined as *PRR* and number of pulses (*N*). The PRR values were chosen as the previously characterized conditions. The values of *N* were fixed over all of the different *PRR* conditions initially, not considering the number of delayed pulses. Five replications were made for each combination. Focus variation based microscopy, using Alicona InfiniteFocus, was used to measure the dimple characteristics diameter (*D*) and depth (*h*). Measurement examples are shown in Figure 96 and Figure 97. Table 25 summarizes the fixed and varied parameters, along with the measured variables of the experimental plan.

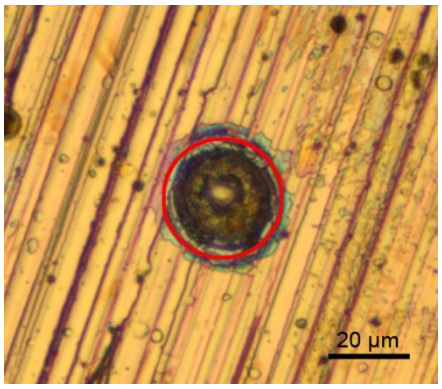

Figure 96. Dimple diameter measured by the fit circle, using the 2D image measurement of Alicona InfiniteFocus.

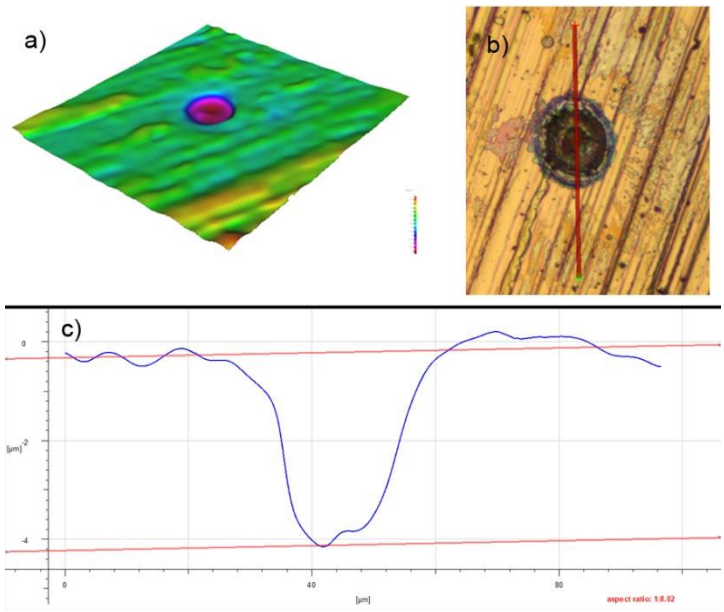

Figure 97. The dimple depth measurement procedure with Alicona InfiniteFocus. a) The acquired dimple in 3D representation, b) the section of measurement passing through dimple centre, c) the section profile along with the fitted planes for the top and bottom of the dimple.

Table 25. Experimental design for multiple pulsed machining TiN coated 39NiCrMo3 steel with MOPA, short ns, 0.5 µm fibre laser.

Fixed parameters		**Levels**
Pump current %	PI%	100%
Pulse energy	E [µJ]	19.3
Focal height	h_f [mm]	0
Varied parameters		**Levels**
Pulse repetition rate	PRR[kHz]	20, 50, 175, 300
No of pulses	N	50, 100, 125, 150, 200, 250
Measured variables		
Dimple diameter	D [µm]	
Dimple depth	h [µm]	

5.3.3 Results and evaluation of the efficacy of the processing strategy

The first outcome of the experimental plan was that the tendency of improving the machining quality with lower pulse durations continued. Similar to the dimples obtained with 12 ns pulses with 1064 nm wavelength, the acquisitions showed high quality holes with the absence of dross, even after the reach of the substrate. Figure 98 shows a 3D acquisition of dimples microdrilled with *E*=19.3 µJ, *PRR*=50 kHz, and *N*=125. Moreover, the dimples on the TiN coating showed absence of cracks present

with longer pulses (see Figure 99). This is attributed to the lower heat penetration and a material removal mechanism based on direct vaporization from solid state.

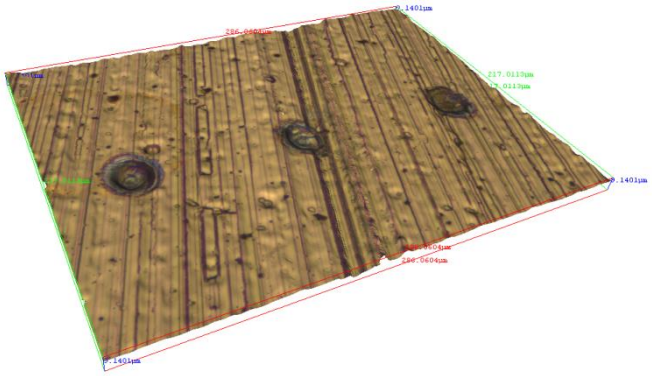

Figure 98.Three dimensional image of dimples realized with *E*=19.3 µJ, *PRR*=50 kHz, and *N*=125.

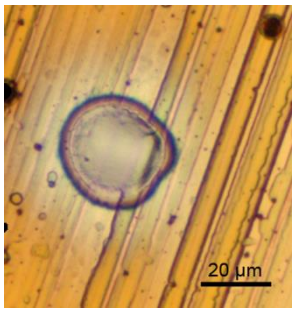

Figure 99. Two dimensional image of a dimple realized with *E*=19.3 µJ, *PRR*=20 kHz, *N*=50 showing absence of cracks.

Quantitative analysis on the measured variables were done using the machine parameter number of pulses (*N*), but also a new parameter namely number of effective pulses (N_{eff}), which described the number of pulses after the end of the emission delay, from the basic relationship:

$$N_{eff} = N - N_{dp} \qquad \text{Eq.(5.17)}$$

Figure 100 reports the measured variables as a function of *PRR* and *N* or N_{eff}. The dimple diameter with the IPG YLPG-5 laser has found to vary between 20-30 µm range, whereas the dimple depth could be up to 14 µm. The smaller dimple diameter is attributed directly to the smaller beam diameter, whereas the increase in the dimple diameter as a function of the number of pulses can be attributed to either increasing pulse energy or the accumulation effect due to the use of multiple pulses. Moreover, it can be seen that a large dispersion in both of the measured variables *D* and *h* between different *PRR* conditions is present, when *N* is used for analysis. It should be noted

that the dependence on *PRR* is primarily due to the change of the N_{dp}. As a matter of fact the plots using N_{eff} explain the dispersion better in terms of the difference in the actual emitted pulses, and free of the effect of *PRR*. Therefore, hereon it was decided to employ N_{eff} for further analysis of the results.

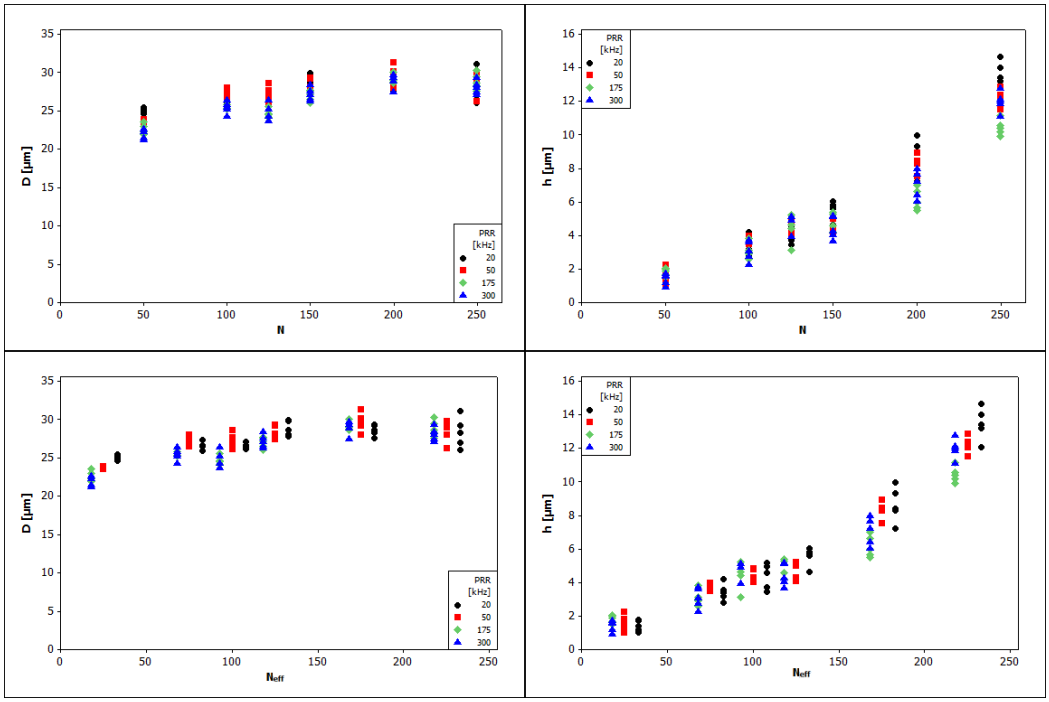

Figure 100. The measured dimple diameter (*D*) and depth (*h*) values as a function of PRR and number of pulses (*N*) in the upper row, and number of effective pulses (N_{eff}) in the lower row.

Concerning the dimple diameter, the measured results showed an asymptotic increase N_{eff} increases. This behaviour recalls the accumulation behaviour observed in the case of 12 ns pulses with 1064 nm wavelength. The existence of such phenomenon was also investigated here rewriting the Eq.(5.7) with the fluence threshold term substituted with the expression given in Eq.(5.15). The final expression is:

$$D = w_0 \sqrt{2 \ln\left(\frac{F}{F_{th}(1) N^{S-1}}\right)} \qquad \text{Eq.(5.18)}$$

With this form, one can estimate the unknowns $F_{th}(1)$ and S, using the non-linear regression method explained before, using the calculated beam radius (w_0=10.85µm) and fluence value (F=10.44 J/cm^2) as in input variables. Figure 101 shows the fitted model along with the measured values. The estimated values of the unknowns were $F_{th}(1)$=1.91±0.10 and S=0.80±0.01. These values are in accordance with the previous results from obtained with the 12 ns pulses at 1064 nm wavelength. However, it should be also considered that the pulse trains are expected to be in the ramped

emission range around this region. Thus, the effect of the increasing diameter, as the N_{eff} increases can be a result of the increasing pulse energy within the ramped pulse train. Therefore, the analysis cannot reach a final conclusion on the validity of these results, even though the model adequately represents the observed phenomenon.

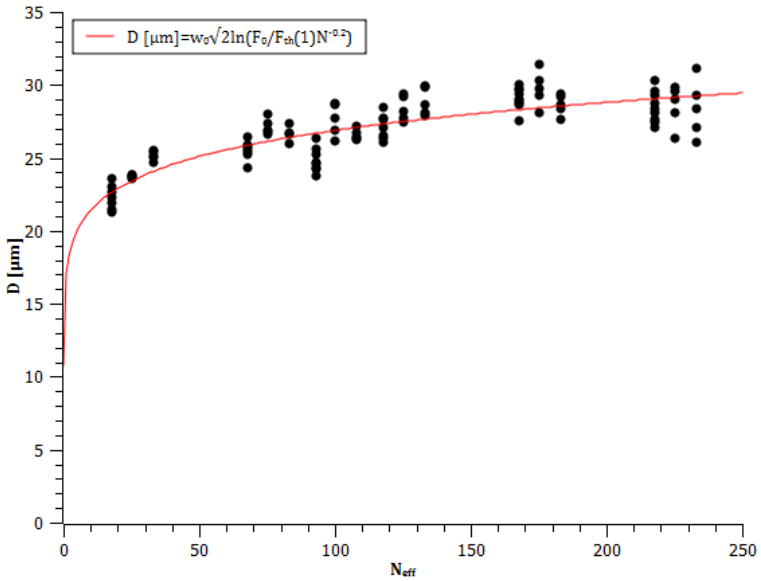

Figure 101. Dimple diameter as a function of effective number of pulses, along with the fit model according to Eq.(16).

Regarding the dimple depth, an increasing trend is visible with the increasing number of effective pulses, without a decrease in the material removal rate as observed with the longer pulses of the SPI G3-20HS laser. The consideration regarding the change in the machined material from the coating to the substrate should also be made here. Therefore two regions were identified below and above the coating thickness (3.87 µm), which was found to correspond roughly around N_{eff}=100. For N_{eff}≤100 the machining was considered to be on the TiN coating, whereas for N_{eff}>100 on the 39CrNiMo3 substrate. Two separate regression models were fitted for the separate regions. Table 26 summarizes the model fitted for the dimple depth on TiN substrate, which showed a linear behaviour without an intercept. The model without the intercept is in agreement with the physical phenomenon, since no dimple depth should be present in existence of the laser pulses. Although this affirmation might seem trivial, it shows that the consideration on the existence of delayed pulses and the use of N_{eff} were correct. Although, the fitted model showed lack-of-fit, due to high R^2_{adj} value and the capacity to represent the physical phenomenon it was found to be adequate.

Table 27 summarizes the model fitted for dimples microdrilled beyond the coating thickness. The model depicts a second order increasing trend in the dimple depth.

High R^2_{adj} value and the absence of lack-of-fit demonstrate the adequacy of the model. Considering the physical interpretation, the non-monotonic increase in the depth can be attributed to the layer change between the coating and substrate. It should be noted that the reach of the substrate initially will occur in a small region at the bottom of the dimple, where the peak fluence is present. As the ablation front proceeds, the microdrilling operation will occur only on the substrate material. Due to lower melting point and higher heat penetration depth of the 39CrNiMo3, the ablation rate is higher, which is observed with a steeper slope.
The two models fitted in different regions along with the measured values can be seen in Figure 102.

Table 26. Summary of the fitted regression model for the dimple depth (*h* [µm]) for $N_{eff} \leq 100$.

Regression Equation

$h\ [\mu m] = 0.0468822\ N_{eff}$

Summary of Model

$S = 0.601306 \quad R^2 = 96.66\% \quad R^2_{adj} = 96.60\%$
$PRESS = 20.1562 \quad R^2_{pred} = 96.55\%$

Analysis of Variance

Source	DF	Seq SS	Adj SS	Adj MS	F	P
Regression	1	565.111	565.111	565.111	1562.94	0
Lack-of-Fit	7	8.999	8.999	1.286	5.74	0.0000775

Table 27 Summary of the fitted regression model for the dimple depth (*h* [µm]) for $N_{eff} > 100$.

Regression Equation

$h\ [\mu m] = 6.14173 - 0.0571785\ N_{eff} + 0.000374848\ N_{eff}^2$

Summary of Model

$S = 0.814279 \quad R^2 = 93.83\% \quad R^2_{adj} = 93.63\%$
$PRESS = 45.2650 \quad R^2_{pred} = 93.20\%$

Analysis of Variance

Source	DF	Seq SS	Adj SS	Adj MS	F	P
Regression	1	624.681	624.681	312.340	1562.94	0
Lack-of-Fit	7	8.425	8.425	1.204	2.025	0.0681059

In conclusion, it has been determined that machining with 532 nm wavelength and 1.2 ns pulse duration allows high quality dimples on the TiN coating. The low pulse duration allows ablation conditions free of thermal affection, thus melt. The shorter wavelength does not contribute in terms of a remarkable change in the absorption of the material, however, it allows smaller beam diameter, thus smaller dimple diameter. Moreover, it was observed that the PRR does not significantly affect the outcome of

the dimple characteristics in the investigated region of 20-300 kHz. Instead N_{eff}, which has been determined from the known characteristics of the laser emission, has been found to be the effective parameter on the dimple diameter and depth.

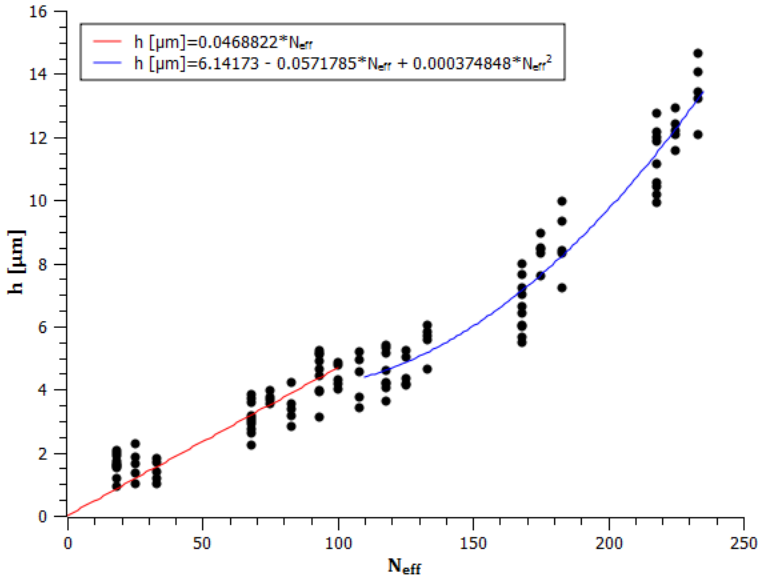

Figure 102. The dimple depth (h) as a function of N_{eff}. The graph shows the fitted models for dimple depth when drilling on the TiN coating (red line), and beyond the coating and on the 39NiCrMo3 substrate (blue line).

5.4 Comparative analysis between the different laser micromachining domains

In laser micromachining parametric studies to make a reliable comparison seems to be highly difficult due to the fact that every material-laser couple constitute diverse machining conditions. As a matter of fact, here it has been shown that not only the machining domain, but also the laser architecture plays a crucial role on the machining nature and also capability. This thesis work considers the LST operation from an industrial perspective as well, thus comparative analysis should be based on not only the physical processing conditions but industrially relevant topics such as the quality, productivity, and applicability in an industrial environment. The following attempts to make comparisons of this kind, using the previous observations on the physical phenomenon, and moreover other aspects regarding the automation capacity.

5.4.1 Quality aspects

The general outcome of the experimental studies is a confirmation on the fact that shorter pulses are beneficial for better micromachining quality also in ns pulse range.

The observations show that the coating material TiN absorbs well both 0.5 µm and 1 µm wavelengths. The machining conditions switch from rapid vaporization, vaporization from melt and slight melt expulsion with pulses in the range of 100-250 ns, to rapid vaporization for pulses between 1-65 ns. The observations on the pulse shape components showed that for ablation initiation, the initial peak is more effective, whereas the increase in the pulse tail results in the increase of depth due to the introduction of non-vaporization based material removal mechanisms. In fact, moving towards shorter pulses, the peak remains and the tail reduces, eliminating the melt generation. Moreover the shorter duration allows smaller heat penetration radially and axially, resulting in a greater control of dimple diameter and depth. The effect of heat penetration is visible also in terms of cracks generated on the TiN coating. Since these coatings are deposited via an arc-PVD method, internal stresses are expected to be generated during deposition, and the laser process seems to relieve them with the rapid thermal cycle. The outcome is larger cracks with longer pulses, and moving towards the lower pulse durations they become smaller.

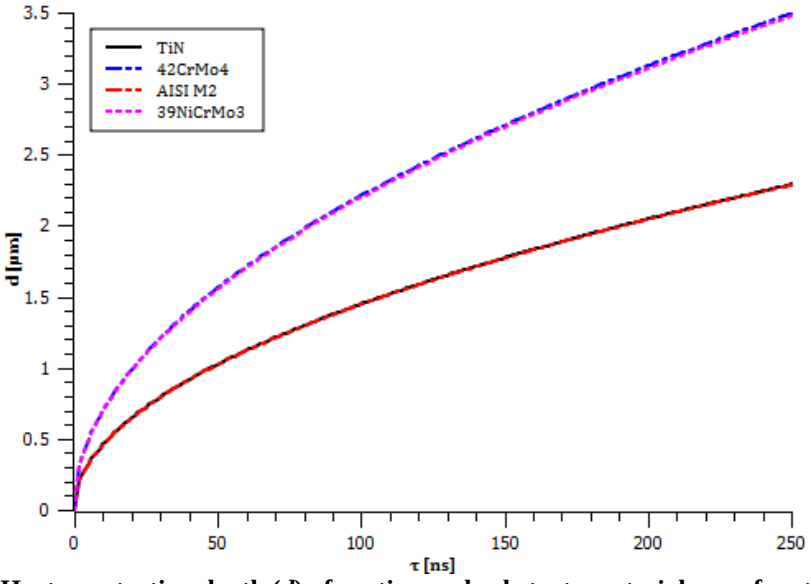

Figure 103. Heat penetration depth (*d*) of coating and substrate materials as a function of pulse duration.

Another important quality factor that needs to be emphasised is the change in the machining behaviour when machining beyond the coating material. Although it is primarily intended to machine only the TiN coating for the LST applications, the possibility of machining beyond the coating material remains attractive for LST applications employing hard lubricants inside the dimples. The change in the material properties from one layer to the other has been observed to cause deposit of substrate material as it ejects from the bottom of the dimple, when longer pulses are used. Such

phenomenon causes clogging of the dimple entrance, and eventually may generate debris within the use of the component. The generation of substrate deposit on the dimple entrance has been effectively avoided with low pulse durations of 1.2 ns and 12 ns. This is a consequence of the limited heat penetration depth in both substrate and coating materials as depicted in Figure 103. For the combination of TiN and 42CrMo4, when microdrilling is carried out with the 250 ns pulses of the IPG YLP-1/100/50/50 source, the difference in heat penetration depth also becomes much larger of about 1.2 µm as well as the difference in melting and boiling points of the materials. In the case of TiN on AISI M2 substrate there is no evident difference of heat penetration depth, where the use of with 12 ns pulses of SPI G3-20HS allows low heat penetration on both materials (about 0.4 µm), evidently allowing limiting the generation of melt. Finally in the case of TiN and 39NiCrMo3 couple, the use of 1.2 ns pulses of IPG YLPG-5 source combines low heat penetration depth and low difference of this property between materials.
Concerning the dimple geometry, the experimental work was concentrated on diameter and depth, however the dimple circularity and depth profile are other aspects, that are of interest and also hard to determine. These quality aspects are mainly influenced by the beam quality and spatial distribution. All of the used laser sources exhibit high beam quality with the highest beam quality parameter M^2 being equal to 2, which belonged to SPI G3-20HS source. Only in this case, some dimples obtained with low energy conditions reflected the beam spatial distribution with an elliptical ablated region circumference and non-uniform dimple bottom.

5.4.2 Process productivity and industrial applicability

As mentioned earlier LST can be conducted using on-the-fly method to obtain a dimple per pulse, and by a point-by-point percussion microdrilling strategy. On-the-fly method constitutes the benchmark for high productivity operations since the process productivity depends on the pulse repetition rate of the laser that is synchronized with the continuous movement of the positioning system, so that dimples are generated with the required pitch. There are two main drawbacks in this scheme:

1- The positioning of the dimples lack precision due to the errors in the scanning system
2- In order to drill on-the-fly high pulse energy with longer pulse durations are required to obtain sufficient dimple depth. This, in contrast, reduces the dimple quality. Moreover, multiple pulsed percussion microdrilling allows better control in dimple depth and diameter.

The process cycle time for a given area to be textured on the fly can be estimated with a simple calculation involving the diameter of the dimple and the pitch for a pattern of equally spaced dimples in x and y directions. The cycle time depends essentially

on the number of dimples. In order to fulfil the on-the-fly microdrilling conditions, the scan speed (v) has to be synchronized to the pulse repetition rate as:

$$v = p \cdot PRR \qquad \text{Eq.(5.19)}$$

where p is the pitch between the dimples. The pitch on the other hand can be expressed as a function of the dimple diameter as there should be at least a pitch size of one diameter for not having overlapped dimples. Thus,

$$v = D \cdot k \cdot PRR \qquad \text{Eq.(5.20)}$$

where D is the dimple diameter and k is the distance coefficient with $k \geq 1$. This points out that there is a limitation regarding the scanning speed as a function of used *PRR*, dimple geometry, and dispersion in space. The graph in Figure 104 shows the required scan speed for different dimple diameters within the range observed in the experimental phase (D=20-60 µm). It is evident that as the dimple spacing increases the required scan speed should increase to synchronize with the *PRR*. As a matter of fact, today the highest scan speed achievable with the commercial scanner heads is about 10 m/s. Therefore a technological feasibility zone is present for the usable *PRR* levels to achieve the desired LST pattern.

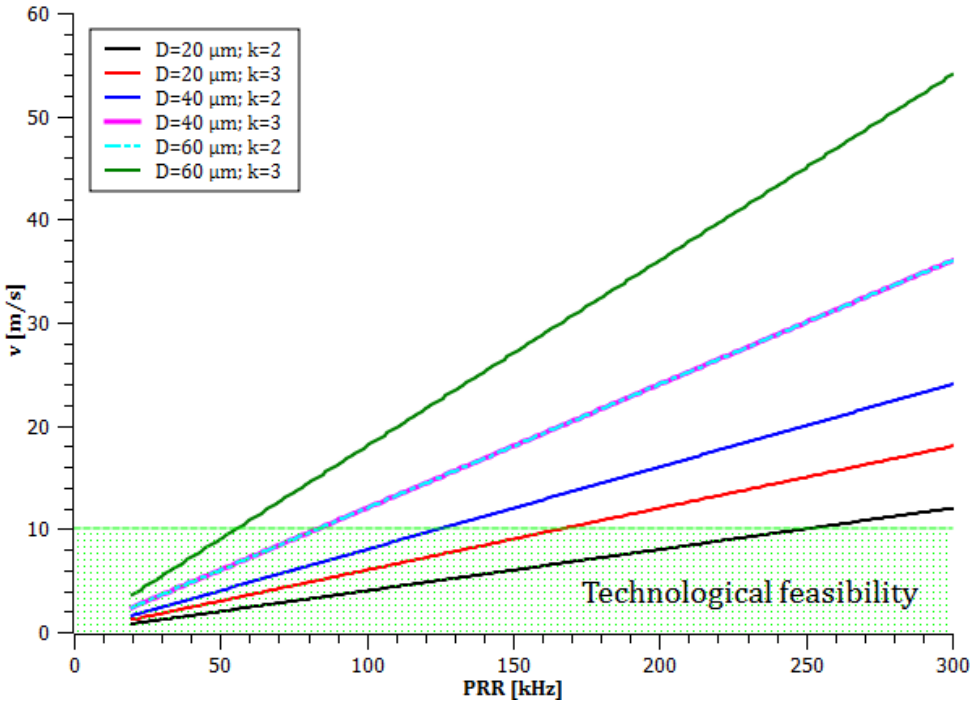

Figure 104. Required scan speed (v) for on-the-fly microdrilling as a function of *PRR*, dimple diameter and spacing.

On the other hand the cycle time for the LST operation could be calculated as:

$$t_{cycle} = \frac{p(n-1)}{v} = \frac{n-1}{PRR} \quad \text{Eq.(5.21)}$$

Assuming that the dimple pattern is a square matrix, the number of dimples to cover the surface area can be calculated as

$$A = \left[\left(\sqrt{n} - 1\right) \cdot p\right]^2 \quad \text{Eq.(5.22)}$$

where *A* is the surface area. It is possible to rewrite the expression substituting the p with its function in diameter,

$$A = \left[\left(\sqrt{n} - 1\right) \cdot D \cdot k\right]^2 \quad \text{Eq.(5.23)}$$

It is now possible to define the cycle time as a function of the geometrical parameters textured area and dimple diameter from:

$$t_{cycle} = \frac{\left(\frac{\sqrt{A}}{D \cdot k} + 1\right)^2 - 1}{PRR} \quad \text{Eq.(5.24)}$$

This expression can be used to calculate the LST productivity for a given unit of area, as a function of the surface design parameters and the laser parameter *PRR* that determines the texturing speed. Figure 105 shows the plot of such dependence, depicting the technological feasibility region determined by the maximum scan speed available. It should be noted that the increase in of cycle time with small *D* and higher *k* values is a consequence of the increase in the number of dimples per area.
The other modality to execute LST is the so called point by point method, in which the scanner head moves from one point to the other, performs the percussion microdrilling operation, and executes a certain delay before departing for the next point. The delay time can be selected empirically in order to have stable and precise positioning of the laser beam and avoid transitory behaviour in the emission. In this modality, evidently the process time becomes a function of the sum of drilling (t_{drill}), delay (t_{delay}), and positioning ($t_{position}$) times as:

$$t_{cycle} = (t_{drill} + t_{delay} + t_{position}) \cdot n \quad \text{Eq.(5.25)}$$

$$t_{cycle} = (t_{drill} + t_{delay} + \frac{p}{v}) \cdot n \quad \text{Eq.(5.26)}$$

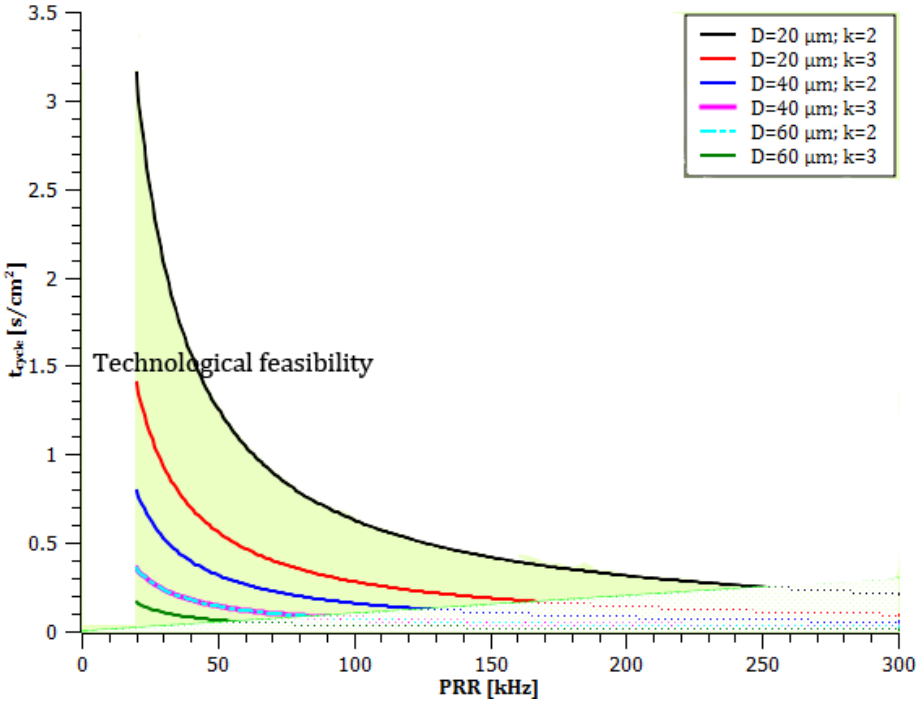

Figure 105. Cycle time (t_{cycle}) per unit area in on-the-fly microdrilling as a function of as a function of PRR, dimple diameter and spacing.

Making the necessary substitutions the expression can be rewritten as a function of area and dimple geometry:

$$t_{cycle} = (t_{drill} + t_{delay} + \frac{D \cdot k}{v}) \cdot \left(\left(\frac{\sqrt{A}}{D \cdot k} + 1\right)^2 - 1\right) \qquad \text{Eq.(5.27)}$$

The drilling and delay times vary between the different laser sources and employed machining strategy. Although a parametric comparison is very difficult to be made due to the differences in the employed machining strategies, and attempt is made based on the conditions reported on Table 28. It should be noted that the dominant factors between the different strategies in terms of productivity is the delay time, as the drilling time is considerably low in comparison. In the case of IPG YLP 1/100/50/50 source the delay time is set to avoid transitory effects in the laser, whereas for the latter two it is the time required for the settling of the scanner on the next position. For calculations *D* was chosen as 25 µm, a value that is achievable with all the available sources

Table 28. Chosen percussion drilling conditions of the used laser sources for productivity analysis. The conditions depict drilling times necessary for drilling the coating material only.

Laser source	t_{drill}	t_{delay}	v
IPG YLP 1/100/50/50*	0.065 ms	8.0 ms	10 m/s
SPI G3-20HS**	0.350 ms	0.5 ms	10 m/s
IPG YLPG-5***	0.440 ms	0.5 ms	10 m/s

*t_{mod}=65 µs
**τ=100 ns; No of pulses=7; PRR=20 kHz
***N_{eff}=100; PRR=300 kHz

Figure 106 shows the cycle time for unit area for the chosen microdrilling conditions belonging to different laser sources. It can be seen that the long delay time of the IPG YLP 1/100/50/50 source renders it very highly unproductive compared to the other two laser sources. The short delay times of the other two sources improve the productivity. However, it should be noted that the productivity is still much lower compared to the slowest condition that is theoretically achievable by on-the-fly drilling. The further industrialization of LST of TiN coatings is highly dependent on the productivity. The holy grail of high productivity LST lies on the applicability of single pulsed on-the-fly drilling, which constitutes other limitation regarding the quality. Point-by-point drilling still remains as a viable option, with possible improvements in productivity enabled by faster and more accurate scanning systems, and more energetic laser sources in shorter ns pulse domain. It should be reminded that industrial applications also require robust laser sources, with flexible operation in industrial environment. The architecture of fibre laser possesses the required robustness and flexibility, providing various possibilities for the system integration of LST in industrial applications. The up-scaling of this method for texturing large areas, such as engine cylinder blocks or machine tool guides, is conveniently possible by employing beam sharing with a single high energy fibre laser source and multiple scanning heads. The scanning heads can be further integrated to Cartesian axes, or robotic arms to cover larger areas without the use of complicated optical paths. Curved or free-form surfaces can be textured with the integration of rotary axes to follow the surface geometry. This would enable texturing stamps and dies with complex geometries.

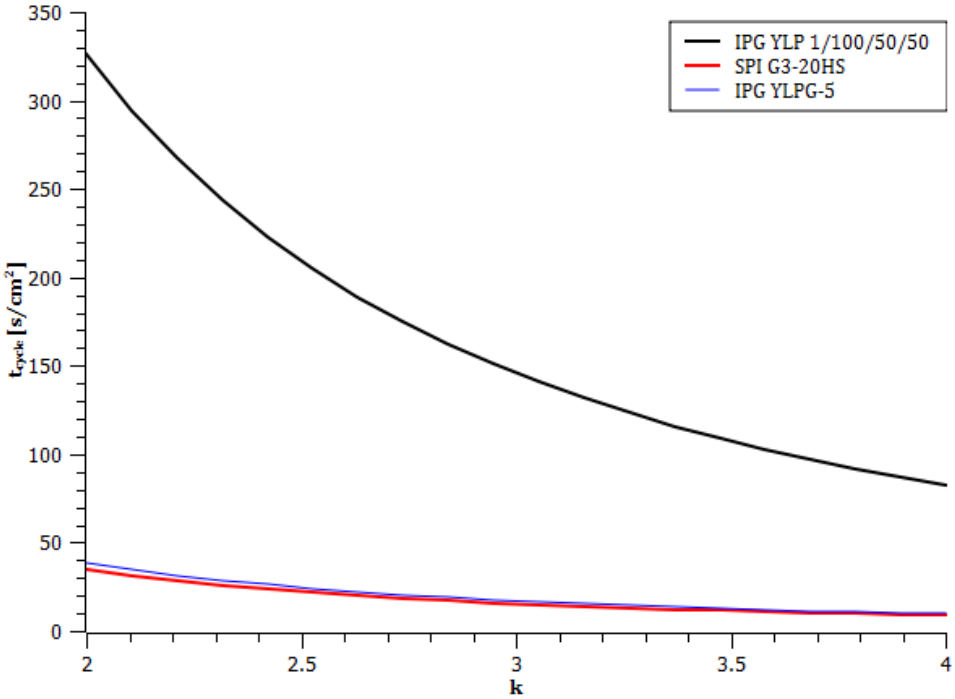

Figure 106. Cycle time (t_{cycle}) per unit area in point-by-point microdrilling for different laser sources as a function of dimple spacing.

Chapter 6

Laser self-mixing interferometry for ablation depth monitoring on TiN coatings

The difficulties in controlling the ablation depth on the limited thickness of the applied TiN coating in percussion drilling have been demonstrated in the previous chapter in detail. The developed processing strategies have shown to be effective for controlling the dimple geometry characteristics. However it should be noted that LST involves micromachining of large surface areas. The process stability over the whole surface area depends on many factors in industrial environment such as, the laser power stability, material impurities, variation in the focal plane, and operator's skills. Depending on the textured component the operation time may vary from minutes to days. In case of small surface areas concerning small components such as milling tools, such error would result in non-conformity of the component and can be tolerable to a certain extent. In case of large surface areas concerning large components such as cold drawing dies, the error mitigation is much more difficult due to higher costs and production times. Again for large components the realization of defected zones is much more difficult due to the difficulty of adapting surface measurement devices to such forms and dimensions. Online monitoring of the process opens up the possibility to realizing errors during operation without the necessity to move the processed component, therefore intervention is possible in short period of time.

Laser self-mixing interferometry is potential solution for online monitoring of ablation depth during the LST of TiN. Compared to conventional interferometry techniques its architecture is much simpler, which renders it less sensitive to the environment. The basic scheme of the applied monitoring technique is represented in Figure 107. The system involves two laser beams combined in space via a dichroic mirror and focused on the same spot, where the machining beam coming from the fibre laser processes the material and the beam coming from a Fabry-Perot type laser diode is used to measure the displacement of the ablation front. The scheme, simple in principle, involves a series of issues that require attention to ensure the functionality of the measurement method.

This chapter investigates the possibility of ablation depth measurement in the scenario of percussion drilling of TiN coating on 39NiCrMo3 substrate with the MOPA, short ns, 0.5 µm fibre laser. The chosen scenario represents the best choice in micromachining quality with high productivity. The aim of the study is to prove the concept and demonstrate the limitation regarding future industrial applications. In the following, the design requirements of the monitoring system and then the solutions incorporated on the realized opto-mechanical system are described. The system is then characterized for operational capabilities, especially in terms of interaction with the process emission and generated plume. The measurement performance is evaluated in comparison to a conventional depth

measurement instrument. The chapter closes with possible improvements for industrial applicability of the demonstrated method.

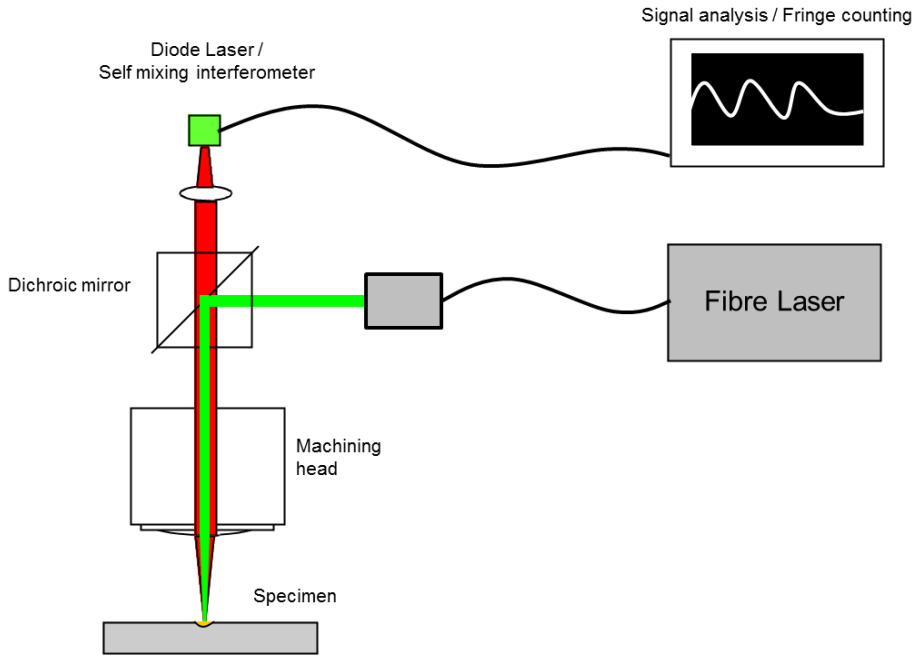

Figure 107. The scheme of laser self-mixing interferometry for ablation depth monitoring

6.1 Requirements of the monitoring method and regarding limitations

For the online measurement of ablation depth, the laser self-mixing interferometry is aimed to be used in the displacement measurement modality. The emerging hole bottom can be treated as a target, which is displaced in a single direction. Each displacement step at $\lambda/2$ distance, where λ is the measurement laser wavelength, is visualized with a single fringe. Fringe counting gives the displacement measurement. The spatial, time dependant, and environmental characteristics of the laser ablation render the measurement scheme essentially different from conventional displacement measurements. The effect of these characteristic on the measurement can be summarized as the following.

- Effect of spatial characteristics: The realized dimples with the chosen laser are 25 µm in diameter and only a few µm in depth. The hole depth that is defined the deepest point of the dimple. The dimension of the measurement beam becomes comparable to the target. This means only a portion of the measurement beam will provide the phase difference that demonstrates the displacement in terms of the advancing hole bottom. This is expected to cause a reduction in signal to noise ratio. Moreover, the measured depth is comparable to the wavelength of the

interferometer. Thus, a measurement technique based on fringe counting results in considerably low resolution compared to a conventional measurement device.

- Effect of time dependant characteristics: The ablation process involves very fast process dynamics, which are still not clearly defined and under study by several research groups. In general, different ablation mechanisms exist that range from direct vaporization to phase explosion, which are essentially different in material removal rate. As a consequence it is not easy to predict whether the material removal occurs during or after the pulse duration, and whether it is constant or time dependant. For the chosen scenario the material removal mechanism was observed to be in direct vaporization, however only an average material removal rate can be estimated providing a value of removal depth per pulse. In the experimental studies the time scale of pulse durations was between 1-250 ns with each pulses arriving in periods between 3-50 µs range. The time scales involved require fast electronics and constitute a threshold for the plausible next-step of online process control.
- Effect of environmental characteristics: The laser ablation causes physical changes in the material and the environment in which the process occurs. Local changes in the atmosphere are present that are manifested as generation of plume that may consist of different components such as dense plasma in core, propagating wavefront, and flying particles removed from the material. Once the measurement beam passes from the ambient atmosphere to the plume a series of optical phenomenon can manifest, such as scattering, change of refraction index, and coherence loss. These factors are limiting to the operational capability of the interferometer, since it is technique based on coherence and amplitude of the reflected light from the target. Moreover, ablation causes plasma emission mainly in visible and UV range. Although the plasma emission is not spatially coherent it may interfere with the measurement beam, if its wavelength is selected in the same region. The adequate choice of the self-mixing interferometer's wavelength can eliminate interference problems, but the plasma emission can be captured by the photodiode of the laser diode that is used to measure the interference in the laser diode cavity.

Figure 108 represents the plausible physical phenomenon in the self-mixing interferometry measurement scheme, highlighting the effect of the ablation characteristics.

The listed characteristics are required to be affronted within the design of the measurement setup. The requirements of the measurement system to overcome the potential problems can be grouped under three fundamental aspects: optical, electronical, and mechanical.

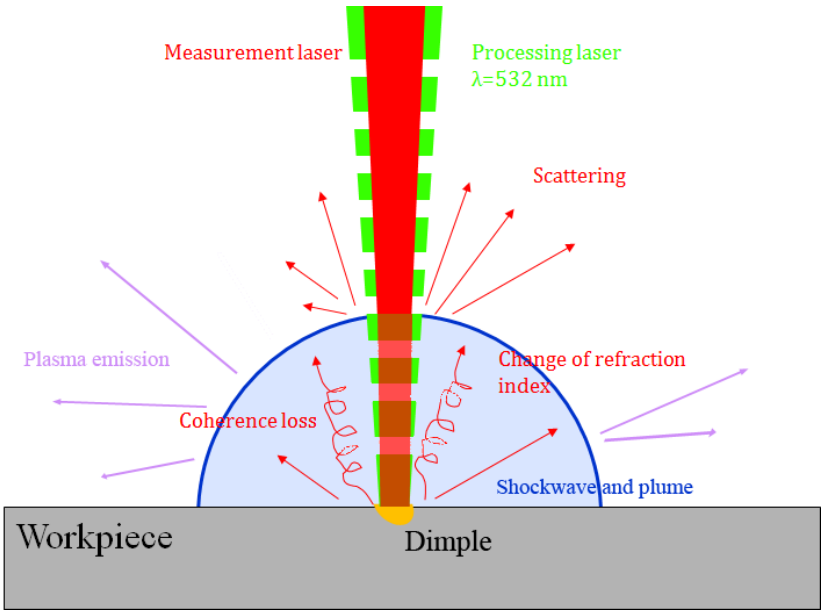

Figure 108. The effects of laser ablation characteristics on self-mixing interferometry

6.1.1 Optical requirements

Optical requirements: The optical requirements involve a series of phenomena, which are often contradictory to each other. These requirements are basically the factors that determine the main characteristics of the probing beam, namely wavelength, divergence, and spatial distribution. The selection of the wavelength of the interferometer determines the intrinsic resolution of the device as fringes will be completed at each λ/2 displacement. On the other hand, small wavelengths would require faster electronics, thus larger bandwidth to be able to acquire more fringes for the same process duration. It should be noted that signal processing can be applied to improve the time resolution of the measurement to more than $\lambda/2$.

The wavelength of the interferometer beam also determines the beam waist diameter, which is a key factor in the spatial resolution of the measurement setup, as expressed in Eq.(3.6). Smaller wavelengths can produce smaller spot diameters, which can potentially improve the spatial resolution of the device. The two beams (processing and measurement) should be matched to obtain same focal position for both the beams, or have overlapping depth of focus regions. This, in fact is a challenging issue as the beams are focused through the same focal lens, which would produce different focal positions for the two different wavelengths due to chromatic aberration (see Figure 109). Adequate optics should be adapted for chromatic aberration correction. The self-mixing interferometry laser should possess sufficient depth of focus or namely Rayleigh range, which is the region where the laser beam is considered to be constant in beam diameter as expressed in Eq.(6.1).

$$z_R = \sqrt{h^2 - 1}\frac{d_o \cdot f}{d_c} \qquad \text{Eq.(6.1)}$$

where $h=2^{0.5}$. The expression points out that for large depth of focus large focused beam diameter is required. However, in order to obtain a reasonable compromise between the contrasting issues it is convenient to limit the size to be small enough to fit into the ablated dimple.

Figure 110 shows an example of emission spectrum during TiN ablation. It can be observed that the ablation emission is concentrated in visible and UV range, while in the IR region the contribution is not present. Furthermore, Ti I and Ti II emission lines are clearly evident. In order to avoid interference with the plasma emission the wavelength band between 300-750 nm requires to be avoided. The region includes the wavelength of the processing laser beam, therefore further considerations regarding it is not required.

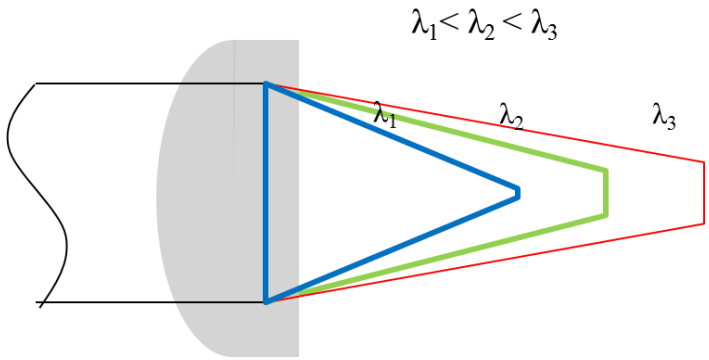

Figure 109. The effect of chromatic aberration on the focal plane of different wavelengths.

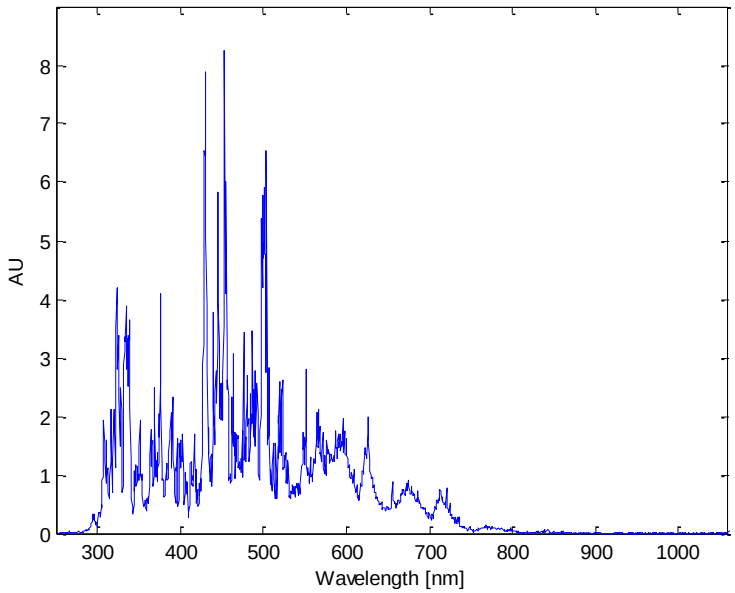

Figure 110. An example to the emission spectrum in laser ablation of TiN coating.

6.1.2 Electronical requirements

If the optical requirements are fulfilled the interference phenomenon is to occur in a time scale determined by the speed of light, therefore theoretically the measurement technique should be able to detect the change in ablation depth without timing restrictions. However, the time scale of the ablation event is a restriction on the electronics used to amplify, digitalize, and record the interference signal. The device should be able to capture the fast ablation phenomenon, occurring in ns-µs scale. This requires fast electronics with high signal to noise ratio, so that fringes can be visible without any aliasing effects. The main parameter determining the speed of signal acquisition is the bandwidth of the electronics used in the self-mixing interferometer. Another contrasting issue with bandwidth is that it is reduced with high signal amplification. Therefore, bandwidth (*BW*) has to consider as a fundamental design parameter for self-mixing interferometry in ablation depth monitoring. A simple relationship can be derived using the wavelength of the self-mixing interferometer (λ_{int}) and average material removal rate (*MRR*) to calculate the time to observe a single fringe (t_{frg}) from:

$$t_{frg} = \frac{\lambda_{int}}{2 \cdot MRR} \qquad \text{Eq.(6.1)}$$

In order to avoid aliasing of the signal the Nyquist criteria has to be fulfilled, which dictates that at least 2 points should be acquired within the period to reconstruct a signal with its correct frequency. Therefore the minimum acquisition frequency (f_{min}) is:

$$f_{min} = \frac{1}{t_{frg}} \cdot 2 \qquad \text{Eq.(6.2)}$$

As a matter of fact for adequate signal representation, the bandwidth of the self- mixing interferometer is required to be sufficiently larger than this frequency. Estimations of f_{min} based on the observed material removal rates can be made as seen in Table 29. The calculations were made with the shortest wavelength usable to avoid interfering with the plasma emission, which was observed to be 750 nm.

Table 29. Estimation of the minimum sampling frequency for representative ablation conditions.

Laser source	IPG YLP-1/100/50/50	SPI G3-20HS	IPG YLPG-5
Wavelength (λ)	1064 nm	1064 nm	532 nm
Pulse duration	250 ns	100 ns	1 ns
Pulse repetition rate (PRR)	50 kHz	20 kHz	50 kHz
Pulse energy (E)	312 µJ	117 µJ	20 µJ
Ablation rate	1.5 µm/1 pulse	2 µm/6 pulses	2 µm/25 pulses
	1.5 µm/20µs	2 µm/300 µs	2 µm/625 µs
Average MRR	0.075 µm/µs	0.007µm/µs	0.004 µm/µs
Fringe occurance time (t_{frg})	5.00 µs	56.25 µs	93.75 µs
Min. sampling frequency (f_{min})	400 kHz	36 kHz	23 kHz

6.1.3 Mechanical requirements

The fulfilment of both optical and electronical requirements ensures the conceptual feasibility of the measurement device. Unless proper mechanical solutions are implemented, the functionality of the device cannot be guaranteed. The mechanical requirements involve the stability of the components used in the setup, the possibility of flexible alignment, and protection from mechanical vibrations from the environment. Standard parts should be preferred for flexibility in part change and adaptation of different solutions in this stage.

6.2 Design of the measurement setup

The measurement setup consists of two main sections: 1- the self-mixing interferometer and electronical acquisition devices, and 2- the opto-mechanical system that combines the processing and measurement beams and focuses them on the same position in space.

6.2.1 Self-mixing interferometer design

The used prototype self-mixing interferometer was designed and produced by the group of Prof. Michele Norgia from the Department of Electronics and Informatics of Politecnico di Milano. The devices constructed by the group are based on the use of commercial laser diodes, which have proven to show the self-mixing interference effect. Therefore a selection of wavelengths is applicable, whereas the bandwidth of the system can be regulated by the constructed electronic circuit to fit the purpose. Based on the listed optical requirements the wavelength of 785 nm was found to be the most suitable as a compromise in measurement resolution, focused beam diameter, and functionality outside the plasma emission band.
In particular the light source used was a GaAlAs laser diode with a multi-quantum well structure (Hitachi HL7851G). The built-in monitor photodiode allowed the measurement of the self-mixing interference. The exiting beam was in elliptical shape that is characteristic for single transverse electronic mode laser diode beams. Single mode laser diodes are considered to have M^2 values between 1.1-1.2, and for calculation purposes the largest value was used [174]. The output power in CW emission was 50 mW, while power modulation was possible up to 500 kHz with 50% duty cycle. The laser diode was used with a 10 mm collimation lens. For Figure 111 shows the collimated beam spatial energy distribution acquired with a beam profiler based on CCD camera (Spiricon SP620U).
Table 30 summarizes the main characteristics of the laser diode.
The laser diode was integrated to a power and amplification circuit. The integrated system consisted of single stage trans-impedance amplification, utilizing an operational amplifier with 4 GHz gain bandwidth product (Texas Instruments OPA 847). A 12 kΩ resistor was used at the amplification stage to limit the bandwidth to the highest value of stable

operation, 35 MHz, which is sufficiently enough to acquire the fast ablation phenomenon. At this bandwidth the root mean square (RMS) voltage output noise was measured around 5 mV. The laser diode was injected with 70 mA current that generated about 15 mW optical power. Depending on the feedback parameter, the self-mixing interference caused a ±0.5 mW fluctuation in the optical power, which was measured as current fluctuation up to 4 mA by the measurement photodiode. The photodiode signal passed through a high-pass filter before the amplification stage, which removed the offset component and permit only the current fluctuation due to the self-mixing effect to pass. The amplified signal or the fringe amplitude was expected to reach up to 48 mV. The whole device was powered by a single supply with 5V. Figure 112 shows the encased device.

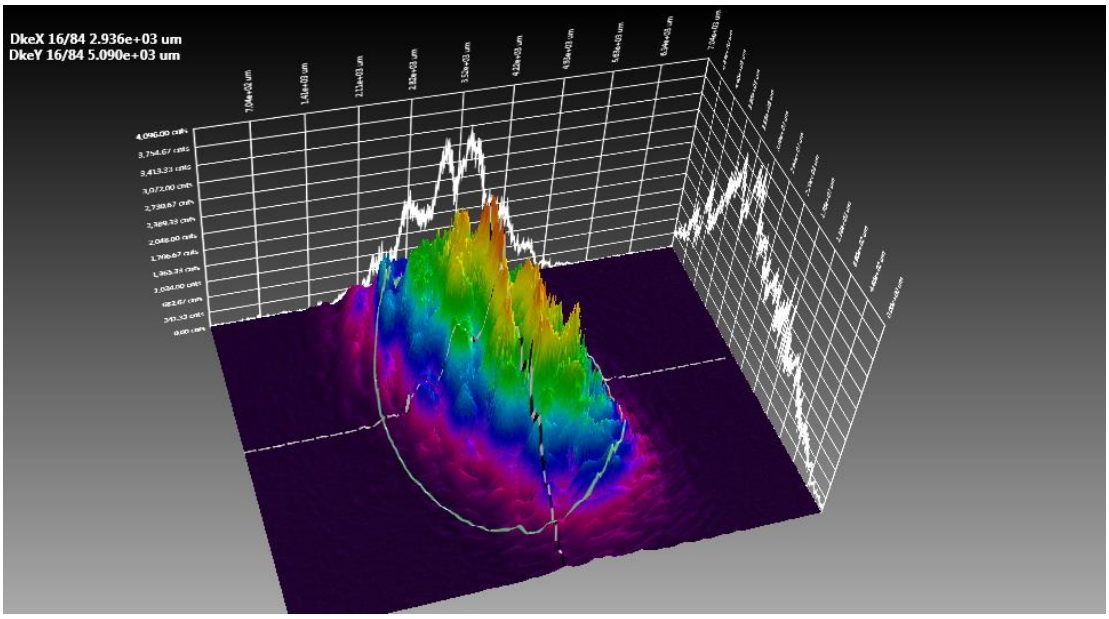

Figure 111. The spatial distribution of the laser diode used in the self-mixing interferometer.

Table 30. The main characteristics of the Hitachi HL7851G GaAlAs laser diode.

Wavelength	785 nm
Max. power	50 mW
Fast axis beam divergence	9.5°
Fast axis beam divergence	23°
M^2	1.1-1.2
Collimation lens	5 mm
Collimated diameter fast axis	2.9 mm
Collimated diameter slow axis	5.1 mm

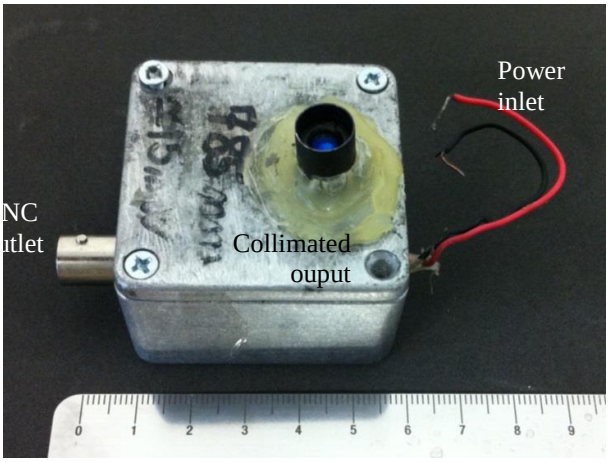

Figure 112. The prototype self-mixing interferometer.

6.2.2 Opto-mechanical system design

The 3D model of the opto-mechanical system can be seen in Figure 113. In detail the system comprised of two modules, namely beam combination and beam focusing. The fundamental optical elements to combine the processing and measurement beams were the dichroic mirror and the focusing lens. To combine the collimated beam in free space a longpass dichroic mirror with 50% transmission/reflection point at 567 nm was chosen (Thorlabs DMLP567). The dichroic mirror was mounted on a rotation and inclination stage for precise alignment. A bandpass filter at 780 nm central wavelength and ±10 nm FWHM bandwidth was employed after the collimation stage of the interferometer (Thorlabs FBH780-10). This allowed filtering out any other optical component to be measured by the photodiode of the laser diode. A diaphragm was implemented to control the amount of returning light into the laser cavity, which is essential to control the feedback parameter (*C*). Finally, a custom inlet for the interferometer has been designed and internally produced to robustly fit and align the interferometer beam. Figure 114 shows an exploded view of the beam combining module.

The focusing module constituted of the focusing lens assembled on a micrometric stage for focal position variation. When focusing the two beams through a singlet lens spatial a large difference in focal positions was observed. Moreover, the alignment was more sensitive to angular errors, thus the two beams were focused in different planes in depth and different positions on these planes. In order to compensate for chromatic aberration an achromatic doublet lens with 100 mm focal distance was chosen that provided a 317 μm focal position difference between the wavelengths of processing and measurement lasers (see Figure Figure 115). Figure 116 demonstrates images of the two beams, when the processing beam was on focal position with a singlet lens and an achromatic doublet lens. The focusing lens was movable in z-axis free from the combining module over 25 mm travel. Figure 117 shows the focusing module detail of the CAD model. The self-mixing interferometry signal was captured with a digital oscilloscope digital with 350

MHz maximum bandwidth, 5 GS/s sampling rate and $16{\cdot}10^6$ record length (Tektronix TDS5034B). Table 31 summarizes the electrical and optical specifications of the build self-mixing interferometry setup. It can be observed that the system is capable of capturing fast ablation phenomenon in time, and in space capable of maintaining focused beam conditions within at least 0.5 mm of depth in slow axis. The beam size in fast axis is compatible with the dimple diameter, whereas in slow axis appears to be bigger.

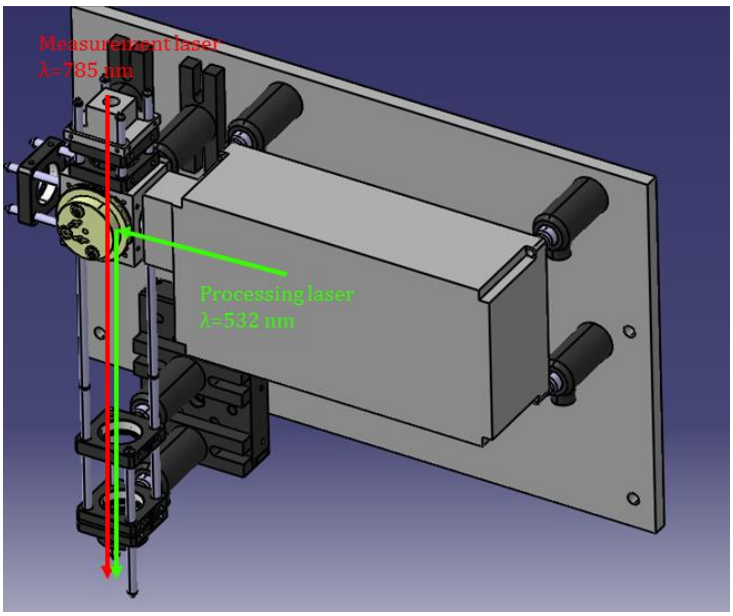

Figure 113. Three dimensional CAD model of the opto-mechanical system for the laser self-mixing interferometry study.

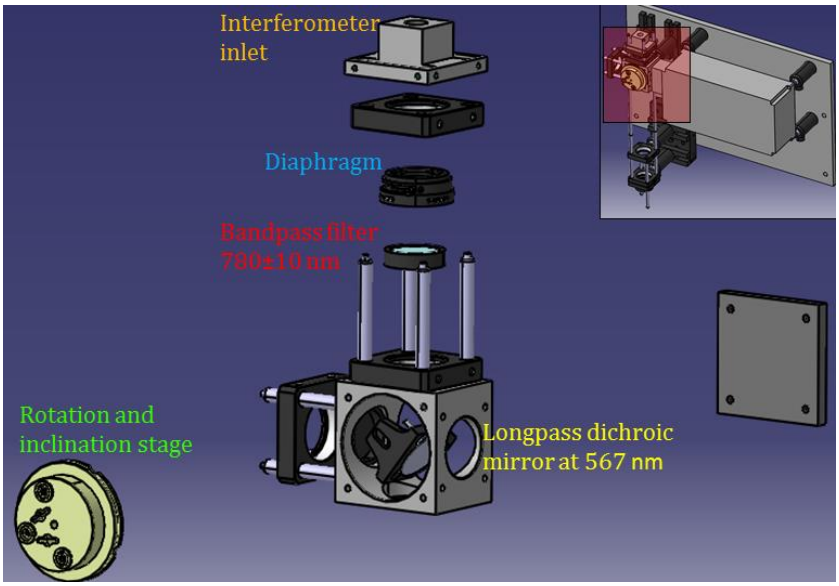

Figure 114. Three dimensional CAD model detailing the beam combining module.

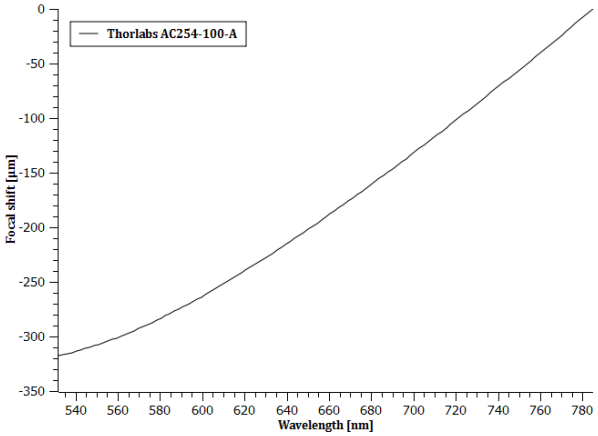

Figure 115. The focal position shift of the chosen achromatic doublet lens as a function of wavelength.

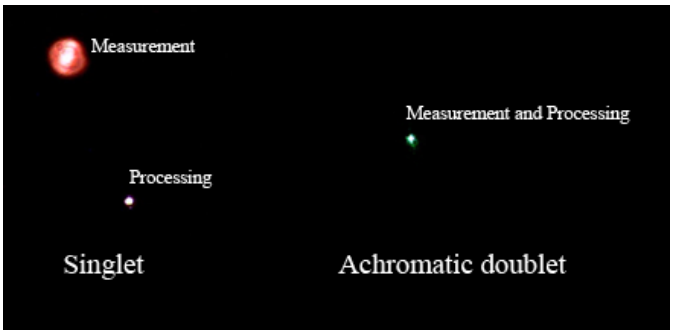

Figure 116. The effect of achromatic lens on the focal plane correction of two different wavelengths. The images have been acquired via a CCD camera with neutral attenuators.

Table 31. General specifications of the laser self-mixing interferometry measurement system.

Electrical	
Supply voltage	5 V
Laser input current	70 mA
Output power	15 mW
Bandwidth	35 MHz
RMS voltage output noise	5 mV
Optical	
Depth resolution (λ/2)	0.3925 µm
Focused fast axis beam diameter	41.4 µm
Focused slow axis beam diameter	23.5 µm
Rayleigh range in fast axis	1426 µm
Rayleigh range in slow axis	461 µm

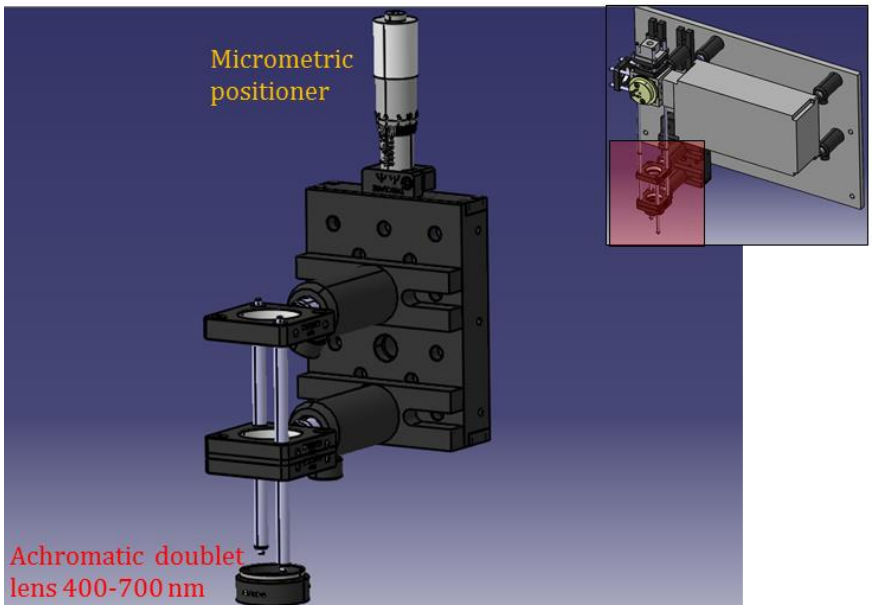

Figure 117. Three dimensional CAD model detailing the beam focusing module

Downstream the opto-mechanical measurement assembly, a workpiece holder was placed for manual positioning of the machined sample. Side assist gas addition was provided via a flexible tube with 6 mm inner diameter, positioned parallel to the material surface. The gas pressure was controlled with the manometer at the gas supply. In addition to the laser self-mixing interferometry measurements, a spectrometer (Avantes AvaSpec 2048-USB2) was implemented in the setup to study the plasma luminescence to better understand the ablation characteristics that limit the applicability of the measurement method. The main characteristics of the spectroscope are summarized in Table 32. In order to supress the laser wavelength a short-pass filter at 500 nm was used (Edmund Optics OD2). This filter supressed also some of the emission band, however it allowed the passage of the main luminescence band in the UV region that covers the larger amount of emission band. Figure 118 shows the assembled system and related components.

Table 32. General characteristics of the Avantes AvaSpec 2048-USB2 spectrometer.

Wavelength range	200 - 1100 nm
Wavelength resolution	0.586 nm
Grating	1200 lines/mm
Slit width	50 µm
Integration time	1.1 ms - 10 min

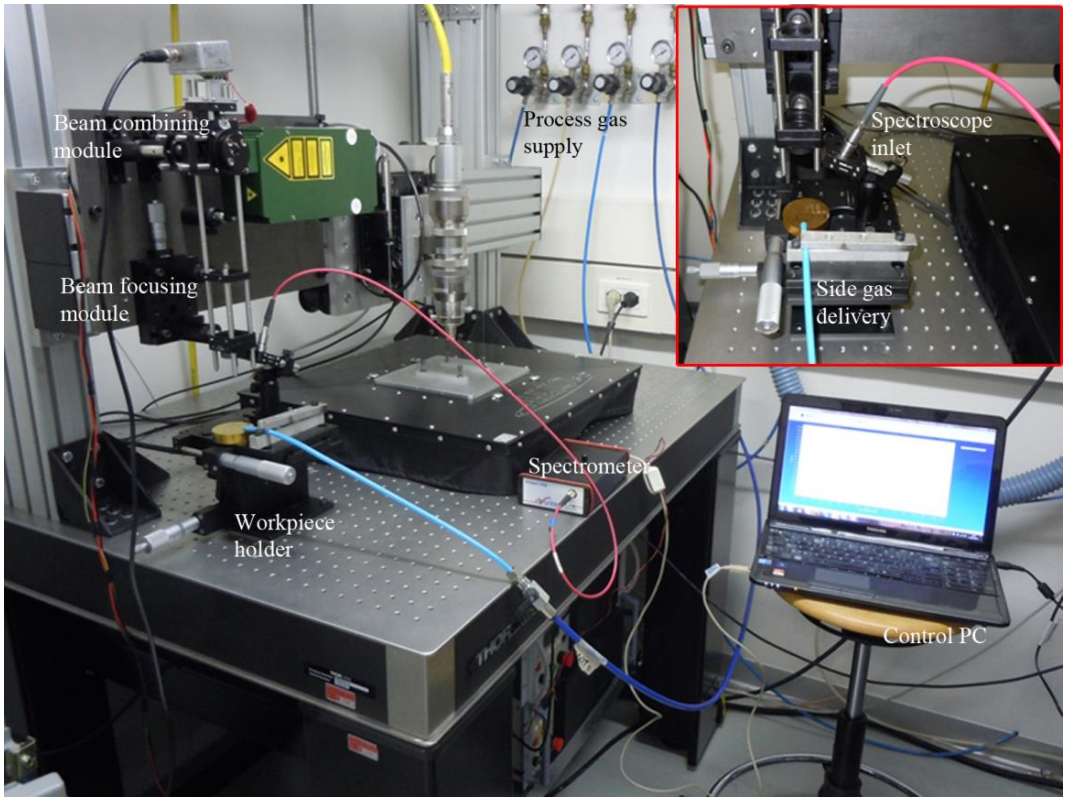

Figure 118. Experimental setup for laser self-mixing interferometry for ablation depth monitoring on TiN coatings, and spectroscopic study of the ablation luminescence.

6.3 Monitoring of dimple depth in LST of TiN coated 39NiCrMo3 steel with MOPA, short ns, 0.5 µm fibre laser

The design criteria ensured the theoretical feasibility of the measurement method. However, the applied optical, electronical, and mechanical solutions could not resolve the problem related to the presence of the ablation plume around the microdrilling region, which is expected to cause coherence loss and loss of scattering effects. The following describes first the solution provided to overcome this limitation via the use of a side gas, which permitted obtaining self-mixing signal of ablation front displacement. Next, the use of spectroscopic analysis to investigate the influence of the gas flow on the ablation characteristics is presented. With the accumulated knowledge from the observations a conceptual model to explain the signal components in case of non-measuring and measuring conditions is developed. These are followed by a benchmark study of the measurement device in comparison to an offline measurement instrument. Prospects regarding possible improvements for enhanced measurement performance conclude this section.

6.3.1 The effect of side gas on the measured self-mixing interferometry signal

The initial experiments carried out in ambient air revealed signals with moderate amplitude, with well-defined saw tooth shape fringes in both ascending and descending directions. The number of fringes in both directions appeared to be equal, resulting in null displacement. Moreover, the fringes within the laser emission duration showed ascending movement, instead of a descending movement due to the movement of the ablation front. This phenomenon was repeatedly observed with different microdrilling conditions as seen in Figure 119 and Figure 120. It was concluded that the observed phenomenon did not belong to the ablation front displacement. However, the signals showed fringe movements start corresponding to the end of the laser emission delay. The examples shown in Figure 119 and Figure 120 clearly show the signal displacement around the related emission delay of 514±13 µs. Moreover, the displacement in the opposite direction occurred after the end of the laser emission, as indicated by the end of the laser gate. These two observations were evidence to the fact that another factor within the ablation region caused interference, which was observed attributed to the generated ablation plume.
As a matter of fact, in absence of the side gas, it is plausible that the self-mixing laser beam measures the displacement of the ablation plume. The ablation plume causes change in refraction index locally, causing change in optical distance that is observed as the ascending movement of the fringes, and at the end of the laser emission the ablation region clears out to return to ambient conditions, thus the refraction index returns to the one belonging to the air, which is observed as the descending movement. This is similar to shockwave propagation measurements carried out with probe beam deflection technique. The technique is based on observing the change in the optical power of a laser beam passing through an ablation plume. The increase or decrease optical power is caused by the deflection of the beam toward or away from the target surface. Differently, in the present scheme the laser beam is coaxial to the processing beam and returns to the laser cavity rather than passing through the plume and exiting from the other side; and the observation is based on the self-mixing interference in the laser diode cavity, rather than a measurement based on a photodiode placed on the other side of the plume
To overcome the plausible effects of the ablation plume, side gas parallel to the material surface and perpendicular to the measurement and processing beams was used. Because the ambient air is composed majorly of N_2 molecules, this gas was chosen to not alter the refraction index significantly, and it was preferred over compressed air due to its inert properties. The outcome was the observation of a signal with low amplitude fringes occurring in the descending direction. The start of fringe occurrence coincided with the end of the emission delay of the processing delay. Figure 121 shows an example signal acquired while N_2 side gas at 1 bar was in use. In particular the signal shows 8 fringes in descending direction, showing a displacement of 3.14 µm. The used processing conditions yielded a dimple depth of 3.43 ± 0.5 µm as measured in Chapter 5.

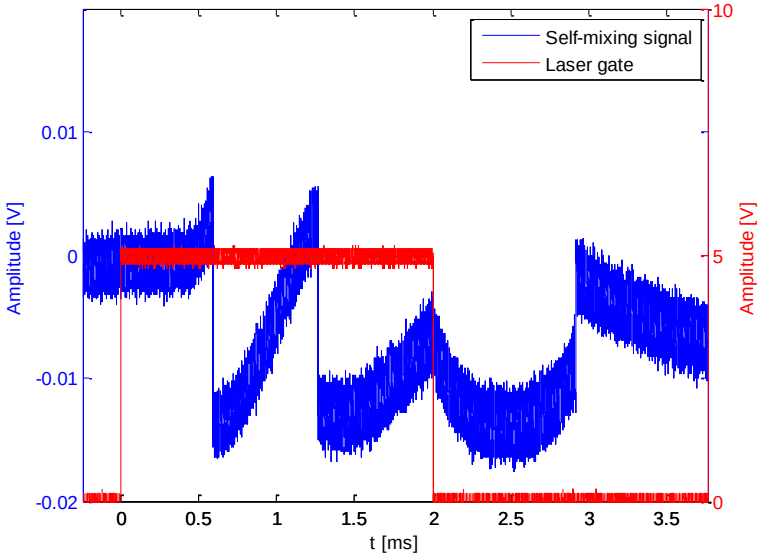

Figure 119. The laser self-mixing signal obtained when drilling without the side gas. Processing laser parameters are E=19.3 µJ, PRR=50 kHz, t_{mod}=2 ms, N_{eff}=75.

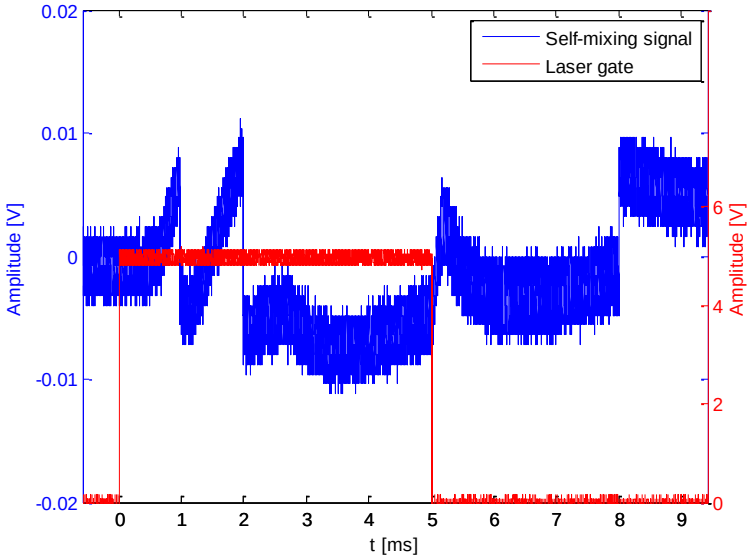

Figure 120. The laser self-mixing signal obtained when drilling without the side gas. Processing laser parameters are E=19.3 µJ, PRR=50 kHz, t_{mod}=5 ms, N_{eff}=188.

The fact that the self-mixing interferometry measurement was in the expected dimple depth range gave way to the further hypothesis on the interaction between the material, processing and measurement beams. It can be expected that the side gas may provide two effects that allow the passage of the measurement beam to observe the dimple bottom,

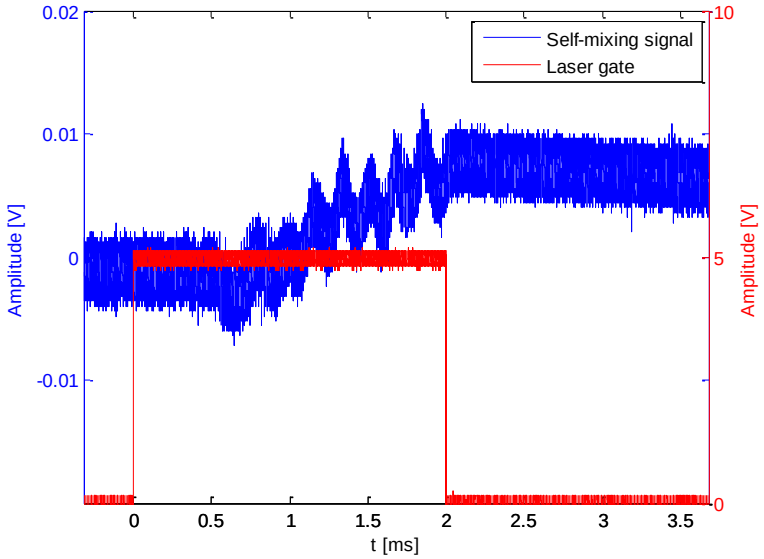

Figure 121. The laser self-mixing signal obtained when drilling with N_2 side gas at 1 bar showing 8 fringes. Processing laser parameters are E=19.3 µJ, PRR=50 kHz, t_{mod}=2 ms, N_{eff}=75.

thus the ablation front displacement. The two effects illustrated schematically in Figure 122 can be summarized as:

- Extinguishing effect: The side gas can maintain a higher ionization threshold, allowing generation of less amount of plasma and the resulting ablation plume could be expected to be less dense, causing minor changes in the refraction index, therefore the measurement beam reaches the dimple bottom without significant coherence loss.
- Deviation effect: The side gas may provide mechanical effect of moving the generated ablation plume away from the dimple opening, allowing the major part of the measurement beam to avoid passing through it. Thus, the change in optical path due to the refraction index change is partially avoided, and the greater part of the measurement beam reaches the bottom of the dimple.

The extinguishing effect would in fact require ambient conditions either free of gas, or inert gases with ionization potentials much higher than the one belonging to air. The ionization potentials of air and N_2 are very similar, being 14.9 eV and 15.6 eV respectively, whereas for instance He has an ionization potential of 24.6 eV [175]. The benefit of using He as an inert side gas has been demonstrated to be highly effective in improving the machining conditions with fs pulses, due to minimising the plasma breakdown [175,176]. In contrast, the use of inert Ar and He side gases resulted in the decrease of machining rate on steel with ns pulses [177]. The authors of the work used a supersonic nozzle directed to the process area, and attributed the reduction in machining rate to the suppression of the ejected material by the action of the gas. In laser welding of

galvanized steel with a CO_2 laser, the use of side gas was demonstrated to effectively reduce the plasma emission and increase welding penetration [178]. The authors pointed out that the gas jet removed ther large diffusive plasma, and allowed the laser beam to penetrate into material without significant loss transmission efficiency of laser energy. it should be noted that the suppressed diffusive plasma plume is characteristically different compared to the plasma plume generated during ablation regarding the dimensions, geometry, and density. Moreover, the ambient gas is not the only source of plasma generation, but the ablated material is expected to ionize and generate plasma as well. However, the removal of the ambient gas should reduce effectively refractive index changes due to gas compression related to wavefront expansion. The plasma emission spectra can contain useful information regarding the changes in the plasma characteristics, especially in terms of temperature and electron number density. Figure 123 reports the emission spectra during laser microdrilling of the TiN coating under different processing and side gas conditions. It can be observed that the spectra exhibit very little difference under different side gas pressure conditions, including its absence. The attempts on analytically calculating the plasma temperature and electron number density were inconclusive, therefore are not reported here. However, the plasma temperature estimates were in the range of 4100 K, while the electron number density was estimated in the range of $1.2 \cdot 10^{13}$ cm^{-3}. It should be noted that these estimates are based on measurements that integrated the emission spectra in space and time.

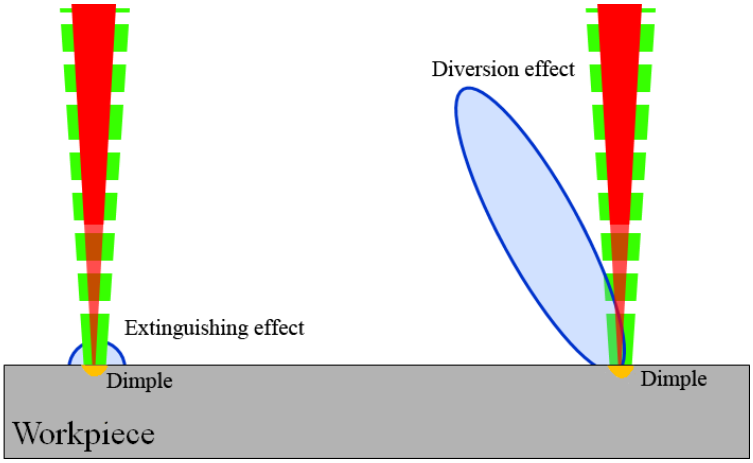

Figure 122. Hypothesized effects of the side gas on the ablation plume.

On the other hand, Dowding and Lawrence reported that the use of a turbulent water flow in close immersion allowed decreasing the ablation threshold of bisphenol A polycarbonate with an excimer laser compared to machining in ambient air [179]. The authors proposed attributed the phenomenon to the distortion of the ablation plume geometry by the flowing immersion fluid in a manner that allowed lower Bremsstrahlung attenuation. Such diversion effect seems to be more plausible for explaining observed phenomenon in the self-mixing interferometry measurements. The extinction of surface

plasma with N_2 seems less likely due to its similar ionization potential compared to air. Furthermore, the ablation plume is expected to be much more ionized compared to the diffusive part of a welding plume, as well as being much smaller in dimension and short-lived. For full comprehension of the exact phenomenon, the hypothesis could be tested via high speed imaging. Combined with techniques such as shadowography [180] or digital holography [181], geometrical changes in the ablation plume as well as the changes in refraction index can be studied spatially.

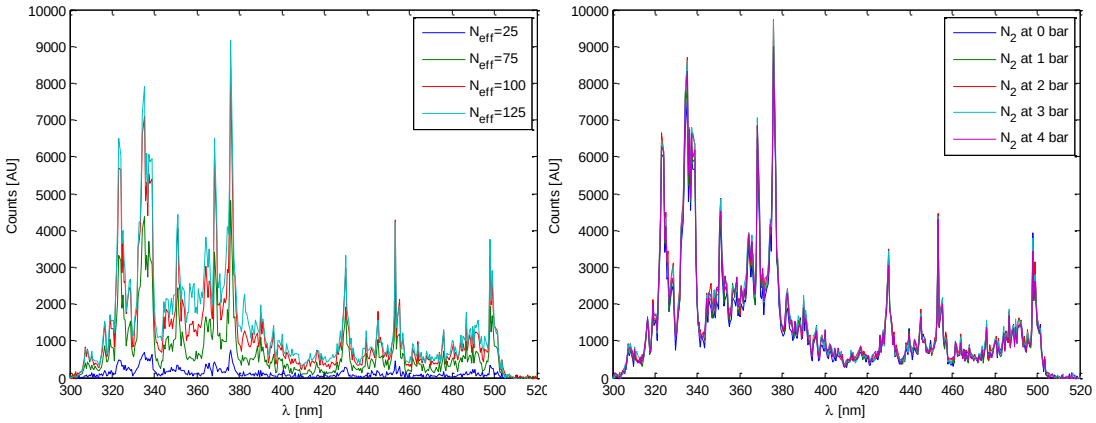

Figure 123. Emission spectra of TiN ablation with different number of effective pulses (N_{eff}) on the left with N_2 at 4 bar, and with different side gas pressure levels on the right with N_{eff}=125. All experiments were carried out with E=19.3 µJ, PRR=50 kHz, and 5 ms of spectroscope integration time.

6.3.2 Decomposition of the self-mixing interferometry signal components

When used in conventional measurement schemes, self-mixing interferometry shows only one signal component belonging to the displacement. This is due to the fact that the measurement beam is much smaller compared to the target. In the case of the measurement scheme to observe the ablation front displacement, the measurement beam passes through and is reflected by different media. Given the fact that the measurement beam has a given energy distribution, the effects of the different media can be observed superimposed on the interferometry signal.
The self-mixing interferometry signals obtained while the side gas was in use showed characteristic components repeatedly. For the sake of better readability of the signals a digital low-pass filter, with filter cut-off frequency at 50 kHz and 3rd order Butterworth window was employed. Figure 124 shows an example of self-mixing interferometry measurement along with the filtered signal. The observations showed superimposed 3 common components that can be listed as the following.

- Low frequency component (0.10-0.25 kHz): An offset of the signal average has been observed within the laser emission range (see Figure 124.a). This offset is

attributed to the presence of the plume, which is partially observed by the interferometer.

- Mid frequency component (2.4-4.0 kHz): This component was the one that carries the information regarding the ablation front displacement. It was visible as fringes with low amplitude (around 10-20 mV) and the shape that tends to lose the fast ascending part, resulting a triangular signal rather than a saw-tooth like one (see Figure 124.b). This is attributed to the fact that the part of the beam reaching the bottom of the dimple is only a portion of the whole intensity distribution. Thus, this signal component possesses a weak feedback parameter (C<1) that is correlated to the reflected beam intensity.
- High frequency component (at *PRR*): This component was visible inside the mid frequency component, in form of very low amplitude (around 4 mV) fringes with saw-tooth like shape (see Figure 124.c). Intriguingly, this component was always in synchrony with the laser pulse repetition rate, thus in 20-300 kHz range. The presence of this contribution was attributed to the perturbations on the expanding plume by the arrival of each new processing pulse. The arrival of a new pulse is expected to cause the generation of another plasma region and expanding wavefront inside the previously formed plume. The high pulse repetition rate of the processing laser permits such phenomenon to occur as the period of pulses varies between 3-50 µs, whereas the laser induced wavefront can expand throughout longer time instances. The change in the optical path due to such perturbations is expected to be much smaller than an equivalent distance to show a complete fringe. Therefore, these high frequency fringes are much smaller in amplitude, but high in feedback factor (C>1). The use of side gas allows the displacement of the perturbed plume, thus the the previously observed high amplitude, high feedback factor fringes do not appear due to plume build up.

Figure 125 shows the conceptual model of the hypothesised system to cause the different components observed in the self-mixing interferometry signals. It should be noted that the energy distribution passing through the deviated plume is relatively larger compared to the portion reaching the dimple bottom. Moreover, the measurement beam is larger than the dimple diameter; therefore a very low portion of the beam is reflected by the material surface.

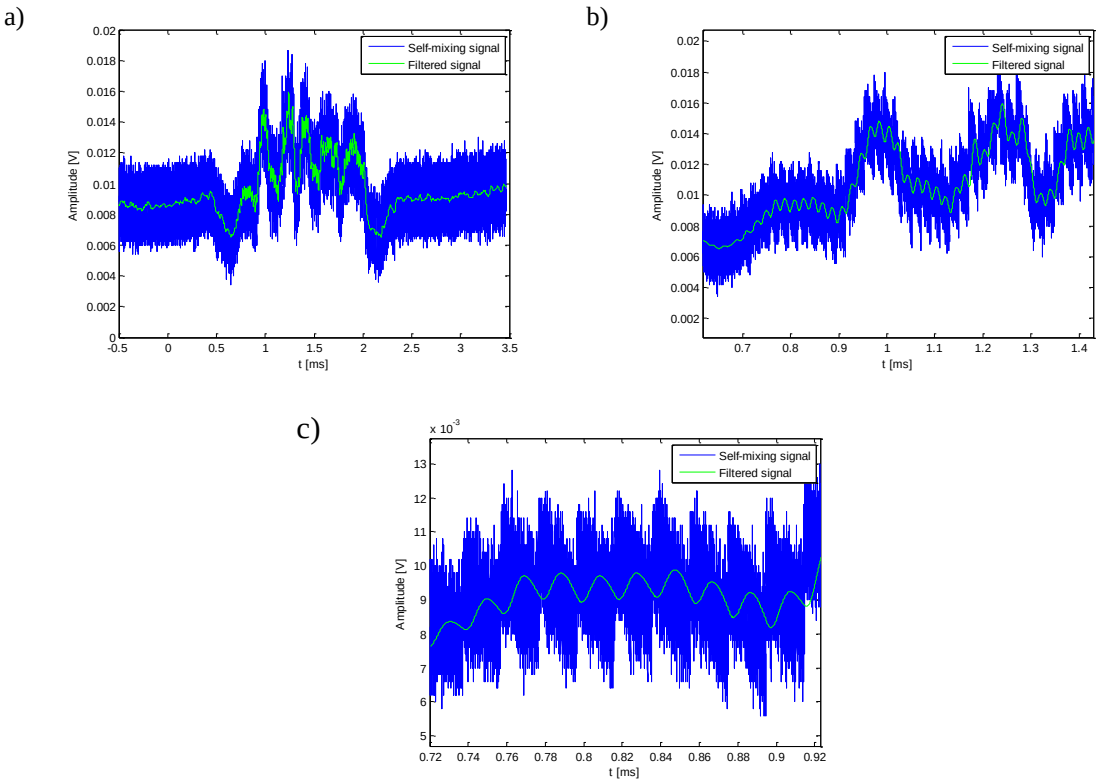

Figure 124. The superimposition of large and small fringes within the self-mixing interferometry signal acquired with N_2 side gas at 1 bar in use. Processing laser parameters are *E*=19.3 µJ, *PRR*=50 kHz, t_{mod}=2 ms, N_{eff}=75

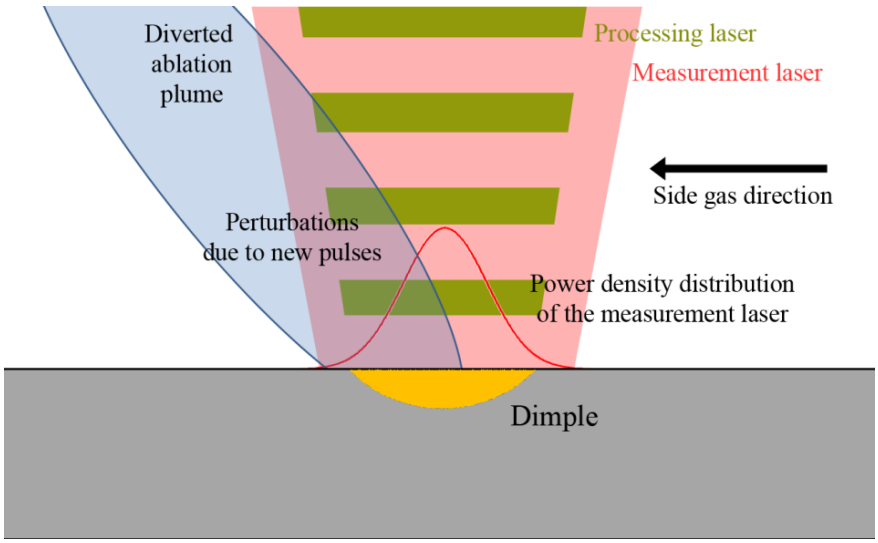

Figure 125. Scheme of the hypothesised conditions during self- mixing interferometry measurement of ablation depth with the use of side gas

6.3.3 Evaluation of the measurement performance with an offline measurement device

The measurement performance of self-mixing interferometry was compared to an industrial measurement device, Alicona InfiniteFocus that is based on the focus variation technique. The device is capable of providing depth resolution down to 0.01 µm, and lateral resolution down to 0.44 µm. The measurement scheme self-mixing interferometry required the use of side gas, whereas the previous measurements were done on dimples microdrilled in ambient atmosphere. Therefore, another group that consisted of dimples drilled with side gas and measured with focus variation microscopy had to be considered for any possible effect of the side gas on the processed depth. The comparison groups in the end were focus variation microscopy on dimples microdrilled without the side gas, focus variation microscopy on dimples microdrilled with the side gas, and self-mixing interferometry on dimples drilled with the side gas. N_2 was used at 1 bar pressure as the side gas. The dimples were drilled with a single combination of processing laser energy and pulse repetition rate, whereas the number of pulses was varied to study increasing depth. Because the comparison groups were realized in different time occasions, they were treated as blocks, with the hypothesis that there is no interaction with the other parameter in the experimental plan. Five replications were made for the conditions using focus variation microscopy. For the self-mixing interferometry condition at least 7 replications were made due to higher variability observed in the acquired signals. Focus variation microscopy acquisitions were made with 50X magnification, and 0.02 µm lateral resolution, the dimple depth was defined as reported in Chapter 5. Whereas for self-mixing interferometry the depth measurement was based on manual fringe counting after a low-pass digital filtering stage (cut-off frequency 50 kHz, with 3rd order Butterworth window). Table 33 summarizes the fixed and varied parameters, along with the measured variable belonging to the employed experimental plan.

Table 33. Experimental design for the comparison of measurement performance of self-mixing interferometry against focus variation microscopy.

Fixed parameters		**Levels**
Pump current %	PI%	100%
Focal height	h_f [mm]	0
Pulse repetition rate	PRR[kHz]	50
Varied parameters		**Levels**
Number of effective pulses	N_{eff}	25, 75, 100, 125
Measurement condition (block)	Type	Focus variation microscopy - without gas Focus variation microscopy – N_2, 1 bar Self-mixing interferometry – N_2, 1 bar
Measured variable		
Dimple depth	h [µm]	

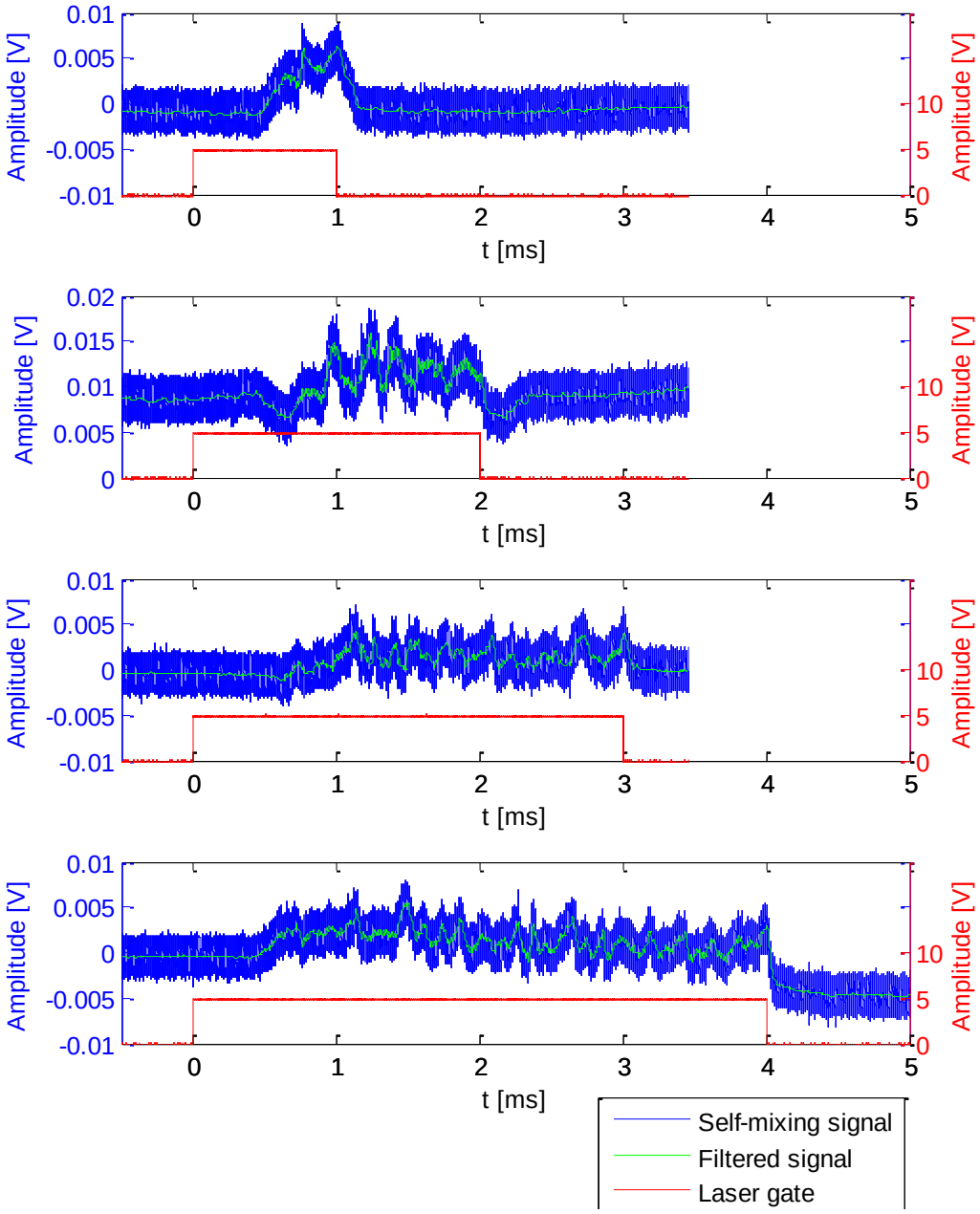

Figure 126. Example self-mixing signals for different laser microdrilling conditions. Signals were filtered with a lowpass filter (cut-off frequency 50 kHz, with 3rd order Butterworth window). t_{mod}=1 ms, N_{eff}=25, 3 fringes; t_{mod}=2 ms, N_{eff}=75, 7 fringes; t_{mod}=3 ms, N_{eff}=125, 15 fringes; t_{mod}=4 ms, N_{eff}=175, 21 fringes.

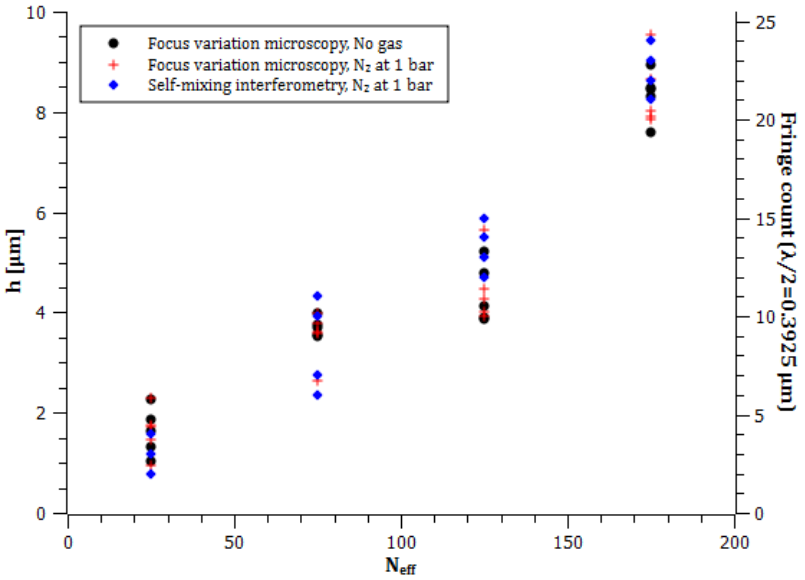

Figure 127. Dimple depth as a function of effective number of pulses and measurement conditions. The ordinate on the right hand side represents the dimple depth in equivalent fringe count.

Table 34. Summary of the Analysis of Variance applied on dimple depth (*h*) as a function of effective pulse number (N_{eff}) and measurement condition (Type).

General Linear Model: h [um] versus N_{eff}, Type

Factor	Type	Levels	Values
N_{eff}	fixed	4	25, 75, 125, 175
Type	fixed	3	FVM - No gas, FVM - N_2 at 1 bar, SMI - N_2 at 1 bar

Analysis of Variance for h [um], using Adjusted SS for Tests

Source	DF	Seq SS	Adj SS	Adj MS	F	P
N_{eff}	3	506.98	501.98	167.33	497.49	0.000
Type	2	0.01	0.01	0.01	0.05	0.978
Error	66	22.20	22.20	0.34		
Total	71	530.62				

S = 0. 58488 R-Sq = 95.75% R-Sq(adj) = 95.42%

Figure 126 shows signal examples from the self-mixing interferometry measurements take with different processing conditions. These signals possess all the signal components with also longer duration of processing laser exposure. The medium frequency fringes carrying the depth information were difficult to observe without filtration especially when the depth increases. Moreover, due to fringe-counting based dimple depth assessment, all conditions showed repetition of the same measured values in different replications.

Figure 127 depicts all the measured dimple depths belonging to different conditions. The dispersion of all the data points suggests that all measurement conditions report the same range of depth. This observation was confirmed by the Analysis of Variance (for the

summary of results see Table 34). The effect of the measurement condition is rejected by a very high p-value (0.978), confirming that both self-mixing interferometry and focus variation based microscopy measurements are statistically the same. Additionally, this confirms that there is no significant effect of the side gas on the drilled hole depth. Additionally, here once again the effect of N_{eff} on the dimple depth is confirmed, especially in terms of the increased material removal rate after the reach of substrate (N_{eff}=125). The capability of ablation depth measurement with self-mixing interferometry is demonstrated in case of changing material layers, which are characterized by different optical properties.

6.4 Possible improvements for enhanced performance of the measurement system

The statistical study confirmed the validity of the self-mixing interferometry measurements. However, it should be noted that the comparison were made on a large quantity of replicates, with a relatively variable process. As a matter of fact, the standard error of the process calculated in the Analysis of Variance was larger than the resolution of the self-mixing interferometer just by a small amount (S=0.585 µm). Moreover, due to restriction, the comparison was based on populations, rather than the same dimples measured by two different devices. Taking these aspects and others that have been observed during experimentation into account, some proposals for the enhanced performance of the measurement system can be listed as the following.

6.4.1 Temporal and spatial resolution

The temporal resolution can be regulated for the given application by changing the bandwidth of the interferometer electronics. It has been observed that the used bandwidth was more than necessary for the present laser microdrilling conditions. Smaller bandwidth is favourable for reduced noise and improved amplitude. Figure 128 shows preliminary studies with a 1 MHz bandwidth self-mixing interferometer with 785 nm wavelength. The observed signal amplitude is up to 20 times higher than the ones observed with 35 MHz bandwidth. The intrinsic removal of noise component allows measurement of the interference signal with a better definition. In this scheme, the medium frequency fringes still show lower and the high frequency fringes show higher feedback parameters. Considering applications with higher material removal rate bandwidth is still required to be high. However, regarding applications with high removal rate and high drilling depth, such as microdrilling of turbine blades, longer interferometer wavelengths can be used to reduce the required wavelength. The increased wavelength would naturally lower the resolution, but compared to the dimple depth it would still remain high. System flexibility can be improved with on-device control of the bandwidth. On the other hand, the depth resolution is hard to be improved by using wavelengths than the one applied in this study. It is possible to interfere with the plasma emission in visible-

UV bandwidth range. There are not commercially available laser diodes operating with wavelengths in deep UV region, but this consideration is not also viable due to high absorption of the beam in ambient air. Spatial resolution can be improved by signal processing, but this requires much cleaner self-mixing signals.

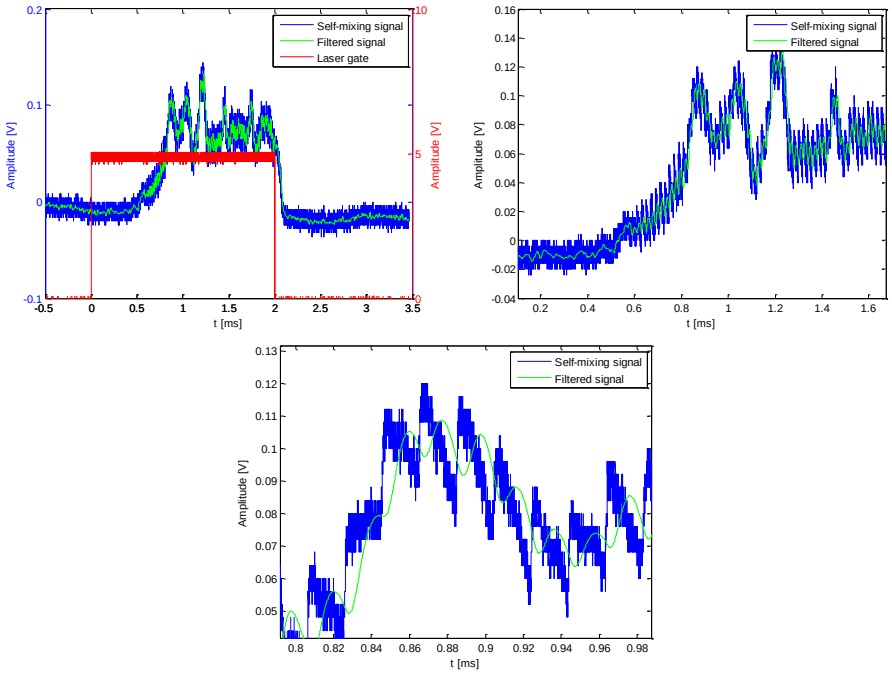

Figure 128. Details of a self-mixing signal obtained with 1 MHz bandwidth, increased amplification, and improved signal to noise ratio showing 8 fringes of displacement for ablation front (top row). The small fringes occurring at the laser pulse repetition rate due to plume perturbation appear much clearer (bottom row). Processing laser parameters are E=19.3 µJ, PRR=50 kHz, t_{mod}=2 ms, N_{eff}=75.

6.4.2 Measurement stability

Although the self-mixing architecture allows much easier operation compared to conventional interferometers, it requires improved stability for operation in industrial environments. The laser diodes change emission wavelength during operation due to change in laser case temperature, injection current change, and optical feedback (back-reflection in cavity). Moreover, this phenomenon manifests in a non-linear fashion called mode-hopping. The laser wavelength hops from an emission wavelength to the other rather than a continuous increase or decrease. The range of emission wavelength change is about ±10 nm, which can be also neglected for given applications. However, mode hopping causes the loss of self-mixing signal. It should be reminded that the self-mixing interferometry is based on optical feedback, therefore the sudden changes in the reflectivity of the ablated material can cause mode-hopping during measurement. The diaphragm that is used to regulate the amount of optical feedback can be set to let only a

conservative amount of optical feedback, but this results in lower signal amplitude in return. However, the most important factor that determines the measurement stability is the use of side gas. The side gas has to be well aligned to the ablation spot, and should not cause deflections or vibrations on the material. Gases with considerably different refraction indexes compared to air have been observed to cause self-mixing fringes without any movement. The applicability of ventilation systems that are conventionally used to suck the ablation fumes from the processing zone should be also investigated to induce a similar effect caused by the side gas. Opto-mechanical design plays critical role on the effective operation. The proposed system resolves many of the problems; however the alignment of the self-mixing interferometry beam is a too delicate operation for industrial environments. Ideally, the two beams can be launched to the same delivery fibre and focused through an achromatic lens.

Chapter 7

Conclusions

In the present work processing and monitoring strategies for laser surface texturing of TiN coatings have been reported. The micromachining conditions constituted complications due to very limited coating thickness (2-5 µm), and the differences between the material properties of the substrate and coating. Therefore the main aim of the work was to control the ablation depth via processing parameters and measure this quantity via an online monitoring method. These two main parts of the thesis dealt with:

- Development of processing strategies with 3 different ns pulsed fibre laser sources covering 1-250 ns pulse duration region with 0.5 µm and 1 µm wavelengths.
- Development of self-mixing interferometry system to measure the ablation depth during laser percussion drilling to provide means for online process monitoring in laser surface texturing

The results regarding the laser micromachining performance of ns pulsed fibre lasers have confirmed the feasibility of obtaining high quality dimples on ceramic coatings with accurate control of processing depth. Dimples with diameters between 20-60 µm were achieved without damaging the coating material with the substrate contamination. When machining beyond the coating thickness, high quality dimples without dross generation was achieved with 1-12 ns pulses. It has been confirmed that the developed processing strategy depends highly on the automation possibilities and the used beam manipulation system. The highly energetic Q-switched system that generated 250 ns pulses was used in a non-conventional manner to obtain pseudo single pulses. Although this approach enabled the feasibility of accurate depth control with the laser, the productivity was reduced compared to less energetic pulse duration variable and long ns MOPA systems. The new generation fibre laser sources enable better automation with faster responding electronics and more sophisticated control schemes, such as pulse synchronization output. Such schemes will be useful for LST of large surfaces with high throughput.

However, the employed processing strategies can be extended to be used on other materials, metallic, polymeric, or dielectric depending on their absorption to the used wavelengths. The strategies can be essentially useful for applications requiring good control in ablation depth with low aspect ratio dimples, and high precision in the spacing of dimples without compromising the productivity. Some other potential application fields are biomedicine, for the texturing of implants to improve adhesion with surface coating to be applied on the device or the body tissue itself; and

aerospace for the improvement of adhesion joint strength of multi layered sandwich-type composites.

It has been observed that pulse durations around 1-12 ns seem to avoid melt generation, whereas longer pulses improve throughput. Pulse tunability therefore appears as an important feature for the next generation laser sources. Inter-pulse interaction is another field that requires further attention, as the results reported here also show substantial differences in multiple pulse machining compared to single pulses. Flexible pulse shape definition, use of different pulse durations and shapes with the pulse train, and shaping the energy content of the whole train are features that are expected to improve machining capabilities. The spatial shape of the laser beam is also another factor that will impact the machining flexibility and quality in the near future. The addition of these new parameters will open up further capabilities in laser micromachining, and ns pulsed lasers are expected to benefit from these features faster than the ultra-short pulsed systems due to simpler architecture.

In terms of industrial application the architecture of fibre laser enables various possibilities for the system integration. The up-scaling of this LST of large areas, such as engine cylinder blocks or machine tool guides, is conveniently possible by employing beam sharing with a single high energy fibre laser source and multiple scanning heads. The scanning heads can be further integrated to Cartesian axes, or robotic arms to cover larger areas without the use of complicated optical paths. Curved or free-form surfaces can be textured with the integration of rotary axes to follow the surface geometry. This would enable texturing stamps and dies with complex geometries.

A self-mixing interferometry system with 0.4 μm depth and 29 ns time resolution was designed and implemented for ablation depth monitoring. The use the system for measuring the displacement of the ablation front was validated in fast ablation conditions with limited machining depth. The critical point in the measurement remains with the fact that the used coherence detection method is prone to disturbances caused by the turbid media around the ablation zone. The problem has been resolved by the use of a side gas jet, which is expected to divert the ablation plume and allow the measurement beam to pass into the drilled microhole. Another possible explanation to the effect of the side gas is the extinguishing effect, however it is found to be less likely due to the similarity of the used gas type (N_2) compared to air in terms of plasma threshold. However, the thesis could not reach a conclusion on the effect of the side gas. Possible approaches to validate the hypotheses of ablation plume extinguishing or diversion effects have been made, which can be addressed in future works. This fact limits the proper understanding of the physical phenomenon that obstructs the functioning of the monitoring device. Although it has not been the primary concern of the work, it is duly noted that an immediate integration of the monitoring system in an industrial environment does not seem possible. For robust functioning of the system, alignment sensitivity of the two beams has to be also confronted.

As mentioned in Chapter 2, the thesis work involved different research groups as partners for the development of LST to improve tribological performance and the development of the monitoring device. Within the collaborative efforts the performance of the laser surface textured TiN coatings were evaluated. The results of these studies are published elsewhere [182-184]. A brief summary of the principal results of these works can be found in Appendix D. The collaborative research also enabled the development of high performance self-mixing interferometers with large bandwidth. The device is expected to be useful for other applications requiring sub µs measurement resolution.

In conclusion, future works that need to be addressed can be listed as the following:

- On the fly machining with high positioning and machining accuracy for number of dimples per unit time to kHz level
- Integration of laser micromachining to 5-axis machining systems or anthropomorphic robots for free form laser surface texturing
- Study of the ablation phenomenon to reveal the effects obstructing the functionality of the self-mixing interferometer
- Close loop control of laser micromachining by integrating the interferometry signal to the automation system.

SITEC micromachining booth, September 2013.

References

[1] J.M. Liu, 1982. Simple technique for measurements of pulsed Gaussian-beam spot sizes, Optics Letters 7 (5), 196-198

[2] Y. Jee, M.F. Becker, R.M. Walser, 1988. "Laser-induced damage on single-crystal metal surfaces," Journal of the Optical Society of America. B, 5(3), 648-659

[3] G. Giuliani, M. Norgia, S. Donati, and T. Bosch, 2002. "Laser diode self-mixing technique for sensing applications," J. Opt. A Pure Appl. Opt., 4 (6), S283–S294

[4] D.C. Montgomery, 2001, Design and Analysis of Experiments, 5th Ed., John Wiley & Sons, New York

[5] W.H. Greene, 2012, Econometric Analysis, 7th Ed., Prentice Hall, New Jersey

[6] User manual of Minitab 16.2.4, Minitab Inc., Pennsylvania

[7] A. Schoenfelder, 1999. Fiber lasers address micromachining methods, Laser Focus World, 35 (6), 95-101

[8] R.C.P. Wong, A.P. Hoult, J.K. Kim, T.X. Yu, 1997. "Improvement of adhesive bonding in aluminium alloys using a laser surface texturing process," Journal of Materials Processing Technology 63 (1-3), 579–584

[9] I. Etsion, 2000. "Improving tribological performance of mechanical seals by laser surface texturing," Proceedings of 17th International Pump Users Symposium 17-21

[10] B. N. Chichkov, C. Momma, S. Nolte, F. von Alvensleben, A. Tünnermann, 1996. "Femtosecond, picosecond and nanosecond laser ablation of solids," Applied Physics A, 63, 109-115.

[11] W. Schultz, E. Eppelt, R. Poprawe, 2013. "Review on laser drilling I. Fundamentals, modeling, and simulation," Journal of Laser Applications, 25 (1), 012006-1 - 012006-17

[12] J. Cheng, C. Liu, S. Shang, D. Liu, W. Perrie, G. Dearden, K. Watkins, 2013. "A review of ultrafast laser materials micromachining," Optics & Laser Technology 46 (2013) 88–102

[13] M. Fox, 2001, Optical Properties of Solids, Oxford University press, New York

[14] A. Schlegel., P. Wachter, J.J. Nickl., H. Lingg, 1977. Optical properties of TiN and ZrN, J. Phys. C: Solid State Phys.10, 4889-4896

[15] H. Huegel, F. Dausinger, 1998. Handbook of the Euro-Laser Academy, Volume 2, 1st Edition

[16] W.M. Steen, 2003. Laser Material Processing, 3rd Ed., Springer-Verlag, London

[17] D. Lin, S.U. Alam, A. Malinowski, K.K. Chen, J.R. Hayes, J.C. Flannagan, V. Geddes, J. Nilsson, S. Ingram, S. Norman, D.J. Richardson, 2011. "Temporally and spatially shaped fully-fiberized ytterbium-doped pulsed MOPA," Laser Physics Letters, 8 (10), 747–753

[18] W. O'Neill, K. Li, 2009. "High-Quality Micromachining of Silicon at 1064 nm Using a High-Brightness MOPA-Based 20-W Yb Fiber Laser," IEEE Journal Of Selected Topics In Quantum Electronics, 15 (2), 462-470

[19] K. Li, W. O'Neill, 2012. "Fibre Laser Microvia Drilling and Ablation of Si with Tuneable Pulse Shapes," International Journal of Precision Engineering and Manufacturing, 13 (5), 641-648

[20] K. Pangovski, W. O'Neill, P.S. Teh, S. Alam, D. Richardson, A.G. Demir, 2012. "Designer Pulses For Precise Machining of Silicon – A Step Towards Photonic Compositions," Proceedings of 31st International Congress on Applications of Lasers & Electro-Optics ICALEO 2012, 999 – 1008

[21] S. Eiselen, D. Wu, P. Galarneau, M. Schmidt, 2013. "The role of temporal energy input in laser micro machining using nanosecond pulses," Physics Procedia 41, 676 – 681

[22] I. Etsion, 2005. "State of the Art in Laser Surface Texturing," J. Tribol., 127 1, 248

[23] A. Erdemir, 2005. "Review of engineered tribological interfaces for improved boundary lubrication," Tribol. Int., 38, 249–256

[24] M. Geiger, S. Roth, W. Becker, 1998. "Influence of laser-produced microstructures on the tribological behaviour of ceramics," Surf. Coatings Technol., 100–101, 17–22

[25] M. Wakuda, Y. Yamauchi, S. Kanzaki, Y. Yasuda, 2003. "Effect of surface texturing on friction reduction between ceramic and steel materials under lubricated sliding contact," Wear, 254 (3–4), 356–363

[26] S. Schreck and K.-H. Zum Gahr, 2005. "Laser-assisted structuring of ceramic and steel surfaces for improving tribological properties," Appl. Surf. Sci., 247, (1–4), 616–622

[27] X. Wang, K. Adachi, K. Otsuka, K. Kato, 2006. "Optimization of the surface texture for silicon carbide sliding in water," Appl. Surf. Sci., 253 (3), 1282–1286,

[28] T. Nanbu, N. Ren, Y. Yasuda, D. Zhu, Q. J. Wang, 2008. "Micro-Textures in Concentrated Conformal-Contact Lubrication: Effects of Texture Bottom Shape and Surface Relative Motion," Tribol. Lett., 29 (3), 241–252

[29] H. Yu, X. Wang, F. Zhou, 2009 "Geometric Shape Effects of Surface Texture on the Generation of Hydrodynamic Pressure Between Conformal Contacting Surfaces," Tribol. Lett., 37 (2), 123–130

[30] E. Gualtieri, A. Borghi, L. Calabri, N. Pugno, S. Valeri, 2009. "Increasing nanohardness and reducing friction of nitride steel by laser surface texturing," Tribol. Int., 42 (5), 699–705

[31] L. M. Vilhena, M. Sedlaček, B. Podgornik, J. Vižintin, A. Babnik, J. Možina, "Surface texturing by pulsed Nd:YAG laser," 2009. Tribol. Int., 42 (10), 1496–1504

[32] Y. Wan, D. Xiong, J. Wang, "Tribological properties of dimpled surface alloying layer on carbon steel," J. Wuhan Univ. Technol. Sci. Ed., 24, 2, 218–222, Jul. 2009.
[33] L. M. Vilhena, B. Podgornik, J. Vižintin, J. Možina, "Influence of texturing parameters and contact conditions on tribological behaviour of laser textured surfaces," Meccanica, 46, 3, 567–575, Jun. 2010.
[34] J. Eichstädt, G. R. B. E. Römer, A. J. H. in't Veld, 2011. "Towards Friction Control using laser-induced periodic Surface Structures," Phys. Procedia, 12, 7–15
[35] J. Van Kuilenburg, M. A. Masen, M. N. W. Groenendijk, V. Bana, E. Van Der Heide, 2012. "Tribology International An experimental study on the relation between surface texture and tactile friction," Tribol. Int., 48, 15–21
[36] I. Etsion, L. Burstein, 1996. "Improving tribological performance of piston rings by partial surface texturing," Tribol. Trans, 127, 632–638
[37] Y. Kligerman, I. Etsion, 2001. "Analysis of the Hydrodynamic Effects in a Surface Textured Circumferential Gas Seal," Tribol. Trans., 44 (3), 472–478
[38] G. Ryk, Y. Kligerman, I. Etsion, 2002. "Experimental Investigation of Laser Surface Texturing for Reciprocating Automotive Components," Tribol. Trans., 45 (4), 444–449
[39] I. Etsion, G. Halperin, V. Brizmer, Y. Kligerman, 2004 "Experimental investigation of laser surface textured parallel thrust bearings," Tribol. Lett., 17 (2), 295–300
[40] I. Etsion, 2004. "Improving tribological performance of mechanical components by laser surface texturing," Tribol. Lett., 17 (4), 733-737
[41] G. Ryk, I. Etsion, A. Shinkarenko, 2005. "Experimental investigation of partial surface texturing for piston ring friction reduction," Tribol. Trans.,48 (4), 583–588
[42] Y. Feldman, Y. Kligerman, I. Etsion, 2006. "A Hydrostatic Laser Surface Textured Gas Seal," Tribol. Lett., 22 (1), 21–28
[43] G. Ryk I. Etsion, 2006. "Testing piston rings with partial laser surface texturing for friction reduction," Wear, 261 (7–8), 792–796
[44] Y. Feldman, Y. Kligerman, I. Etsion, 2007. "Stiffness and Efficiency Optimization of a Hydrostatic Laser Surface Textured Gas Seal," J. Tribol., 129 (2), 407
[45] Y. Wan, D.-S. Xiong, 2008. "The effect of laser surface texturing on frictional performance of face seal," J. Mater. Process. Technol., 197 (1–3), 96–100
[46] A. Borghi, E. Gualtieri, D. Marchetto, L. Moretti, S. Valeri, 2008. "Tribological effects of surface texturing on nitriding steel for high-performance engine applications," Wear, 265 (7–8), 1046–1051
[47] I. Etsion, E. Sher, 2009. "Improving fuel efficiency with laser surface textured piston rings," Tribol. Int., 42 (4), 542–547

[48] V. G. Marian, D. Gabriel, G. Knoll, S. Filippone, 2011. "Theoretical and Experimental Analysis of a Laser Textured Thrust Bearing," Tribol. Lett., 44 (3), 335–343,.
[49] Z. Wang, L. Gu, L. Li, 2013. "Experimental studies on the overall efficiency performance of axial piston motor with a laser surface textured valve plate," Proc. Inst. Mech. Eng. Part B J. Eng. Manuf., 227 (7), 1049–1056
[50] N.G. Semaltianos, W. Perrie, P. French, M. Sharp, G. Dearden, K.G. Watkins, 2008. "Femtosecond laser surface texturing of a nickel-based superalloy," Applied Surface Science 255, 2796–2802
[51] M. Geiger, U. Popp, U. Engel, 2002. "Excimer Laser Micro Texturing of Cold Forging Tool Surfaces," CIRP Ann. - Manuf. Technol., 51 (1), 231–234
[52] D. Du, Y. F. He, B. Sui, L. J. Xiong, H. Zhang, 2005. "Laser texturing of rollers by pulsed Nd:YAG laser," J. Mater. Process. Technol., 161 (3), 456–461
[53] U. Popp, U. Engel, 2006. "Microtexturing of Cold-Forging Tools - Influence on Tool Life," Proc. Inst. Mech. Eng. Part B J. Eng. Manuf., 220 (1), 27–33
[54] P. Andersson, J. Koskinen, S. Varjus, Y. Gerbig, H. Haefke, S. Georgiou, B. Zhmud, W. Buss, 2007. "Microlubrication effect by laser-textured steel surfaces," Wear, 262 (3–4), 369–379
[55] K. Wagner, R. Völkl, U. Engel, 2008. "Tool life enhancement in cold forging by locally optimized surfaces," J. Mater. Process. Technol., 201 (1–3), 2–8
[56] N. Kawasegi, H. Sugimori, H. Morimoto, N. Morita, I. Hori, 2009. "Development of cutting tools with microscale and nanoscale textures to improve frictional behavior," Precis. Eng., 33 (3), 248–254
[57] P. W. Butler-Smith, D. A. Axinte, M. Daine, 2009. "Preferentially oriented diamond micro-arrays: A laser patterning technique and preliminary evaluation of their cutting forces and wear characteristics," Int. J. Mach. Tools Manuf., 49 (15), 1175–1184
[58] J. Xuan, C. Shih, Z. Pan, T. Nguyen, S. Yang, 1999. "Optimization of bump shape and pattern in laser-texture design for improving media tribological performances," IEEE Trans. Magn., 35, (5), 2436–2438
[59] B. Raeymaekers, I. Etsion, F. Talke, 2007. "Reducing the Magnetic Tape/Guide Friction Coefficient by Laser Surface Texturing: Experimental Analysis," in Proceedings of the STLE/ASME International Joint Tribology Conference IJTC2007, 1–3
[60] J. Yu, J. Zhang, I. Boyd, 2001. "Laser-assisted mechanical texturing of magnetic media," Appl. Phys. A Mater. Sci. Process., 72 (6), 687–690
[61] U. P. Hausmann, P. Joerges, J. Heinzl, F. E. Talke, 2009. "Nano-texturing of magnetic recording sliders via laser ablation," Microsyst. Technol., 15, (10–11), 1747–1751
[62] T. Velasquez, H. Peidong, J. Cao, K. F. Ehmann, 2013. "Feasibility of Laser Surface Texturing for Friction Reduction in Surgical Blades," in Proceedings of

the ASME 2013 International Manufacturing Science and Engineering Conference MSEC2013, 1–9.

[63] G. Dumitru, V. Romano, Y. Gerbig, H. P. Weber, H. Haefke, 2005. "Femtosecond laser processing of nitride-based thin films to improve their tribological performance," Appl. Phys. A, 80 (2), 283–287

[64] A.A. Voevodin J. S. Zabinski, 2006. "Laser surface texturing for adaptive solid lubrication," Wear, 261 (11–12), 1285–1292,

[65] L. Rapoport, a. Moshkovich, V. Perfilyev, I. Lapsker, G. Halperin, Y. Itovich, I. Etsion, 2008. "Friction and wear of MoS_2 films on laser textured steel surfaces," Surf. Coatings Technol., 202 (14), 3332–3340

[66] D. Wan, B. Chen, Y. Shao, S. Wang, D. Hu, 2008. "Microstructure and mechanical characteristics of laser coating–texturing alloying dimples," Appl. Surf. Sci., 255 (5), 3251–3256,

[67] H. Liu, D. Wan, D. Hu, 2009. "Microstructure and wear behavior of laser-textured and micro-alloyed Co-based WC and TiC composite sintered-carbide coating," J. Mater. Process. Technol., 209 (2), 805–810

[68] L. Rapoport, a. Moshkovich, V. Perfilyev, a. Gedanken, Y. Koltypin, E. Sominski, G. Halperin, I. Etsion, 2009. "Wear life and adhesion of solid lubricant films on laser-textured steel surfaces," Wear, 267 (5–8), 1203–1207

[69] J. Li, D. Xiong, J. Dai, Z. Huang, R. Tyagi, 2010. "Effect of surface laser texture on friction properties of nickel-based composite," Tribol. Int., 43 (5–6), 1193–1199

[70] Y. Wan, D. Xiong, J. Li, 2010. "Cooperative effect of surface alloying and laser texturing on tribological performance of lubricated surfaces," J. Cent. South Univ. Technol., 17, 906–910

[71] J. Deng, W. Song, H. Zhang, P. Yan, A. Liu, 2011. "Friction and wear behaviors of the carbide tools embedded with solid lubricants in sliding wear tests and in dry cutting processes," Wear, 270 (9–10), 666–674

[72] A. H. Garrido, R. González, M. Cadenas, a. H. Battez, 2011. "Tribological behavior of laser-textured NiCrBSi coatings," Wear, 271 (5–6), 925–933,

[73] D. Jianxin, W. Ze, L. Yunsong, Q. Ting, C. Jie, 2012. "Performance of carbide tools with textured rake-face filled with solid lubricants in dry cutting processes," Int. J. Refract. Met. Hard Mater., 30 (1), 164–172

[74] T. Hu, Y. Zhang, L. Hu, 2012. "Tribological investigation of MoS_2 coatings deposited on the laser textured surface," Wear, 278–279, 77–82

[75] L.M. Galantucci, A. Gravina, G. Chita, M. Cinquepalmi, 1996. "Surface treatment for adhesive-bonded joints by excimer laser". Composites Part A 27A (1996) 1041-1049

[76] P. Molitor, T. Young, 2004. "Investigations into the use of excimer laser irradiation as a titanium alloy surface treatment in a metal to composite adhesive bond," International Journal of Adhesion & Adhesives 24, 127–134

[77] E.G. Baburaj, D. Starikovb, J. Evans, G.A. Shafeev, A. Bensaoula, 2007. "Enhancement of adhesive joint strength by laser surface modification". International Journal of Adhesion & Adhesives 27, 268–276
[78] C. Spadaro, C. Sunseri, C. Dispenza, 2007. "Laser surface treatments for adhesion improvement of aluminium alloys structural joints". Radiation Physics and Chemistry 76, 1441–1446
[79] H.C. Man, K.Y. Chiu, X. Guo, 2010. "Laser surface micro-drilling and texturing of metals for improvement of adhesion joint strength". Applied Surface Science 256, 3166–3169
[80] A. Lamraoui, S. Costil, C. Langlade, C. Coddet, 2010. "Laser surface texturing (LST) treatment before thermal spraying: A new process to improve the substrate-coating adherence". Surface & Coatings Technology 205, S164–S167
[81] A. Samad-Zadeh, M. Harsono, A. Belikov, K. V Shatilova, A. Skripnik, P. Stark, C. Egles, G. Kugel, 2011. "The influence of laser-textured dentinal surface on bond strength.," Dent. Mater., 27 (10), 1038–44
[82] M. Abbott J. Cotter, 2006. "Optical and electrical properties of laser texturing for high-efficiency solar cells," *Prog. Photovoltaics Res. Appl.*, 14 (3), 225–235
[83] I. A. Palani, 2010. "Investigation on Laser-annealing and Subsequent Laser-nanotexturing of Amorphous Silicon (a-Si) Films for Photovoltaic Application," *J. Laser Micro/Nanoengineering*, 5 (2), 150–155
[84] V.V. Iyengar, B. K. Nayak, K. L. More, H. M. Meyer, M. D. Biegalski, J. V Li, M. C. Gupta, 2011. "Properties of ultrafast laser textured silicon for photovoltaics," *Sol. Energy Mater. Sol. Cells*, 95 (10), 2745–2751
[85] B. K. Nayak, M. C. Gupta, K. W. Kolasinski, 2007. "Ultrafast-laser-assisted chemical restructuring of silicon and germanium surfaces," *Appl. Surf. Sci.*, 253, (15), 6580–6583
[86] B. K. Nayak, M. C. Gupta, K. W. Kolasinski, 2007. "Formation of nano-textured conical microstructures in titanium metal surface by femtosecond laser irradiation," *Appl. Phys. A*, 90 (3), 399–402
[87] B. K. Nayak, M. C. Gupta, K. W. Kolasinski, 2007. "Spontaneous formation of nanospiked microstructures in germanium by femtosecond laser irradiation," *Nanotechnology*, 18 (19), 195302 B. K. Nayak M. C. Gupta, 2010. "Self-organized micro/nano structures in metal surfaces by ultrafast laser irradiation," *Opt. Lasers Eng.*, 48 (10), 940–949
[88] V. Iyengar, B. Nayak, M. Gupta, 2010. "Ultralow reflectance metal surfaces by ultrafast laser texturing," *Appl. Opt.*, 49 (31), 5983-5987
[89] B.K. Nayak, M.C. Gupta, 2010. "Self-organized micro/nano structures in metal surfaces by ultrafast laser irradiation," Opt. Lasers Eng., 48 (10), 940–949,
[90] J.L. Ricci, H. Alexander, 2001. "Laser Microtexturing of Implant Surfaces for Enhanced Tissue Integration," Key Engineering Materials, 179, 198–199

[91] N. Mirhosseini, P. L. Crouse, M. J. J. Schmidth, L. Li, D. Garrod, "Laser surface micro-texturing of Ti–6Al–4V substrates for improved cell integration," Appl. Surf. Sci., 253, 19, 7738–7743, Jul. 2007.
[92] A. Y. Fasasi, S. Mwenifumbo, N. Rahbar, J. Chen, M. Li, A. C. Beye, C. B. Arnold, W. O. Soboyejo, 2009. "Nano-second UV laser processed micro-grooves on Ti6Al4V for biomedical applications," Mater. Sci. Eng. C, 29 (1), 5–13
[93] J. Lu, C. Yang, L. Zhang, A. Feng, Y. Jiang, 2009. "Mechanical Properties and Microstructure of Bionic Non-Smooth Stainless Steel Surface by Laser Multiple Processing," J. Bionic Eng., 6 (2), 180–185
[94] H. C. Man, Q. Wang, X. Guo, 2010. "Laser surface microdrilling of Ti and laser gas nitrided Ti for enhancing fixation of dental implants," Opt. Lasers Eng., 48, (5), 583–588
[95] S. Çelen, C. Efeoğlu, H. Özden, 2011. "Pulsed Laser-Induced Micro-Pits: As Bone Stabilizers," Phys. Procedia, 12, 245–251
[96] D. G. Waugh, J. Lawrence, E. M. Brown, 2012. "Osteoblast cell response to a CO_2 laser modified polymeric material," Opt. Lasers Eng., 50.(2), 236–247
[97] D. G. Waugh, J. Lawrence, 2011. "Wettability and osteoblast cell response modulation through UV laser processing of nylon 6,6," Appl. Surf. Sci., 257 (21), 8798–8812
[98] A.-M. Kietzig, S. G. Hatzikiriakos, P. Englezos, 2009. "Patterned superhydrophobic metallic surfaces.," Langmuir, 25 (8), 4821–7
[99] M. Silvennoinen, 2010. "Controlling the Hydrophobic Properties of Material Surface Using Femtosecond Ablation," J. Laser Micro/Nanoengineering, 5 (1), 97–98
[100] P. Bizi-Bandoki, S. Benayoun, S. Valette, B. Beaugiraud, E. Audouard, 2011. "Modifications of roughness and wettability properties of metals induced by femtosecond laser treatment," Appl. Surf. Sci., 257 (12), 5213–5218
[101] W. Guo, Z. B. Wang, L. Li, D. J. Whitehead, B. S. Luk'yanchuk, Z. Liu, "Near-field laser parallel nanofabrication of arbitrary-shaped patterns," Appl. Phys. Lett., 90, 24, p. 243101, 2007.
[102] Z. Wang, W. Guo, A. Pena, D. J. Whitehead, B. S. Luk'yanchuk, L. Lin, Z. Liu, Y. Zhou, M. H. Hong, "Laser micro/nano fabrication in glass with tunable-focus particle lens array," Opt. Express, 16, 24, 19706–19711, 2008.
[103] L. Li, W. Guo, Z. B. Wang, Z. Liu, D. Whitehead, B. Luk'yanchuk, "Large-area laser nano-texturing with user-defined patterns," J. Micromechanics Microengineering, 19, 5, p. 054002, May 2009.
[104] Y. Zhou, T. Shao, L. Yin, "A method of micro laser surface texturing based on optical fiber focusing," Laser Phys., 19, 5, 1061–1066, May 2009.
[105] J. Huang, S. Beckemper, A. Gillner, K. Wang, "Tunable surface texturing by polarization-controlled three-beam interference," J. Micromechanics Microengineering, 20, 9, p. 095004, Sep. 2010.

[106] A. F. Lasagni, T. Roch, D. Langheinrich, M. Bieda, A. Wetzig, 2011. "Large Area Direct Fabrication of periodic Arrays using Interference Patterning," Phys. Procedia, 12, 214–220

[107] V. Oliveira, N. I. Polushkin, O. Conde, R. Vilar, 2012. "Optics & Laser Technology Laser surface patterning using a Michelson interferometer and femtosecond laser radiation," Opt. Laser Technol., 44, 7, 2072–2075

[108] R. J. Beck, J. P. Parry, W. N. MacPherson, A. Waddie, N. J. Weston, J. D. Shephard, D. P. Hand, 2010. "Application of cooled spatial light modulator for high power nanosecond laser micromachining," Opt. Express, 18, 16, 17059–17065

[109] J. P. Parry, R. J. Beck, J. D. Shephard, D. P. Hand, 2011. "Application of a liquid crystal spatial light modulator to laser marking," Appl. Opt., 50, 12, 1779–1785

[110] M. Silvennoinen, J. Kaakkunen, K. Paivasaari, P. Vahimaa, "Parallel microstructuring using femtosecond laser and spatial light modulator," Phys. Procedia, 41, 693–697, 2013.

[111] H.E. Rebenne, D.G. Bhat, 1994. Review of CVD TiN coatings for wear-resistant applications: deposition processes, properties and performance. Surface and Coatings Technology 63, 1-13

[112] S. Hogmark, S. Jacobson, M. Larsson, 2000. "Design and evaluation of tribological coatings," Wear, 246, 20–33

[113] A. Shenhar, I. Gotman, S. Radin, P. Ducheyne, E.Y. Gutmanas, Titanium nitride coatings on surgical titanium alloys produced by a powder immersion reaction assisted coating method: residual stresses and fretting behaviour. Surface and Coatings Technology 126 (2000) 210-218

[114] J. Baumann , M. Markert, T. Werner, A. Ehrlich b, M. Rennau, Ch. Kaufmann, T. Gessner, W/TiN double layers as barrier system for use in Cu metallization, Microelectronic Engineering 37/38 (1997) 229-236

[115] A.J. Dowling, M.K. Ghantasala, J.P. Hayes, E.C. Harvey, E.D. Doyle, 2002. "Excimer laser micromachining of TiN films from chromium and copper sacrificial layers," Smart Mater. Struct., 11, 715–721

[116] M.S. Trtica, B.M. Gakovic, L.T. Petkovska, V.F. Tarasenko, A.V. Fedenev, E.I. Lipatov, M.A. Shulepov, 2004. "Surface modifications of TiN coating by the pulsed TEA CO_2 and KrCl laser," Applied Surface Science, 225, 362–371

[117] M. Trtica, V. F. Tarasenko, B. Gakovi, A. N. Panchenko, B. Radak, J. Stasi, 2009. "Micro and Nanosecond Laser TiN Coating/Steel Modification: Morphology Studies," Russian Journal of Physical Chemistry A, 83 (9), 1577–1581

[118] S. Marimuthu, A.M.Kamara, D. Whitehead, P. Mativenga, L. Li, 2010. "Laser removal of TiN coatings from WC micro-tools and in-process monitoring", Optics & Laser Technology, 42, 1233–1239

[119] B. Gakovic, M. Trtica, B Radak, S Petrovic, P Panjan,M Cekada, T Desai, D Batani, 2009. "Modification of multilayered TiAlN/TiN coating by nanosecond and picosecond laser pulses," J. Opt. A: Pure Appl. Opt., 11, 015601 (6pp)

[120] J. Bonse, M.Geuß, S. Baudach, H. Sturm, W.Kautek, 1999. "The precision of the femtosecond-pulse laser ablation of TiN films on silicon", Appl. Phys. A, 69 [Suppl.] S399–S402

[121] T.V. Kononenko, S.V. Garnov, S.M. Pimenov, V.I. Konov, V. Romano, B. Borsos, H.P. Weber, 2000. "Laser ablation and micropatterning of thin TiN coatings," Appl. Phys. A, 71, 627–631

[122] G. Dumitru, V. Romano, H.P. Weber, M. Sentis, W.Mari, 2002. "Femtosecond ablation of ultrahard materials," Appl. Phys. A, 74, 729–739

[123] T. Kurita, T. Ono, T. Nakai, 2001. "A study of processed area monitoring using the strength of YAG laser processing sound," Journal of Materials Processing Technology 112, 37-42

[124] V.E. Bordatchev, K.S. Nikumb, 2002. "Informational properties of surface acoustic waves generated by laser-material interactions during laser precision machining," Measurement Science and Technology, 13, 836-845

[125] A. Stournaras, G. Chryssolouris, 2009. "On acoustic emissions in percussion laser drilling" International Journal of Advanced Manufacturing Technology, 46, 611–620

[126] S. Strgar, J.Mozina, 2001. "An optodynamic method for the real-time determination of the depth of a laser-drilled hole," Ultrasonics 40, 791–795

[127] M. Stafe, C. Negutu, I.M. Popescu, 2005. "Real-time determination and control of the laser-drilled holes depth," Shock Waves, 14 (1-2), 123-126

[128] V. Kanicky, J. Musil, J.-M. Mermet, 1997. "Determination of Zr and Ti in 3-mu m-Thick ZrTiN Ceramic Coating Using Laser Ablation Inductively Coupled Plasma Atomic Emission Spectrometry," Applied Spectroscopy, 51 (7), 1037-1041

[129] D.P. Hand, C. Peters, F.M. Haran, J.D.C. Jones, 1997. "A fibre-optic-based sensor for optimization and evaluation of the laser percussion drilling process," Measurement Science and Technology, 8, 587-592

[130] J.S. Liu, L.J. Li, X.Z. Jin, 1999. "Accuracy control of three-dimensional Nd:YAG laser shaping by ablation," Optics & Laser Technology 31, 419-423

[131] R. Lausten, P. Balling, 2001. "On-the-fly depth profiling during ablation with ultrashort laser pulses: A tool for accurate micromachining and laser surgery," Applied Physics Letters, 79 (6), 884-886

[132] E. Aperathitis, Z.Hatzopoulos, A. Georgakilas, L. Richeboeuf, 2002. "Laser interferometry as a diagnostic tool for the fabrication of reactive ion etching-edge-emitting lasers," Journal of Vacuum Science and Technology B, 20 (5), 1994-1999

[133] S. Bosch-Charpenay, J. Haigis, P. Rosenthal, P.R. Solomon, J.M. Bustillo, 2002. "Real-time etch-depth measurements of MEMS devices," Journal of Microelectromechanical Systems, 11 (2), 111-117
[134] D.G. Papazoglou, V. Papadakis, D. Anglos, 2004. "In situ interferometric depth and topography monitoring in LIBS elemental profiling of multi-layer structures," Journal of Analytical Atomic Spectrometry, 19, 483–488
[135] H. Balzer, M. Hoehne, V. Sturm, R. Noll, 2005 "Online coating thickness measurement and depth profiling of zinc coated sheet steel by laser-induced breakdown spectroscopy," Spectrochimica Acta Part B, 60, 1172–1178
[136] S. Bera, J. Sabbah, C.G. Durfee, J. Squier, 2005. "Development of a femtosecond micromachining workstation by use of spectral interferometry". Optics Letters, 30 (4), 373-375
[137] F. Leguern, F. Brygo, P. Fichet, E. Gauthier, C. Hubert, C. Lascoutuna, D. Menut, S. Mousset, A. Semerok, M. Tabarant, 2006. "Co-deposited layer characterisation and removal control by optical emission spectroscopy coupled to nano-second laser ablation," Fusion Engineering and Design, 81, 1503–1509
[138] R. Petkovsek, I. Panjan, A. Babnik, J. Mozina, 2006. "Optodynamic study of multiple pulses micro drilling," Ultrasonics, 44, e1191–e1194
[139] V. Temnov, K. Sokolowski-Tinten, P. Zhou, D. von der Linde, "Ultrafast imaging interferometry at femtosecond-laser-excited surfaces," Journal of the Optical Society of America. B, 23 (9), 1954-1964
[140] W.Y. Oh, S.H. Yun, B.J. Vakoc, G.J. Tearney, B.E. Bouma, 2006. "Ultrahigh-speed optical frequency domain imaging and application to laser ablation monitoring," Applied Physics Letters, 88, 103902-1-103902-3
[141] C.S. Nielsen, P. Balling, 2006. "Deep drilling of metals with ultrashort laser pulses: A two-stage process," Journal of Applied Physics, 99, 093101-1-093101-4
[142] C. Grisolia, A. Semerok, J. Weulersse, F. Leguern, S. Fomichev, F. Brygo, P. Fichet, P. Thro, P. Coad, N. Bekris, 2007. "In-situ tokamak laser applications for detritiation and co-deposited layers studied," Journal of Nuclear Materials 363–365, 1138–1147
[143] R. Petkovsek, J. Mozina, 2007"Monitoring of the laser microdrilling of glass by the optodynamic method," Journal of Applied Physics, 102, 044905-1-044905-5
[144] P.J.L. Webster, M.S. Muller, J.M. Fraser, 2007. "High speed in situ depth profiling of ultrafast micromachining," Optics Express, 15 (23), 14967-14972
[145] A. Stournaras, K. Salonitis, G. Chryssolouris, 2010. "Optical emissions for monitoring of the percussion laser drilling process," International Journal of Advanced Manufacturing Technology, 46 (5-8), 589-603
[146] S. Döring, S. Richter, S. S. Nolte, A. Tünnermann, 2010. "In situ imaging of hole shape evolution in ultrashort pulse laser drilling," Optics Express, 18 (19), 20395-20400

[147] J. Ruiz, A. González, L.M. Cabalín, J.J. Laserna, 2010. "On-line laser-induced breakdown spectroscopy determination of magnesium coating thickness on electrolytically galvanized steel in motion," Applied Spectroscopy, 64 (12), 1342-1349
[148] P.J.L. Webster, J.X.Z. Yu, B.Y.C. Leung, M.D. Anderson, V.X.D. Yang, M. James, 2010. "In situ 24 kHz coherent imaging of morphology change in laser percussion drilling," Optics Express, 35 (5), 646-648
[149] M. Wiesner, J. Ihlemann, H.H. Müller, E. Lankenau, G. Hüttmann, 2010. "Optical coherence tomography for process control of laser micromachining," Review of Scientific Instrumentation, 81, 033705-1-033705-7
[150] C.-H. Lin, R. Powell, L. Jiang, H. Xiao, S.-J. Chen, H.-L. Tsai, 2010. "Real-time depth measurement for micro-holes drilled by lasers"
[151] F.P. Mezzapesa, A. Ancona, T. Sibillano, F. De Lucia, M. Dabbicco, L. Maurizio, M. Pietro, G. Scamarcio, 2011. "High-resolution monitoring of the hole depth during ultrafast laser ablation drilling by diode laser self-mixing interferometry"
[152] F.P. Mezzapesa, A. Ancona, T. Sibillano, F. De Lucia, M. Dabbicco, P. Lugarà, M. Pietro, G. Scamarcio, 2011. "Direct In-Situ Inspection of the Penetration Depth During Laser Ablation of Metal Targets"
[153] P.J.L. Webster, L.G. Wright, K.D. Mortimer, B.Y. Leung, J.X.Z. Yu, J.M. Fraser "Automatic real-time guidance of laser machining with inline coherent imaging," Journal of Laser Applications, 23 (2), 022001-1-022001-6
[154] B.Y.C. Leung, P.J.L. Webster, J.M. Fraser, V.X.D. Yang, 2012. "Real-Time Guidance of Thermal and Ultrashort Pulsed Laser Ablation in Hard Tissue Using Inline Coherent Imaging," Lasers in Surgery and Medicine 44, 249–256
[155] V. Spagnolo, A. Ancona, G, Scamarcio, 2012. Detection of ultrafast laser ablation using quantum cascade laser-based sensing," Applied Physics Letters, 101, 171107-1-171107-4
[156] F.P. Mezzapesa, T. Sibillano, F. Di Niso, A. Ancona, P. Lugarà, M. Dabicco, G. Scamarcio, 2012. "Real time ablation rate measurement during high aspect-ratio hole drilling with a 120-ps fiber laser," Optics Express, 20 (1), 663-671
[157] A. Ancona, M. Dabbicco, F. De Lucia, P.M. Lugarà, F. Mezzapesa, G. Scamarcio, T. Sibillano, 2 August 2012. "Laser system for ablation monitoring" WO2012101570 A1
[158] C. Dunsby, P.M.W. French, 2003. "Techniques for depth-resolved imaging through turbid media including coherence-gated imaging," *J. Phys. D. Appl. Phys.*, 36 (14), R207–R227
[159] M.J. Rudd, 1968. "A laser Doppler velocimeter employing the laser as a mixer-oscillator," *J. Phys. E.*, 1 (7), 723–726
[160] S. Donati, 1978. "Laser interferometry by induced modulation of cavity field," *J. Appl. Phys.*, 49 (2), 495-497

[161] M. Norgia S. Donati, 2003. "A displacement-measuring instrument utilizing self-mixing interferometry," IEEE Trans. Instrum. Meas., 52 (6), 1765–1770, L. Scalise, Y. Yu, G. Giuliani, G. Plantier, T. Bosch, 2004. "Self-Mixing Laser Diode Velocimetry: Application to Vibration and Velocity Measurement," IEEE Trans. Instrum. Meas., 53 (1), 223–232

[162] A. Magnani, A. Pesatori, M. Norgia, 2012. "Self-mixing vibrometer with real-time digital signal elaboration," Appl. Opt., 51 (21), 5318–25

[163] M. Norgia, A. Magnani, A. Pesatori, 2012. "High resolution self-mixing laser rangefinder.," Rev. Sci. Instrum., 83 (4), p. 045113

[164] U. Zabit, O. D. Bernal, T. Bosch, 2013. "Self-Mixing Laser Sensor for Large Displacements: Signal Recovery in the Presence of Speckle," IEEE Sens. J., 13 (2), 824–831

[165] ASM Handbook, Online Edition, American Society for Metals, Metals Park

[166] Data sheet of 1.3343 tool steel, IMS S.p.A.

[167] H.O. Pierson, 1996. Handbook of refractory carbides and nitrides: properties, characteristics, processing, and applications, William Andrew, New Jersey

[168] A. Bendavid, P.J. Martin, R.P. Netterfield, T.J. Kinder, 1994. The properties of TiN films deposited by filtered arc evaporation, Surface and Coatings Technology 70, 97-106

[169] C.A. Biffi, B. Previtali, 2008. "Spatter reduction during titanium microdrilling using pulsed fiber laser," Proceedings of 27th International Congress on Applications of Lasers & Electro-Optics ICALEO 2008, 27-36

[170] G3.1 Pulsed Fibre Laser Installation Guide and User Manual, SPI Lasers Uk, Ltd. 2010

[171] J. Bonse, P. Rudolph, J. Kruger, S. Baudach, W. Kautek, 2000. "Femtosecond pulse laser processing of TiN on silicon," Applied Surface Science 154–155, 659–663

[172] G.B. Blanchet, P. Cotts, C.R. Fincher Jr., 2000. "Incubation: Subthreshold ablation of poly-(methyl methacrylate) and the nature of the decomposition pathways," Journal of Applied Physics, 88 (5), 2975-2978

[173] S. Xiao, E.L. Gurevich, A. Ostendorf, 2012. "Incubation effect and its influence on laser patterning of ITO thin film," Applied Physics A 107, 333–338

[174] H.Sun, 2012. Laser Diode Beam Basics, Manipulations and Characterizations, Springer, New York

[175] J. Sun, J. P. Longtin, 2001. "Inert gas beam delivery for ultrafast laser micromachining at ambient pressure," J. Appl. Phys., 89 (12), p. 8219

[176] W. Perrie, M. Gill, G. Robinson, P. Fox, W. O'Neill, 2004. "Femtosecond laser micro-structuring of aluminium under helium," Appl. Surf. Sci., 230, 1–4, 50–59

[177] M.J. Jackson, G.M. Robison, B. Mills, W. O'Neill, 2003. "Laser micromachining of chromium-rich die steels under controlled atmosphere," Proc. Inst. Mech. Eng. Part B J. Eng. Manuf 217 (4), 553-562

[178] C.-M. Wang, X.-X. Meng, W. Huang, X.-Y. Hu, A.-Q. Duan, 2011. "Role of side assisting gas on plasma and energy transmission during CO_2 laser welding," J. Mater. Process. Technol., 211 (4), 668–674

[179] C. Dowding, J. Lawrence, 2010. "Effects of closed immersion filtered water flow velocity on the ablation threshold of bisphenol A polycarbonate during excimer laser machining," Appl. Surf. Sci., 256 (12), 3705–3713

[180] R.E. Russo, X.L. Mao, H.C. Liu, J.H. Yoo, S.S.Mao, 1999. "Time-resolved plasma diagnostics and mass removal during single-pulse laser ablation," Appl. Phys. A 69 [Suppl.], S887–S894

[181] E. Amer, P. Gren, A.F.H. Kaplan, M. Sjödahl, M. El Shaer. 2010. "Comparison of the laser ablation process on Zn and Ti using pulsed digital holographic interferometry," Applied Surface Science 256, 4633–4641

[182] L. Vandoni, A.G. Demir, B. Previtali, N. Lecis, D. Ugues, 2012. "Wear Behavior of Fiber Laser Textured TiN Coatings in a Heavy Loaded Sliding Regime," Materials 5, 2360-2382

[183] A.G. Demir, N. Lecis, B. Previtali, D. Ugues, 2013. "Scratch resistance of fiber laser surface textured TiN coatings," Surface Engineering, 29 (9), 654-659

[184] S. Bettiga, 2013. "Effetto del substrato e della lavorazione di texturing superficiale su acciai rivestiti in TiN," MSc. Thesis in Mechanical Engineering, Politecnico di Milano

Acknowledgements

With great satisfaction and pride I reach the end of this journey. Indeed, these four years have been quite a ride and full of surprises. By far, the biggest surprise for me has been how I have grown fond of what I did. I stepped in this laboratory with great worry (almost fear), a good deal of confusion, and lots of curiosity. In the end I believe I can say I made it *mine*. Before closure, I would like to express my gratitude to those who have helped me achieve what is before you.

My dearest and deepest thanks go to my supervisor, mentor, and inspirer Prof. Barbara Previtali. She has invested in me, followed me, encouraged me, and moreover reminded me of humanly values throughout what we do. I am grateful for her trust in me and pushing me to expand what I thought were my boundaries. Under her supervision, I believe I have gained autonomy and a wide vision in research, but also grew personally. Above all, I thank her for giving us a family environment at SITEC, of which I am proud to be a part. I am proud to be a part of *la scuola della Previtali.*

I would like to thank my co-supervisor Prof. William O'Neill for an inspiring period with his group in Cambridge. These 6 months have broadened my view in research. I gained a better comprehension of laser physics not only using the facilities at the CIP, but throughout our everyday discussions with the members of the group.

I thank my colleagues from SITEC, which are the essential parts of this family. I thank Dr. Daniele Colombo for his kindness and help throughout the good and bad times. He has become an older brother throughout these years. And without a coffee with Daniele, the work day does not start off. I thank my dear friends Dr. Bruno Valsecchi and Giovanni Riva. They have inspired me with their exceptional work in maintaining our laboratory. Their ability and even agility to work in a workshop environment has encouraged me to be more courageous in my own work. I also thank my friends belonging to the newer generation of SITEC, Stefano Zarini, Pietro Maressa, Erica Librera, Giorgia Galimberti and Valentina Furlan. They surely have added colours to this environment. I feel lucky to share and interact with them every day, seeing their bright ideas and exceptional work. I am most definitely grateful for the additional laughter they brought to the laboratory. My salutes and thanks are to former member of SITEC, Dr. Patrick Pradel, who continues his career in China. He put a little bit of design into micro.

I thank the great people of CIP at the University of Cambridge. They have made my period very special and something more than only research. I would like to thank especially Krste Pangovski, who has made me a part of his research and shared the same passion of research with me.

I gratefully acknowledge the help of IPG Italy by allowing us to use their laser sources in the micromachining section of SITEC. Their YLPG-5 system has been used within this PhD thesis. I thank Prof. Nora Lecis and Prof. Daniele Ugues for

providing the TiN coated samples and their collaboration in the tribological analyses. I express my gratitude to Prof. Michele Norgia and his colleagues Dr. Alessandro Pesatori and Alessandro Magnani for their collaboration throughout the development of the self-mixing interferometry system. I thank my tutor Prof. Bortolino Saggin for his timely critics on my work that have enabled me to pinpoint the issues and resolve them. I also thank all the students that have worked with me during their thesis works and projects. It has been a great pleasure sharing my knowledge and learning with them.

More personal thanks are to my beloved friends in Italy, Turkey, and other parts of the world. I am proud to be a part of this international community. Throughout these four years, I have represented both my country of origin and country of residence in various occasions. I have been accepted both as a Turk and an Italian. I have been to different countries, and seen exceptional people in research, which were often very young. I have made friendships that will last. I have always received great feedback and nourishment from my friends in Turkey. I acknowledge the contribution of all these people in my growth, which surely has reflected to my work.

I finally thank my family for their endless support and love. My mother, father, and sister have been always encouraging and curious of what I have been doing. I hope to have made them proud.

3rd January 2014, Istanbul

Appendix A

Images of the dimples obtained on TiN coated 42CrMo4 steel with Q-switched, long ns, 1 µm fibre laser

Table A.1 SEM images of the dimples obtained on TiN coated 42CrMo4 steel with Q-switched, long ns, 1 µm fibre laser using the developed processing method.

h_f [mm]	t_{mod}=65 µs	t_{mod}=72.5 µs	t_{mod}=80 µs
-0.9	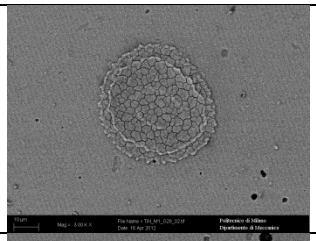	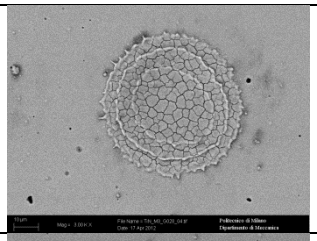	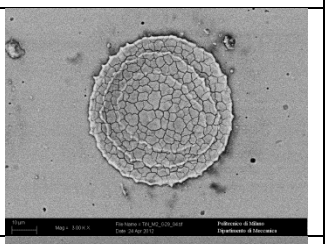
-0.8	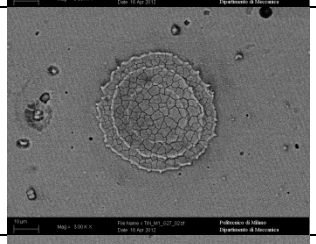	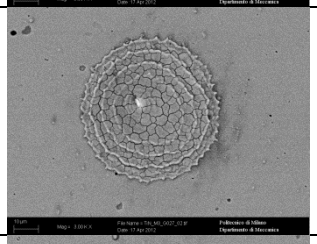	
-0.7		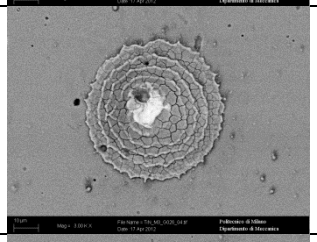	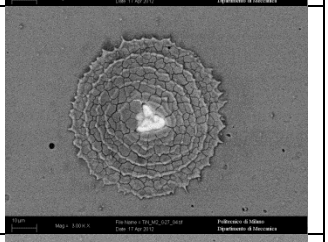
-0.6	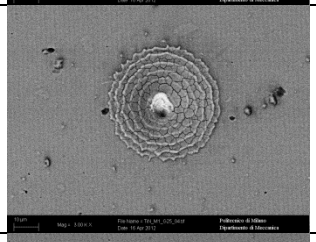		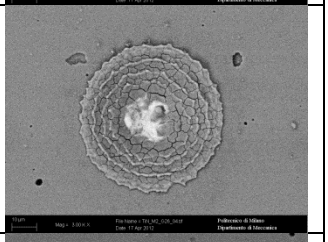
-0.5	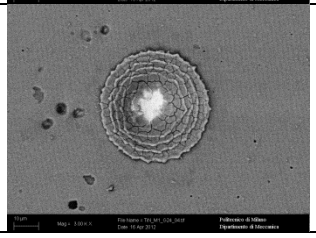		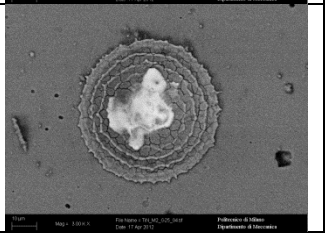

-0.4	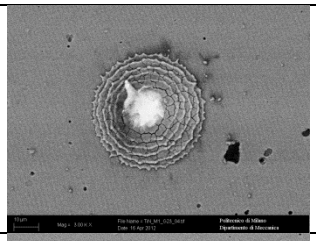	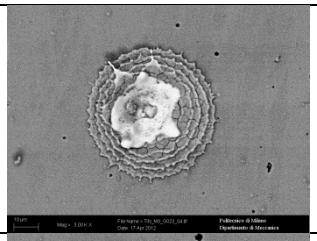	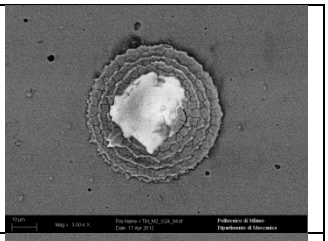
-0.3	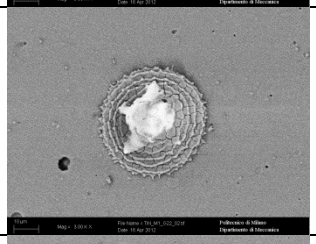	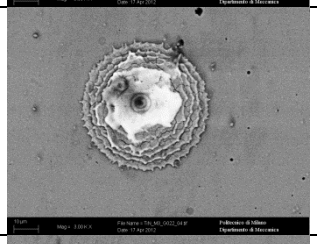	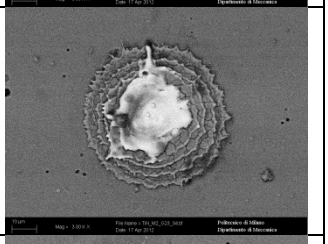
-0.2	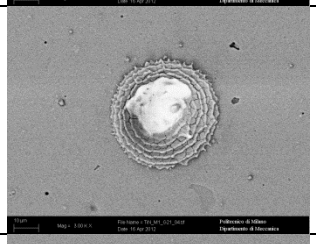		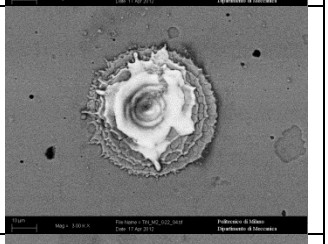
-0.1	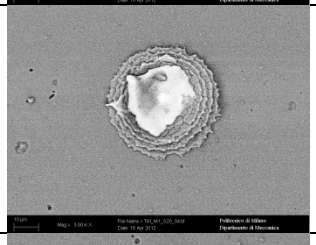	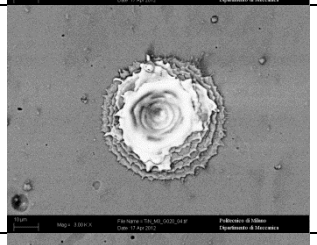	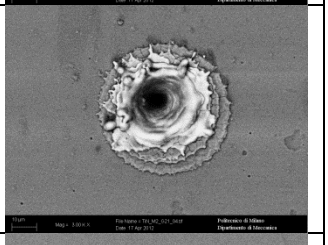
0			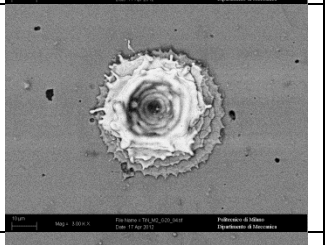
0.1	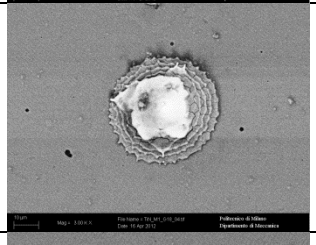		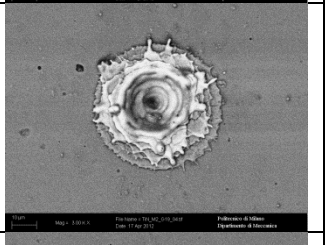
0.2	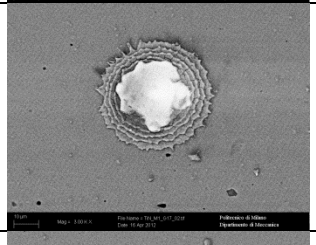	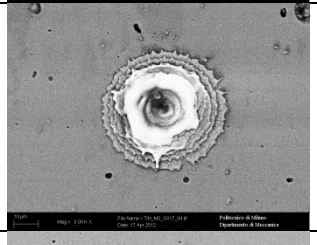	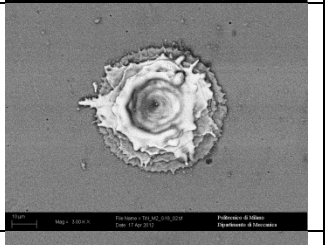
0.3	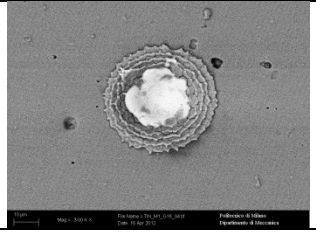	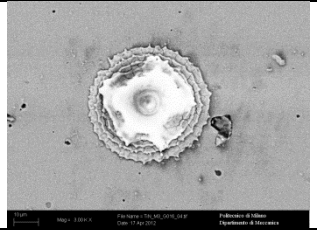	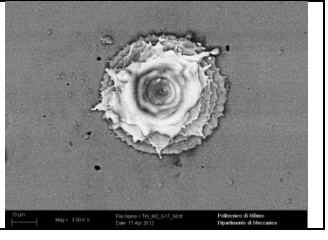

0.4	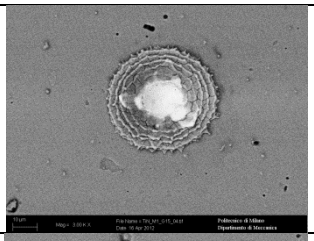		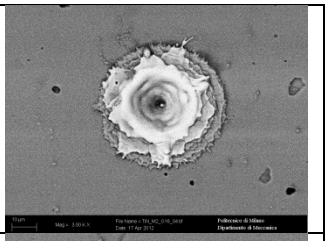
0.5	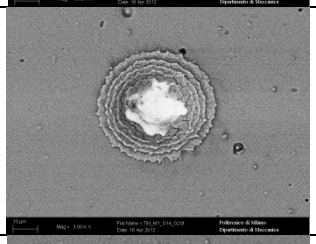	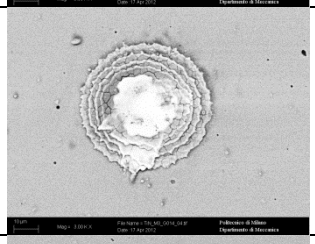	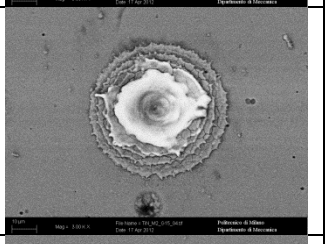
0.6			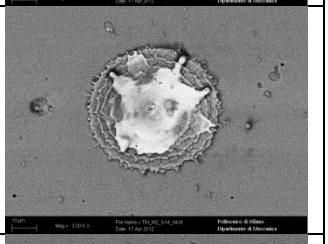
0.7	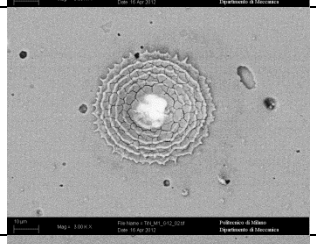	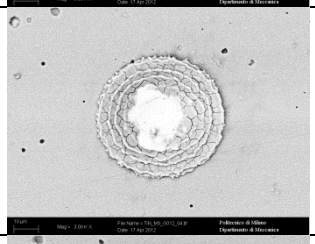	
0.8	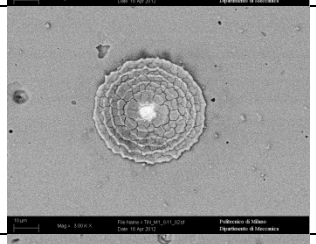	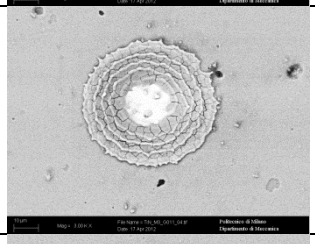	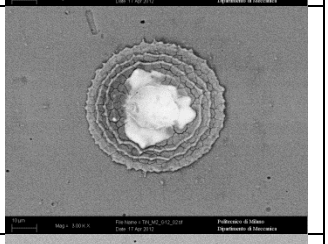
0.9	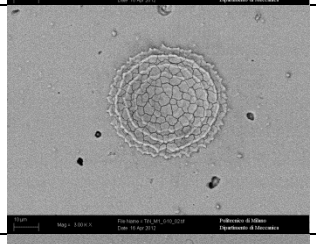	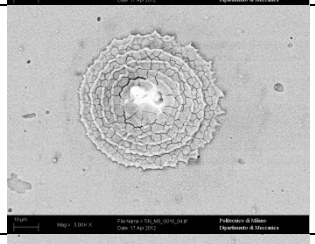	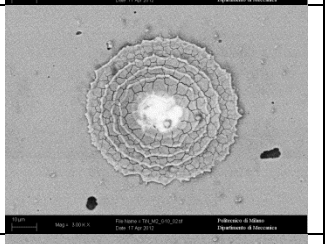
1.0	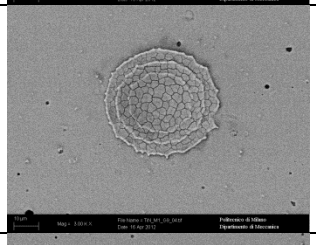	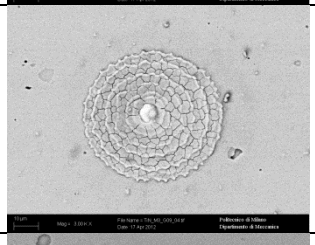	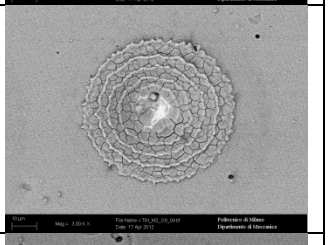
1.1	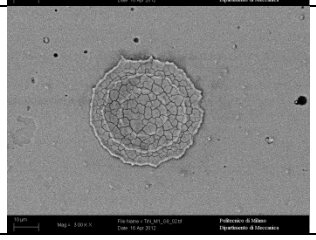	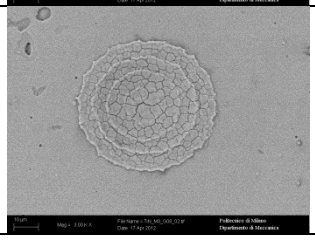	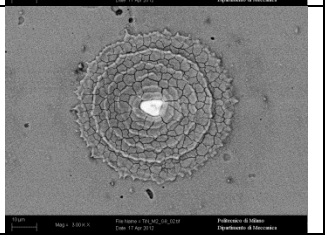

1.2	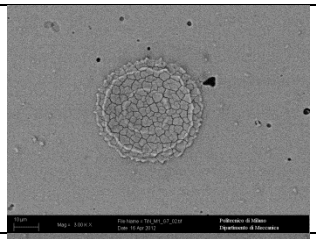	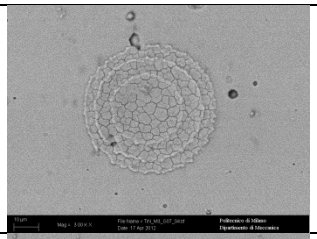	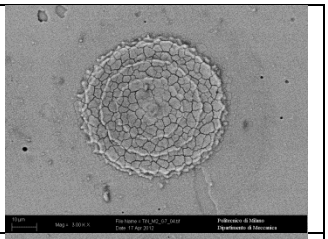
1.3	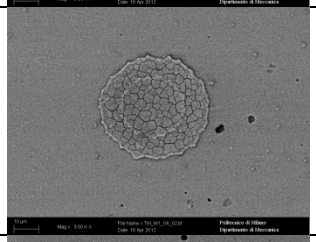	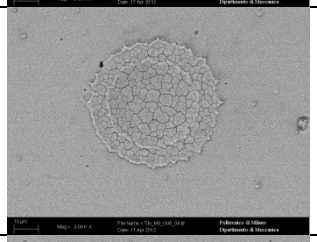	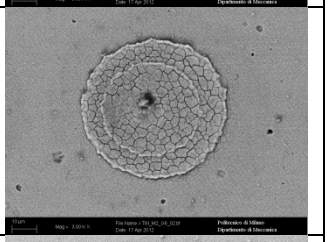
1.4	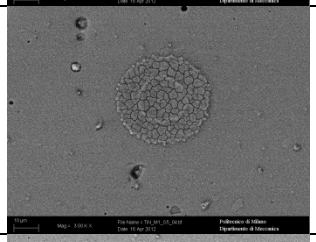	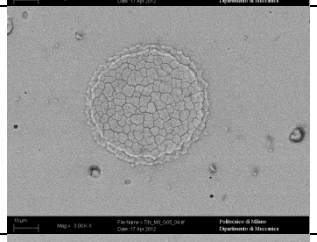	
1.5	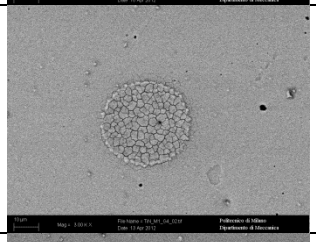	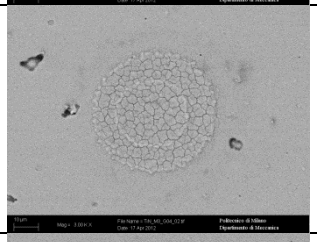	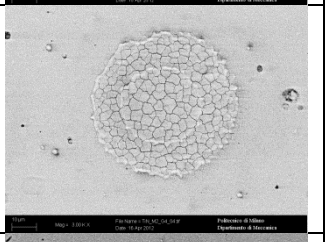
1.6		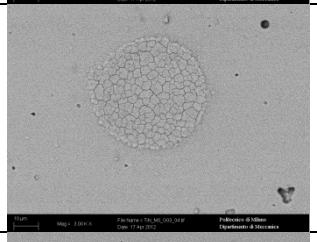	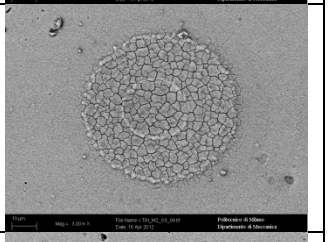
1.7	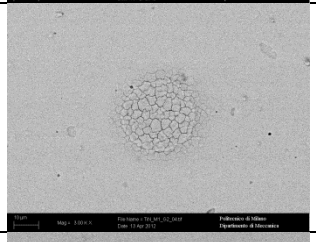	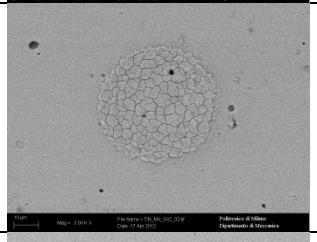	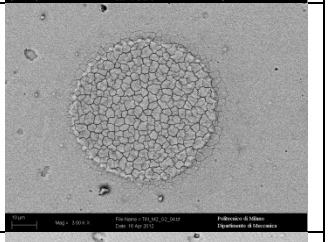
1.8	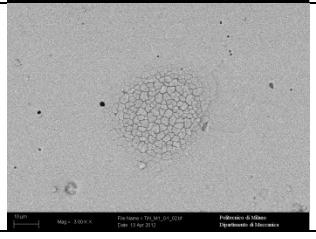		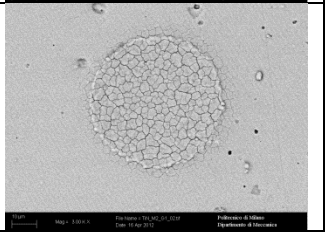

Appendix B

Images of the dimples obtained on TiN coated AISI M2 steel with MOPA, pulse duration variable, 1 µm fibre laser

Table B.1. Optical microscopy images of the dimples obtained on TiN coated AISI M2 steel with MOPA, pulse duration variable, 1 µm fibre laser using single pulses.

SI%	E [µJ]	WF 0 – τ=200 ns
73	35	n/a
76	50	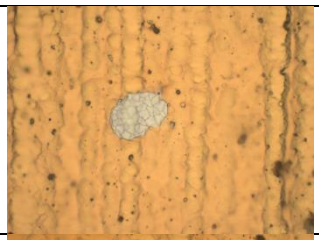
79	72	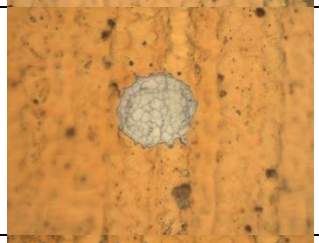
82	103	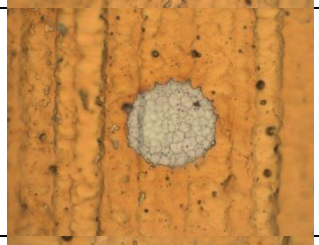
85	134	
88	177	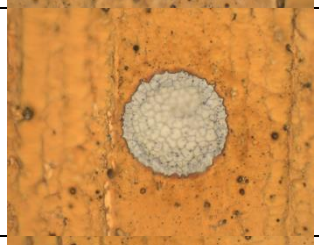
91	216	

94	261	
97	318	
100	356	

SI%	E [µJ]	WF 16 – τ=150 ns
73	31	n/a
76	43	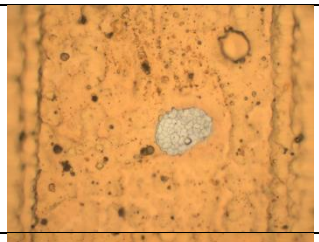
79	60	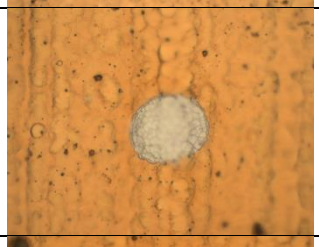
82	81	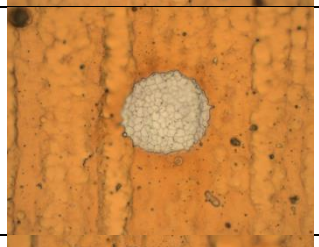
85	112	

88	151	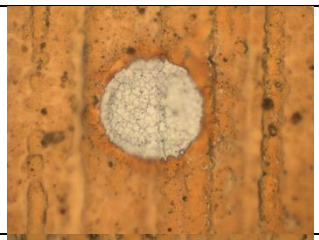
91	183	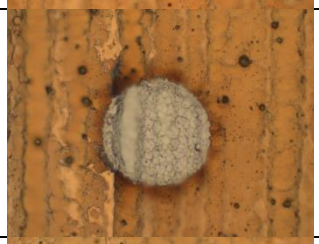
94	231	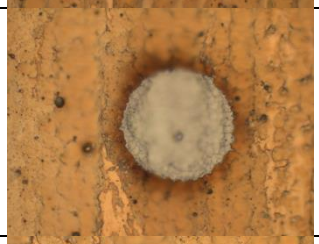
97	276	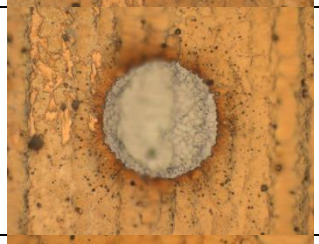
100	320	

SI%	E [µJ]	WF 21 – τ=100 ns
73	19	n/a
76	34	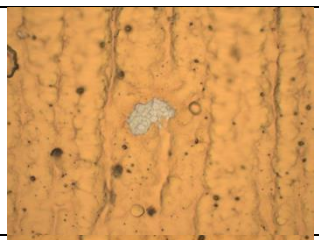
79	50	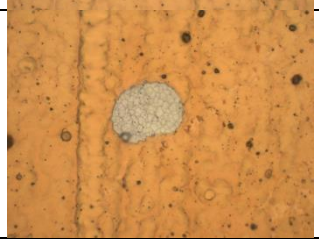

82	61	
85	83	
88	117	
91	150	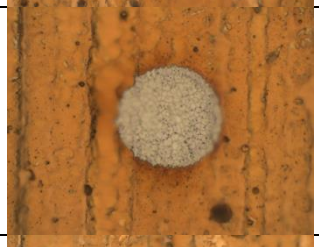
94	191	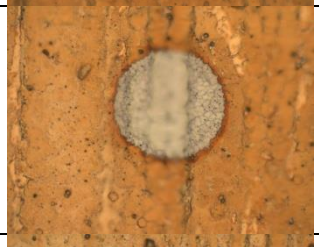
97	229	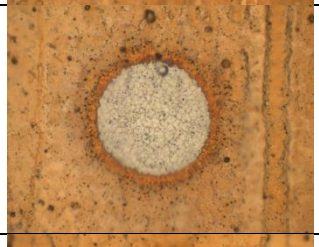
100	262	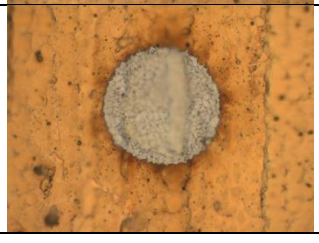

SI%	E [µJ]	WF 1 – τ=65 ns
73	13	n/a
76	19	n/a

79	30	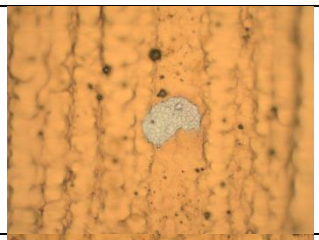
82	39	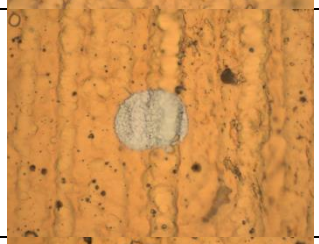
85	57	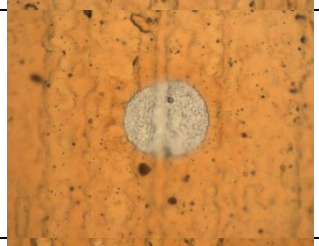
88	76	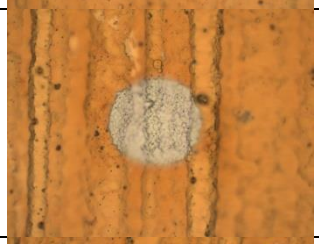
91	100	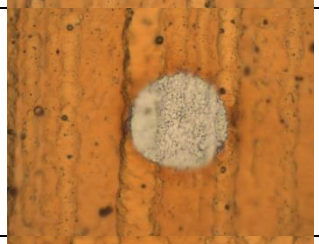
94	128	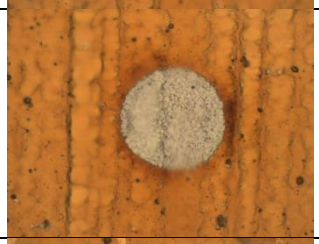
97	162	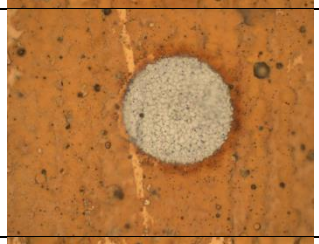
100	193	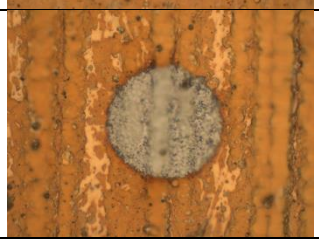

SI%	E [µJ]	WF 2 – τ=30 ns
73	7	n/a
76	10	n/a
79	14	n/a
82	19	
85	28	
88	40	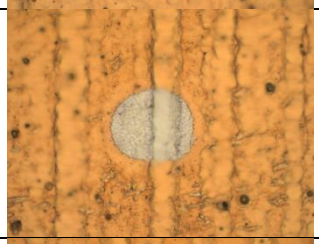
91	53	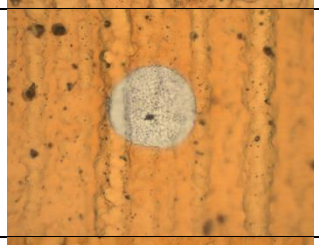
94	72	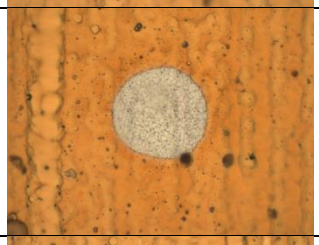
97	94	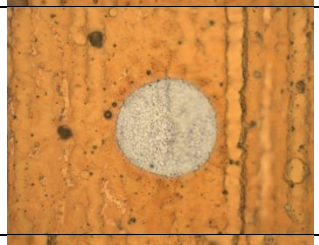
100	114	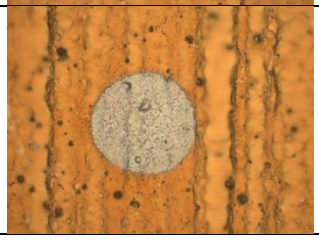

SI%	E [µJ]	WF 4 – τ=12 ns

73	5	n/a
76	7	n/a
79	9	n/a
82	13	n/a
85	17	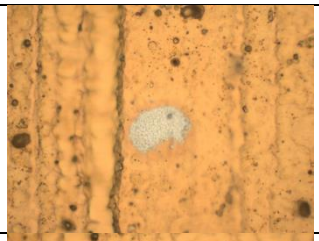
88	27	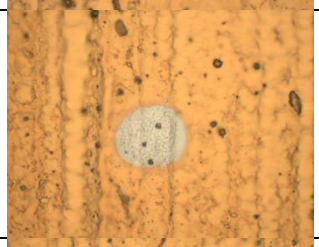
91	36	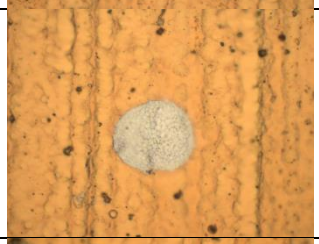
94	46	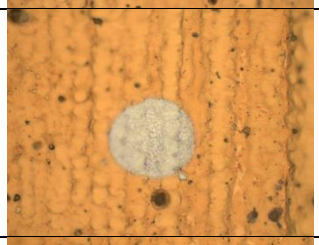
97	64	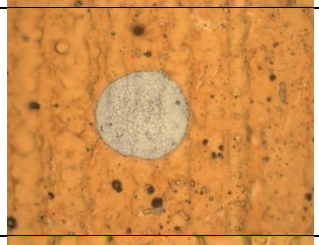
100	77	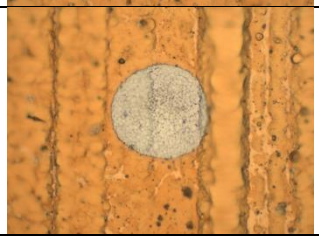

Table B.2. Optical microscopy images of the dimples obtained on TiN coated AISI M2 steel with MOPA, pulse duration variable, 1 µm fibre laser using multiple pulses.

SI%	Set P	E [µJ]	No of pulses	WF 0 – τ=200 ns
73	3.3	35	2	n/a

76	3.9	50	2	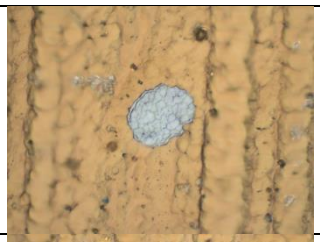
79	4.7	72	2	
82	5.5	103	2	
85	6.6	134	2	
88	7.8	177	2	
91	8.8	216	2	
94	10.5	261	2	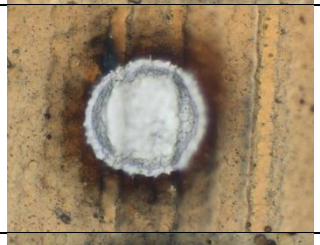
97	12	318	2	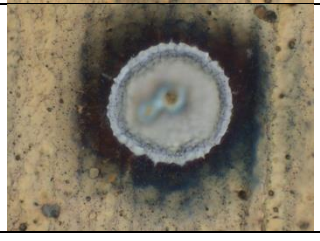

100	13.5	356	2	

73	3.3	35	3	
76	3.9	50	3	
79	4.7	72	3	
82	5.5	103	3	
85	6.6	134	3	
88	7.8	177	3	

91	8.8	216	3	
94	10.5	261	3	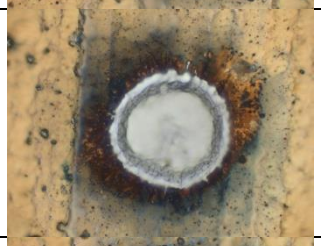
97	12	318	3	
100	13.5	356	3	

73	3.3	35	4	
76	5.5	50	4	
79	4.7	72	4	

82	5.5	103	4	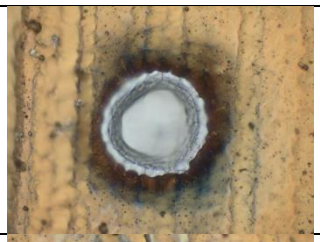
85	6.6	134	4	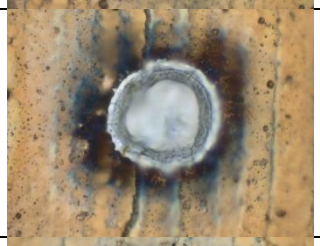
88	7.8	177	4	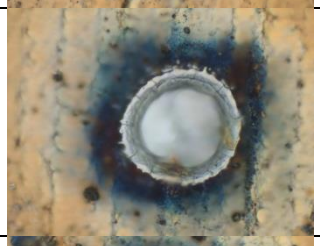
91	8.8	216	4	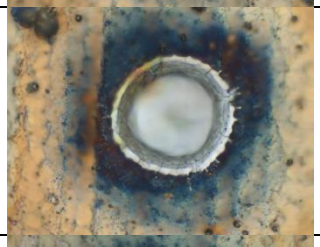
94	10.5	261	4	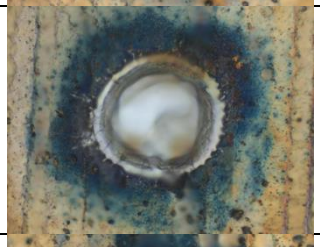
97	12	318	4	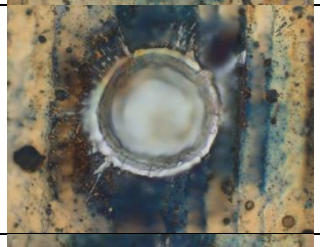
100	13.5	356	4	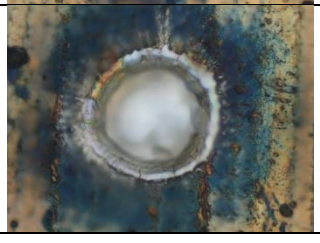

73	3.3	35	5	
76	5.5	50	5	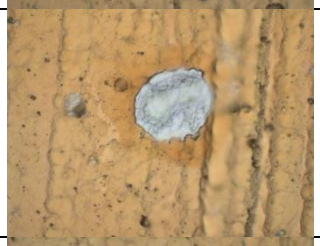
79	4.7	72	5	
82	5.5	103	5	
85	6.6	134	5	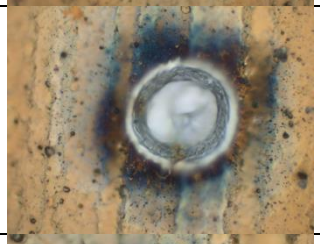
88	7.8	177	5	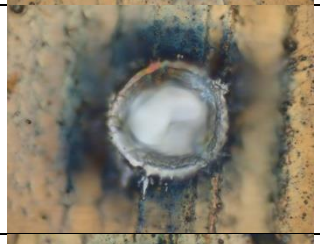
91	8.8	216	5	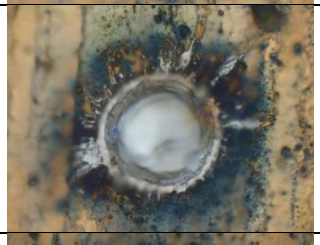
94	10.5	261	5	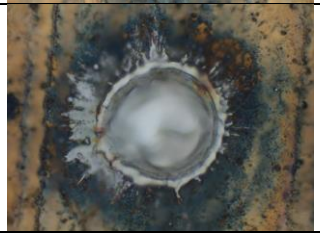

97	12	318	5	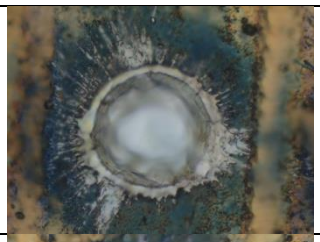
100	13.5	356	5	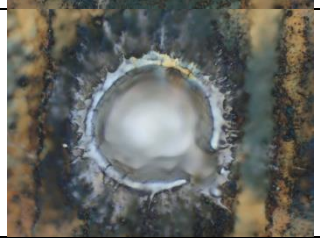

73	3.3	35	6	
76	3.9	50	3	
79	4.7	72	6	
82	5.5	103	6	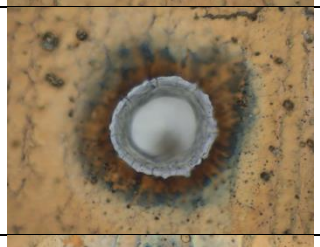
85	6.6	134	6	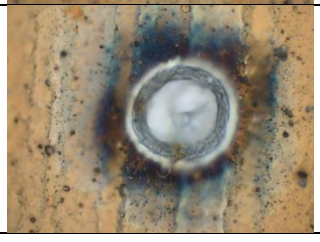

88	7.8	177	6	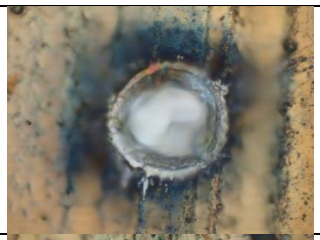
91	8.8	216	6	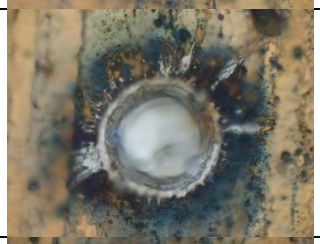
94	10.5	261	6	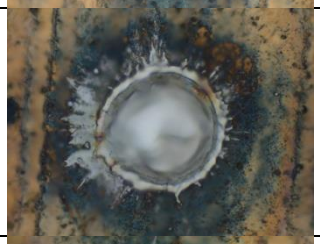
97	12	318	6	
100	13.5	356	6	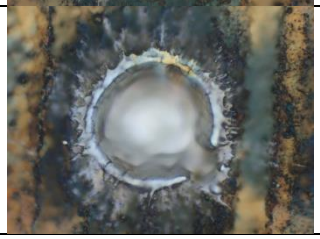

73	3.3	35	7	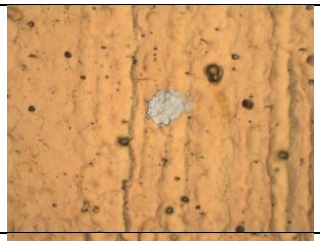
76	5.5	50	7	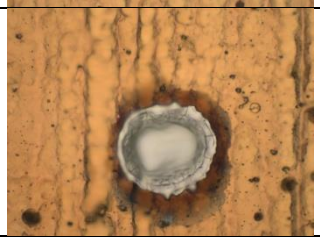

79	4.7	72	7	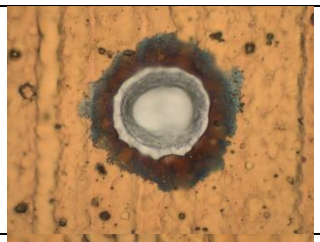
82	5.5	103	7	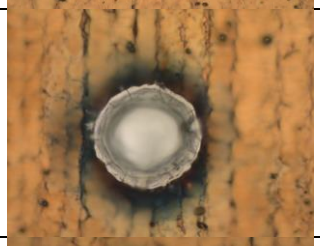
85	6.6	134	7	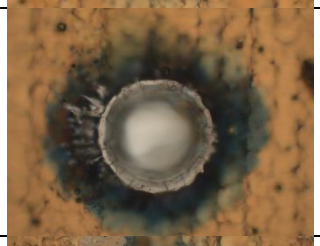
88	7.8	177	7	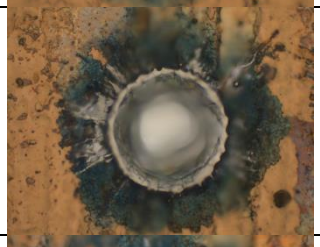
91	8.8	216	7	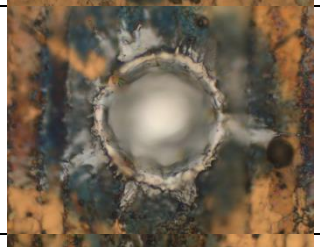
94	10.5	261	7	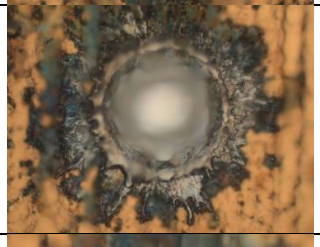
97	12	318	7	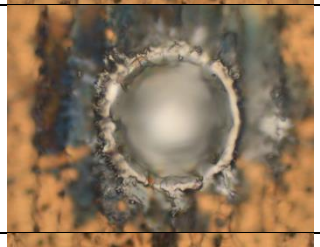
100	13.5	356	7	

73	3.3	35	8	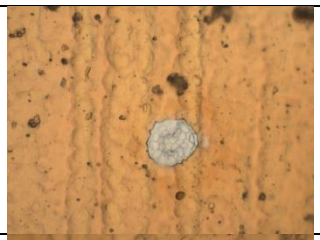
76	5.5	50	8	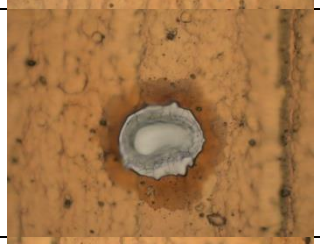
79	4.7	72	8	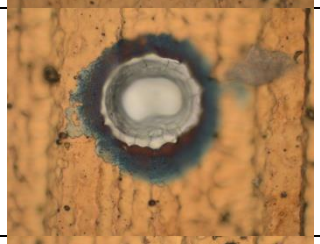
82	5.5	103	8	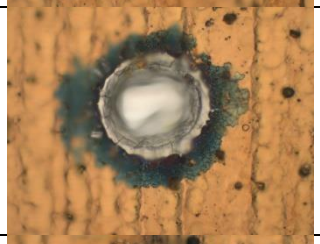
85	6.6	134	8	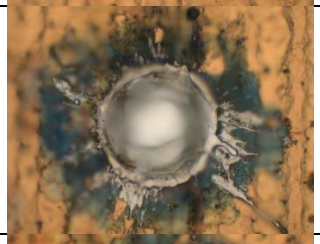
88	7.8	177	8	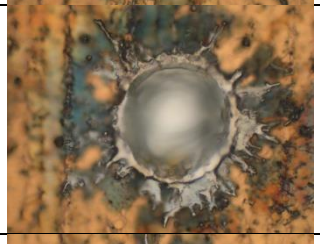
91	8.8	216	8	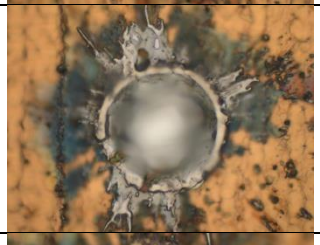
94	10.5	261	8	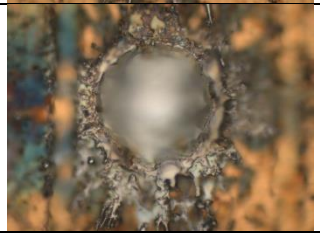

97	12	318	8	
100	13.5	356	8	

73	3.3	35	9	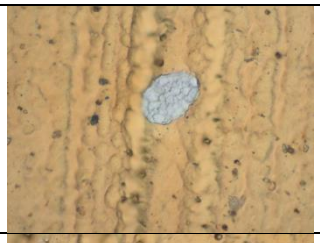
76	3.9	50	9	
79	4.7	72	9	
82	5.5	103	9	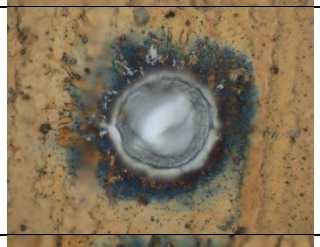
85	6.6	134	9	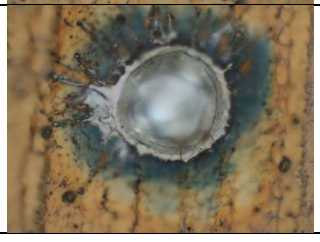

88	7.8	177	9	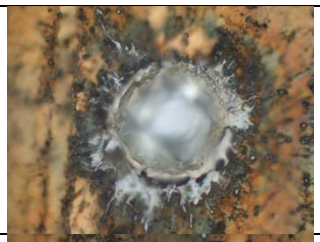
91	8.8	216	9	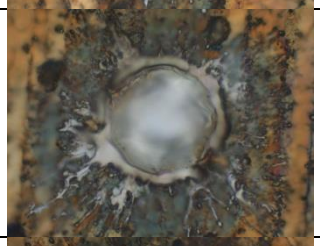
94	10.5	261	9	
97	12	318	9	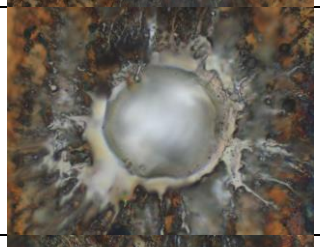
100	13.5	356	9	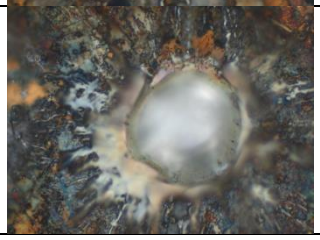

SI%	Set P	E [µJ]	No of pulses	WF 21 – τ=100 ns
73	3.3	19	3	n/a
76	4	34	3	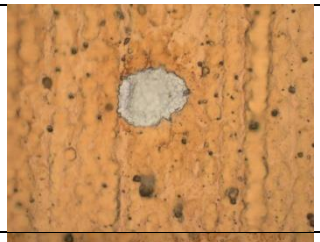
79	4.7	50	3	

82	5.5	61	3	
85	6.7	83	3	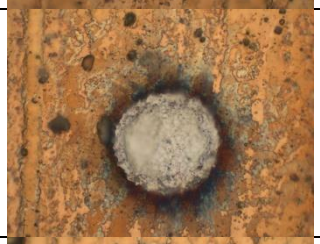
88	7.8	117	3	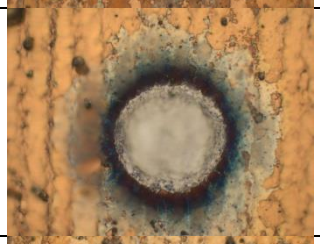
91	9.3	150	3	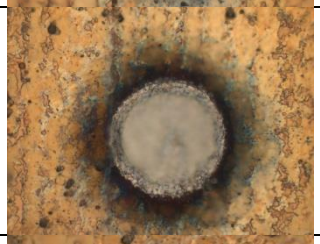
94	11	191	3	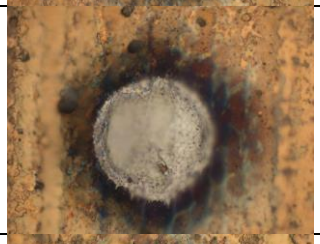
97	13.5	229	3	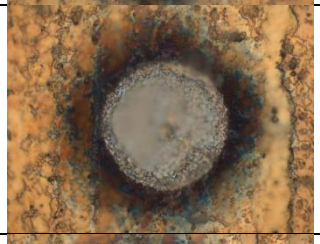
100	15.5	262	3	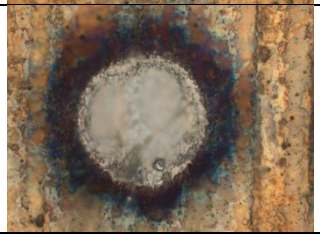

73	3.3	19	6	n/a

76	4	34	6	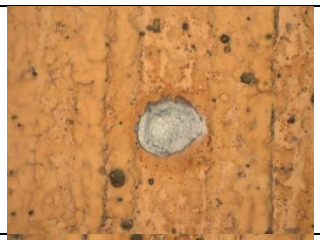
79	4.7	50	6	
82	5.5	61	6	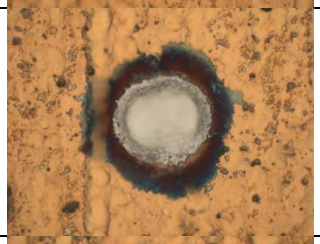
85	6.7	83	6	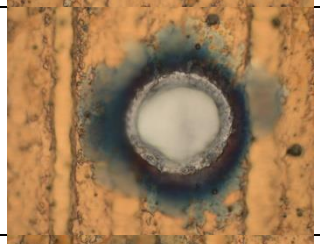
88	7.8	117	6	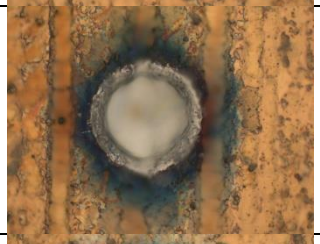
91	9.3	150	6	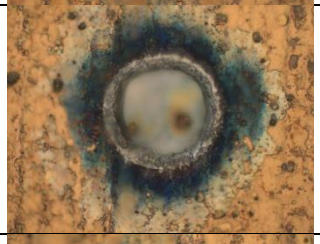
94	11	191	6	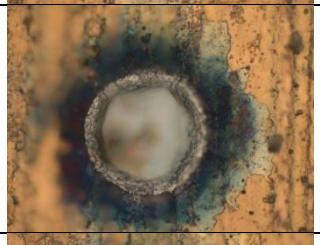
97	13.5	229	6	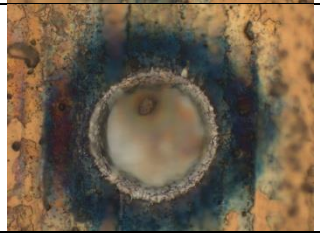

100	15.5	262	6	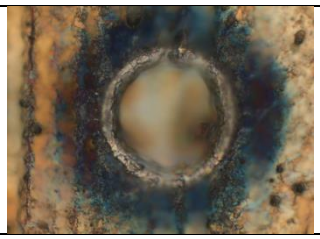

73	3.3	19	7	n/a
76	4	34	7	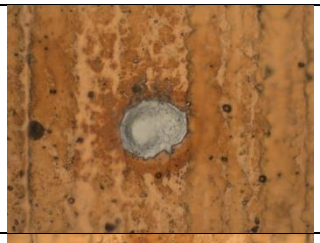
79	4.7	50	7	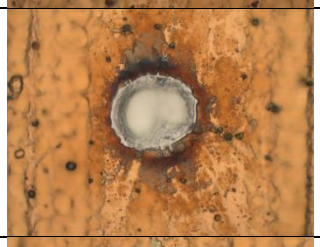
82	5.5	61	7	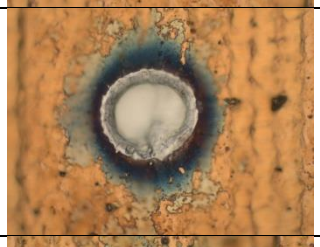
85	6.7	83	7	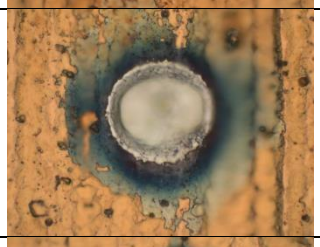
88	7.8	117	7	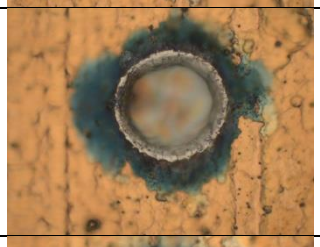
91	9.3	150	7	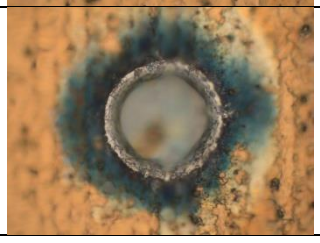

94	11	191	7	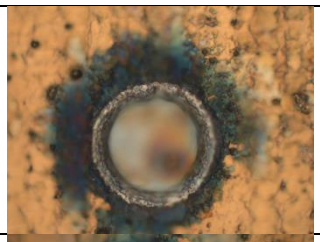
97	13.5	229	7	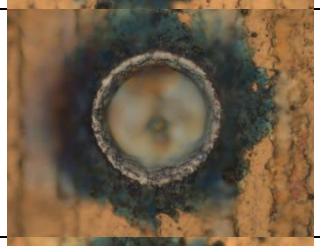
100	15.5	262	7	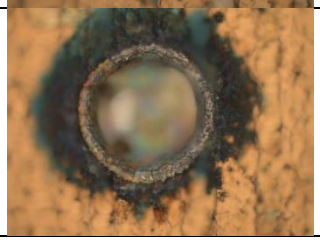

73	3.3	19	9	n/a
76	4	34	9	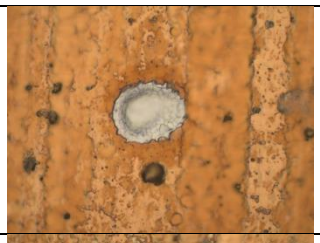
79	4.7	50	9	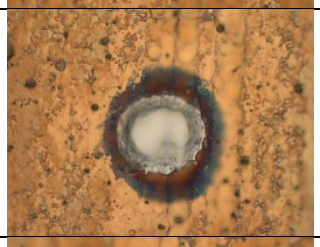
82	5.5	61	9	
85	6.7	83	9	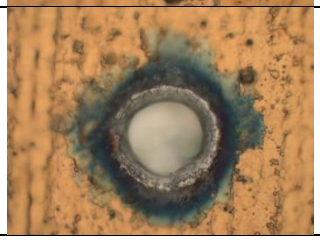

88	7.8	117	9	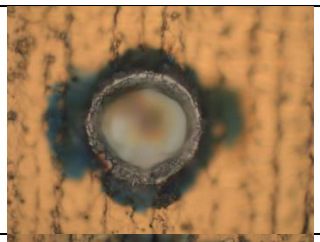
91	9.3	150	9	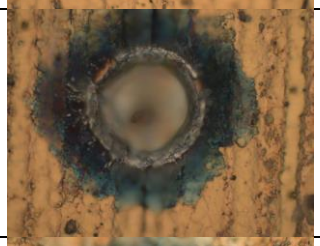
94	11	191	9	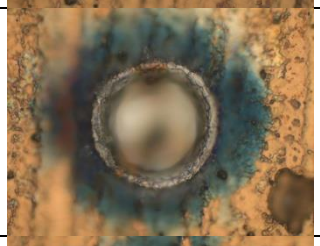
97	13.5	229	9	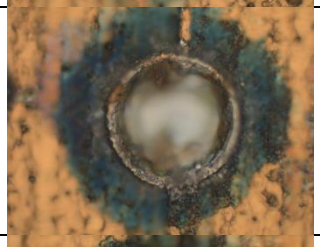
100	15.5	262	9	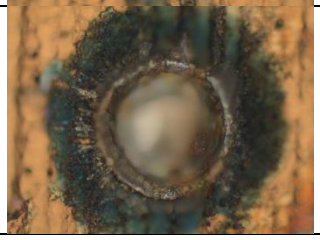

73	3.3	19	10	n/a
76	4	34	10	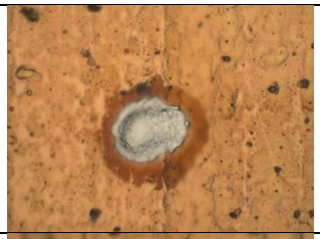
79	4.7	50	10	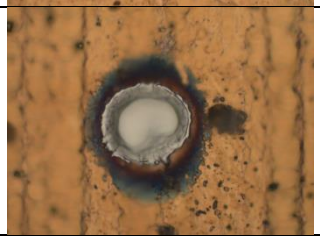

82	5.5	61	10	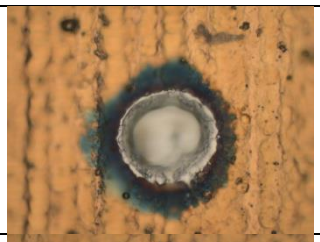
85	6.7	83	10	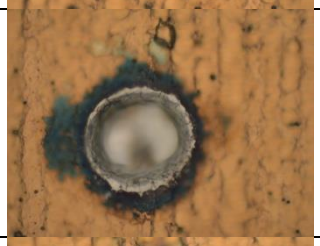
88	7.8	117	10	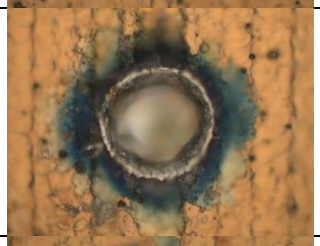
91	9.3	150	10	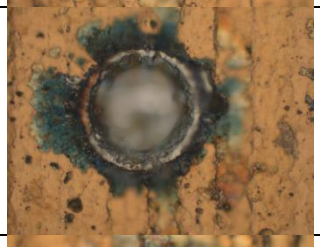
94	11	191	10	
97	13.5	229	10	
100	15.5	262	10	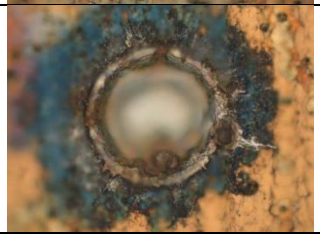

73	3.3	19	12	n/a

76	4	34	12	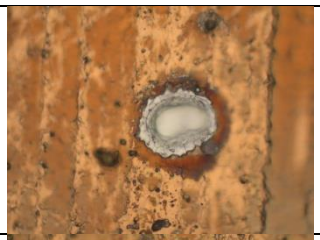
79	4.7	50	12	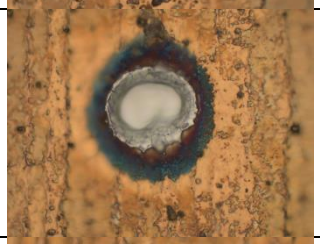
82	5.5	61	12	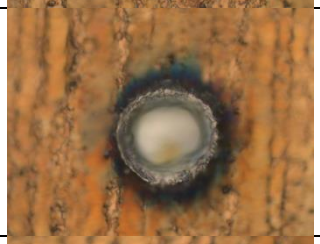
85	6.7	83	12	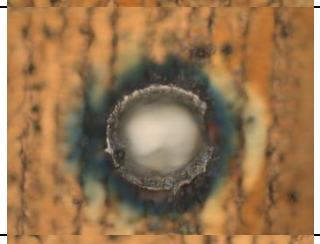
88	7.8	117	12	
91	9.3	150	12	
94	11	191	12	
97	13.5	229	12	

100	15.5	262	12	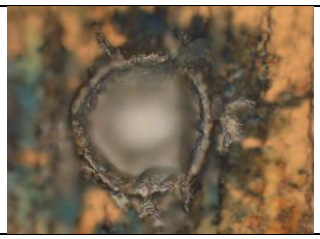

73	3.3	19	14	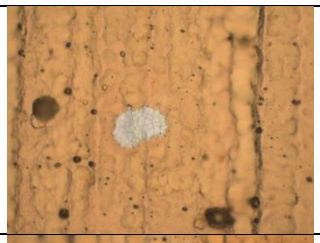
76	4	34	14	
79	4.7	50	14	
82	5.5	61	14	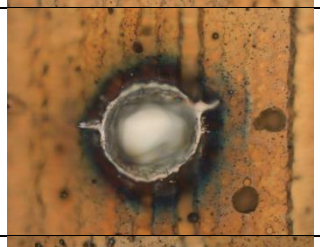
85	6.7	83	14	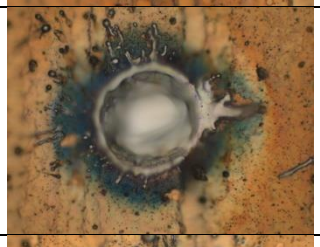
88	7.8	117	14	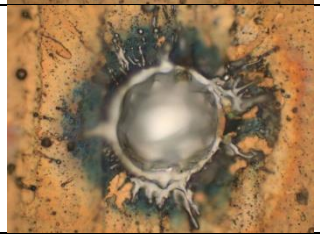

91	9.3	150	14	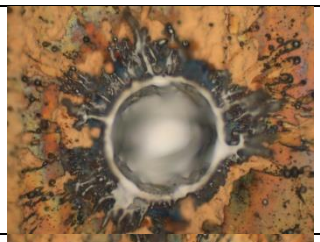
94	11	191	14	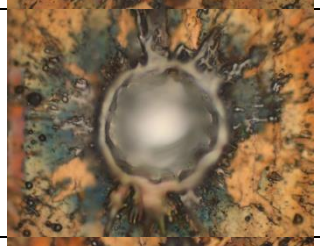
97	13.5	229	14	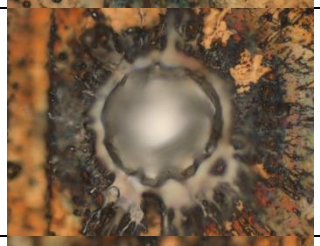
100	15.5	262	14	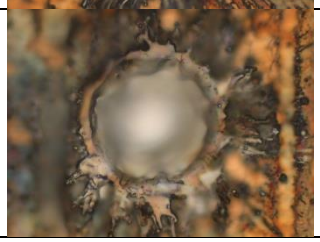

SI%	Set P	E [µJ]	No of pulses	WF 4 – τ=12 ns
82	11	13	9	
85	14	17	9	
88	17	27	9	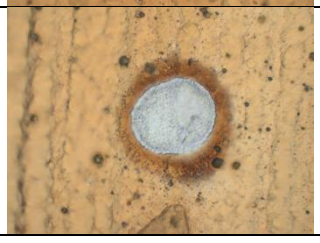

91	20	36	9	

82	11	13	18	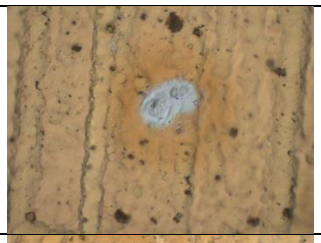
85	14	17	18	
88	17	27	18	
91	20	36	18	

82	11	13	27	
85	14	17	27	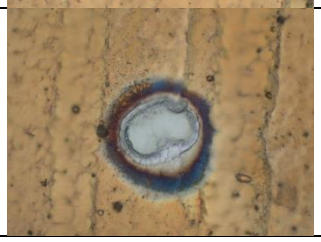

88	17	27	27	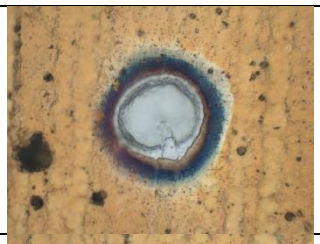
91	20	36	27	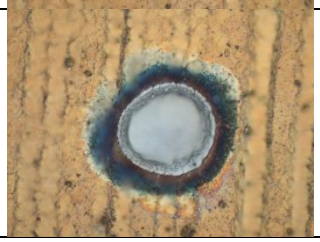

82	11	13	36	
85	14	17	36	
88	17	27	36	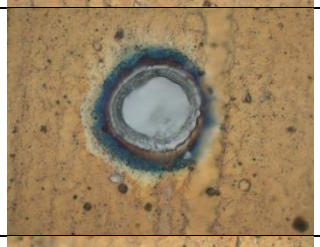
91	20	36	36	

82	11	13	45	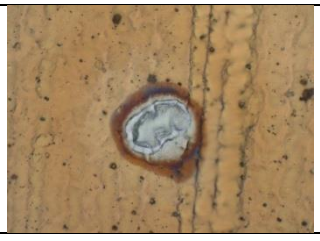

85	14	17	45	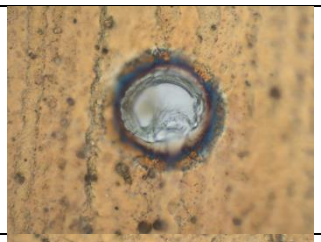
88	17	27	45	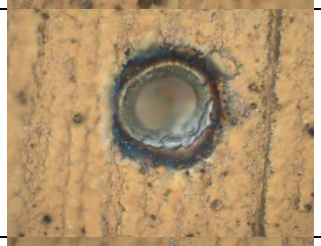
91	20	36	45	

82	11	13	63	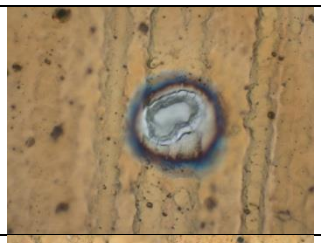
85	14	17	63	
88	17	27	63	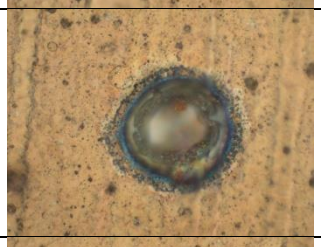
91	20	36	63	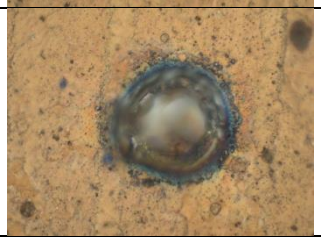

82	11	13	81	
85	14	17	81	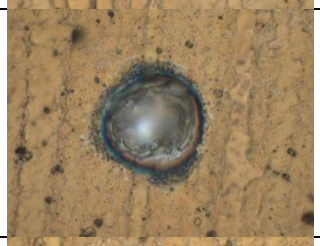
88	17	27	81	
91	20	36	81	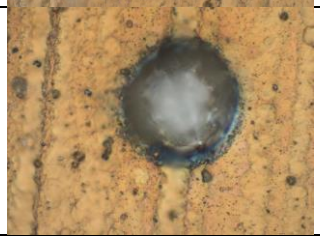

Appendix C

Images of the dimples obtained on TiN coated 39NiCrMo3 steel with MOPA, short ns, 0.5 µm fibre laser

Table C.1. Focus variation microscopy images of the dimples obtained on TiN coated 39NiCrMo3 steel with MOPA, short ns, 0.5 µm fibre laser using the developed processing method.

PRR [kHz]	N	N_{eff}	
20	50	33	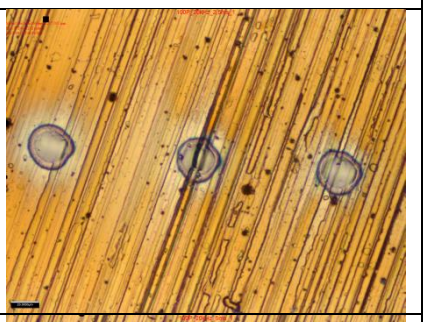
20	100	83	
20	125	108	
20	150	133	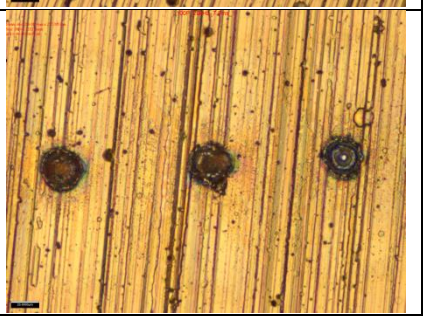

20	200	183	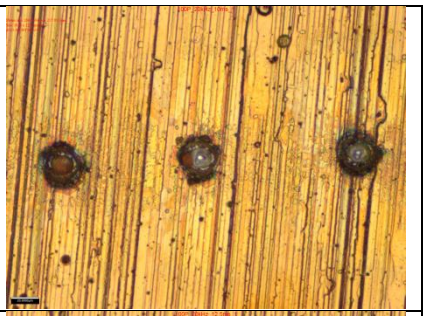
20	250	233	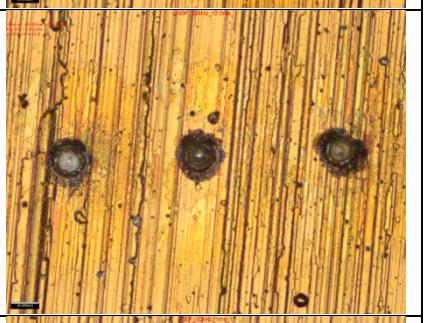
50	50	25	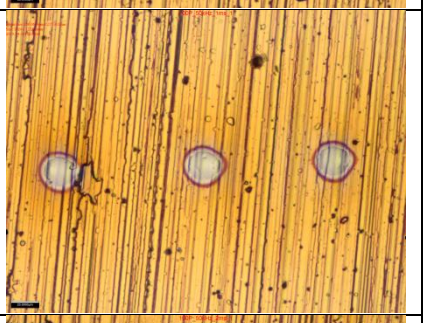
50	100	75	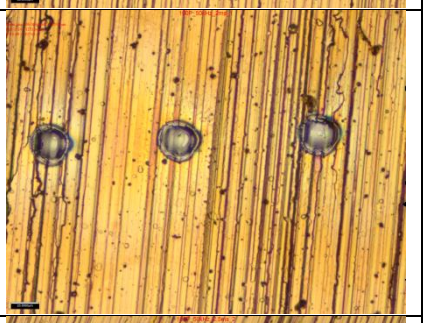
50	125	100	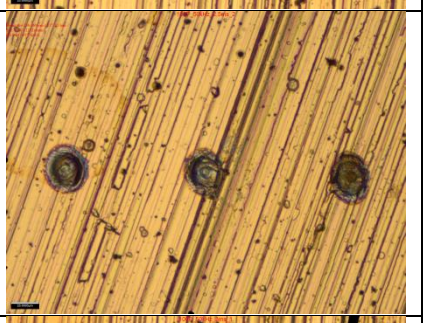
50	150	125	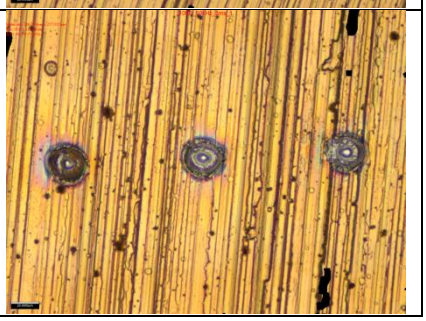

50	200	175	
50	250	225	
175	50	25	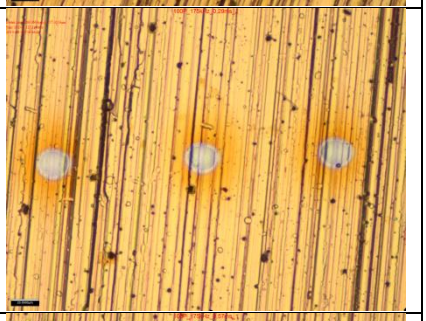
175	100	68	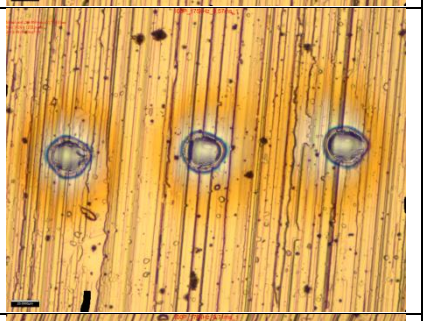
175	125	93	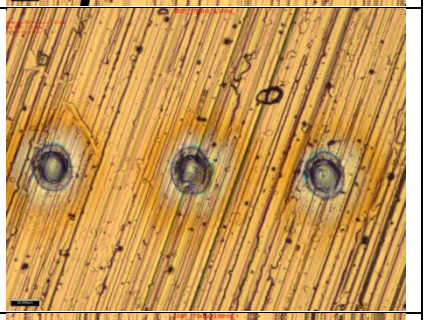
175	150	118	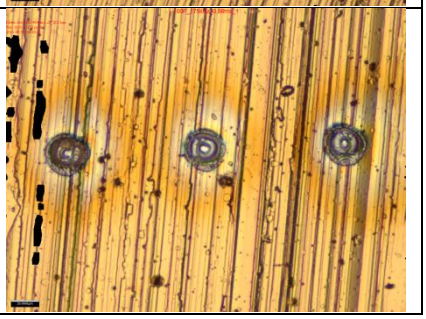

175	200	168	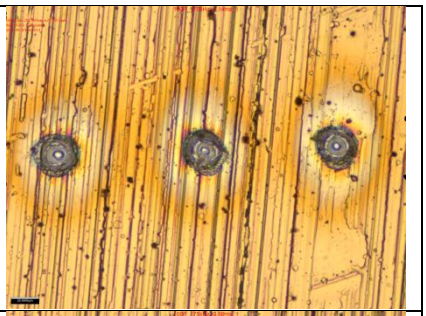
175	250	218	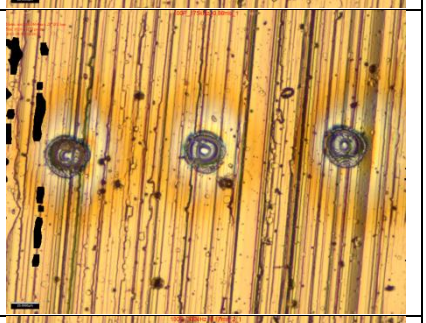
300	50	18	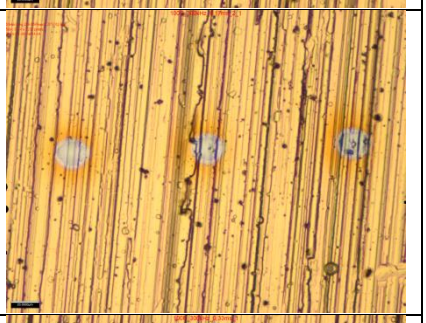
300	100	68	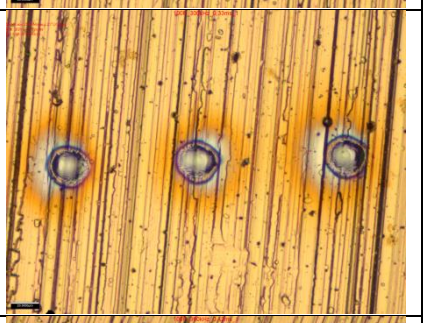
300	125	93	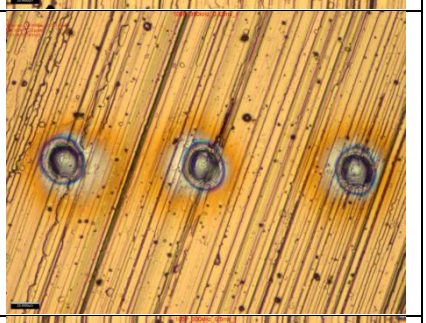
300	150	118	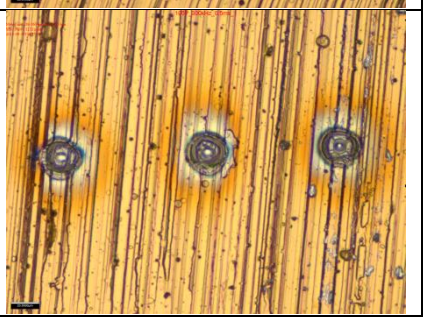

300	200	168	
300	250	218	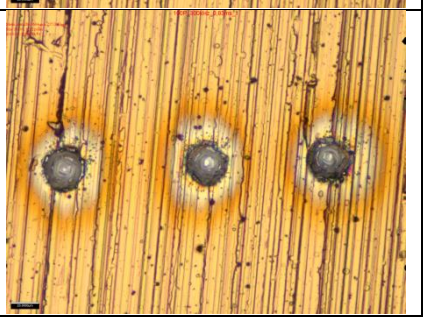

Appendix D

Primary results of the tribological performance of Laser Surface Textured TiN coatings

Wear Behavior of Fiber Laser Textured TiN Coatings in a Heavy Loaded Sliding Regime
L. Vandoni, A.G. Demir, B. Previtali, N. Lecis, D. Ugues
Materials 5 (2012) 2360-2382

The laser dimpling conditions that allowed machining without substrate contamination were used to characterize the textured TiN coatings' tribological performance via flat end pin on disk tests [182]. Chosen dimple geometry was applied with a 100 µm pitch on both axes (see Figure D.1). In particular laser surface textured TiN coatings were compared to plain TiN, self-lubricating WC/C coatings.

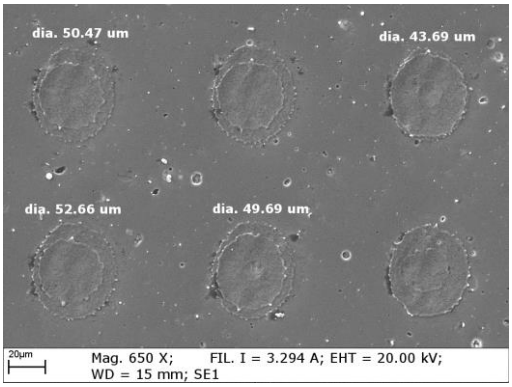

Figure D.1. Morphology of the laser surface textured TiN coating.

Tests were carried out with a flat end counterpart pin made of 18NiCrMo35 steel heat treated and carburized up to a superficial hardness of 58 HRC. The tests were performed with an average sliding speed of $3.86 \cdot 10^{-2}$ m/s and an applied normal force of 1760 N. Such level of force on the contact area provides a nominal pressure of about 90 MPa, giving a PV factor of 3.46 MPa·m/s. The test was carried out using commercial lubricant oil generally used in sliders made from self-lubricating materials (Castrol Hyspin AW 46). The test rig used for the wear test was a NC lathe (Cortini), specifically equipped with a load cell to monitor the tangential force (see Figure D.2). The total sliding distance of the test was 1000 m. Periodical stops and inspections were done at every 250 m. Figure D.1 shows the details of the details of the pin on disc test setup.

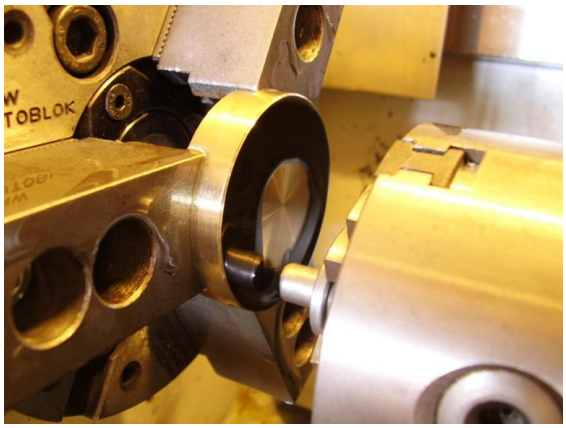

Figure D.2. Details of the pin on disc assembly.

Figures D.3, D.4, and D.5 show the friction coefficients, average wear, and maximum wear depth of the tested coating grades. The results showed a 30% reduction in the friction coefficient, which resulted in a 73% reduction in average wear volume, and 50% reduction in maximum wear depth compared to plain TiN. On the other hand, the textured TiN surfaces exhibited similar friction coefficient compared to WC/C coating. Although WC/C coating initially showed low average wear volume and maximum wear depth levels, it lost its integrity by the end of the pin on disc tests coating failure. It was concluded that the laser surface texturing improved friction performance of TiN coatings to very similar values to the one of WC/C coating, but also improved its lifetime preventing coating failure.

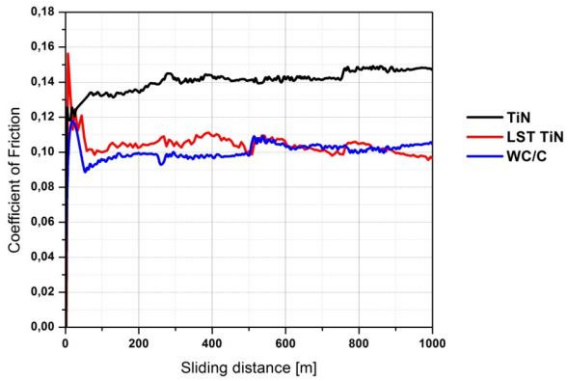

Figure D.3. Friction coefficient as a function of sliding distance for the three coating grades.

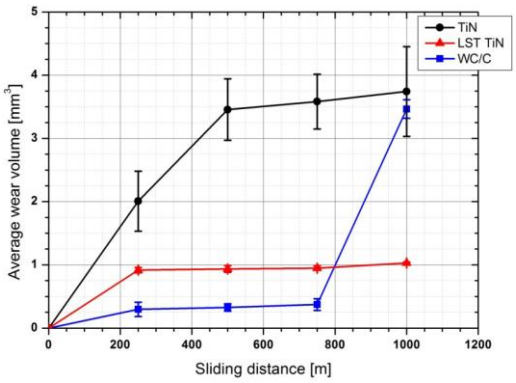

Figure D.4. Average wear volume as a function of sliding distance for the three coating grades.

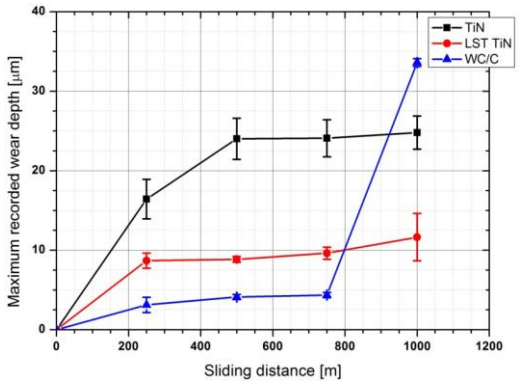

Figure D.5. Maximum wear depth as a function of sliding distance for the three coating grades.

Scratch resistance of fibre laser surface textured TiN coatings

A.G. Demir, N. Lecis, B. Previtali, D. Ugues
Surface Engineering (2013) 29 (9) 654-659

The damage generated by laser surface texturing on the TiN coatings was evaluated via scratch tests [183]. Both substrate contaminated and non-contaminated laser surface texturing conditions were evaluated. Pitch was also studied between 100-200 µm to evaluate the effect of dimple distance on coating failure. Scratch tests were performed using a scratch tester with an increasing load from 0.3 to 30 N. Scratches were made 3 mm in length using a diamond Rockwell indenter with a spherical tip radius of 200 µm sliding at a constant speed of 1.26 mm/min. Severe detachments were observed in dimples with a large amount of substrate contamination, and cracks occurred at 12.8 N ± 3.9. The contamination free dimples did not show cracks until coating failure.

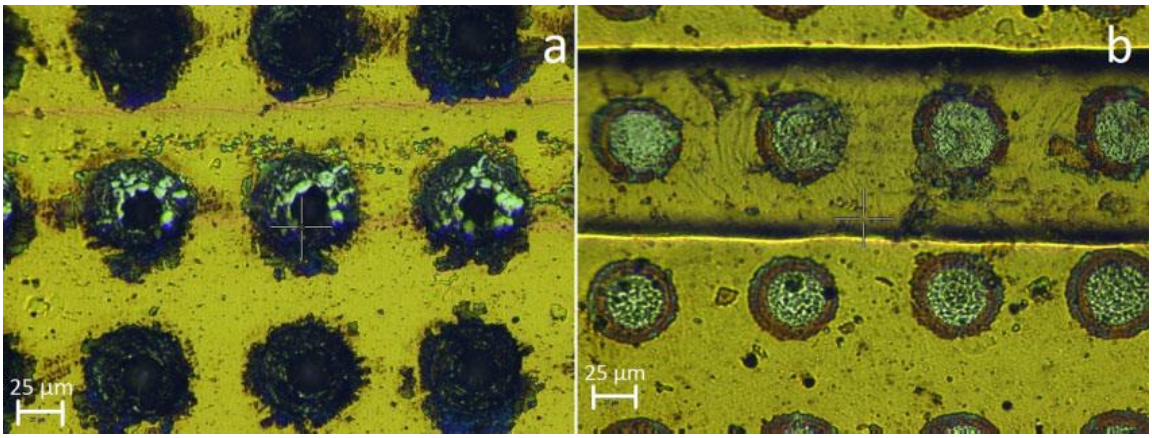

Figure D.6. Optical microscopy images taken during scratch test belonging to a) worst and b) best LST conditions: applied load is 10 N at frame instance.

No significance was found for the parameter that determines the distance between dimples: pitch. This finding suggests that even if partial detachment of dimples occurs, no connection of cracks will be present. Therefore, it can be assumed that under lubricated conditions, partial dimple detachment is more likely, which can contribute to third body wear in the form of debris. However, coating failure due to crack propagation is not expected. Moreover, to increase the proportion of the textured surface compared to the total surface area, smaller, shallow dimples with smaller pitch can be used.

Effetto del substrato e della lavorazione di texturing superficiale su acciai rivestiti in TiN

The effect of substrate and surface texturing on TiN coated steels

MSc. Thesis in Mechanical Engineering, Politecnico di Milano, 2013

S. Bettiga

Supervisor: Prof. N. Lecis

Co-Supervisor: Prof. B. Previtali

The effect of substrate material and lubrication conditions on laser surface textured TiN coatings was studied [184]. Within this study 39NiCrMo3 and AISI M2 substrates were used and evaluated with ball on disc test. The ball material was alumina and the applied load was 1N with a point contact. Along with the non-textured condition (plain), three distinct texturing conditions were chosen representing shallow (LST No 9), medium (LST No 11), and deep conditions (LST No 7) as seen in Table D.1. Friction coefficient and wear volume were evaluated under non lubricated and lubricated conditions using water as lubricant. Figure D.7 shows the volumetric wear of TiN coatings as a function of substrate, texturing, and lubrication conditions. It can be observed that the substrate and the lubrication conditions play a major role in reducing the wear. Deep drilling conditions with substrate contamination resulted in excessive wear on the softer 39NiCrMo3 substrate. Figures D.8 and D.9 show the friction coefficients of the laser surface textured TiN coatings on 39NiCrMo3 and AISI M2 substrates respectively. It can be seen that the surface texture is more beneficial in dry conditions with softer 39NiCrMo3 substrate. The best performing surface texture (LST No 11) compared to plain TiN enabled a reduction of 50% in friction coefficient in dry condition. In lubricated conditions the friction reduction was about 25% compared (LST No 11) to plain TiN but overall the friction coefficient values were much lower than dry condition.

On the other hand, in lubricated conditions textured TiN coatings on AISI M2 substrates did not show significant improvement. However, in dry conditions the best performing surface texture (LST No 11) showed a reduction of 12.5% compared to plain TiN.

In dry conditions the deep texturing resulted in high friction coefficients for both substrate types. This is expected to be due to the detachment of the substrate contaminated area, which later on contributes to friction as third body.

The results confirm that the LST system is required to be evaluated along with the substrate and lubrication conditions. Overall, LST can reduce friction under non-lubricated contact as well, but substrate contamination should be avoided. LST on TiN coatings is more effective on substrates characterized by lower hardness. Therefore, the use of LST can be beneficial for the protection of steel dies made of less expensive materials.

Table D.1. The chosen LST conditions on 39NiCrMo3 and AISI M2 substrates.

LST No.	39NiCrMo3	AISI M2
9	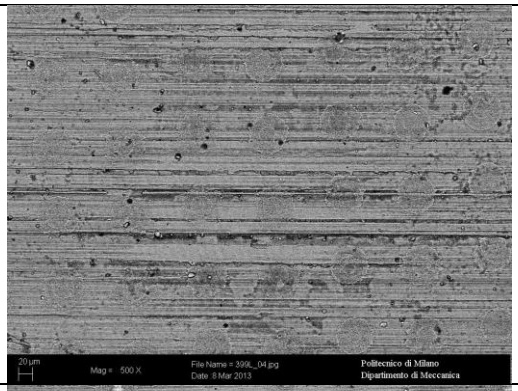	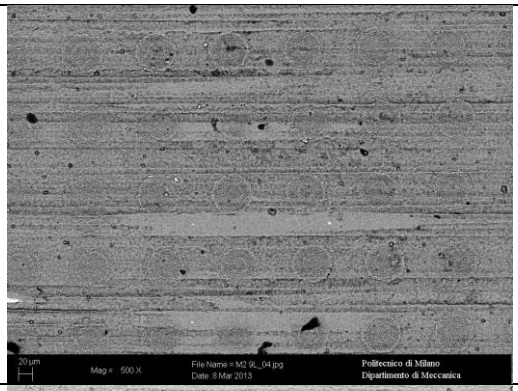
11	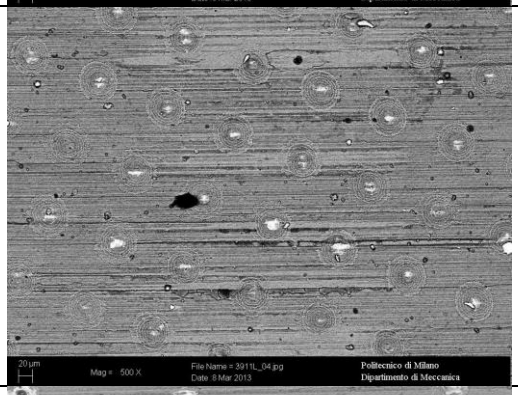	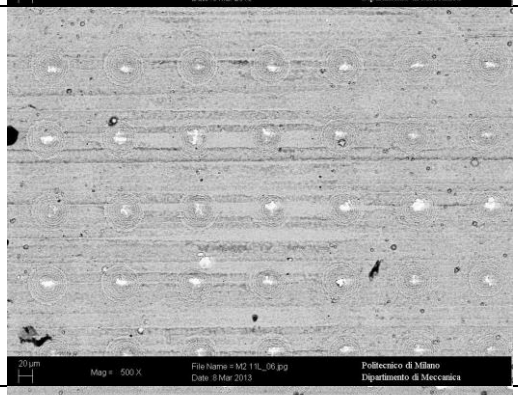
7	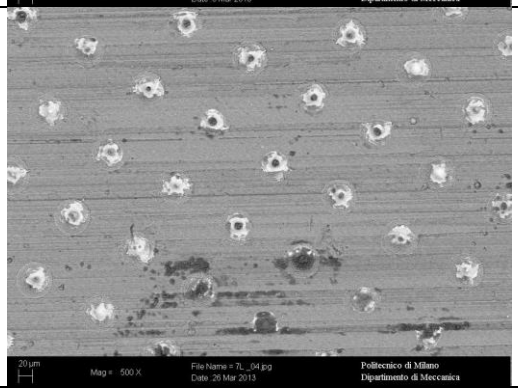	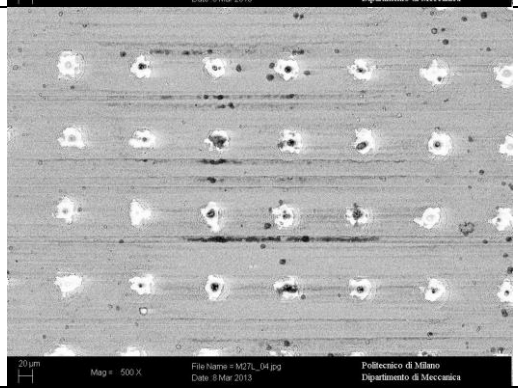

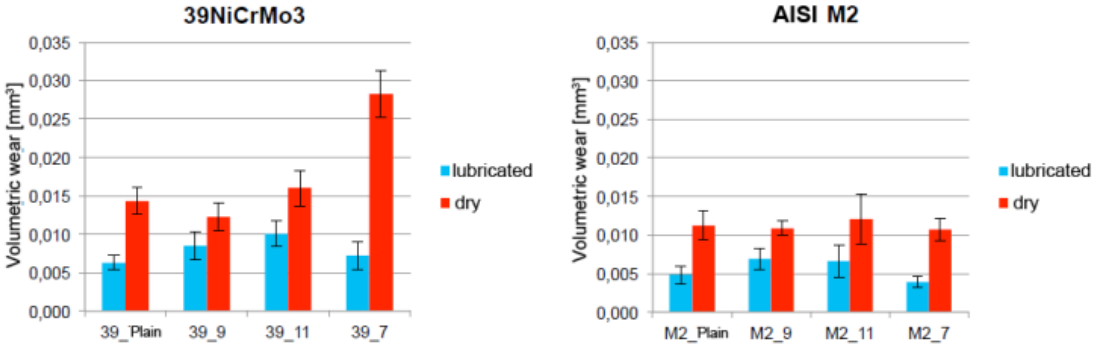

Figure D.7. Volumetric wear of laser surface textured TiN coatings as a function of substrate, lubrication, and texturing conditions.

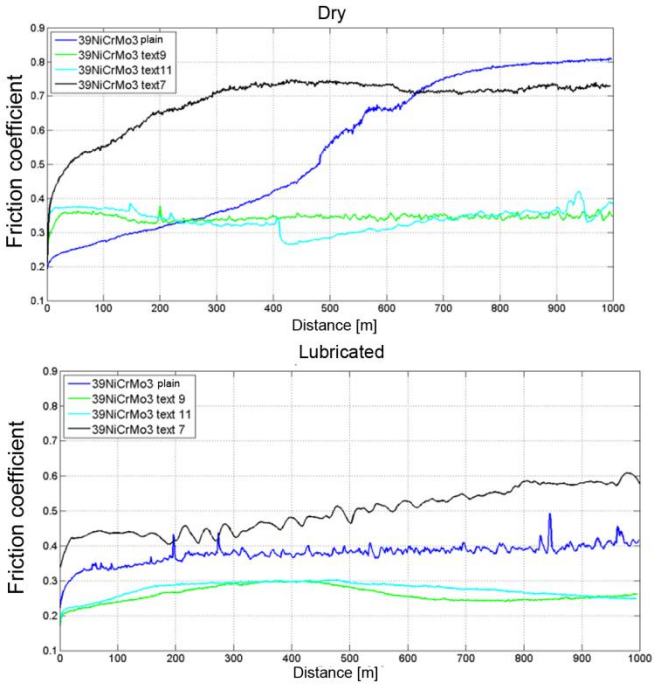

Figure D.8. Friction coefficient of laser surface textured TiN coatings on 39NiCrMo3 substrate in dry and lubricated conditions.

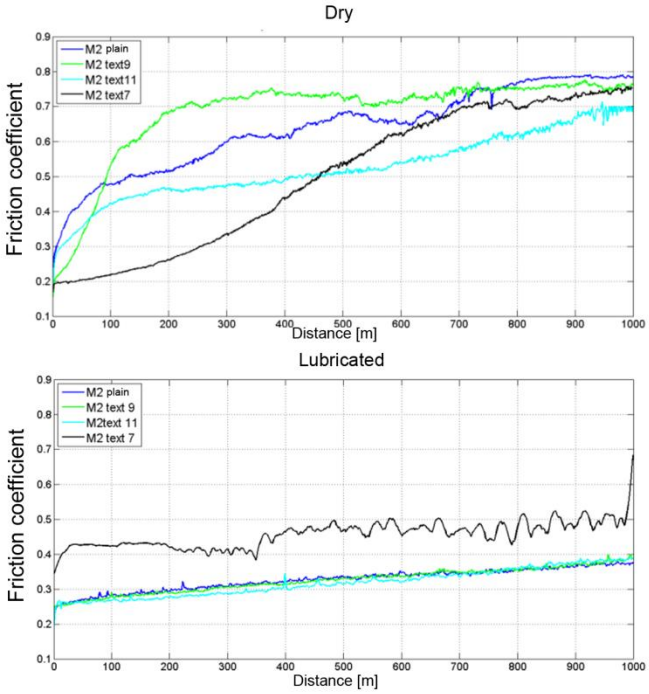

Figure D.9. Friction coefficient of laser surface textured TiN coatings on AISI M2 substrate in dry and lubricated conditions.